Vol. 17, No. 2, 2021

Journal of Global Positioning Systems

ISSN 1446-3156 (Print Version) ISSN 1446-3164 (CD-ROM Version)

International Association of Chinese Professionals
in Global Positioning Systems (CPGPS)

Journal of Global Positioning Systems

Aims and Scope

The Journal of Global Positioning Systems is a peer-reviewed international journal for the publication of original research papers, review articles, invited contributions, also including selected papers presented at non-referred conferences and symposiums. Articles should present discussions of technologies and applications of any positioning systems, including Global Navigation Satellite Systems (GNSS) and their various augmentations and local components, and other positioning and navigation technologies, such as indoor positioning, and inertial, visual navigation systems and their integrations. Articles presenting advances of other related areas, such as wireless communications, intelligent vehicle systems, sensor networks, spatial information and geosciences are also welcome. Short research and technical notes, book reviews, lecture series and commercial advertisements can be included. Specific questions about the suitability of prospective manuscripts may be directed to the Editor-in-Chief.

Editor-in-Chief

Jianguo Wang, Dr.-Ing., P.Eng., FEC
York University, Toronto, Canada
Email: jgwang@yorku.ca

Associate Editor-in-Chiefs (*alphabetic*)

Jianghui Geng, jgeng@whu.edu.cn
Wuhan University, *Wuhan*
George Liu, lszzliu@polyu.edu.hk
The Hongkong Polytechnic University, HK
Jian Wang,wangjian@bucea,edu.cn
Beijing University of Civil Engineering and Architecture, China
Dongkai Yang, edkyang@buaa.edu.cn
Beihang University, Beijing
Yunbin Yuan, yybgps@whigg.ac.cn
Institute of Geodesy & Geophysics, Academy of Sciences, Wuhan

Editorial Board (*alphabetic*):

Changsheng Cai, csucai@csu.edu.cn
Central South University, Changsha
Wu Chen, lswuchen@polyu.edu.hk
Hong Kong Polytechnic University, HK
Yuwei Chen, yuwei.chen@nls.fi
National Land survey of Finland
Junping Chen, junping@shao.ac.cn
Shanghai Astronomic Observertory
Kai-Wei Chiang,
kwchiang@geomatics.ncku.edu.tw
National Cheng Kung University, Tainan
Shaojun Feng, dr.shaojunfeng@yahoo.com
Qianxun Spatial Intelligence Inc., Shanghai
Yang Gao, ygao@ucalgary.ca
University of Calgary, Calgary, Canada
Xiufeng He, xfhe@hhu.edu.cn
Hehai University, Nanjing
Kaifei He, kfhe@upc.edu.cn
China University of Petroleum, Qingdao
Guanwen Huang, guanwen@chd.edu.cn
Chang'An University, Xi'An
Shuanggen Jin, sgjin@shao.ac.cn
Shanghai Astronomical Observatory, Shanghai
Xingxing Li, xxli@sgg.whu.edu.cn
Wuhan University, Wuhan
Zhenghong Li, zhenhong.li@chd.edu.cn
Chang'An University, Xi'An
Jingbin Liu, jingbin.liu@whu.edu.cn
Wuhan University, Wuhan
Xiaolin Meng, mengxl@bjut.edu.cn
Beijing University of Technology, Beijing
Xiaoji Niu, xjniu@whu.edu.cn
Wuhan University, Wuhan
Ling Pei, ling.pei@sjtu.edu.cn
Shanghai Jiaotong University, Shanghai
C. K. Shum, ckshum@osu.edu
Ohio State University, USA
Qian Sun, qsun@hrbeu.edu.cn
Harbin Engineering University, Harbin
Caijun Xu, cjxu@sgg.whu.edu.cn
Wuhan University, Wuhan
Lei Yang, yanglei@sdau.edu.cn
Shandong Agricultural University
Ling Yang, lingyang@tongji.edu.cn
Tongji University, Shanghai
Baocheng Zhang, b.zhang@whigg.ac.cn
Institute of Geodesy & Geophysics, China Academy of Sciences, Wuhan
Kefei Zhang, kefei.zhang@rmit.edu.au
RMIT University, Australia
Xiaohong Zhang, xhzhang@sgg.whu.edu.cn
Wuhan University, Wuhan
Ya Zhang, yazhang@hit.edu.cn
Harbin Institute of Technology, Harbin
Dongsheng Zhao,
dszhao_gnss@foxmail.com
China University of Mining and Technology, Xuzhou
Huizhong Zhu, zhuhuizhong@lntu.edu.cn
Liaoning Technical University, Fuxin

Administrative Support Team

(**Assistants** to Editor-in-Chief and to Associate Editor-in-Chiefs)

Benjamin Brunson, brunson@yorku.ca
York University, Toronto, Canada
Dongsheng Zhao, dszhao_gnss@foxmail.com
China University of Mining and Technology Xuzhou
Xingxing Li, xxli@sgg.whu.edu.cn
Wuhan University, Wuhan
Changsheng Cai, csucai@csu.edu.cn
Central South University, Changsha
Guanwen Huang, guanwen@chd.edu.cn
Chang'An University, *Xi'An*
Lei Yang, yanglei@sdau.edu.cn
Shandong Argricultural University, Taian
Baocheng Zhang, b.zhang@whigg.ac.cn
Institute of Geodesy & Geophysics, CAS, Wuhan

Editorial Advisory Board

Junyong Chen, PhD, Academician CAS
National Administration of Surveying, Mapping and Geoinformation, China

Yongqi Chen, PhD
Hong Kong Polytechnic University, Hong Kong

Günter Hein, Dr.-Ing., Habil. Dr. h.c.
University FAF Munich, Germany

Gerard Lachapelle, PhD, Dr. Techn, P.Eng.
University of Calgary, Canada

Jingnan Liu, Academician CAE
Wuhan University, China

Washington Yotto Ochieng, PhD
Imperial College London, UK

Chris Rizos, PhD
The University of New South Wales, Australia

Peter J.G. Teunissen, dr.ir.
Delft University of Technology, The Netherlands

The Past Editor-in-Chiefs

Jinling Wang *(Founding Editor-in-Chief), The University of New South Wales, Sydney, Australia*
Yanming Feng, *Queensland University, Brisbane, Australia*
Ruizhi Chen, *Wuhan University, Wuhan, China*

Publication and Copyright

The Journal of Global Positioning Systems is an official publication of the International Association of Chinese Professionals in Global Positioning Systems (CPGPS). It is published twice a year, in June and December. The Journal is available in both print version (ISSN 1446-3156) and CD-ROM version (ISSN 1446-3164), which can be accessed through the CPGPS website at http://www.cpgps.org/journal.php. Whilst CPGPS owns all the copyright of all text material published in the Journal, the authors are responsible for the views and statements expressed in their articles. Neither the authors, the editors nor CPGPS can accept any legal responsibility for the contents published in the journal.

© CPGPS, 2002 - 2021. All the rights reserved.

Journal of Global Positioning Systems (*2021*)
Vol. 17, No. 2

Table of Contents

ABSTRACTS OF PHD DISSERTATIONS

Journal of Global Positioning Systems (*2021*)
Vol. 17, No. 2: 135-150
DOI: 10.5081/jgps.17.2.135

On long-baseline relative positioning with BDS-2/BDS-3/GPS data

Xiaoting Lei[1],Huizhong Zhu[1*], Jingfa Zhang[1] ,Jun Li[1] , Yangyang Lu[1]

1 School of Geomatics, Liaoning Technical University (LNTU), Fuxin 123000, China;
***** Correspondence: Huizhong Zhu, zhuhuizhong@lntu.edu.cn

Abstract: BeiDou global navigation satellite system (BDS-3) reached the global coverage in June 2020. To study the performance of the precise relative positioning using the BDS-3 alone and the improvement due to adding BDS-3 satellites to BDS-2 and GPS, this paper analysed the data of 033-039d provided by the MGEX in 2021. The fusion of BDS-2, BDS-3 and GPS data was conducted for static and dynamic high-precision long-baseline solution experiments. The influence of the individual BDS-2 / BDS-3 / GPS and by adding BDS-3 satellites to BDS-2 and GPS on precise relative positioning convergence speed and positioning accuracy were analyzed, respectively. The experimental results show that the current BDS-3 positioning performance (convergence speed and positioning accuracy) is similar to GPS, and the BDS-3 satellites effectively improve the positioning convergence speed upon BDS-2 and GPS. In the static positioning processing mode, with the aid of the BDS-3 satellites, the RMS (Root-Mean-Square) of the positioning errors using GPS only and the combination of BDS-2 and GPS was increased only by 20 % in the up direction, and for the BDS-2 system alone, the positioning accuracies in the E, N and U components were increased by 60%, 71% and 65%, respectively. In the dynamic positioning processing mode, after the addition of BDS-3 satellites, the positioning accuracies using GPS and GPS+BDS-2 in the E, N and U components were improved by about 15 %, 23 % and 23 %, respectively, and the BDS-2 positioning accuracies were improved by about 46 %, 38 % and 36 % in the E, N and U components, respectively.

Keywords: BDS-3; baseline solution; Multi-system Fusion; convergence speed

1 Introduction

The Beidou Navigation Satellite System (BDS) is one of the Global Navigation Satellite Systems (GNSS), developed by China. By following the "three-step" strategic policy, China has steadily been promoting the development of the BDS. The BDS-1 was officially launched in 1994, and the BDS-2 system started in 2004 and was completed at the end of 2012 with the service for Asia-Pacific region [1]. BDS-3 has been developed since 2015 and put into a global service on July 31, 2020 [2]. The complete BDS-3 constellation consists of 24 Medium Earth Orbit (MEO) satellites, 3 Geostationary Earth Orbit (GEO) satellites and 3 Inclined Geo Synchronous Orbit (IGSO) satellites. In terms of its signals, BDS-3 satellites broadcast the B1I and B3I frequencies to achieve the compatibility with BDS-2. At the same time, in order to strengthen the compatibility and interoperability with other GNSS systems, BDS-3 has also been equipped with three new signals B2a, B2b and B1C [3], which can provide better positioning, navigation and timing (PNT) services for users globally [4].

Since the BDS was put into use, many scholars in China and abroad have done plenty of researches on its performance of BDS alone, or GPS + BDS combined [5-8]. Zhang et al. [9] show that the accuracy of a static baseline (medium baseline,

Editor in charge: Dr. Baocheng Zhang

<100km) using the four-hour long BDS measurement data based on the broadcast ephemeris reached ±4cm. Pu et al and Wu et al. [10, 11] analyzed the relative positioning performance using the combination of the GPS, BDS and Galileo systems with the short baseline hybrid double-difference and short baseline single epoch tight combination. Their results showed that the dual-system or triple-system hybrid double-differencing technique can effectively accelerate the convergence speed toward the positioning accuracy improvement, and the tight combination model significantly improved the success rate and reliability in ambiguity fixing process. Jin et al. [12] showed that, in the solution of 5km short baseline, the accuracy through the combined BDS-2 and BDS-3 was improved in comparison with GPS or BDS-2 alone, at the positioning accuracy of within ±5mm.

To date, most researches have got involved in all aspects of BDS-2 positioning functions based on BDS-2, and mostly on precise relative positioning using BDS-2 alone or GPS + BDS-2 combined for short baselines. Therefore, this paper focuses on analyzing how significant the addition of BDS-3 satellites to each single GNSS, GPS and BDS-2 and the combined GPS+BDS-2 contributes to the performance of long-baseline solutions. Section 1 presents the mathematical model employed in this research, while Section 2 details the experiments of the chosen baselines of different lengths using the BDS-3 observation data and discusses the stability, convergence speed and positioning accuracy of the different GNSS constellations and their combinations in static and dynamic relative positioning from the results. Section 3 ends the manuscript with the conclusions and remarks. The outcomes from this research provide a valuable reference for the use of BDS-3 and its combined positioning with GPS.

2 Mathematical model and data processing strategy

2.1 Mathematical model

In this paper, the common frequencies of B1I, B3I from BDS-2 and BDS-3, and GPS L1 and L2 are used to form the double-differenced ionosphere-free combination to eliminate the influence of first-order error of the ionospheric delay. The equations of the original observables are:

$$\left.\begin{aligned} P &= \rho + H_k^j X + c \cdot dt_k - c \cdot dt^j + b_{r,k} - b_k^j + I_k^j + d_{trop} + \varepsilon_P \\ \Phi &= \rho + H_k^j X + c \cdot dt_k - c \cdot dt^j + \lambda_j \left(B_{r,k} - B_k^j \right) - I_k^j + \lambda N_k^j + d_{trop} + \varepsilon_\Phi \end{aligned}\right\} \tag{1}$$

where: P and Φ are the pseudo-range and carrier-phase measurements, respectively; ρ represents the geometric distance from a receiver station to a satellite; H is the linearized coefficient vector of the receiver's position, X is the 3D position correction vector of the receiver with respect to their approximations, k represents the receiver station; j represents the satellite (j = 1, 2, …); c is the speed of light in vacuum; dt_k is the receiver's clock error; dt_j is the satellite's clock error; $b_{r,k}$ and b_k^j represent the code hardware delays of the receiver and satellite, respectively; $B_{r,k}$ and B_k^j represent the phase hardware delays of the receiver and satellite, respectively; $\boldsymbol{I}$ is the ionosphere delay error; $\boldsymbol{N}$ is the carrier phase ambiguity with respect to the satellite; d_{trop} is the troposphere delay; ε_P、ε_Φ are other errors of pseudo-range and phase observations, including noise, multipath effect and so on. A pair of the observation equations as (1) could be made available for each of the visible satellites corresponding to each of a specific signal frequency, respectively. The equations of the double-differenced ionosphere-free combinations are:

$$\left.\begin{aligned} \Delta\nabla P_{IF} &= \Delta H_k^j X + \Delta\nabla\rho + \Delta\nabla d_{trop} + \Delta\nabla\varepsilon_P \\ \Delta\nabla\Phi_{IF} &= \Delta H_k^j X + \Delta\nabla\rho + \lambda_{IF}\Delta\nabla N_{IF} + \Delta\nabla d_{trop} + \Delta\nabla\varepsilon_\Phi \end{aligned}\right\} \tag{2}$$

where $\Delta\nabla$ represents the double-differencing operator; the subscript *IF* represents the ionosphere-free combination, and the others are the same as in (1).

As well known, the zenith troposphere delay is divided into the dry and wet components. The dry component accounts for 80% - 90% of the total delay [16] and is corrected by using the Saatamoinen formulae, Then, the remaining wet component of tropospheric delay is estimated as follows:

$$d_{trop} = M_{dry}T_{dry} + M_{wet}T_{wet} \tag{3}$$

The ambiguity associated with a double-differenced ionosphere-free combination is expressed as:

$$\lambda_{IF}\Delta\nabla N_{IF} = \frac{f_1^2}{f_1^2 - f_2^2}\lambda_1\Delta\nabla N_1 - \frac{f_2^2}{f_1^2 - f_2^2}\lambda_2\Delta\nabla N_2 \tag{4}$$

$$\Delta\nabla N_{IF} = \frac{f_1}{f_1 - f_2}\Delta\nabla N_1 - \frac{f_1 f_2}{f_1^2 - f_2^2}\Delta\nabla N_{NW} \tag{5}$$

where $\Delta\nabla N_{NW} = \Delta\nabla N_1 - \Delta\nabla N_2$ is the wide-lane ambiguity, which can obtained by Melbourne-Wübbena (M-W) combination for inter epoch smoothing. The ambiguity $\Delta\nabla N_1$ in (5) has the integer characteristic and can be fixed by applying the Least-square AMBiguity Decorrelation Adjustment (LAMBDA).

1.2 Stochastic model

In general, the quality of the GNSS observation data and the elevation angles of the visible satellites are apparently related to each other. A consensus on the elevation angle of a satellite tells that the lower it is, the negative impact on the GNSS observations, the troposphere delay and multipath effect etc. would have [17]. This research specifically adopted the elevation angle based weighting model to determine the weight of corresponding observations:

$$\sigma^2 = \begin{cases} \dfrac{\sigma_0^2}{sin^2(E)}, E < 30° \\ \dfrac{\sigma_0^2}{sin(E)}, E \geq 30° \end{cases} \tag{6}$$

Moreover, the variances for pseudoranges and carrier phases are specified as follows:

$$D\left\{\begin{pmatrix} \tilde{\Phi}_{IF} \\ P_{IF} \end{pmatrix}\right\} = \begin{pmatrix} \sigma_\Phi^2 & 0 \\ 0 & \sigma_P^2 \end{pmatrix} \tag{7}$$

wherein σ^2 means the variance of an observation; σ_0^2 is the a priori variance factor; E is the elevation angle of a satellite; $D\{\bullet\}$ represents the variance (matrix) operator; σ_φ^2 and σ_P^2 represent the variances of a pseudorange and a carrier phase observation, respectively..

2 Experiments and their analysis

The stations, YAR2 and NNOR in Australia and TASH, KITG, KIT3, USUD and MIZU in Asia provided by the Multi-GNSS Experiment (MGEX) observation network were chosen for our experiments in this research (Figure 1). By using the seven-day observation data from 033d to 039d in 2021, four baselines, KITG-KIT3 (190 m), YAR2-NNOR (236 km), TASH-KITG (318 km) and USUD-MIZU (413km) were formed. An overview of the formed baselines is given in Table 1. The station coordinates in the Solution INdependent EXchange Format (SINEX) weekly solution file released by the international GNSS service (IGS) were taken as their true coordinates, whilst the phase center offsets (PCO) and phase center variation (PCV) corrections of GPS satellites and receiver antennas were taken from the ANTEX file issued by IGS. However, the current international service center only provides the BDS satellite PCO correction [18]. The positioning performance of the different GNSS systems was analyzed in terms of the convergence speed and positioning accuracy with the BDS-2, BDS-3 and GPS individually and their varied combinations, which are specified in the context of the individual tests.

In data processing, the cut off elevation angle was set to 7° and the used sample interval of the observation data was 30s. The precise orbital products provided by the German Research Center for Geosciences (GFZ) were used. The troposphere delays were corrected by the Saatamoinen model and their residual errors were modeled, whilst the first-order ionosphere delay was eliminated by applying the ionosphere-free combination. The least-square method was implemented for baseline estimation. The LAMBDA algorithm was used to fix the ambiguity parameters. The systematic errors such as the phase winding up, Earth’s rotation, relativistic effect and solid tide were corrected by the commonly available models accordingly. A summary of data processing strategy is given in Table 2.

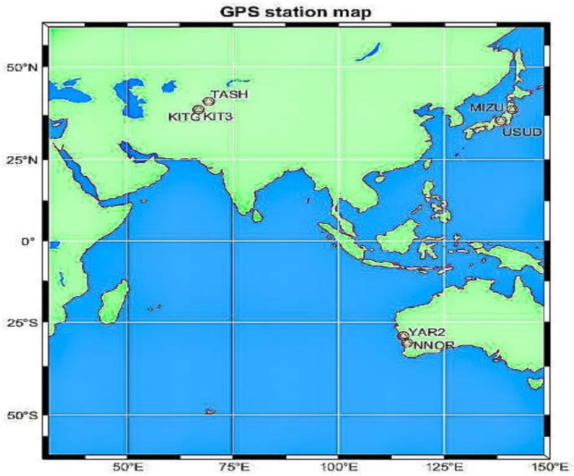

Figure 1: Distribution of stations

2.1 Data quality analysis

To ensure the data availability in the experiments before the data processing, the data quality is analyzed in three aspects: the satellite visibility, signal-to-noise ratio and multipath error effect. By taking the data on the DOY of 033 in 2021 as an example, it can be seen from Figure 2 that the number of the common visible BDS-3 satellites was more than that of the BDS-2 satellites, and the number of the common visible BDS-3 satellites was between 6 and 11. Specifically, the number of the common visible BDS-3 satellites for the baseline of USUD-MIZU (413km) in Asia was 9, and the number of the common visible BDS-2 satellites was about 8. With GPS, the number of the common visible satellites between stations maintained between 6 and 12. The number of the common visible GPS satellites for the baselines of KITG-KIT3 (190 m) and DASH-KITG (318 km) was significantly more than the one of the common visible BDS satellites, which was about 9 to 10 satellites. In general, The numbers of the common visible satellites from BDS-2, BDS-3 and GPS were sufficient for conducting our experiments.

Table 1: Baseline information

length	station	longitude	latitude	Antenna type	
190 m	YAR2	115°E	29°S	AOAD/M_T	NONE
	NNOR	116°E	31°S	SEPCHOKE _B3E6	NONE
236 km	TASH	69°E	41°N	SEPCHOKE _B3E6	NONE
	KITG	66°E	39°N	TRM59800.00	SCIS
318 km	USUD	138°E	36°N	AOAD/M_T	JPLA
	MIZU	141°E	39°N	SEPCHOKE _B3E6	NONE
413 km	KITG	66°E	39°N	TRM59800.00	SCIS
	KIT3	66°E	39°N	SEPCHOKE _B3E6	NONE

Table 2: Data processing strategy

DOY (observation data)	033d - 039d, 2021
Positioning mode	Precise relative positioning
Satellite systems	BDS-2、BDS-3、GPS
Satellite orbital products	Precise products provided by GFZ
Cut off elevation angle	7°
Sample interval	30 seconds
Troposphere dry delay	Saastamoinen
Troposphere wet delay	Estimated as parameters
Ionosphere	Ionosphere-free combination
Estimation method	Least-square
Ambiguity fixing method	LAMBDA

The average values of Signal-to-Noise Ratio (SNR) and multipath error in the data at each station during 7 days from 033d to 039d were analysed and presented in Figure 3 and Figure 4, respectively. The SNR, the ratio of signal strength of carrier observation to noise strength [19], can be used to measure the quality of the acquired satellite signals and the unit in dB-Hz. The higher the SNR, the higher data quality the carrier phases would have. As can be seen from Figure 3, the SNR of B3I was the highest. L1 and B1I were similar which maintained above 40 dB−Hz. The SNR of the L2 signal was low, but still higher than the minimum threshold of 30 dB−Hz required by a standard data processing.

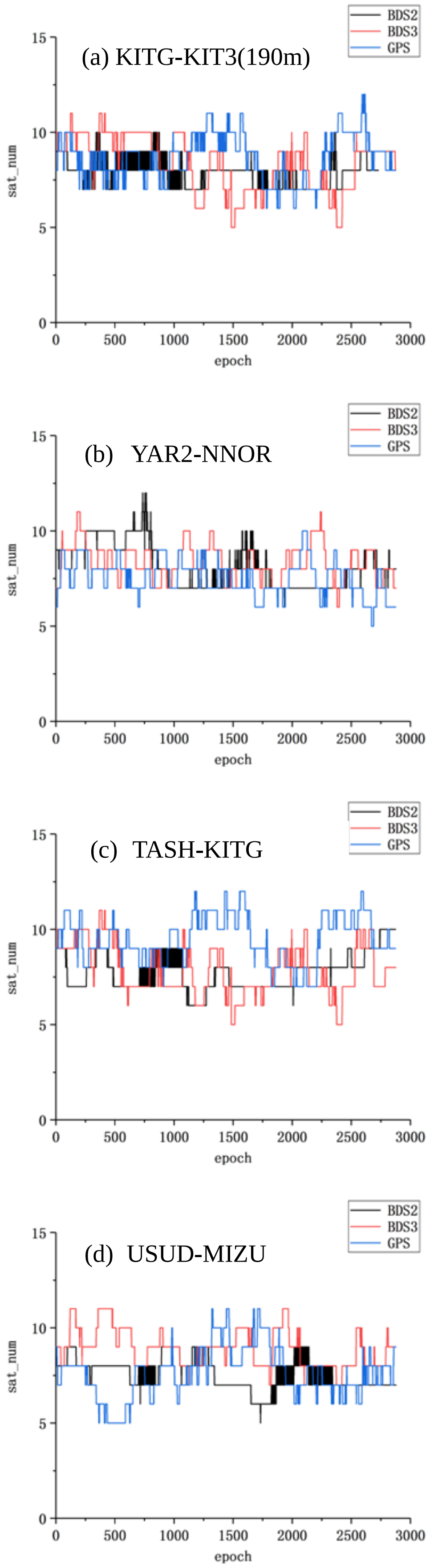

Figure 2: Total Number of common visible Satellites among Stations

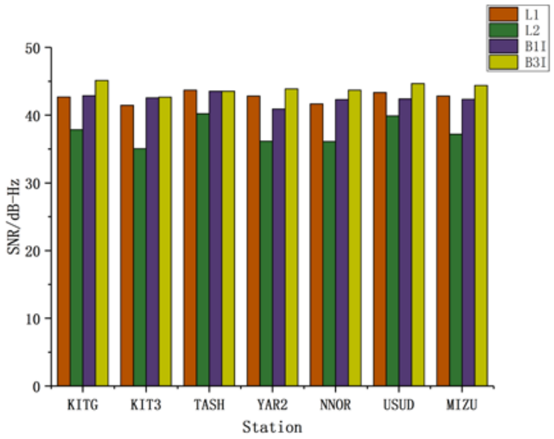

Figure 3: Signal-Noise Ratio of Each Station

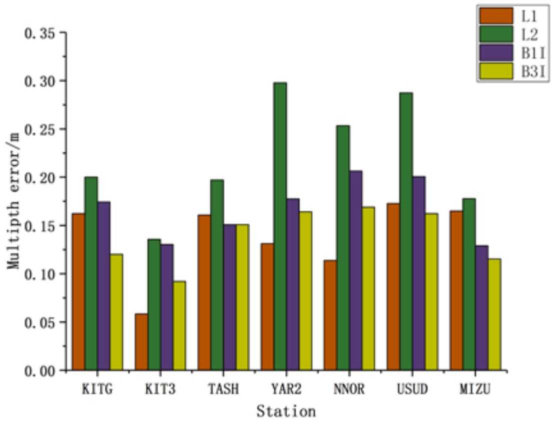

Figure 4: Multipath Error on Signals at Each Station

In the process of signal propagation, the acquired satellite signal could be affected by the observation environment. For example, a receiver may receive the excess reflected signal from a certain type of the signal reflections, which is called multipath error. In comparison with the phase observations, the multipath error on pseudo-ranges could be large, even reach 0.5 code element width [20]. Figure 4 presents the multipath errors from four signals, of which the GPS L2 signal suffered from the largest multipath error, the multipath errors on BDS B1I were larger than that on B2I, whilst the GPS L1 signal had the best suppression of the multipath errors and possessed the best observation quality. In general, the multipath error in pseudo-ranges at each station signal was within 0.3 m.

2.2 Convergence speed

The commonly used evaluation measure is the convergence speed, which statistically analyses the convergence time, i.e., the Time To First Fix (TTFF). In order to introduce the TTFF analysis, with the 7-day data from 033d to 039d in 2021, the 24-hour daily data were divided into the 6-hour long sub-periods. The starting hour of each sub-period is one hour shifted from its previous one, which are 00:00:00, 01:00:00,..., Respectively (e.g., 00:00:00-06:00:00, 01:00:00-07:00:00…). In the static and dynamic positioning processing mode, seven different combinations of GPS, BDS-2 and BDS-3 are solved, and the baseline vector (i.e., the ECEF incremental coordinates) between two stations need to be converted into their E, N, and U components relative to the base station. To ensure a reliable statistics, the differences in E, N, U directions of 20 consecutive epochs after the convergence time needs to reach and maintain their magnitudes relative to their references at the centimeter level. Hereupon, the statistics of the convergence time with the different combinations within each sub-period of the four groups of baselines was carried out respectively, and then the dynamic and static convergence rates associated with the seven combinations were analyzed. The statistical results are shown in Table 3 and Table 4, respectively while the convergence time statistics of static and dynamic solutions are shown in Figure 5 and Figure 6, respectively.

In the static positioning processing mode, as shown in Table 3, the convergence process of resolving the short baseline is faster than the one of resolving the long baseline. The average convergence time with GPS alone remained within 20 min. Due to the sufficient number of common visible GPS satellites observed over the baseline of TASH-KITG (318 km) in Asia, the convergence speed was the fastest, reaching the centimeter accuracy in about 6 minutes. The number of the observed BDS-3 satellites in Asia was large, and its convergence speed was equivalent to or even better than with GPS. The average convergence time of GPS+BDS-3 dual-system was within 10 min, 63% higher than that of GPS alone. The convergence speed of BDS-2 alone was the slowest with the average convergence time of nearly 50 min. The average convergence time of BDS-2+ BDS-3 dual-system remained about 15 min, about 70% higher than that of BDS -2 only. As can be seen from Figure 5, the worst convergence process happened to BDS-2 only on the DOY of 034d in 2021 for 58 min. With the aid of BDS-3 satellites, the convergence time was decreased down to 9 min, and the convergence speed was increased by 84%. The improvement of the convergence process of GPS+BDS-2 dual-system was good, which reached the centimeter accuracy in about 10 minutes. Furthermore, the overall convergence speed was increased by about 40% after having integrated the BDS-3 satellites.

In the dynamic positioning processing mode, the baseline results are summarized in Table 4. The convergence time of GPS only was about 50 min. By adding BDS-3 satellites, the convergence time was decreased down to about 20 min, an incensement of the convergence speed by about 60%. The convergence speed of BDS-3 only was the same as that of GPS, which maintained to be about 50 min, as the convergence speed of BDS-2 only was the slowest in dynamic mode. As can be seen from Figure 6, the convergence speed of BDS-2 only was consistent in various regions and the average convergence time was about 140 min. With the aid of the BDS-3 satellites, it took about 30 min to achieve cm level convergence accuracy, and the overall convergence speed was increased by 80%. From the combined GPS+BDS-2, the convergence time was stably about 30 minutes. The addition of the BDS-3 satellites decreased the convergence time down to 15 minutes, i.e., a 50% improvement.

In general, the BDS-2 positioning process in static and dynamic modes went convergent significantly slower than GPS. Although the number of the BDS-2 satellites at most of epochs was not less than the number of the GPS satellites, the number of the BDS-2 MEO satellites was low, and the orbit accuracy of the BDS-2 satellites was lower than that of the GPS satellites. So, the BDS-2 convergence time was much longer than GPS. Many more MEO

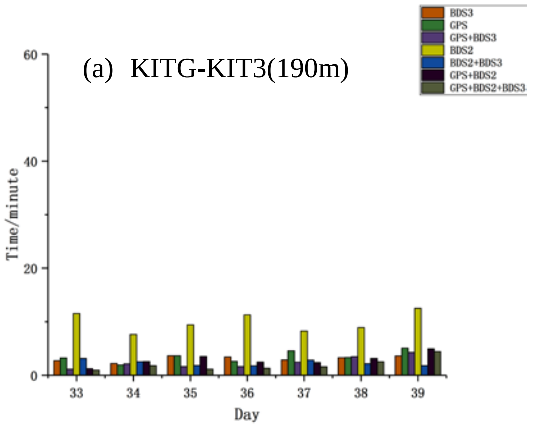
(a) KITG-KIT3(190m)

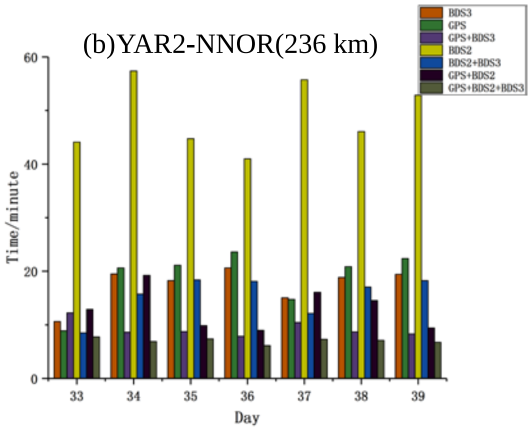
(b)YAR2-NNOR(236 km)

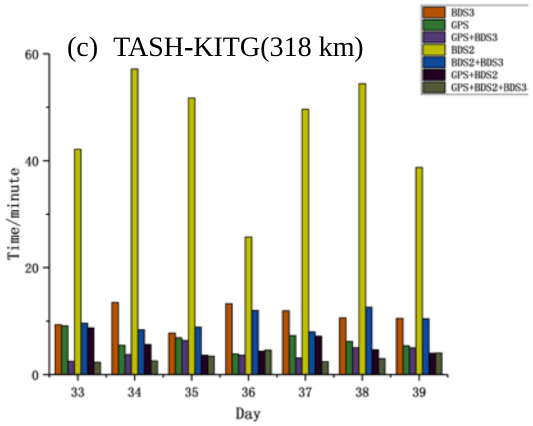
(c) TASH-KITG(318 km)

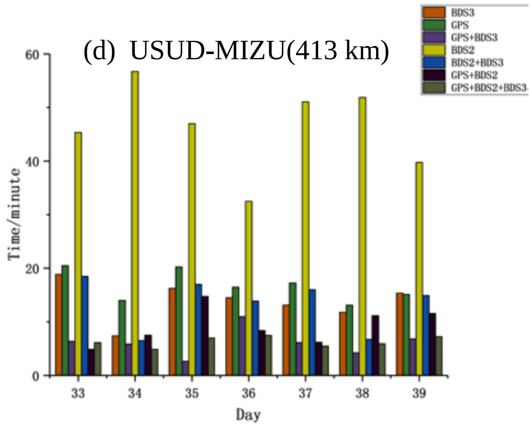
(d) USUD-MIZU(413 km)

Figure 5: Static Mode Convergence Time Statistics

Table 3: Statistics of Mean Convergence Time of Static Mode (min)

TYPE	190 m	236 KM	318 KM	413 KM
BDS-3	3.12	17.78	11	13.9
GPS	3.49	18.89	6.32	16.68
GPS+BDS-3	2.39	9.28	4.21	6.16
BDS-2	9.95	48.84	45.65	45.33
BDS-2+BDS-3	2.29	15.46	9.99	13.37
GPS+BDS-2	2.9	13.01	5.46	9.21
GPS+BDS-2+BDS-3	1.97	7.04	3.2	6.31

Table 4: Statistics of mean convergence time for dynamic models (min)

TYPE	190 m	236 km	318 km	413 km
BDS-3	18.82	51.89	51.24	51.41
GPS	20.76	47.93	48.79	55.29
GPS+BDS-3	12.07	23.42	20.16	17.23
BDS-2	53.74	141.64	136.36	138.9
BDS-2+BDS-3	16.18	33.86	32.22	25.58
GPS+BDS-2	17.74	33.66	26.54	27.19
GPS+BDS-2+BDS-3	10.32	17.82	15.79	15.09

satellites have been launched with the BDS-3 system, and their orbit accuracy has been better than that of BDS-2 satellites. The BDS-3 convergence speed has been better than BDS-2 and became equivalent to GPS.

With the addition of BDS-3 satellites to the GPS+BDS-2 combined system, the convergence speed has been increased by about 30% in both static and dynamic modes. The convergence speed of the GPS positioning solution reached about 60% improvement with the aid of the BDS-3 satellites. The BDS-2 only solution convergence speed was slow. However the addition of the BDS-3 satellites to the BDS-2 improved the convergence speed by about

70-80%, which significantly reduced the BDS-2's convergence time. The BDS system (BDS-2+BDS-3) functioned better than that of GPS only in terms of the positioning convergence speed.

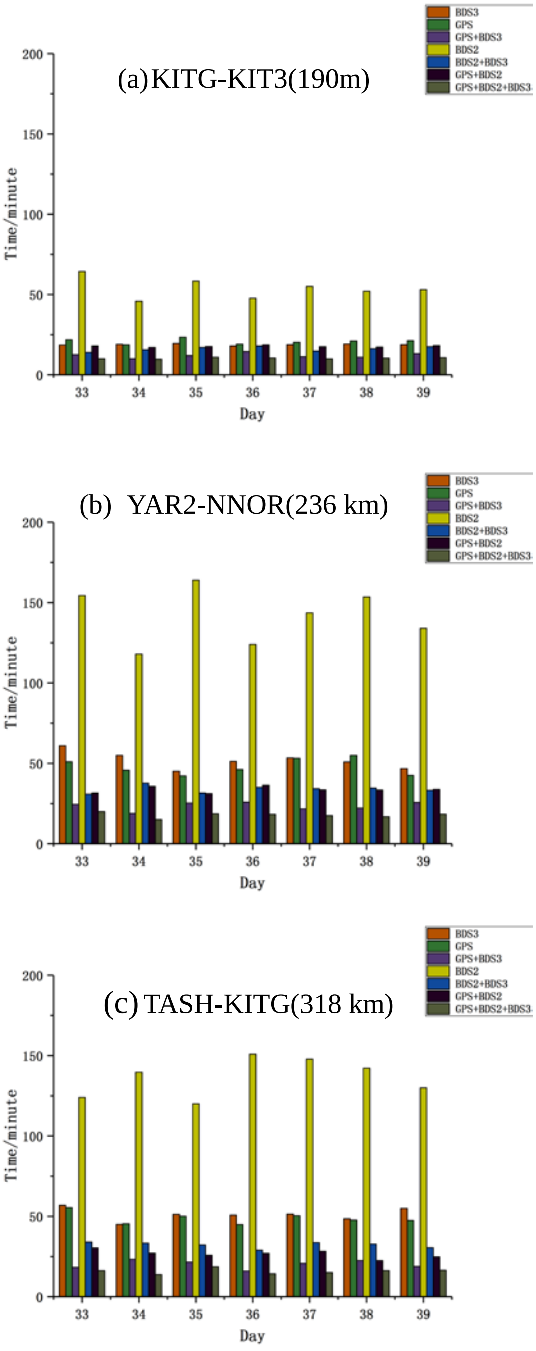

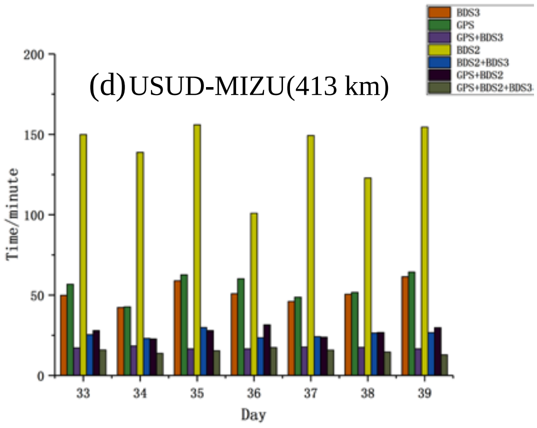

Figure 6: Dynamic Model Convergence Time Statistics

2.3 Positioning accuracy

This sub-section mainly analyzed how the addition of the BDS-3 satellites improves the positioning accuracy in different positioning modes by overviewing the solutions of each sub-period with the data from 33d-39d in 2021. In the static mode, the resulted differences of the E, N and U components at the last epoch of each sub-period were taken as the final positioning deviations. The average values of all the differences were considered as the static positioning errors. The results are given in Table 5 whilst the detailed positioning deviations of each station from the DOY 033d to the DOY 039d is shown in Figure 7. In the dynamic mode, by taking the results from the remaining epochs after the convergence was reached during each sub-period, the RMS in E, N and U were calculated, and the average values of RMS of all data deviation sequences were considered as the dynamic positioning results (shown in Table 6). The detailed positioning deviations of each station on each day are shown in Figure 9.

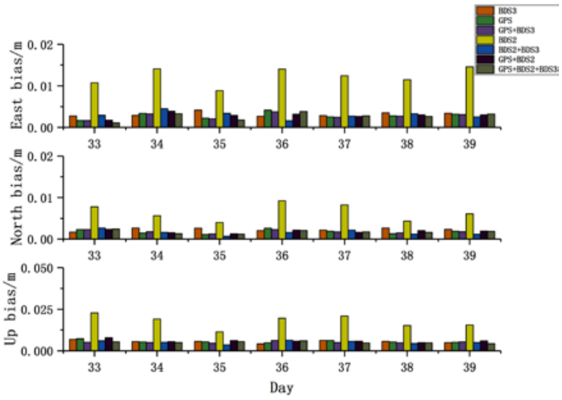

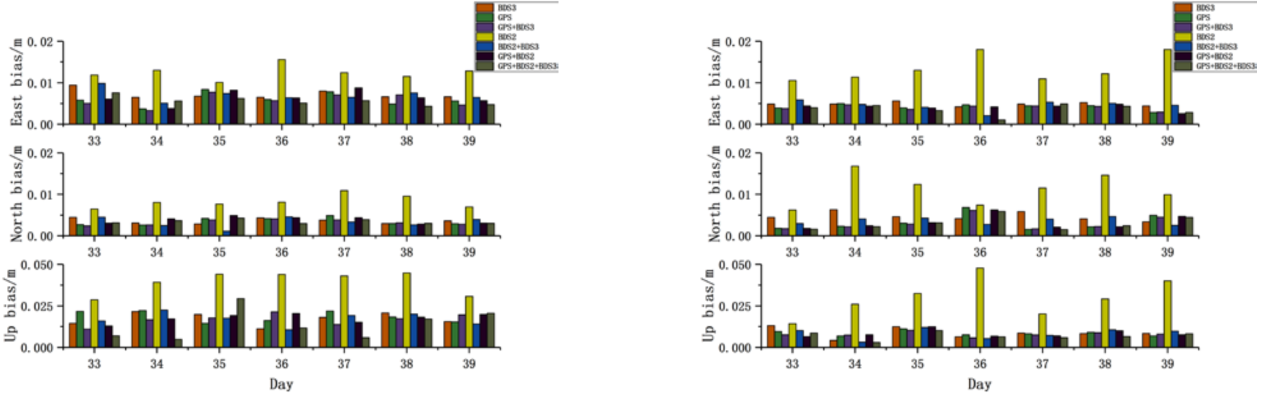

(a) KITG-KIT3(190 m)

(c) TASH-KITG(318 km)

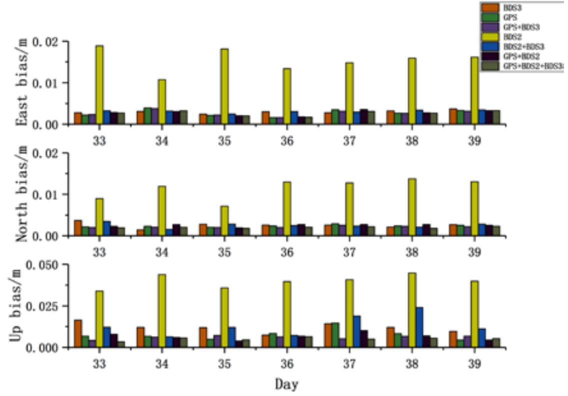

(b) YAR2-NNOR(236 km)

(d) USUD-MIZU(413 km)

Figure 7: Static Positioning Results RMS Comparison Histogram

Table 5: Seven Day Average RMS Statistics of Static Positioning Results (cm)

TYPE	190 m			236 km			318 km			413 km		
	E	N	U	E	N	U	E	N	U	E	N	U
BDS-3	0.32	0.23	0.56	0.72	0.36	1.73	0.3	0.26	1.19	0.46	0.47	0.88
GPS	0.28	0.18	0.56	0.6	0.35	1.85	0.28	0.24	0.77	0.41	0.32	0.85
GPS+BDS-3	0.27	0.18	0.51	0.58	0.32	1.68	0.27	0.22	0.61	0.4	0.3	0.79
BDS-2	1.2	0.65	1.8	1.24	0.82	3.92	1.54	1.15	3.98	1.34	1.12	2.99
BDS-2+BDS-3	0.3	0.16	0.51	0.7	0.32	1.71	0.31	0.25	1.31	0.45	0.36	0.83
GPS+BDS-2	0.29	0.18	0.6	0.61	0.37	1.76	0.28	0.23	0.66	0.41	0.32	0.83
GPS+BDS-2+BDS-3	0.26	0.17	0.51	0.57	0.34	1.38	0.27	0.2	0.51	0.39	0.3	0.69

In the static positioning processing mode, as can be seen from Table 5, the long-baseline static relative positioning horizontal accuracy using GPS plus BDS-3 in each region was approximately the same as using GPS only., however, the vertical accuracy was improved to a certain extent. Specifically with the TASH-KITG (318) baseline in Asia , the GPS RMS of positioning differences in the E, N and U directions were 0.28 cm, 0.24 cm and 0.77 cm, respectively. With BDS-3 satellites together, the RMS in the E, N and U directions were about 0.27, 0.22 and 0.61 cm. The horizontal accuracies in the E and N directions were similar to the ones from GPS only solution, but the accuracy in the vertical direction was increased by about 20%. It can be seen from Figure 7 that the positioning accuracy of the BDS-3 only is slightly lower than that of the GPS only. The BDS-2 only performance was poor in comparison with the BDS-3 and GPS individually, but the combined BDS-2 and BDS-3 significantly improved the positioning accuracy. The most significant accuracy improvement was with the baseline of TASH-KITG (318) in Asia. Specifically, the positioning accuracy in E, N and U directions were increased to 0.31 cm, 0.25 cm and 1.31 cm from 1.54 1.15 cm and 3.98 cm, respectively, , which presented the positioning accuracy improvement by 80% (East), 78% (North) and 67% (Up), respectively. With GPS, BDS-2, and BDS-3 together, although the positioning accuracy remained quite the same horizontally as without using the BDS-3 satellites and only 20% improvement vertically, the positioning reliability and measurement availability have been clearly improved.

In order to more specifically compare the influential effect of the addition of the BDS-3 satellites to BDS-2, BDS-2 and BDS-2+BDS-3 are analyzed in detail, taking DOY 34d in 2021 as an example(The data segmentation method is the same as that in Section 2.2). As can be seen from figure 8, adding the BDS-3 satellites has significantly improved the positioning performance upon of the BDS-2, which reached a horizontal accuracy at the millimeter level, specifically by about 60%, 71% and 65% (the RMS from 1.49, 1.0 and 3.27 cm to 0.59, 0.29 and 1.14 cm) in three directions (E, N, Up). This is similar to GPS.

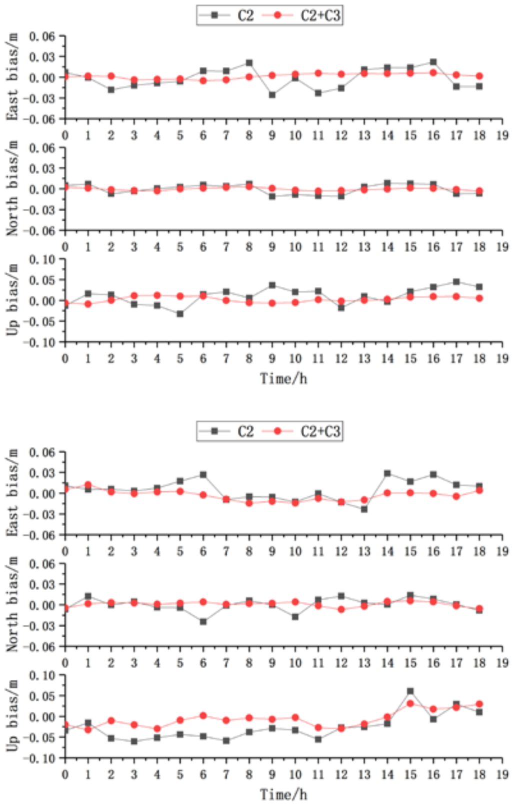

（a）KITG-KIT3(190 m)
（b）YAR2-NNOR(236 km)

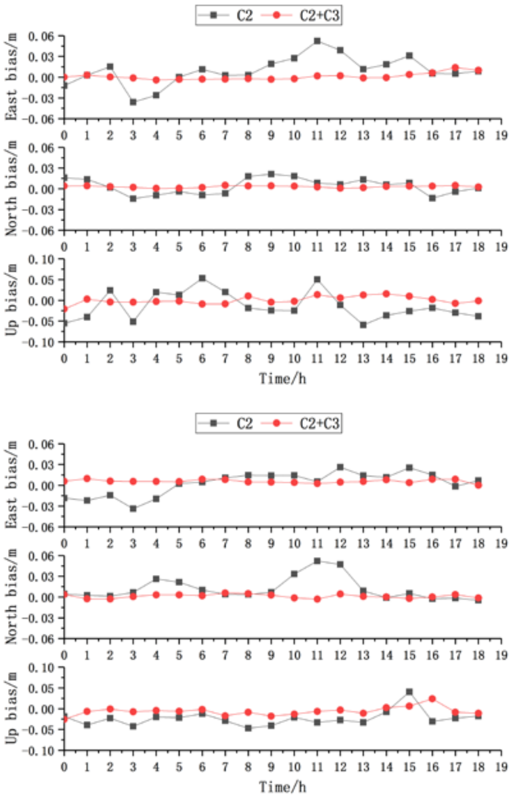

（c）TASH-KITG(318 km)
（d）USUD-MIZU(413 km)

Figure 8: Static Positioning Results of BDS-2 and BDS-2+BDS-3

In the dynamic positioning processing mode, it can be seen from Figure 9 that in the four sets of baselines, GPS and BDS-2 single system and GPS+BDS-2 dual-system have different degrees of improvement in E, N and U directions after adding BDS-3 satellites. The average RMS of positioning differences in the E, N and U directions of single GPS is 1.84 cm, 1.4 cm and 3.15 cm respectively. After adding BDS-3 satellites to form GPS+BDS-3 dual-system, the average RMS in three directions is 1.59 cm, 1.1 cm and 2.5 cm respectively, which increased by about 14%, 21% and 21%. The BDS-2 and BDS-3 single system compared to GPS single system, The following conclusions can be obtained that the GPS positioning accuracy is optimal and BDS-3 positioning accuracies is slightly lower than GPS but better than BDS-2. The BDS-2 maximum differences are close to 4 cm in the E direction and 6 cm in the U direction, respectively. With the aid of BDS-3 satellites, BDS-2 RMS values are decreased from 3.26 cm, 2.53 cm and 5.13 cm to 1.75 cm, 1.56 cm and 3.29 cm in E, N and U, respectively, i.e., their accuracies are increased by 46%, 38% and 36%, correspondingly. Compared with GPS, the dynamic relative positioning performance with the BDS-2+BDS-3 dual-system is better. After having added the BDS-3 satellites to the GPS+BDS-2 dual-system, the dynamic and the static positioning mode are improved in the E, N and U directions. The average RMS increases from 1.74 cm, 1.28 cm and 2.94 cm to 1.47 cm, 0.96 cm and 2.24 cm, which promoted about 16%, 25% and 24%, respectively.

To more intuitively study the impact of adding BDS-3 on positioning, in the dynamic positioning processing mode, using the data of DOY 34d in 2021 and the dynamic positioning performance is analyzed by seven different combinations(BDS-2, BDS-3, GPS, GPS + BDS-3, BDS-2 + BDS-3, GPS + BDS-2, GPS + BDS-2 + BDS-3).

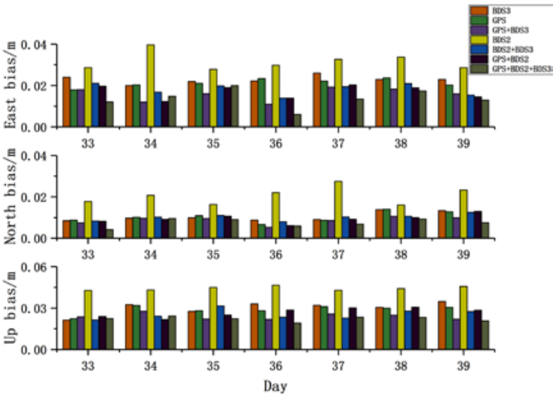

（a）KITG-KIT3(190 m)

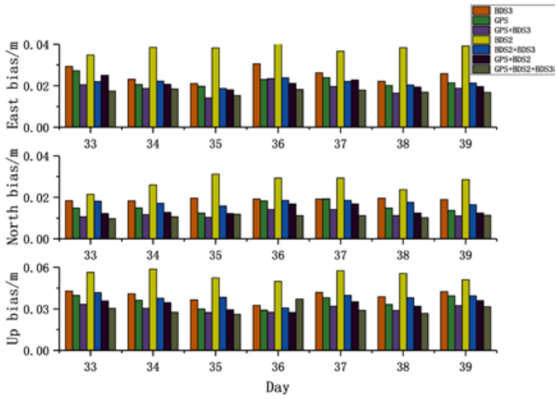

(b) YAR2-NNOR(236 km)

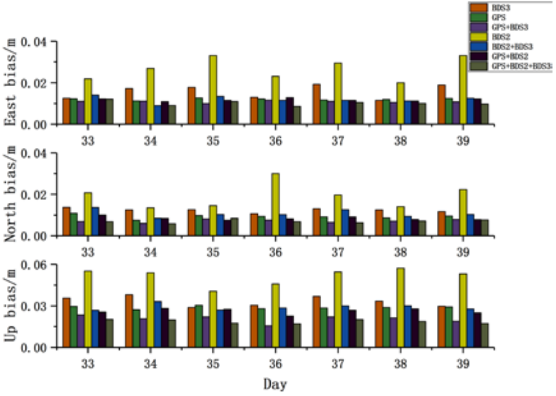

(c) TASH-KITG(318 km)

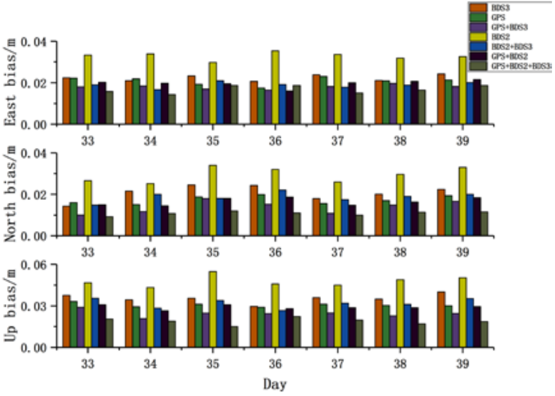

(d) USUD-MIZU(413 km)

Figure 9: Dynamic Positioning Results RMS Comparison Histogram

Table 6: Seven Day Average RMS Statistics Result of Dynamic Positioning Mode (cm)

TYPE	190 m			236 km			318 km			413 km		
	E	N	U	E	N	U	E	N	U	E	N	U
BDS-3	2.29	1.04	3.03	2.55	1.9	3.94	1.57	1.24	3.33	2.24	2.07	3.54
GPS	2.12	1.02	2.89	2.23	1.54	3.51	1.21	0.93	2.88	2.09	1.73	3.06
GPS+BDS-3	1.57	0.87	2.39	1.88	1.19	3.02	1.09	0.71	2.05	1.8	1.39	2.44
BDS-2	3.16	2.05	4.43	3.8	2.71	5.45	2.68	1.93	5.15	3.3	2.95	4.78
BDS-2+BDS-3	1.82	1.01	2.56	2.15	1.74	3.8	1.19	1.07	2.9	1.9	1.88	3.18
GPS+BDS-2	1.69	0.95	2.69	2.09	1.36	3.29	1.18	0.84	2.62	1.96	1.65	2.9
GPS+BDS-2+BDS-3	1.38	0.75	2.22	1.73	1.09	2.98	1.01	0.7	1.86	1.68	1.09	1.89

The GPS+BDS-3 combination possessed the best and most stable solution, as the BDS-2 only solution was the worst, partially with the large fluctuation. The combination of the BDS-3 and BDS-2 speeded up the solution convergence. Besides, the positioning accuracy also received a better lifting effect. By taking the baseline of USUD-MIZU (413 km) in Asia as an example, the number of the observed BDS-2 satellites was relatively low during the 12-16 h on that day so that the result can’t go convergent during dynamic data processing. However, after having included the BDS-3 satellites, the solution accuracy was effectively improved down to centimeter-level. The combined BDS-3+GPS and BDS-3+GPS+BDS-2 have also improved the solution accuracy in all of the three directions. It can be seen from Figure 10 that the data will jump in the last 15 minutes of each day, which is due to the influence of the daily boundary discontinuities (DBD) [21,22].

3 Conclusion

Based on the observation data provided by MGEX and the precise products released by GFZ, this research conducted specific experiments on the long baseline relative positioning in static and dynamic modes using BDS-2, BDS-3 and GPS individually and different combinations of them and obtained the following conclusions through the comparative analysis in terms of data quality, convergence speed and positioning accuracy:

(1) In the static and dynamic data processing modes, the convergence speed and positioning accuracy using BDS-3 are similar to GPS, and the positioning accuracy meets the requirements of current high-precision positioning;

(2) The inclusion of the BDS-3 satellites in addition to GPS, BDS-2 and GPS+BDS-2 in precise relative positioning can effectively improve the solution convergence speed, especially for BDS-2;

(3) In the static precise relative positioning mode, the addition of the BDS-3 satellites to GPS, and GPS+BDS-2does not significantly improve the horizontal positioning accuracy, but the vertical accuracy by about 20%. The formation of BDS-2+BDS-3 has increased the accuracy in the E, N and U directions by about 60%, 71% and 65% respectively. The accuracy in E and N directions maintained within 1 cm while the accuracy in the U direction was kept within 2 cm;

(4) In the dynamic precise relative positioning mode, The inclusion of the BDS-3 satellites in GPS and in GPS+BDS-2 has made a consistent improvement. The positioning accuracy in the E, N and U directions has been improved by about 15%, 23% and 23%, respectively. The positioning accuracy with using BDS-2+BDS-3 has been improved by about 46%, 38% and 36% in E, N and U directions, respectively.

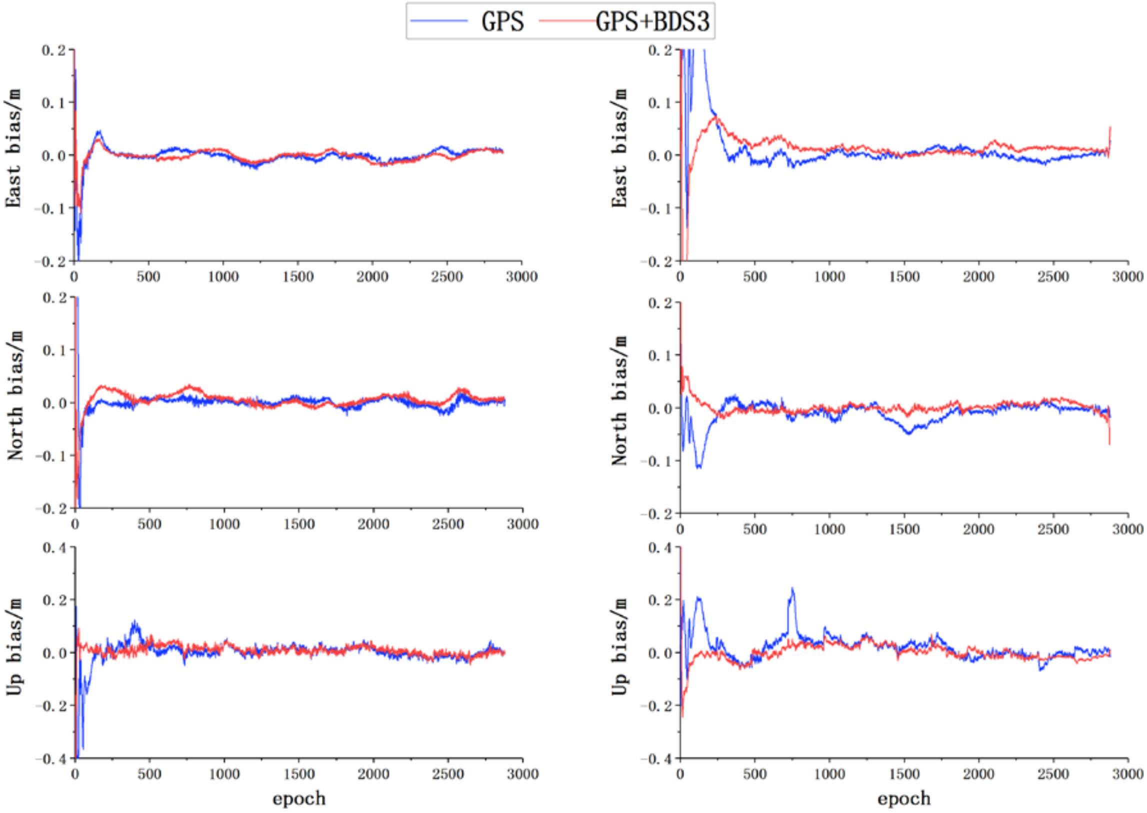

（a）TASH-KITG(318 km)　　（b）USUD-MIZU(413 km)

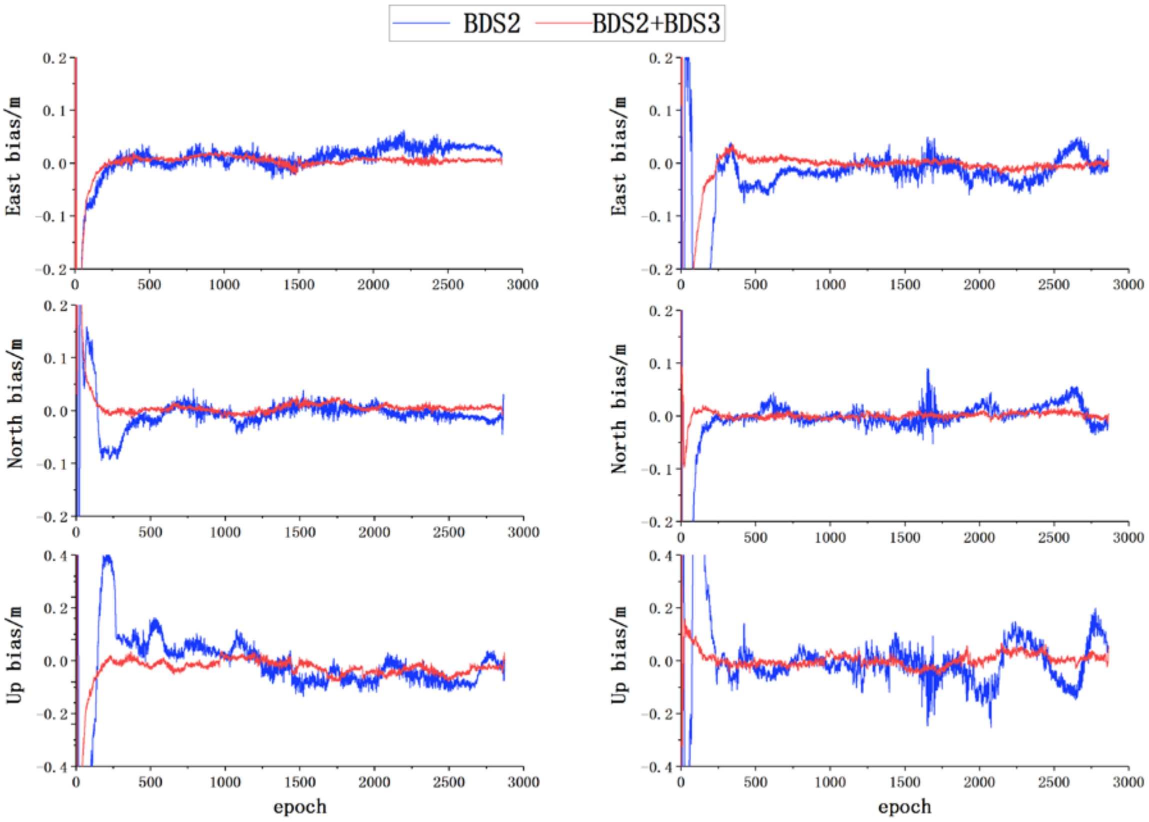

（c）TASH-KITG(318 km)　（d）USUD-MIZU(413 km)

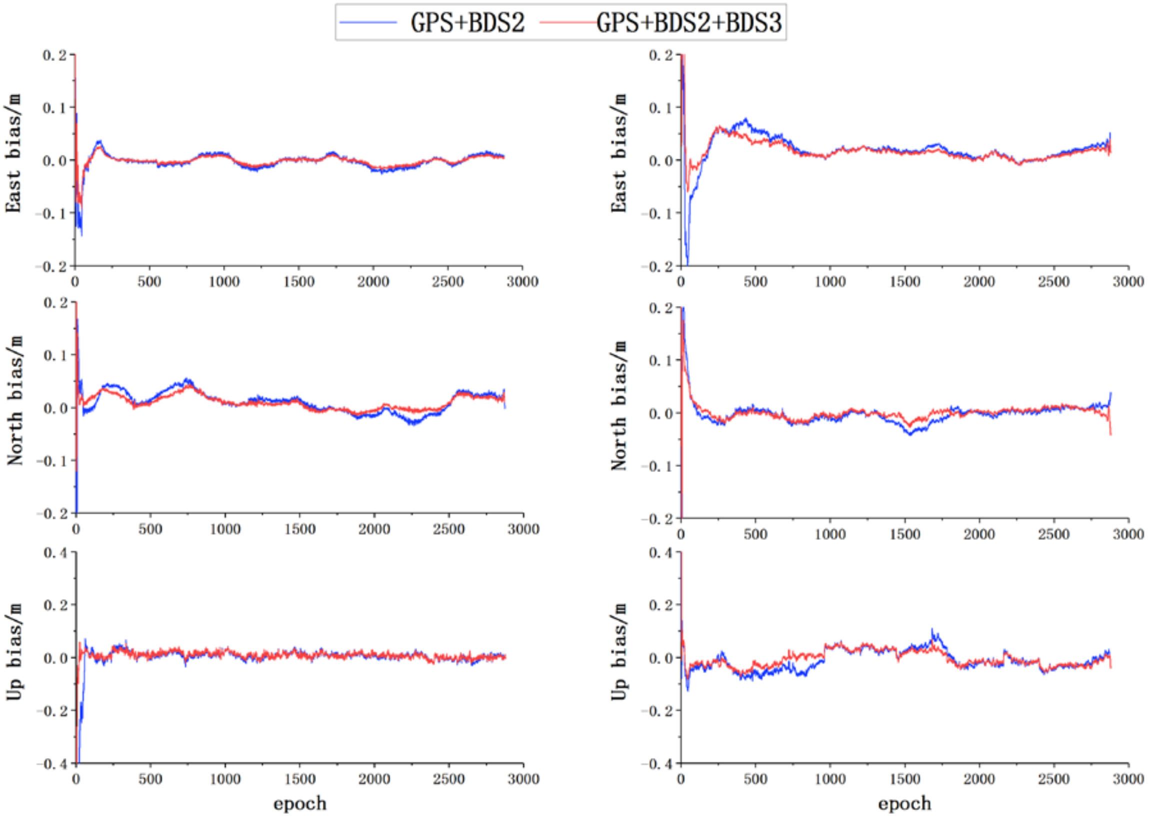

（e）TASH-KITG(318 km)　（f）USUD-MIZU(413 km)

Figure 10: All-day Dynamic Mode Positioning Deviation Statistics with 24 h

References

[1] Development Report of the Beidou Satellite Navigation System [J]. International Space, 2012(04):6-11.

[2] Zhou, Yan (2020): Beidou-3 Global Satellite Navigation system completion and opening ceremony [EB/OL], July 31 2020, http://www.beidou.gov.cn/yw/gfgg/202007/t20200729_20864.html

[3] Su, Chengeng; Guo, Shuren; Liu, Xunan; et al (2020): Evaluation of Spatial Signal Quality in Beidou-3 Basic System Journal of Electronics and Information, 2020, 42(11):2689-2697.

[4] Yang, Yuanxi; Gao, Weiguang; Guo, Shuren; et al(2019): Introduction to BeiDou-3 navigation satellite system. Navigation, 2019, 66: 7–18.

[5] Zang, Nan; Li, Bofeng; Shen, Yunzhong (2017): Comparison and Analysis PPP 3 GPS BDS Combination Models Journal of Surveying and Mapping 2017, 46(12):1929-1938.

[6] Yan, Li; Li, Meng (2017): BDS GPS Relative Positioning Accuracy Factor Analysis [J].] Journal of surveying and Mapping, 2017, 46(03):325-331.

[7] Wang, Shijin; Bei, Jinzhong; Gu, Shouzhou (2014): BDS/GPS Combination Relative Positioning Method and Precision Analysis [J]. Survey and Mapping Bulletin, 2014(05):1-4.

[8] Jin, Biao; Yang, Shaowen; Liu, Wanke (2013): GPS/BDS Combined Single Point Positioning Algorithm and Analysis of Results [J] and Marine surveying and mapping, 2013, 33(04):39-41 65.

[9] Zhang, Shuhong; Li, Jinlong; Ma, Junfeng (2017); A Preliminary Evaluation of Static Measurement Precision of Beidou Medium-length Base Line Surveying and Mapping Engineering 2017, 26(04):27-3.

[10] Pu, Yakun; Yuan, Yunbin; Ding, Wenwu (2020):Study on the Application of GPS/BDS-2/Galileo Hybrid Double Difference Relative Positioning Model to Precision Positioning of Short Base Line Geodesy and Geodynamics, 2020, 40(01):56-61.

[11] Wu, Mingkui; Liu, Wanke; Zhang, Xiaohong (2020): Preliminary Evaluation of Relative Positioning Performance of Short Base Line Tight Combination of GPS/Galileo/BDS-3 Tests Journal of Wuhan University (Information Science Edition) 2020, 45(01):13-20.

[12] Jin, Jianjian; Gao, Chengfa; Zhang, Ruicheng (200):.Precision Analysis of Short Base Line Resolution for GPS and BDS-2、BDS-3 Fusion Data Survey and Mapping Bulletin, 2020(03): 83-86 95.

[13] Zhang, Baocheng; ou, Jikun; Yuan, Yunbin (2010):Precision Single Point Positioning Algorithm and Application [J] Based on GPS Two-Frequency Original Observations Journal of Surveying and Mapping, 2010, 39(05): 478-483.

[14] Zhang, Xiaohong; Liu, Gen; Guo, Fei (2018): Comparison and Analysis of Positioning Performance of Beidou Three Frequency Precision Single Point Positioning Model [J] and Journal of Wuhan University (Information Science Edition) 2018, 43 (12):2124-2130.

[15] Liu, Tianjun (2019): GPS/Galileo Non-differential Non-combination Real-time Precision Single Point Positioning Fast Convergence and Fuzzy Fixation [D]. China University of Mining and Technology, 2019.

[16] Geng, Jianghui; Meng, Xiaolin; Alan H.Dodson; et al (2010). Integer Ambiguity Resolution in Precise Point Positioning: Method Comparison, Journal of Geodesy, 2010, 84 (9) : 569-581.

[17] Yang, Xu; Xu, Aigong; Qin, Xiaoxi;et al (2017): Single Point Location Analysis of BDS/GPS Pseudo-Speed Distance for elevation Angle Weighting Model [J]; and Journal of Navigation and Positioning 2017, 5(02):72-78+85.

[18] Zhang, Xiaohong; Zuo, Xiang; Li, Pan; et al (2015): BDS/GPS Comparison of Convergence Time and Positioning Precision of Precision Single Point Positioning [J].10 Journal of Surveying and Mapping, 2015, 44(03):250-256.

[19] Ding, Pan; Xi, Ruijie; Xiao, Yugang (2016): Analysis of Performance of Beidou Satellite Navigation System for High Precision

Deformation Monitoring in Northeast China Survey and Mapping Bulletin, 2016(04):33-37.

[20] He, Yilei; Wang, Zhiwen; Wang, Zhong; et al (2018):Analysis of the quality of observational data from the Beidou Global Test Satellite Survey and Mapping Bulletin, 2018(12):1-5.

[21] Zhang Qiang (2018): Low-orbit satellite using GPS and Beidou [D].Wuhan University, 2018.

[22] Dong Zhihua, Chen Junping, Zhou Xuhua (2019): GNSS Discontinuuity Analysis and Evaluation of Precision Track Products, Astronomy Journal, 2019, 60 (05): 45-55.

Authors

Xiaoting Lei

Huizhong Zhu is an Associate Professor of School of Surveying and Geographic Science of Liaoning Technical University. He obtained his PhD from Wuhan University University in 2012. His research is focused on high-precision GNSS positioning and data processing and has authored and coauthored 87 peer-reviewed papers.

Jingfa Zhang is a MEng student of School of Surveying and Geographic Science of Liaoning Liaoning Technical University. His research is focused on high-precision GNSS positioning and data processing.

Jun Li is a PhD student of School of Surveying and Geographic Science of Liaoning Technical University. His research is focused on high-precision GNSS positioning and data processing

Yangyang Lu is a MEng student of School of Surveying and Geographic Geographic Science of Liaoning Technical University. His research is focused on high-precision GNSS positioning and data processing

***Journal of Global Positioning Systems* (*2021*)**
Vol. 17, No. 2: 151-163
DOI: 10.5081/jgps.17.2.151

Multi-GNSS RTK positioning with integer ambiguity resolution: From double-differenced to single-differenced

Xiaolong Mi[1,2,3], Baocheng Zhang[2,4], Yunbin Yuan[2*]

1. School of Earth and Planetary Sciences, Curtin University, Perth, Australia
2. State Key Laboratory of Geodesy and Earth's Dynamics, Innovation Academy for Precision Measurement Science and Technology, Chinese Academy of Sciences, Wuhan, China
3. University of Chinese Academy of Sciences, Beijing, China
4. State Key Laboratory of Satellite Navigation System and Equipment Technology, the 54th Research Institute of China Electronics Technology Group Corporation, Shijiazhuang, China

* Corresponding author: Yunbin Yuan, yybgps@whigg.ac.cn

Abstract

The development of global navigation satellite systems (GNSS), especially BeiDou navigation satellite system with global coverage (BDS-3), has brought benefits for high-precision positioning. Real-time kinematic (RTK) positioning based on double-differenced (DD) observations has been widely used in high-precision positioning as common errors are eliminated. However, the biases at the receiver-end, which can be dynamically constrained, are also eliminated during the DD process. Therefore, it makes sense to turn RTK from DD to single-differenced (SD) as the advantages of dynamic constraints of the receiver biases can be exploited. In this contribution, we first present RTK models based on DD observations suitable for short, medium and long baselines. Then, based on SD observations, the full-rank RTK models are constructed with the *S*-system theory. Using observations from GPS, BDS-3 and Galileo, we first demonstrate the short-term stability of receiver-related biases. The SD RTK positioning performance with the stability of those receiver-related biases regarding integer ambiguity resolution success rate and positioning accuracy are analyzed. With those biases, RTK can achieve high performance, and this is more advantageous in multi-GNSS scenarios.

Keywords: Real-time kinematic (RTK), double-differenced (DD), single-differenced (SD), integer ambiguity resolution (IAR), BeiDou-3, global coverage, receiver biases

Introduction

Global and regional satellite navigation systems are developing rapidly, offering excellent opportunities for scientific and engineering applications [Li et al. 2019; Pignalberi et al. 2019; Ruhl et al. 2017]. Currently, GPS, GLONASS and Galileo are undergoing modernization while BeiDou navigation satellite system (BDS-3) completed its global deployment in July 2020 [Karutin 2020; Liu et al. 2021; Yalvac and Berber 2018; Yang et al. 2021; Yuan et al. 2020]. The advent of regional navigation satellite systems (RNSS) such as quasi-zenith satellite system (QZSS) and Navigation Indian Constellation (NavIC) has also increased the number of satellites in orbit [Santra et al. 2019; Zaminpardaz et al. 2018]. More satellites and frequencies are becoming available in this situation that benefits positioning, navigation, and timing (PNT) applications.

Editor in charge: Dr. Zhizhao Liu

Precise point positioning (PPP) and real-time kinematic (RTK) positioning are two representative techniques [Paziewski et al. 2018; Shi et al. 2020]. Based on precise orbit and clock products, PPP can provide centimeter-level positioning services [Bahadur and Nohutcu 2019]. However, traditional PPP solutions typically require a 5-30 min convergence period and do not consider integer ambiguity resolution, which is defective in real-time and high-precision applications [Xiao et al. 2019]. Some commercial high-precision services have reduced PPP convergence time to a few minutes, but this requires additional precise corrections [Atiz et al. 2021]. With the help of a reference network, RTK can achieve fast integer ambiguity resolution and thus provide millimeter-level positioning services. Although integer ambiguity resolution enabled PPP (PPP-RTK) as a new representative technology is attracting widespread attention [Khodabandeh and Teunissen 2016], RTK is still the technology which real-time high-precision GNSS services depend on.

The classical RTK is usually based on double-differenced (DD) observations, which can benefit from serval advantages. First, DD RTK eliminates common errors from both the receiver-end and satellite-end; thus, the full-rank model can be obtained directly. Second, errors in propagation such as ionospheric and tropospheric delays are greatly reduced during the DD process. However, the DD observations amplify the effect of observation noise and multipath effect. In addition, the DD model eliminates the biases at the receiver-end, thus losing the opportunity to impose dynamic constraints to enhance the model strength [Odolinski et al. 2015b]. There is a mathematical correlation between the DD observations, which is not conducive to quality control and judging the source of gross error [Zhang et al. 2019].

The advantages of a SD model compared with a DD one have already been recognized for a long time in the case of RTK positioning [Liu et al. 2003; Mi et al. 2019a; Odijk and Teunissen 2008; Odolinski et al. 2015a]. With an SD formulation, one has the advantage of using a more straightforward observational variance matrix than the one used in a DD formulation. Receiver-end biases that are not considered of interest in positioning are eliminated in a DD model while retained in an SD one, which a dynamic model can constrain to improve model strength [Mi et al. 2020]. Those receiver-related biases include differential code bias (DCB), differential phase bias (DPB) and inter-system bias (ISB). DCBs and DPBs are stable that can be pre-corrected or estimated as time-invariants, both of which can enhance the model strength. ISBs can promote the signal integration of multi-frequency and multi-constellation, which is beneficial to PNT in terms of accuracy, integrity, and availability [Odijk et al. 2017; Tian et al. 2019].

With the SD observations, rank deficiencies have to be solved as not all unknowns can be estimated without biases [Odolinski et al. 2020]. Fortunately, the *S*-system theory can be used to identify the source of rank defects, select appropriate *S*-basis and construct a full-rank model, which was developed for terrestrial geodetic networks at first [Odolinski and Teunissen 2017a]. It should be noted that the choice of *S*-basis is not unique, which dictates the estimability and the interpretation of parameters.

In this contribution, we first review the ionosphere-float, -weighted and -fixed DD RTK models considering different ionospheric constraints, suitable for long, medium and short baselines. Then, based on the SD observations, we propose the ionosphere-float, -weighted and -fixed SD RTK models. As for the rank deficiencies in the SD models, the *S*-system theory is used to construct the full-rank model.

The remainder of this paper proceeds as follows. Section 2 first reviews the DD RTK model and then develops the RTK model based on SD observations. Section 3 presents the experimental setup and RTK positioning results for GPS, BDS-3 and Galileo. Finally, we summarize our findings and conclusions in Section 4.

Methodology

This section first gives the DD RTK models suitable for short to long baselines, namely ionosphere-float, -weighted and -fixed model. Then, the SD RTK models of ionosphere-float, -weighted and -fixed are constructed.

GNSS observation equations

The starting point of developing RTK models is the equations for GNSS code and phase observables [Leick et al. 2015], which read, respectively

$$\begin{aligned} p^s_{r,j} &= \rho^s_r + \tau^s_r + dt_r - dt^s + \mu_j I^s_r + d_{r,j} - d^s_{,j} + \varepsilon^s_{p,r,j} \\ \phi^s_{r,j} &= \rho^s_r + \tau^s_r + dt_r - dt^s - \mu_j I^s_r + \lambda_j N^s_{r,j} + \delta_{r,j} - \delta^s_{,j} + \varepsilon^s_{\phi,r,j} \end{aligned} \tag{1}$$

with r , s and j the receiver, satellite and frequency. $p^s_{r,j}$ and $\phi^s_{r,j}$ are the code and phase observations measured by receiver r from satellite s on frequency j . ρ^s_r is the satellite-receiver range, τ^s_r is the tropospheric delay, dt_r is the receiver clock and $d_{r.j}$ ($\delta_{r.j}$) is the receiver code (phase) bias. I^s_r is the ionospheric delay and $\mu_j = \lambda^2_j / \lambda^2_1$ is its coefficient with λ_j the wavelength, $N^s_{r,j}$ is the integer phase ambiguity. dt^s is the satellite clock and $d^s_{,j}$ ($\delta^s_{,j}$) is the satellite code (phase) bias. $\varepsilon^s_{p,r,j}$ and $\varepsilon^s_{\phi,r,j}$ are the code and phase observation noise and miss-modeled random effects.

DD RTK model

The common errors at the satellite-end and the receiver-end are eliminated in DD RTK without rank deficiency. Therefore, DD RTK can be directed used for precise positioning. Considering that different ionospheric delay processing strategies, three variants are given.

DD ionosphere-float variant

During the DD process, one receiver and one satellite have to be selected as pivot receiver and satellite (represented by 1). Then, the DD code and phase observations can be given as follows,

$$\begin{aligned} p^{1s}_{1r,j} &= \rho^{1s}_{1r} + \tau^{1s}_{1r} + \mu_j I^{1s}_{1r} + \varepsilon^{1s}_{p,1r,j} \\ \phi^{1s}_{1r,j} &= \rho^{1s}_{1r} + \tau^{1s}_{1r} - \mu_j I^{1s}_{1r} + \lambda_j N^{1s}_{1r,j} + \varepsilon^{1s}_{\phi,1r,j} \end{aligned} \tag{2}$$

where $p^{1s}_{1r,j}$ and $\phi^{1s}_{1r,j}$ are the DD code and phase observations, respectively. τ^{1s}_{1r} and I^{1s}_{1r} are the DD tropospheric and ionospheric delays. $N^{1s}_{1r,j}$ is the DD phase ambiguity. For long baselines, the DD tropospheric and ionospheric delays cannot be neglected. For tropospheric delay, it is common practice to divide it into two parts, dry and wet delays where $\tau^s_r = (\tau_d)^s_r + m^s_r \tau_r$. The dry part $(\tau_d)^s_r$ is directly corrected in the code and phase observations using an a-priori troposphere model [Leandro et al. 2008]. The wet part τ_r zenith troposphere delay (ZTD) is estimated as unknown with m^s_r an elevation-dependent mapping function [Hadas et al. 2020; Tuka and El-Mowafy 2013]. For the DD ionospheric delays, they are estimated as unknown parameters together with the other parameters in long baselines. Therefore, the DD ionosphere-float model can be given as

$$\begin{aligned} \tilde{p}^{1s}_{1r,j} &= \rho^{1s}_{1r} + m^{1s}_r \tau_{1r} + \mu_j I^{1s}_{1r} + \varepsilon^{1s}_{p,1r,j} \\ \tilde{\phi}^{1s}_{1r,j} &= \rho^{1s}_{1r} + m^{1s}_r \tau_{1r} - \mu_j I^{1s}_{1r} + \lambda_j N^{1s}_{1r,j} + \varepsilon^{1s}_{\phi,1r,j} \end{aligned} \tag{3}$$

with $\tilde{p}^{1s}_{1r,j} = p^{1s}_{1r,j} - (\tau_d)^{1s}_{1r}$ and $\tilde{\phi}^{1s}_{1r,j} = \phi^{1s}_{1r,j} - (\tau_d)^{1s}_{1r}$.

DD ionosphere-weighted variant

It is acceptable to use Eq. (3) for RTK positioning of medium baselines with no more than 100 kilometers. However, the ionospheric delays from the same satellite are approximately equal for the different receivers at this distance [Teunissen 1998]. Therefore, it is wise to include the ionospheric delay in the model of Eq. (3) as an additional observable [Zha et al. 2021]. The DD ionosphere-weighted model can be given as follows,

$$\begin{aligned} \tilde{p}_{1r,j}^{1s} &= \rho_{1r}^{1s} + m_r^{1s}\tau_{1r} + \mu_j I_{1r}^{1s} + \varepsilon_{p,1r,j}^{1s} \\ \tilde{\phi}_{1r,j}^{1s} &= \rho_{1r}^{1s} + m_r^{1s}\tau_{1r} - \mu_j I_{1r}^{1s} + \lambda_j N_{1r,j}^{1s} + \varepsilon_{\phi,1r,j}^{1s} \\ \bar{I}_{1r}^{1s} &= I_{1r}^{1s} + \varepsilon_{I,1r,j}^{1s} \end{aligned} \tag{4}$$

where $\bar{I}_{1r}^{1s}$ is the DD ionospheric pseudo-observables, and can be interpolated by reference network or assumed as zero for medium baselines. The reasonable stochastic model of those observables is necessary, which is usually determined by both baseline length and satellite elevation angle. It is worth noting that the stochastic model is limited by the region and time, so it is necessary to model the stochastic model for the operating area in advance [Mi et al. 2019b].

DD ionosphere-fixed variant

For baselines within a few tens of kilometers, it is safe to assume the DD ionospheric and tropospheric delays are zero. Therefore, the DD ionosphere-fixed model can be written as,

$$\begin{aligned} \tilde{p}_{1r,j}^{1s} &= \rho_{1r}^{1s} + \varepsilon_{p,1r,j}^{1s} \\ \tilde{\phi}_{1r,j}^{1s} &= \rho_{1r}^{1s} + \lambda_j N_{1r,j}^{1s} + \varepsilon_{\phi,1r,j}^{1s} \end{aligned} \tag{5}$$

The unknown parameters to be estimated are position and phase ambiguity, and the strength of the model is improved.

SD RTK model

Unlike the DD RTK model, the SD model needs to be solved uniquely, as it is a rank-deficient system. This means that not all the unknowns in the SD model can be estimated separately, but only their combinations. Therefore, to construct the full-rank SD model, the *S*-system theory is used. The details of *S*-system theory can be referred to Odijk et al. [2016], which will not be repeated here. Similar to the DD model, ionosphere-float, -weighted and -fixed variants are constructed, respectively.

SD ionosphere-float variant

As a starting point of developing the SD algorithm, we first give the SD code and phase observations which reads,

$$\begin{aligned} p_{1r,j}^{s} &= \rho_{1r}^{s} + \tau_{1r}^{s} + dt_{1r} + \mu_j I_{1r}^{s} + d_{1r,j} + \varepsilon_{p,1r,j}^{s} \\ \phi_{1r,j}^{s} &= \rho_{1r}^{s} + \tau_{1r}^{s} + dt_{1r} - \mu_j I_{1r}^{s} + \lambda_j N_{1r,j}^{s} + \delta_{1r,j} + \varepsilon_{\phi,1r,j}^{s} \end{aligned} \tag{6}$$

where $p_{1r,j}^{s}$ and $\phi_{1r,j}^{s}$ are the SD code and phase observations. ρ_{1r}^{s} is the SD satellite-receiver range, τ_{1r}^{s} and I_{1r}^{s} are the SD tropospheric and ionospheric delays. dt_{1r} is the SD receiver clock, $d_{1r,j}$ and $\delta_{1r,j}$ are the SD receiver code and phase biases. $N_{1r,j}^{s}$ is the SD phase ambiguity.

Although the satellite clock, code and phase biases are eliminated during this process, Eq. (5) can still not be used for RTK positioning, as it is rank-deficient. The rank-deficient occurs in three ways [Mi et al. 2021; Odolinski and Teunissen 2016; Odolinski and Teunissen 2017b]. First, the linear dependency between the columns of the receiver clock and the receiver code/phase biases. Second, the column dependency between the receiver clock, the code/phase biases and the ionosphere delay. Third, the columns of the design matrix between the receiver phase bias and phase ambiguity are linear dependent. As we mentioned earlier, those rank deficiencies can be eliminated by the *S*-system theory. The first two rank deficiencies can be eliminated by fixing the SD receiver code biases on $j = 1$ ($d_{1r,1}$)and on $j = 2$ ($d_{1r,2}$), respectively. As for the third one, one satellite has to be selected as pivot satellite to overcome this rank deficiency.

Once the rank deficiencies have been solved, the full-rank SD ionosphere-float RTK model can be given as,

$$
\begin{aligned}
\tilde{p}^s_{1r,j} &= \rho^s_{1r} + m^s_r \tau_{1r} + d\tilde{t}_{1r} + \mu_j \tilde{I}^s_{1r} + \tilde{d}_{1r,j} + \varepsilon^s_{p,1r,j} \\
\tilde{\phi}^s_{1r,j} &= \rho^s_{1r} + m^s_r \tau_{1r} + d\tilde{t}_{1r} - \mu_j \tilde{I}^s_{1r} + \lambda_j N^{1s}_{1r,j} + \tilde{\delta}_{1r,1} + \tilde{\delta}_{1r,j} + \varepsilon^s_{\phi,1r,j}
\end{aligned} \tag{7}
$$

where $\tilde{p}^s_{1r,j} = p^s_{1r,j} - (\tau_d)^s_{1r}$ and $\tilde{\phi}^{1s}_{1r,j} = \phi^s_{1r,j} - (\tau_d)^s_{1r}$, the dry tropospheric delay is directly corrected in the observations. The reparametrized estimable unknowns in Eq. (7) are given in Table 1.

Table 1 The reparametrized estimable unknowns and their interpretation for SD ionosphere-float model, where $d_{1r,GF} = \frac{1}{\mu_2-\mu_1}(d_{1r,2} - d_{1r,1})$ and $d_{1r,IF} = \frac{\mu_2}{\mu_2-\mu_1} d_{1r,1} - \frac{\mu_1}{\mu_2-\mu_1} d_{1r,2}$

Notation and interpretation	Estimable parameter	Conditions
$d\tilde{t}_{1r} = dt_{1r} + d_{1r,IF}$	Between-receiver clock	
$\tilde{d}_{1r,j} = d_{1r,j} - d_{1r,IF} - \mu_j d_{1r,GF}$	Between-receiver DCB	$j \geq 3$
$\tilde{\delta}_{1r,1} = \delta_{1r,1} - d_{1r,IF} + \mu_j d_{1r,GF} + \lambda_j N^1_{1r,1}$	Between-receiver DPB of the first frequency	
$\tilde{\delta}_{1r,j} = \delta_{1r,j} - \delta_{1r,1} + \lambda_j N^1_{1r,j} - \lambda_j N^1_{1r,1}$	Between-receiver DPB	$j \geq 2$
$\tilde{I}^s_{1r} = I^s_{1r} + d_{1r,GF}$	Between-receiver iono delays biased by receiver code bias	

SD ionosphere-weighted variant

With the ionosphere pseudo-observables available, the second rank deficiency gets eliminated, which increases the redundancy and thus strengthens the model. After the first and third rank deficiencies have been solved, the full-rank SD ionosphere-weighted RTK read,

$$
\begin{aligned}
\tilde{p}^s_{1r,j} &= \rho^s_{1r} + m^s_r \tau_{1r} + d\tilde{\tilde{t}}_{1r} + \mu_j I^s_{1r} + \tilde{\tilde{d}}_{1r,j} + \varepsilon^s_{p,1r,j} \\
\tilde{\phi}^s_{1r,j} &= \rho^s_{1r} + m^s_r \tau_{1r} + d\tilde{\tilde{t}}_{1r} - \mu_j I^s_{1r} + \lambda_j N^{1s}_{1r,j} + \tilde{\tilde{\delta}}_{1r,1} + \tilde{\tilde{\delta}}_{1r,j} + \varepsilon^s_{\phi,1r,j} \\
\bar{I}^s_{1r} &= I^s_{1r} + \varepsilon^s_{I,1r,j}
\end{aligned} \tag{8}
$$

where $\bar{I}^s_{1r}$ is the SD ionospheric pseudo-observables. The reparametrized estimable unknowns and their interpretation are different from the SD ionosphere-float model, which is presented in Table 2.

Table 2 Reparametrized estimable unknowns and their interpretation for the SD ionosphere-weighted and -fixed model

Notation and interpretation	Estimable parameter	Conditions
$d\tilde{\tilde{t}}_{1r} = dt_{1r} + d_{1r,1}$	Between-receiver clock	
$\tilde{\tilde{d}}_{1r,j} = d_{1r,j} - d_{1r,1}$	Between-receiver DCB	$j \geq 2$
$\tilde{\delta}_{1r,1} = \delta_{1r,1} - d_{1r,1} + \lambda_j N^1_{1r,1}$	Between-receiver DPB of the first frequency	
$\tilde{\delta}_{1r,j} = \delta_{1r,j} - \delta_{1r,1} + \lambda_j N^1_{1r,j} - \lambda_j N^1_{1r,1}$	Between-receiver DPB	$j \geq 2$

SD ionosphere-fixed variant

For short baselines, the SD ionospheric and tropospheric delays can be assumed as zero to strengthen the model. Similar to the SD ionosphere-weighted model, the SD ionosphere-fixed also needs to solve the first and third rank deficiencies. Thus, the *S*-basis choices are also the same as in the ionosphere-weighted model. The full-rank SD ionosphere-fixed model follows as,

$$\begin{aligned}\tilde{p}^{s}_{1r,j} &= \rho^{s}_{1r} + d\tilde{\tilde{t}}_{1r} + \tilde{\tilde{d}}_{1r,j} + \varepsilon^{s}_{p,1r,j} \\ \tilde{\phi}^{s}_{1r,j} &= \rho^{s}_{1r} + d\tilde{\tilde{t}}_{1r} + \lambda_j N^{1s}_{1r,j} + \tilde{\tilde{\delta}}_{1r,1} + \tilde{\tilde{\delta}}_{1r,j} + \varepsilon^{s}_{\phi,1r,j}\end{aligned} \tag{9}$$

where the estimable unknowns and their interpretation are also the same as in the Eq. (8) in Table 2.

Experimental Analysis

This section starts with an outline of the experimental setup, including the relevant characteristics of the experimental datasets considered for this study and our data processing strategies. Then, the characterization of the receiver-end biases, including DCB and DPB. Following that is an evaluation of the SD RTK positioning performance in terms of integer ambiguity resolution success rate and positioning accuracy.

Experimental setup

We collected multi-GNSS data from three receivers in Wuhan, China, including one Septentrio POLARx5 (APM3), one Septentrio POLARx5TR (APM7) at the campus of the Innovation Academy of Precision Measurement Science and Technology, Chinese Academy of Sciences and one JAVAD TRE_3 (WHU2) at the campus of Wuhan University. We connected the receivers (APM3 and APM7) to a single antenna that is 1.7 km away from WHU2. Those data were collected for GPS, BDS-3 and Galileo on June 9-10, 2021, with a sampling interval of 30 s. The detailed characteristics of the experimental data used in our study are summarized in Table 3.

Table 3 An overview of GNSS data considered in our study

Station ID	Receiver type	Antenna type	Constellation
APM3	Septentrio POLARx5	TRM159800.00 NONE	GPS L1, L2
APM7	Septentrio POLARx5TR		BDS-3 BIC, B2a
WUH2	JAVAD TRE_3	JAVRINGANT_G5T NONE	Galileo E1 E5a

The cut-off elevation was set to 15° to reduce the impact of the multipath effect, and the elevation-dependent weighting function was used [Shen et al. 2009]. GPS, Galileo, and BDS-3 are assumed to be equal-weighted, where the undifferenced zenith-referenced a priori code and phase standard deviations are 0.3 m and 0.003 m, respectively. The LAMBDA and the ratio test were used for integer ambiguity resolution and the validation of the correctness of the resolved ambiguities [Teunissen and Verhagen 2009; Teunissen et al. 1997]. In addition, the effect of the outliers was detected and eliminated through the Detection, Identification and Adaptation (DIA) procedure [Teunissen 2018].

Characterization of receiver-related biases

As we can see from those SD models, three receiver-related biases are included, including DCB, DPB of the first frequency and DPB. See the interpretation of the DPB of first frequency ($\tilde{\delta}_{1r,1} = \delta_{1r,1} + d_{1r,IF} - \mu_j d_{1r,GF} + \lambda_j N^{1}_{1r,1}$ in ionosphere- float model and $\tilde{\delta}_{1r,1} = \delta_{1r,1} + d_{1r,1} + \lambda_j N^{1}_{1r,1}$ in ionosphere-weighted and fixed models), which contains a combination of code and phase biases. Thus, the DPB of the first frequency is influenced by code observations while the DPB, which is only related to phase observation, is not.

As a typical example, we show in Figs. 1-3 those three receiver-related biases for GPS, BDS-3 and Galileo with the zero baseline APM3-APM7 on June 9, 2021. The purpose of this is to characterize these biases to determine whether they can be pre-corrected or estimated as time invariants in RTK positioning. See Fig. 1 first, showing the DCB for GPS, BDS-3 and Galileo. Focusing on each panel, we can see that the DCB of all three systems is significant, which can not be ignored in RTK positioning. These DCB estimates fluctuate randomly around their mean values with no apparent trend over time. The standard deviations of DCB estimates for GPS, BDS-3 and Galileo are 0.029 m, 0.014 m and 0.019 m, exhibiting noise much smaller than the code observations with decimeter level. That is to say, DCB is stable enough over short-time, so it can be pre-corrected or used as time-invariant parameter estimation in RTK positioning.

Then turn attention to Fig.2, depicting the DPB of the first frequency. As the DPB of the first frequency is the difference between code and phase biases, its estimate has a similar noise level to DCB as expected. The standard deviations of DPB of the first frequency estimates for GPS, BDS-3 and Galileo are 0.025 m, 0.012 m and 0.015 m, slightly smaller than that of DCB. This is because DCB is the difference of the code bias between the second frequency and the first frequency, while DPB is the difference between the code bias and the phase bias of the first frequency, and the noise of the phase bias is less than the code one.

We confirm and extend our findings from Fig.3, showing the DPB estimates for GPS, BDS-3 and Galileo. First, those DPB estimates fluctuate randomly around their mean values, just like DCB and DPB of the first frequency, but with more negligible noise. The standard deviations of DPB of the first frequency estimates for GPS, BDS-3 and Galileo are below 1 mm, showing minimal noise. This is because that DPB is only related to phase observations with slight noise. However, DPB is more difficult to pre-correct due to the introduction of the ambiguity with two frequencies. Thus, the usual practice is to treat DPB as a time-invariant parameter in RTK positioning.

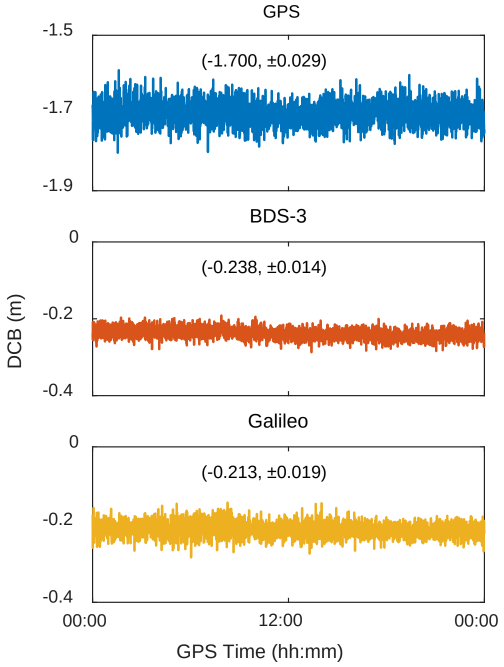

Fig. 1 Time series of DCB for APM3-APM7 with GPS, BDS-3 and Galileo on DOY 159 of 2021

SD RTK positioning performance

As we have shown above, receiver-related DCB, DPB of the first frequency and DPB have good short-term stability, thus can be estimated as time-invariants. Thus, for multi-frequency multi-GNSS RTK positioning, the SD method can achieve better performance than the DD method [Liu et al. 2004]. To test the performance of SD RTK, we select GNSS data from two baselines, a zero one (APM3-APM7) and a short one (APM7-WUH2) with 1.7 km, on June 10, 2021. In our analysis, receiver-related biases are estimated as time-invariants for each constellation, and the integer ambiguity resolution success rate and positioning accuracy are assessed.

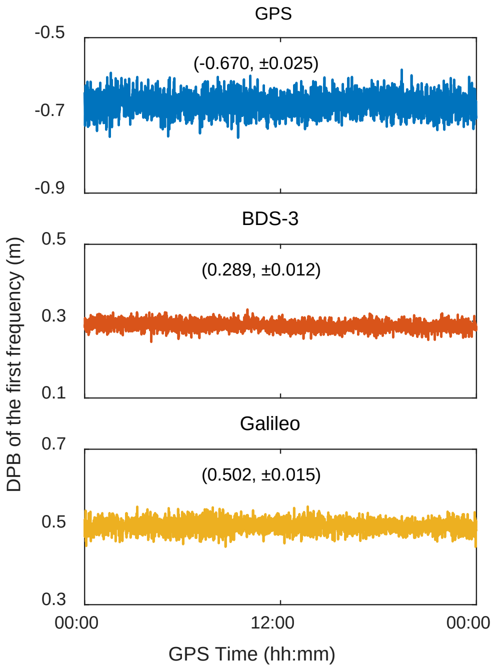

Fig. 2 Time series of DPB of the first frequency for APM3-APM7 with GPS, BDS-3 and Galileo on DOY 159 of 2021

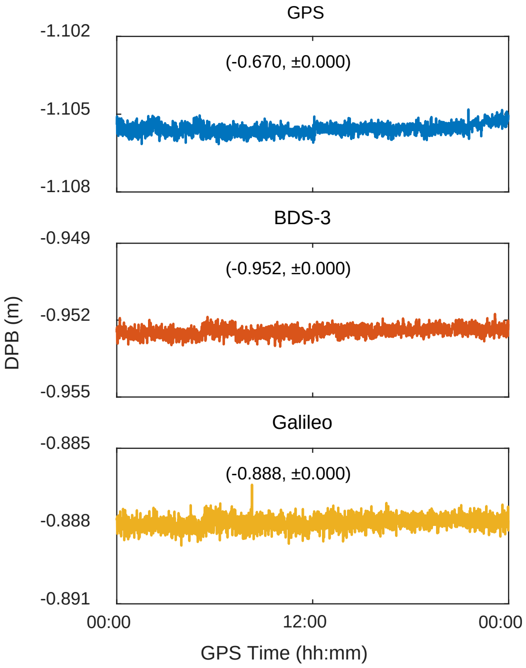

Fig. 3 Time series of DPB for APM3-APM7 with GPS, BDS-3 and Galileo on DOY 159 of 2021

Table 4 presents the integer ambiguity resolution success rate results with GPS, BDS-3, Galileo and their combination for APM3-APM7 and APM7-WUH2 on June10, 2021. Our analysis defines the success rate as the epochs with ambiguity corrected resolved divided by the total epochs. For zero baseline APM3-APM7, as the atmospheric delays are fully eliminated, the integer ambiguity resolution success rate for GPS-only, BDS-3-only, Galileo-only and their combination are all 100%. The short baseline APM7-WUH2, limited by atmospheric delays and multipath effect, does not achieve the same performance as the zero baseline APM3-APM7. The success rate for GPS-only, BDS-3-only, Galileo-only and GPS+BDS-3+Galileo is 96.7%, 97.1%, 95.2% and 99.7%. For a single constellation, the success rate of BDS-3 is higher than that of GPS and Galileo, which is owing to the more visible satellites of BDS-3 in China. With the combination of those three constellations, the success rate reaches 99.7%, demonstrating the advantages of multi-GNSS.

Fig. 4 shows the positioning results of the zero baseline APM3-APM7 with GPS, BDS-3, Galileo and GPS+BDS-3+Galileo on June 10, 2021. As we can see that BDS-3 achieves the highest positioning accuracy (1.6 mm, 1.9 mm and 4.1 mm for E, N, U) among three single constellations. This may be due to BDS-3 has more satellites observable in China than GPS and Galileo. For GPS+BDS-3+Galileo, the root-mean-square (RMS) of the positioning errors in the North/East/Up is 1.3 mm, 1.2 mm and 3.5 mm, better than the other three single constellations.

Fig. 5 depicts the positioning performance of the short baseline APM7-WUH2. The impact of residual atmospheric errors and multipath effects is shown in the positioning results, reflected in the RMS of positioning errors. For three single constellations, BDS-3 performs the best, followed by GPS and Galileo. The advantages of combining the three systems are also demonstrated, where the RMS of the positioning errors in the North/East/Up is 1.0.6 cm, 0.6 cm and 1.3 cm, respectively.

Conclusions

Real-time kinematic (RTK) positioning based on double-differenced (DD) observations has been wildly used. Although the DD RTK eliminates the common parameters, it loses the opportunity to constrain some parameters dynamically. In this contribution, we focused on single differenced (SD) observations with receiver-end parameters. However, the RTK model based on SD observations is rank-deficient, so the *S*-system theory was used to construct the full-rank model. Considering different ionospheric constraints, we derived three SD models: ionosphere-float, -weighted and -fixed.

Table 4 Integer ambiguity resolution success rate for the zero baseline APM3-APM7 and the short baseline APM7-WUH2 with GPS, BDS-3 and Galileo on June 10, 2021

Constellation	APM3-APM7	APM7-WUH2
GPS	2880/2880=100%	2786/2880=96.7%
BDS-3	2880/2880=100%	2797/2880=97.1%
Galileo	2880/2880=100%	2742/2880=95.2%
GPS+BDS-3+Galileo	2880/2880=100%	2872/2880=99.7%

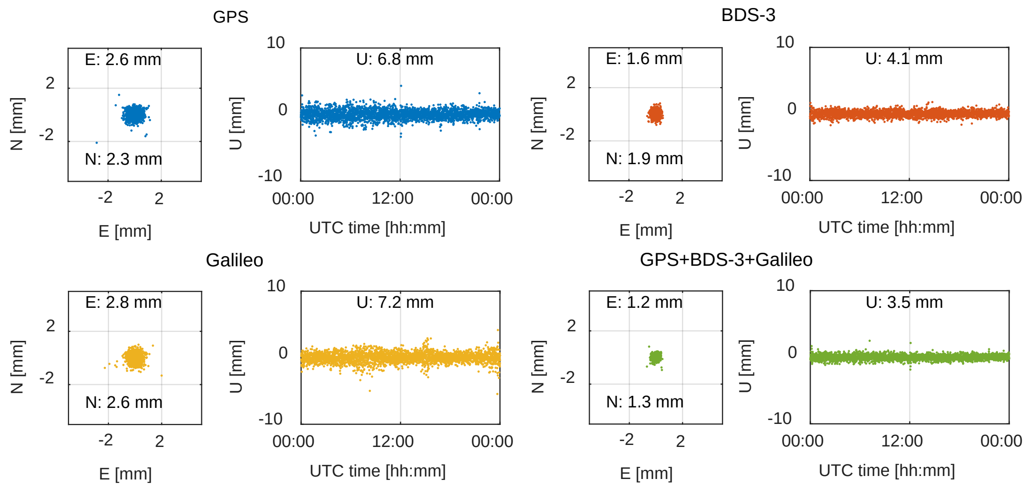

Fig. 4 Horizontal (E = East and N = North) position scatter and vertical (U = Up) time series for the zero baseline APM3-APM7

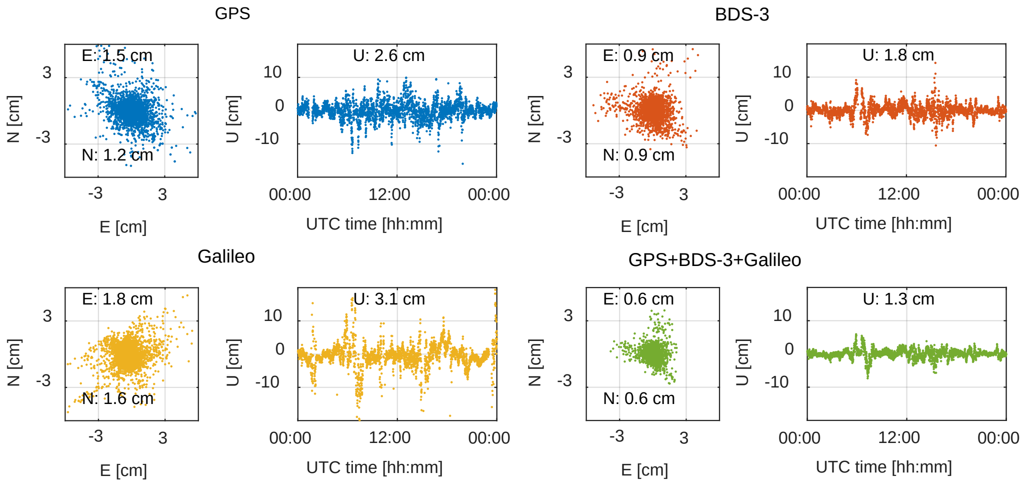

Fig. 5 Horizontal (E = East and N = North) position scatter and vertical (U = Up) time series for the short baseline APM7-WUH2

Based on a zero baseline, we analyzed receiver-related biases in the SD model with GPS, BeiDou navigation satellite system with global coverage (BDS-3) and Galileo, including differential code bias (DCB), differential phase bias (DPB) of the first frequency, and DPB. The number analysis showed two findings. First, the DPB of the first frequency was similar to DCB with centimeter accuracy and can be pre-corrected or estimated as time-invariants in RTK positioning. Second, DPB that is associated with phase observations only thus had sub-millimeter accuracy. However, DPB contained ambiguity of two frequencies, therefore can only be estimated as time-invariants.

With the stability of receiver-related biases, the SD RTK performance of zero and short baselines was tested using GPS, BDS-3 and Galileo in terms of integer ambiguity resolution success rate and positioning accuracy. We found that the SD RTK with BDS-3-only can perform better than GPS-only and Galileo-only as more visible satellites are available. In addition, the SD RTK with GPS+BDS-3+Galileo can achieve higher performance than with a single constellation.

This study preliminarily shows the stability of the receiver-related biases using zero baselines, which can be dynamically constrained to benefit RTK positioning. However, this work is limited to short baselines, and RTK positioning performance for medium and long baselines has not yet been covered. In addition, in multi-constellation scenarios, inter-system bias (ISB) is also a parameter of interest and can be dynamically constrained to improve positioning performance. The understanding and analysis of these works will be a point of interest for future research.

Acknowledgments

Two anonymous reviewers made valuable and helpful comments. Their contributions are highly appreciated.

Data availability

The datasets generated during the current study are available from the author on a reasonable request.

Reference

Atiz O, Shakor A, Ogutcu S, Alcay S (2021) Performance investigation of Trimble RTX correction service with multi-GNSS constellation. Survey Review, 1-11. doi: 10.1080/00396265.2021.1999128

Bahadur B, Nohutcu M (2019) Comparative analysis of MGEX products for post-processing multi-GNSS PPP. Measurement 145:361-369. doi:10.1016/j.measurement.2019.05.094

Hadas T, Hobiger T, Hordyniec P (2020) Considering different recent advancements in GNSS on real-time zenith troposphere estimates. GPS Solutions 24. doi:10.1007/s10291-020-01030-w

Karutin S (2020) The Status of Glonass System. In Proceedings of the 34th International Technical Meeting of the Satellite Division of The Institute of Navigation (ION GNSS+ 2021). doi:10.33012/2020.17553

Khodabandeh A, Teunissen P (2016) PPP-RTK and inter-system biases: the ISB look-up table as a means to support multi-system PPP-RTK. Journal of Geodesy 90:837-851. doi:10.1007/s00190-016-0914-9

Leandro R, Langley R, Santos M (2008) UNB3m_pack: a neutral atmosphere delay package for radiometric space techniquess GPS Solutions 12:65-70. doi:10.1007/s10291-007-0077-5

Leick A, Rapoport L, Tatarnikov D (2015) GPS satellite surveying. Wiley, Hoboken.

Li C, Ching K, Chen K (2019) The ongoing modernization of the Taiwan semi-dynamic datum based on the surface horizontal deformation model using GNSS data from 2000 to 2016. Journal of Geodesy 93:1543-1558. doi:10.1007/s00190-019-01267-5

Liu W, Hu Y, Hsieh T, Zhao J, Wang S (2021) Quinary Offset Carrier Modulations for Global Navigation Satellite System. IEICE Transactions on Communications. doi:10.1587/transcom.2020EBP3121

Liu X, de Jong K, Tiberius C (2003) Reparameterization of single difference and undifferenced kinematic GPS positioning models. Geo-Spatial Information Science, 6(2), 1-7. doi: 10.1007/BF02826746

Liu X, Tiberius C, de Jong K (2004) Modelling of differential single difference receiver clock bias for precise positioning. GPS Solutions, 7(4), 209-221. doi: 10.1007/s10291-003-0079-x

Mi X, Sheng C, El-Mowafy A, Zhang B (2021) Characteristics of receiver-related biases between BDS-3 and BDS-2 for five frequencies including inter-system biases, differential code biases, and differential phase biases. GPS Solutions 25:1-11. doi:10.1007/s10291-021-01151-w

Mi X, Zhang B, Odolinski R, Yuan Y (2020) On the temperature sensitivity of multi-GNSS intra- and inter-system biases and the impact on RTK positioning. GPS Solutions 24:1-14. doi:10.1007/s10291-020-01027-5

Mi X, Zhang B, Yuan Y (2019a) Multi-GNSS inter-system biases: estimability analysis and impact on RTK positioning. GPS Solutions 23:1-13. doi:10.1007/s10291-019-0873-8

Mi X, Zhang B, Yuan Y (2019b) Stochastic modeling of between-receiver single-differenced ionospheric delays and its application to medium baseline RTK positioning. Measurement Science and Technology 30:095008. doi:10.1088/1361-6501/ab11b5

Odijk D, Nadarajah N, Zaminpardaz S, Teunissen PJG (2017) GPS, Galileo, QZSS and IRNSS differential ISBs: estimation and application. GPS Solutions 21:439-450. doi:10.1007/s10291-016-0536-y

Odijk D, Teunissen P (2008) ADOP in closed form for a hierarchy of multi-frequency single-baseline GNSS models. Journal of Geodesy 82:473-492. doi:10.1007/s00190-007-0197-2

Odijk D, Zhang B, Khodabandeh A, Odolinski R, Teunissen P (2016) On the estimability of parameters in undifferenced, uncombined GNSS network and PPP-RTK user models by means of *S*-system theory. Journal of Geodesy, 90(1), 15-44. doi: 1007/s00190-015-0854-9

Odolinski R, Teunissen P, Odijk D (2015a) Combined BDS, Galileo, QZSS and GPS single-frequency RTK. GPS Solutions 19:151-163. doi:10.1007/s10291-014-0376-6

Odolinski R, Teunissen P (2016) Single-frequency, dual-GNSS versus dual-frequency, single-GNSS: a low-cost and high-grade receivers GPS-BDS RTK analysis. Journal of Geodesy 90:1255-1278. doi:10.1007/s00190-016-0921-x

Odolinski R, Teunissen P (2017a) Low-cost, 4-system, precise GNSS positioning: a GPS, Galileo, BDS and QZSS ionosphere-weighted RTK analysis. Measurement Science and Technology 28. doi:10.1088/1361-6501/aa92eb

Odolinski R, Teunissen P (2017b) Low-cost, high-precision, single-frequency GPS-BDS RTK positioning. GPS Solutions 21:1315-1330. doi:10.1007/s10291-017-0613-x

Odolinski R, Teunissen P, Odijk D (2015b) Combined GPS + BDS for short to long baseline RTK positioning. Measurement Science and Technology 26. doi:10.1088/0957-0233/26/4/045801

Odolinski R, Teunissen P, Zhang B (2020) Multi-GNSS processing, positioning and applications. Journal of Spatial Science 65:3-5. doi:10.1080/14498596.2020.1687170

Paziewski J, Sieradzki R, Baryla R (2018) Multi-GNSS high-rate RTK, PPP and novel direct phase observation processing method: application to precise dynamic displacement detection. Measurement Science and Technology 29. doi:10.1088/1361-6501/aa9ec2

Pignalberi A, Habarulema J, Pezzopane M, Rizzi R (2019) On the development of a method for updating an empirical climatological ionospheric model by means of assimilated vTEC measurements from a GNSS receiver network. Space Weather 17:1131-1164. doi:10.1029/2019sw002185

Ruhl C, Melgar D, Grapenthin R, Allen R (2017) The value of real-time GNSS to earthquake early warning. Geophysical Research Letters 44:8311-8319. doi:10.1002/2017gl074502

Santra A, Mahato S, Mandal S, Dan S, Verma P, Banerjee P, Bose A (2019) Augmentation of GNSS utility by IRNSS/NavIC constellation over the Indian region. Advance in Space Research 63:2995-3008. doi:10.1016/j.asr.2018.04.020

Shen Y, Li B, Xu G (2009) Simplified equivalent multiple baseline solutions with elevation-dependent weights. GPS Solutions 13:165-171. doi:10.1007/s10291-008-0109-9

Shi J, Ouyang C, Huang Y, Peng W (2020) Assessment of BDS-3 global positioning service: ephemeris, SPP, PPP, RTK, and new signal. GPS Solutions 24. doi:10.1007/s10291-020-00995-y

Teunissen P (2018) Distributional theory for the DIA method. Journal of Geodesy 92:59-80. doi:10.1007/s00190-017-1045-7

Teunissen P, Verhagen S (2009) The GNSS ambiguity ratio-test revisited: a better way of using it. Survey Review 41:138-151. doi:10.1179/003962609x390058

Teunissen P (1998) The ionosphere-weighted GPS baseline precision in canonical form. Journal of Geodesy 72:107-117. doi: 10.1007/s001900050152

Teunissen P, deJonge P, Tiberius C (1997) The least-squares ambiguity decorrelation adjustment: its performance on short GPS baselines and short observation spans. Journal of Geodesy 71:589-602 doi: 10.1007/s001900050127

Tian Y, Yuan L, Tan L, Yan H, Xu S (2019) Regularization and particle filtering estimation of phase inter-system biases (ISB) and the lookup table for Galileo E1-GPS L1 phase ISB calibration. GPS Solutions 23. doi:10.1007/s10291-019-0908-1

Tuka A, El-Mowafy A (2013) Performance Evaluation of Different Troposphere Delay Models and Mapping Functions. Measurement 46:2, 928–937. doi:10.1016/j.measurement.2012.10.015

Xiao G, Li P, Sui L, Heck B, Schuh H (2019) Estimating and assessing Galileo satellite fractional cycle bias for PPP ambiguity resolution. GPS Solutions 23. doi:10.1007/s10291-018-0793-z

Yalvac S, Berber M (2018) Galileo satellite data contribution to GNSS solutions for short and long baselines. Measurement 124:173-178. doi:10.1016/j.measurement.2018.04.020

Yang Y, Liu L, Li J, Yang Y, Zhang T, Mao Y, Sun B, Ren X (2021) Featured services and performance of BDS-3. Science Bulletin 66:2135-2143. doi:10.1016/j.scib.2021.06.013

Yuan Y, Mi X, Zhang B (2020) Initial assessment of single-and dual-frequency BDS-3 RTK positioning. Satellite Navigation. 1(1):1-7. doi: 10.1186/s43020-020-00031-x

Zaminpardaz S, Wang K, Teunissen P (2018) Australia-first high-precision positioning results with new Japanese QZSS regional satellite system. GPS Solutions 22. doi:10.1007/s10291-018-0763-5

Zha J, Zhang B, Liu T, Hou P (2021) Ionosphere-weighted undifferenced and uncombined PPP-RTK: theoretical models and experimental results. GPS Solutions 25. doi:10.1007/s10291-021-01169-0

Zhang B, Chen Y, Yuan Y (2019) PPP-RTK based on undifferenced and uncombined observations: theoretical and practical aspects. Journal of Geodesy 93:1011-1024. doi:10.1007/s00190-018-1220-5

Author Biographies

Xiaolong Mi is a Ph.D. candidate at the Innovation Academy for Precision Measurement Science and Technology, Chinese Academy of Sciences, China and Curtin University, Australia. His research focuses on high-precision GNSS positioning, time and frequency transfer with integer ambiguity resolution, multi-GNSS inter-operability and software development.

Baocheng Zhang is a professor at the Innovation Academy for Precision Measurement Science and Technology, Chinese Academy of Sciences. His research focuses on modeling multiple global navigation satellite systems for integer ambiguity resolution-enabled precise point positioning (PPP-RTK) applications.

Yunbin Yuan is a professor and the director of the GNSS Application and Research Group at the Innovation Academy for Precision Measurement Science and Technology at the Chinese Academy of Sciences. His current research interests are the following: (1) GNSS-based spatial environmental monitoring and analysis, (2) high-precision GNSS satellite navigation and positioning, and (3) GNSS applications to orbit determination for LEO satellites.

Journal of Global Positioning Systems (2021)
Vol. 17, No. 2: 164-178
DOI: 10.5081/jgps.17.2.164

Journal of Global Positioning Systems
2021
© CPGPS

Research on the UWB High Precision Indoor Positioning Method with the Heterogeneous Information Constraints

GUO, Nan[1]; JIANG, Wei[2]; LI, Jing[3]; LIU, Fei[1*]; DONG, Jie[3]
1 School of Geomatics and Urban Spatial Informatics, Beijing University of Civil Engineering and Architecture, Beijing 102616
2 State Grid Corporation of China, Beijing 100031
3 State Grid Siji Shenwang Location-Based Service (Beijing) Co., Ltd, Beijing 102209
* Corresponding author: Fei Liu, liufei1@bucea.edu.cn

Abstract: There are many obstacles in the UWB indoor positioning, such as installation location limitation of base stations, non-line-of-sight and so forward. In this paper, the high-precision indoor positioning model was discussed, and then the UWB indoor positioning method was given based on the heterogeneous data constraints, such as PDR, map and vision. Three indoor positioning models, the kinematic adaptive robust EKF UWB model based on the gain matrix, the UWB/PDR/Map coupled model, and the UWB/Vision fusion model were built and assessed, respectively. Afterward, the precision and the potential application scenarios of the three models were discussed via the practical tests. The test results showed that, with our method, the overall positioning accuracy reached around ±0.2 m under the conditions of the full or partial UWB signal coverage, available or interrupted line-of-sight, or undergoing other situational challenges such as the sparse texture and the continuous variation of the light strength.

Key words: Heterogeneous information; UWB; Robust EKF; Indoor location

1 Introduction

In spatial information science and engineering, the acquisition and processing of high-precision positioning information belong to the frontier research worldwide [1]. Many efforts have been made to consistently advance the techniques in this area, for example [2], the "Xihe" plan in China, the “Insight into the battlefield” and the “Next Generation 911 Project” in US, and the “Galileo Local Technology Plan” in Europe. With the completion of global coverage of the BDS (Beidou System) and other global satellite navigation systems, the real-time, all-weather operational condition, and global high precision PNT (Positioning, Navigation and Timing) are enabled to survey many outdoor applications [3,4].

With the indoor positioning and navigation techniques, even there are many options, such as WiFi [5], UWB (Ultra Wide Band) [6], RF (Radio Frequency) [7], and Bluetooth [8, 9], the meter-level positioning results may be easily to be achieved, however, developing the higher precision of indoor positioning techniques is still extremely challenging.

Specifically, the UWB positioning can reach the accuracy level of decimeters or even centimeters by measuring the transmission time, the angle, and the strength of electromagnetic wave signals between a positioning tag and a base station [10]. When UWB is used in positioning, its methods can be divided into RSSI (Received Signal Strength Indication), TDOA (Time Difference of Arrival), AOA(Angle-of-Arrival), TOA (Time of Arrival), etc. The positioning based on RSSI needs to be modeled according to the signal propagation fading to realize ranging. It can not reflect the advantages of UWB when applied to UWB [11]. AOA can overcome the influence of NLOS

Editor in charge: Dr. Xiaolin Meng

(Non Line of Sight) propagation to a certain extent and can locate with fewer sensors, but the cost is high due to the need to use antenna array and directional antenna angle measurement [12]. TOA can make full use of the advantages of high UWB time resolution, but the problem of clock synchronization at the transceiver must be solved first [13]. TDOA can overcome the problem of synchronization at the transceiver, but the synchronization between anchor nodes still needs to be considered [14].

However, due to the signal obstruction or reflection of variant structural objects and/or other solid features indoors, there may exist serious multipath effect, irregular LOS (Line of Sight) propagation, etc., which negatively affect the positioning accuracy, as well as the configuration of tags and base stations, pre-installation and measurement of the precise location of the base stations, etc., which restrict the positioning accuracy and even working area. Wymeersch [15] analyzed the characteristics of a large number of UWB signals in LOS and NLOS environments. Using SVM (Support Vector Machine, SVM) to identify the NLOS state and weaken the error can effectively eliminate the NLOS error and improve the ranging accuracy, but a large amount of data statistics is needed. Li [16] used Kalman filter to smooth the original ranging information and proposes a colored noise adaptive Kalman method to eliminate NLOS error. The simulation effect is obvious, but the amount of calculation is large. Meng [17] analyzed the geometric structure of the wall when the IR-UWB (Impulse Radio UWB) signal propagated through the wall, deduced the upper limit of the ranging error caused by the additional delay, and directly corrected the TOA ranging result by using the NLOS distance error information. This method requires more a priori knowledge and is difficult to be applied to the ranging elimination of moving targets.

Essentially, INS (Inertial navigation system) used in PDR (Pedestrian dead reckoning) algorithm uses accelerometers, and gyroscopes to obtain position, velocity, and attitude information and plays an important role in the field of navigation and location services. But its sensor technology and integration calculation principle restrict its popularization. A standalone INS system is difficult to satisfy the demand of the long-term navigation and positioning accuracy requirements [18]. As a streaming media technology, the video sensors have the capability of positioning and the acquisition of the environmental information, and the relative positioning accuracy may reach 0.1% to 2% of the working ranges. However, one find the use the visual method very challenging in environments such as sparse textures, too bright or too dark indoors [19, 20]. In this case, these sensors to assist UWB for fusion positioning can effectively make up for the shortcomings of each system. Building a hybrid positioning system can enhance the continuity and robustness of positioning in complex indoor environment. Renaudin [21] designed an optimal combined filter to fuse the arrival angle and arrival time difference of UWB signal with the acceleration, angular velocity and magnetic field intensity output by MEMS inertial system, so as to further suppress the UWB NLOS error. Zhang [22] used extended Kalman filter to fuse MEMS, UWB and barometer to form a position and heading estimation system, and obtained more reliable vertical positioning results. Nyqvist [23] presented a method for global pose estimation using INS, monocular vision, and UWB sensors, and showed the benefit of the suggested sensor combination. Qiao [24] used the position information output by monocular vision ORB (Oriented Fast and Rotated Brief)-SLAM (Simultaneous Localization and Mapping) and the positioning information calculated by UWB as measurement information, and used extended Kalman filter for data fusion to realize indoor positioning, which effectively overcomes the problem of unable positioning caused by monocular vision ORB-SLAM tracking failure, and effectively suppresses the influence of UWB NLOS error.

Our research has been targeting such problems mentioned above. This manuscript particularly discusses three different indoor positioning methods based on using UWB, PDR, and the vision sensors, and assesses the performance improvement with the proposed models. In the practical tests, the challenging environment were considered through the reduction of the number of UWB base stations, varying the LOS obstruction, environmental texture and light strength through their influence on the indoor positioning accuracy. Afterward, the overall precision and potential application scenarios of the three methods were discussed based on the practical tests.

2 Extended Kalman filter

The classical Kalman filter is based on the linear system, that is, both the measurement model and the system model are linear systems. For discrete linear systems, the state equation can be described as:

$$\boldsymbol{x}_k = \boldsymbol{\Phi}_{k,k-1}\boldsymbol{x}_{k-1} + \boldsymbol{G}_{k-1}\boldsymbol{w}_{k-1} \tag{1}$$

where, $\boldsymbol{x}_k$ represents the state vector, $\boldsymbol{\Phi}_{k,k-1}$ represents the state transition matrix, $\boldsymbol{G}_{k-1}$ represents the system noise drive matrix and $\boldsymbol{w}_{k-1}$ represents the process noise vector. k is represented as an observation epoch.

Observation vectors and state vectors should simultaneously satisfy certain functional relationships. The observation equation of a discrete linear system can be expressed as:

$$\boldsymbol{z}_k = \boldsymbol{H}_k\boldsymbol{x}_k + \boldsymbol{v}_k \tag{2}$$

where, $\boldsymbol{z}_k$ represents the system observation vector, $\boldsymbol{H}_k$ represents the observation coefficient matrix and $\boldsymbol{v}_k$ represents the observed noise vector. For a classical Kalman filter, the process and observation noise vectors should conform to the following normal distributions:

$$\begin{cases} \boldsymbol{w}_k \sim N(\boldsymbol{0},\boldsymbol{Q}_k) \\ \boldsymbol{v}_k \sim N(\boldsymbol{0},\boldsymbol{R}_k) \end{cases} \tag{3}$$

where $\boldsymbol{Q}_k$ and $\boldsymbol{R}_k$ are the positive definite covariance matrices of process noise and observation noise vectors, respectively [25].

Kalman filter is a recursive estimation process based on system state and noisy observation sequence, which usually includes time update process and measurement update process.

The time update process is as follows[26]:

$$\begin{cases} \hat{\boldsymbol{x}}_k^- = \boldsymbol{\Phi}_{k,k-1}\hat{\boldsymbol{x}}_{k-1}^+ \\ \boldsymbol{P}_k^- = \boldsymbol{\Phi}_{k,k-1}\boldsymbol{P}_{k-1}^+\boldsymbol{\Phi}_{k,k-1}^T + \boldsymbol{G}_{k,k-1}\boldsymbol{Q}_{k-1}\boldsymbol{G}_{k-1}^T \end{cases} \tag{4}$$

where the symbols “^”, “-” and “+” represent the estimated, predicted, and filtered value, respectively. $\hat{\boldsymbol{x}}_k^-$ and $\boldsymbol{P}_k^-$ are the state prediction and its covariance matrix at t_k, $\hat{\boldsymbol{x}}_{k-1}^+$ and $\boldsymbol{P}_{k-1}^+$ are the state estimate and its covariance matrix at t_{k-1}, respectively.

The measurement updating process is as follows:

$$\begin{cases} \boldsymbol{K}_k = \boldsymbol{P}_k^-\boldsymbol{H}_k^T(\boldsymbol{H}_k\boldsymbol{P}_k^-\boldsymbol{H}_k^T + \boldsymbol{R}_k)^{-1} \\ \hat{\boldsymbol{x}}_k^+ = \hat{\boldsymbol{x}}_k^- + \boldsymbol{K}_k(\boldsymbol{z}_k - \boldsymbol{H}_k\hat{\boldsymbol{x}}_k^-) \\ \boldsymbol{P}_k^+ = (\boldsymbol{I} - \boldsymbol{K}_k\boldsymbol{H}_k)\boldsymbol{P}_k^- \end{cases} \tag{5}$$

where, $\boldsymbol{K}_k$ is the filter gain matrix, which is calculated with the minimum state variance as the constraint condition.

The predicted residual is as follows:

$$\boldsymbol{V}_k = \boldsymbol{z}_k - \boldsymbol{H}_k\hat{\boldsymbol{x}}_k^- = \boldsymbol{z}_k - \hat{\boldsymbol{z}}_k \tag{6}$$

Linear system is only an ideal system. In practical applications, system state models or observation models mostly contain non-linear characteristics. The EKF (Extended Kalman filter) is one of the most commonly used estimation method for nonlinear filtering problems in scientific and engineering applications. The system model is as follows:

$$\boldsymbol{x}_k = \boldsymbol{f}_{k-1}(\boldsymbol{x}_{k-1},\boldsymbol{w}_{k-1}) \tag{7}$$

along with the observation model:

$$\boldsymbol{z}_k = \boldsymbol{h}_k(\boldsymbol{x}_k,\boldsymbol{v}_k) \tag{8}$$

The noise matrix of EKF non-linear system still satisfies the requirement of Formula (3). Before time update, the system needs to linearize the state equation by first order Taylor series expansion to get the state transition matrix and noise drive matrix, which can then be solved as KF.

$$\begin{cases} \boldsymbol{\Phi}_{k,k-1} = \left.\dfrac{\partial \boldsymbol{f}_{k-1}}{\partial \boldsymbol{x}}\right|_{\hat{\boldsymbol{x}}_{k-1}^+} \\ \boldsymbol{G}_{k-1} = \left.\dfrac{\partial \boldsymbol{f}_{k-1}}{\partial \boldsymbol{w}}\right|_{\hat{\boldsymbol{x}}_{k-1}^+} \end{cases} \tag{9}$$

At the same time, the observation equation needs to be linearized to obtain the observation coefficient matrix before updating the measurements.

$$\boldsymbol{H}_k = \left.\frac{\partial \boldsymbol{h}_k}{\partial \boldsymbol{x}}\right|_{\hat{\boldsymbol{x}}_k^-} \tag{10}$$

After the state equation and the observation equation are discretized, the state can be updated by the methods of equations (4) and (5).

3 The UWB indoor positioning with the heterogeneous information constraints

3.1 The robust EKF using UWB

Under the consideration that the motion process involves position, velocity and acceleration information, this paper proposes a 9-dimensional state vector UWB dynamic positioning model based on EKF model. The state vectors are as follows:

$$\boldsymbol{x}_k = [\Delta \boldsymbol{x} \quad \Delta \dot{\boldsymbol{x}} \quad \Delta \ddot{\boldsymbol{x}} \quad \Delta \boldsymbol{y} \quad \Delta \dot{\boldsymbol{y}} \quad \Delta \ddot{\boldsymbol{y}} \quad \Delta \boldsymbol{z} \quad \Delta \dot{\boldsymbol{z}} \quad \Delta \ddot{\boldsymbol{z}}] \tag{11}$$

where $\Delta \boldsymbol{u}, \Delta \dot{\boldsymbol{u}}, \Delta \ddot{\boldsymbol{u}}$ ($\boldsymbol{u} = x, y, z$) represent the position, velocity and acceleration errors in the $\boldsymbol{u}$ direction, respectively. The accelerations can be considered as a first-order Markov process [27]. Both of the process noise vector and the observation noise vector are considered to the zero-mean white noise processes. The state coefficient matrix can be obtained from the motion model:

$$\boldsymbol{\Phi}_k = \begin{bmatrix} \boldsymbol{\Phi}_{x,k} & 0 & 0 \\ 0 & \boldsymbol{\Phi}_{y,k} & 0 \\ 0 & 0 & \boldsymbol{\Phi}_{z,k} \end{bmatrix} \tag{12}$$

with

$$\boldsymbol{\Phi}_{u,k} = \begin{bmatrix} 1 & T & \dfrac{T^2}{2} \\ 0 & 1 & T \\ 0 & 0 & 1 \end{bmatrix} \tag{13}$$

where T represents the time interval. The observable is the range from a UWB mobile station to each base station, and the spatial geometric distance P is:

$$P_i = \sqrt{\left(x_i - x_a\right)^2 + \left(y_i - y_a\right)^2 + \left(z_i - z_a\right)^2} \tag{14}$$

where, $\left(x_a, y_{a,} z_a\right)$ is the location coordinates of UWB mobile station, $\left(x_i, y_{i,} z_i\right)$ is the coordinates of the i-th base station. After linearizing the above formula, the approximate coordinates $\left(x_{a0}, y_{a0,} z_{a0}\right)$ of the mobile station tag are brought in as the initial value to obtain the observation equation:

$$P_i' = P_{a0}' - \left[l_a \quad m_a \quad n_a\right] \begin{bmatrix} \Delta x \\ \Delta y \\ \Delta z \end{bmatrix} \tag{15}$$

with $P_{a0}' = \sqrt{\left(x_i - x_{a0}\right)^2 + \left(y_i - y_{a0}\right)^2 + \left(z_i - z_{a0}\right)^2}$,

$l_a = \dfrac{x_i - x_{a0}}{P_{a0}'}$, $m_a = \dfrac{y_i - y_{a0}}{P_{a0}'}$ and $n_a = \dfrac{z_i - z_{a0}}{P_{a0}'}$.

Therefore, the observation matrix is:

$$H = [l_a \quad 0 \quad 0 \quad m_a \quad 0 \quad 0 \quad n_a \quad 0 \quad 0] \tag{16}$$

But, when the observations contain gross errors, the state estimation will be biased so that the influence of gross errors in measurements cannot be ignored. In this paper we construct a robust EKF gain matrix that can restrict the effect of the gross errors on the state estimation as [28]:

$$\left.\begin{array}{ll} \bar{\boldsymbol{K}}_{ij} & s_j \le c_0 \\ \tilde{\boldsymbol{K}}_{ij} = \bar{\boldsymbol{K}}_{ij} \times \dfrac{c_0}{s_j} \times \left[\dfrac{c_1 - s_j}{c_1 - c_0}\right]^2 & c_0 < s_j \le c_1 \\ 0 & s_j > c_1 \end{array}\right\} \tag{17}$$

where, c_0 and c_1 are robust parameters. c_0 is 2.5-3.5, c_1 is 3.5-4.5[28].

$$s_j = \left|V_{k,j}\right| \Big/ \sqrt{r_j \sigma_j} \tag{18}$$

where i represents the i-th component in the state vector, and j represents the j-th component in the observation vector, $V_{k,j}$, r_j and σ_j represents the prediction residual(Equation 6), redundancy index [29] and a-priori standard deviation of the j-th observation, respectively. At epoch k, the redundancy index r_{j} of the *j*-th observation is generally defined by:

$$r_i(k) = (\boldsymbol{Q}_{V_y}(k)\boldsymbol{W}_y(k))_i \tag{19}$$

where $\boldsymbol{Q}_{V_y}(k)$ is the covariance matrix of the residual vector and $\boldsymbol{W}_y(k)$ is the weighting matrix of the observation vector under the assumption of a diagonal matrix. The covariance matrix of the residual vector for the observation vector is:

$$\boldsymbol{Q}_{V_y}(k) = \boldsymbol{H}_k \boldsymbol{P}_k^- \boldsymbol{H}_k^T + \boldsymbol{R}_k \tag{20}$$

3.2 The UWB/PDR/Map fusion

The range and its accuracy from the UWB indoor positioning technique are restricted by the number of the base stations and their distribution. The positioning performance degrades if the UWB signals become weak. Sometime, the UWB system may even become unavailable. Hence, the integration of UWB, PDR (pedestrian dead reckoning) and Map is introduced. The corresponding EKF is designed to include the position errors dN and dE, the moving distance error ds and the heading error $d\theta$ in its state vector [30]:

$$\boldsymbol{x}_k = \begin{bmatrix} dN & dE & ds & d\theta \end{bmatrix}^T \tag{21}$$

According to the PDR motion model, the state transition matrix should be:

$$\boldsymbol{\Phi}_k = \begin{bmatrix} 1 & 0 & \cos\theta_k & -s_k \sin\phi_k \\ 0 & 1 & \sin\phi_k & s_k \cos\theta_k \\ 0 & 0 & 1 & 0 \\ 0 & 0 & 0 & 1 \end{bmatrix} \tag{22}$$

When the position of the UWB system is updated, the position difference between the UWB and PDR system is taken as the observation as follows:

$$\boldsymbol{z}_k = [\Delta N \ \ \Delta E]^T = [N_{k,u} - N_{k,p} \ \ E_{k,u} - E_{k,p}] \tag{23}$$

Then the observation matrix is：

$$H_k = \begin{bmatrix} 1 & 0 & 0 & 0 \\ 0 & 1 & 0 & 0 \end{bmatrix} \tag{24}$$

where ΔN and ΔE are the north and east position differences between the two positioning systems, $N_{k,u}$ and $E_{k,u}$ are the north and east UWB positions, $N_{k,p}$ and $E_{k,p}$ are the north and east positions calculated according to the PDR algorithm at time *k*.

When the output of the UWB position is not updated, the differences between the system prediction coordinates and the PDR observation coordinates are taken as the observations, and the rest remains unchanged, and the PDR position is recursively corrected.

The position errors obtained through filtering are used to update the predicted positions at the current time. So, the final position is updated as follows [31]:

$$\begin{cases} N_{p,k}^+ = N_{p,k} + dN \\ E_{p,k}^+ = E_{p,k} + dE \end{cases} \tag{25}$$

In order to suppress the divergence of the heading estimate obtained from the INS, we match the position with the indoor map based on the UWB positioning result, and virtually design 16 possible equally spaced directions around this position, i.e., every other 22.5 degrees. The direction of the center of the section is adopted as the moving direction of a pedestrian. Relative to the heading angle of the inertial navigation system, the center direction of the nearest interval is used as the heading. If the difference between the heading from the inertial navigation and the nearest map direction is less than 5 degrees, the heading angle of the inertial navigation is used as the current heading [30].

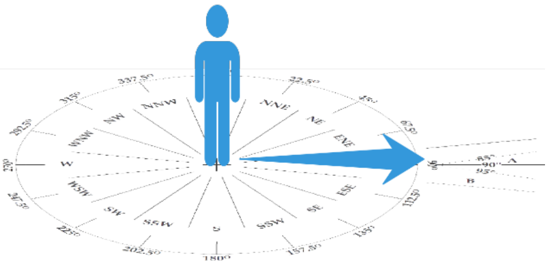

Fig.1 Heading angle calculating strategy

3.3 UWB/Vision Fusion

Visual sensors can be used not only for positioning during emergency rescues such as urban fires and earthquakes, but also for acquiring the environment information to compensate the UWB's insufficient environmental perception. However, the visual positioning technique is affected by a single texture, light and dark changes, etc., which are prone to positioning failure. Moreover, monocular vision SLAM (simultaneous localization and mapping) suffers from scale drift and axial blur. For this reason, upon the UWB EKF positioning model and the monocular vision SLAM model [32], a UWB/vision fusion model is proposed here for indoor positioning under the consideration of the visual scale factors and heading deviations [33] with the following state vector at t_k:

$$\boldsymbol{x}_k = [\boldsymbol{X}_k \quad \boldsymbol{Y}_k \quad \boldsymbol{v}_k \quad \boldsymbol{\theta}_k \quad \boldsymbol{s}_k \quad \boldsymbol{\varphi}_k]^T \qquad (26)$$

where, $\boldsymbol{X}_k$ and $\boldsymbol{Y}_k$ represent plane coordinates, $\boldsymbol{v}_k$ represents pedestrian speed, $\boldsymbol{\theta}_k$ represents the angle of movement direction, $\boldsymbol{s}_k$ represents the ambiguity of the scale, and $\boldsymbol{\phi}_k$ represents the deflection angle between the plane coordinates calculated by vision and the plane coordinates calculated by UWB.

According to the error equation of vision and UWB, the corresponding state equation is:

$$\boldsymbol{x}_{k+1} = \begin{bmatrix} 1 & 0 & sin\theta & 0 & 0 & 0 \\ 0 & 1 & cos\theta & 0 & 0 & 0 \\ 0 & 0 & 1 & 0 & 0 & 0 \\ 0 & 0 & 0 & 1 & 0 & 0 \\ 0 & 0 & 0 & 0 & 1 & 0 \\ 0 & 0 & 0 & 0 & 0 & 1 \end{bmatrix} \boldsymbol{x}_k + \begin{bmatrix} \boldsymbol{w}_x \\ \boldsymbol{w}_y \\ \boldsymbol{w}_v \\ \boldsymbol{w}_\theta \\ \boldsymbol{w}_s \\ 0 \end{bmatrix} \qquad (27)$$

Where $\boldsymbol{w}_x$ and $\boldsymbol{w}_y$ respectively represent the plane position error, $\boldsymbol{w}_v$, $\boldsymbol{w}_\theta$ and $\boldsymbol{w}_s$ represent the speed error, heading angle error and visual scale factor error respectively. If the visually measured position, heading, and the UWB measured position are taken as the observations, the UWB/vision observation equations are as given below:

$$\begin{bmatrix} \boldsymbol{X}_{uwb} \\ \boldsymbol{Y}_{uwb} \end{bmatrix} = \begin{bmatrix} 1 & 0 & 0 & 0 & 0 & 0 \\ 0 & 1 & 0 & 0 & 0 & 0 \end{bmatrix} \boldsymbol{X} + \boldsymbol{e}_{uwb} \qquad (28)$$

$$\begin{bmatrix} \boldsymbol{X}_{vision} \\ \boldsymbol{Y}_{vision} \end{bmatrix} = \begin{bmatrix} cos\phi & -sin\phi & 0 & 0 & \boldsymbol{X}_{vision} & 0 \\ sin\phi & cos\phi & 0 & 0 & \boldsymbol{Y}_{vision} & 0 \end{bmatrix} \boldsymbol{X} + \boldsymbol{e}_{vision} \qquad (29)$$

wherein $\boldsymbol{X}_{vision}$ and $\boldsymbol{Y}_{vision}$ are the position coordinates derived from the vision sensor, $\boldsymbol{X}_{uwb}$ and $\boldsymbol{Y}_{uwb}$ are the position derived by UWB, $\boldsymbol{e}_{vision}$ is the vision position measurement noise vector, and $\boldsymbol{e}_{uwb}$ is the UWB position measurement noise vector.

4 The Multisource indoor positioning fusion framework

In order to overcome the obstacles that are oftern faced in UWB indoor positioning technique, the robust EKF UWB positioning model based on adaptive gain matrix, the UWB/PDR/map integrated positioning model and the UWB/vision integrated positioning model shown in Figure 2 have been proposed, repectively, and used to improve the UWB indoor positioning technique inclusive of reducing the number of the UWB base stations and the impact of the indoor non-line-of-sight, as well as the indoor environment perception, frequent changes in light and localization of areas with sparse texture.

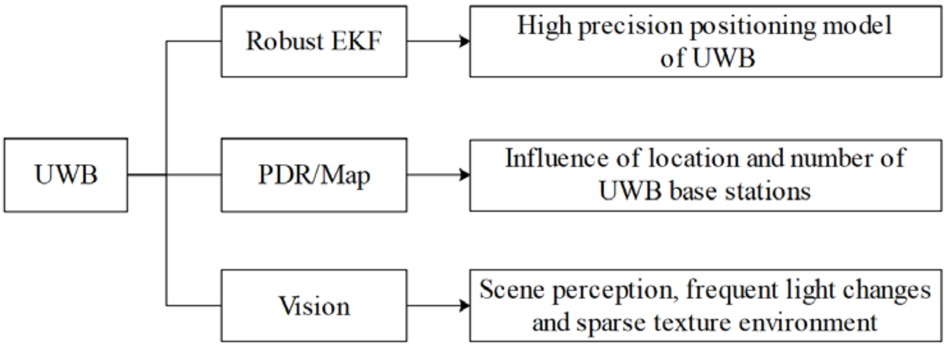

Fig. 2 Heterogeneous information fusion positioning framework

5 Results and their analysis

5.1 UWB robust EKF positioning results analysis

The UWB equipment used in this paper is shown in Figure 3, which can be set as base station or mobile station by command, and automatically change the working mode. The equipment mainly consists of UWB chip, 4G communication module and a package structure. When it is set as a mobile station, it can measure the distance between it and each base station, and transmit the distance information to the upper computer system through 4G module. Its performance is shown in the Table 1.

Fig.3 UWB anchor and tag two-in-one device

Table 1 Performance of UWB anchor and tag two-in-one device

Performance	Parameter
Size	12.5*9.5*2cm
Receiving sensitivity	-118dBm
Ranging accuracy	≤12cm
Positioning accuracy	≤30cm
Line-of-sight ranging distance	Max 800m
Positioning sampling rate	1Hz

The experimental scene is on the laboratory floor (as shown in Figure 4), and the corridor is about 65m long and 3M wide. Several positioning base stations (red triangle in the figure in Figure 5) are set in the classroom and corridor, and their point coordinates are determined by the total station to establish a relative coordinate system. The experimenter walked at a constant speed (from left to right) along the established route with UWB mobile station, as shown in Figure 5, the trajectory results of different algorithms are showed.

Fig.4 Experimental environment

Figure 6 shows the positioning errors resulted from least squares, EKF and the robust EKF method in this paper. It can be seen that the three positioning trajectories well agree with the real trajectory. The 2D root mean square error was ±1.18m from the least square method. The same root mean square error was ±0.28m from the EKF and ±0.13mfrom the proposed method, from which 94% of the point error was better than ±0.50m, and 6% of the point error between ±0.50m-±1.00m.

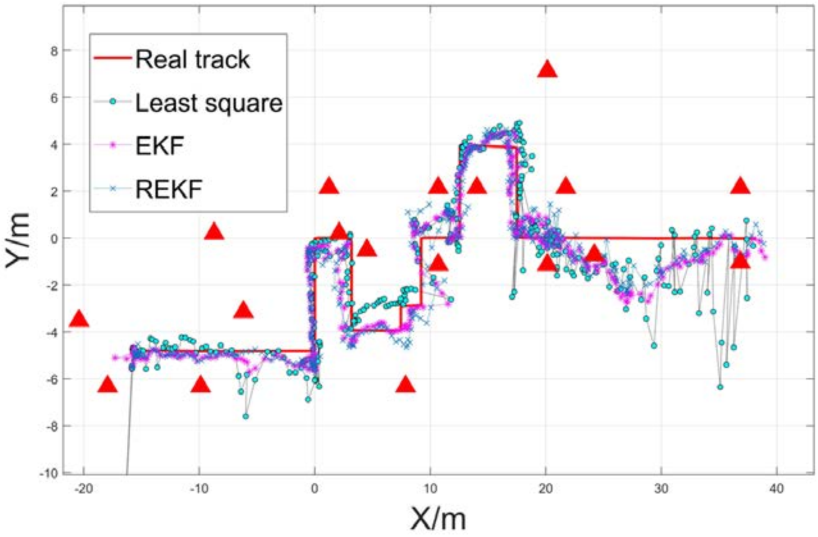

Fig.5 Positioning result track

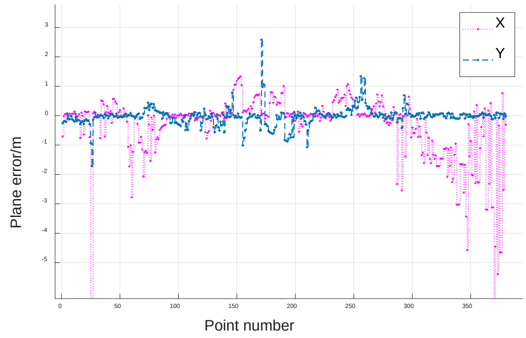

(a) Least square positioning error

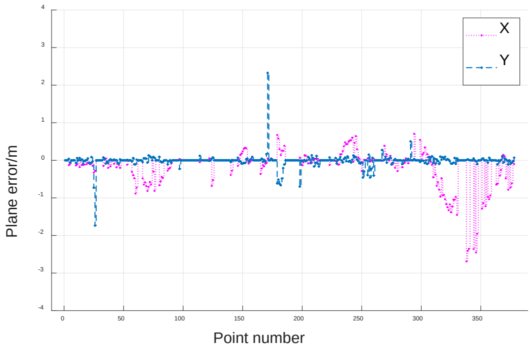

(b) EKF positioning error

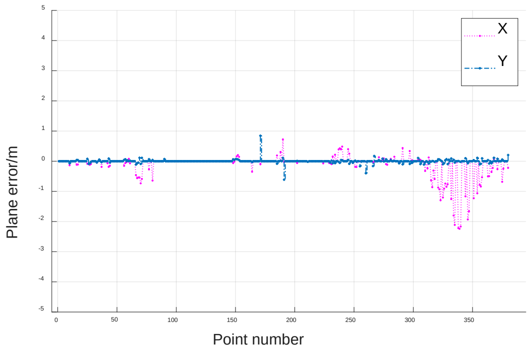

(c) Robust EKF positioning error

Fig.6 Positioning trajectory and errors

5.2 UWB/PDR/Map Fusion

5.2.1 UWB with full signal coverage

In this experiment, a MEMS IMU named MPU9250 is used, which has 9-axis accelerpmeter, gyroscope and magnetometer producted by InvenSense Company(Sunnyvale, CA,USA). Some of its performance parameters are as Table 2. During the experiment, UWB and IMU were bound to the instep of the experimenter, as shown in Figure 7.

Table2. MPU9250 partial parameters

Performance	Parameter
Operating Voltage Supply	2.4V to 3.6V
Gyro Full Scale Range	±250 ±500 ±1000 ±2000 °/s
Gyro Rate Noise	0.01 dps/Hz
Gyro Sensitivity Scale Factor	TYP 32.8 LBS/(°/s)
Gyro Rate Noise Spectral Density	0.01d°/s/√ Hz
Accel Sensitivity Scale Factor	4,096 LSB/g
Accel Noise Power Spectral Density	300μg/√ Hz
Accel Full Scale Range	±2 ±4 ±8 ±16 g
Accel Sensitivity	±4800 LSB/g

Fig.7 Equipment placement

For the best performance, an ideal working environment was introduced for conducting our experiments, in which the UWB signal covered the entire positioning area. 12 UWB base stations cover part of the corridor and a laboratory, as shown in the red triangle in the Figure 8. The experiment takes the north as the Y axis and the East as the X axis.

So, as in Figure 8, the positioning trajectories from the UWB, unconstrained PDR, and map-constrained PDR could be obtained. The UWB positioning result was basically coicided with the actual trajectory and had the root mean square errors: ±0.13m in the X direction and ±0.16m in the Y direction. However, due to the low positioning frequency (1 Hz) of UWB and the long time interval of updating the position information, it is easy to cause the problem of positioning discontinuity at the corner. The PDR positioning track has ranged from indoor to outdoor and had the root mean square errors about ±1.55m in the X direction and about ±2.06m in the Y direction. The PDR positioning method on map constraints escaped from the above situation, and its solution was in good agreement with the real trajectory, but early or late turns did happen. The corresponding root mean square errors were about ±0.25m in the X direction and about ±0.40m in the Y direction. By using this method, the estimated trajectory was basically consistent with the actual one, and further the integration with the PDR data, the positioning rate was improved, and the problem of discontinuous positioning at the corner is avoided. The solution had the root mean square errors of about ±0.15m in the X direction and about ±0.18m in the Y direction.

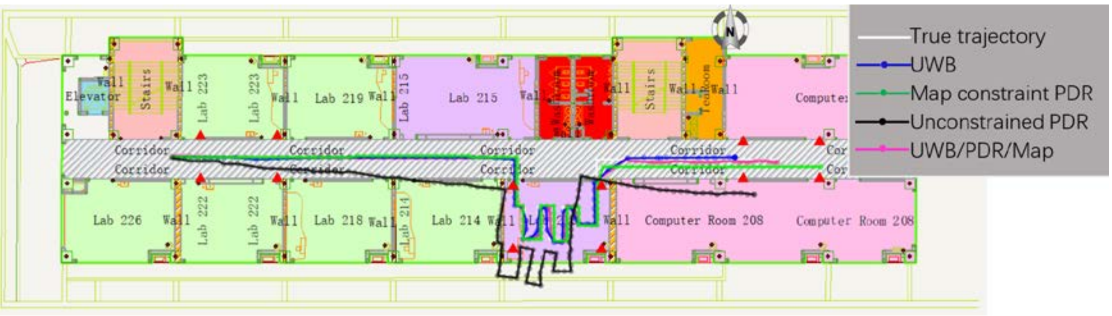

Fig.8 UWB location results with the full signal coverage

5.2.2 UWB partial coverage scenarios

In order to study the UWB performance with the partial singal coverage, two signal lock-out scenarios were simulated. Figure 9(a) shows the scenario where the UWB signal lost lock three times, and the time interval of each loss of lock was 5 seconds. Figure 9(b) shows the scenario where UWB signals were only available at both ends of the corridor and indoors.

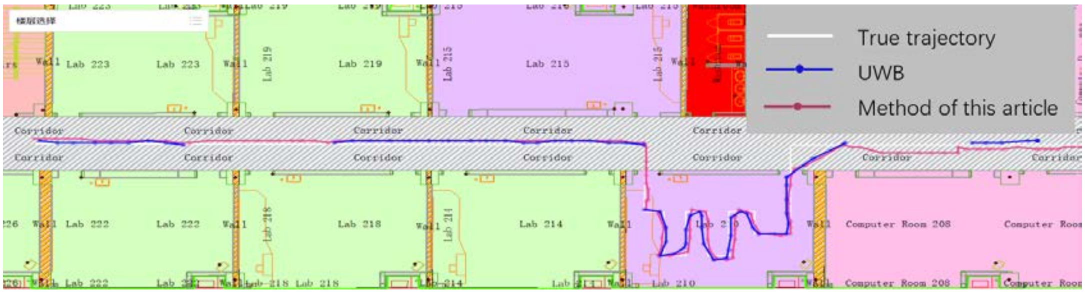

(a) Locate the track when the signal is out of lock 3 times

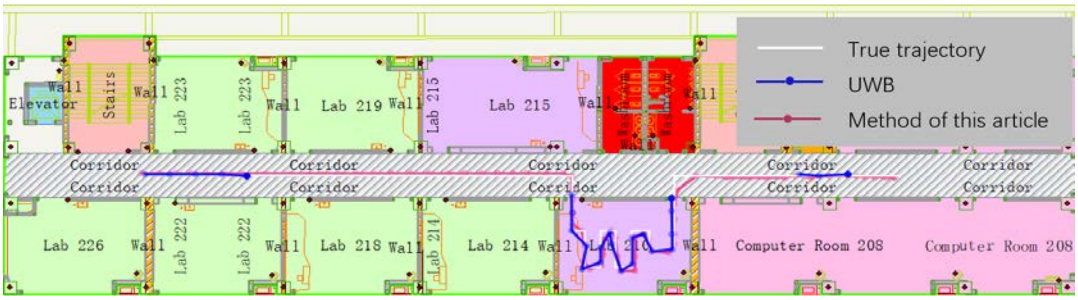

(b) Locate the trajectory when most UWB signals in the corridor lose lock

Fig.9 Positioning results when UWB signal is partially covered

A summary is given here. The blue line in Figure 9 represents the UWB positioning track, with the missing parts where the UWB signals were not available. As can be seen, with the UWB signals, high-precision positioning can still be achieved. In the uncovered area, even if there was no UWB positioning result, the positioning was still achieved with the aid of PDR data. However, the positioning accuracy was quickly droped down as only the map-constrained PDR positioning result was made available in 1-2 seconds after the UWB signal lost lock. The quantitative analysis of the results in Figures 9(a) and 9(b) gave the root mean square errors of about ±0.11m in the X direction and about ±0.20m in the Y direction from the former. From the latter, the root mean square error of X direction was about ±0.19m and the Y direction was about ±0.38m, which means that, when indoors, the base station equipment was located on the ground and affected by non-line-of-sight, the positioning accuracy was degraded. In addition, the availability of the UWB positioning solution was low, which resulted in an increased trajectory inconsistency at short-distance turns, further with increasing of the positioning errors.

5.3 UWB/visual fusion

5.3.1 Experiments in light change environment

The camera used in the experiment is the Guardian camera(Figure 10) purchased by Taobao, and its performance parameters are shown in the Table 3. The experimental scenario is shown in the Figure11. We placed four UWB base stations in four corners of the laboratory. The experimenter held the camera and UWB bound together and circled clockwise three times along the established route.

Fig.10 Guardian camera

Fig.11 Experimental scene

Table 3.Performance of the Guardian camera

Performance	Parameter
Frame rate(FPS)	10
Fx(pixels)	3637.74
Fy(pixels)	3658.25
Resolution(pixels)	1920 * 1080
Brightness mode	AUTO

When a camera faces the window, the brightness of its images will decrease, especially when it is rotating. Conversely, when it faces the opposite direction, the brightness will increase. Frequent changes in light brightness may cause SLAM positioning to fail. Figure 12 shows the positioning results from UWB, vision and their fusion. The blue circles and red triangles in the figure represent the location points from the UWB and the combination of UWB and vision, respectively, while the blue line represents the actual trajectory. Besides, Figure 12(b) presents the visual location result while Figure 12(c) plots the positioning errors of the UWB/vision fusion solution. From Figure 12(a), most of the UWB positioning results were consistent with the designed route, but there were also a certain number of the positioning points with large differences from the actual route, for example, the points at the left bottom corner, on the top and at some other positions. The 2D root mean square error was ±0.32m. From Figure 12(b), firstly, some of the results accurately described the walking trajectory; secondly,the monocular positioning method only delivers the relative positioning information; thirdly, a few of the factors, such as sparse texture, brightness changes and in-situ turns etc., caused positioning failures many times. Finally, in the process, although SLAM's loopback detection and back-end optimization improved the positioning results, there were still some large errors at the upper right corner. In the fusion positioning results, almost all the red dots were distributed on both sides of the actual route, which indicated that the integrated solution was more accurate than the solution using the UWB technique alone and gave the 2D root mean square error of ±0.18m. In addition, the fusion algorithm also functions to limit the visual positioning errors (Figure 12(b)) and solve the problem due to the scale blur.

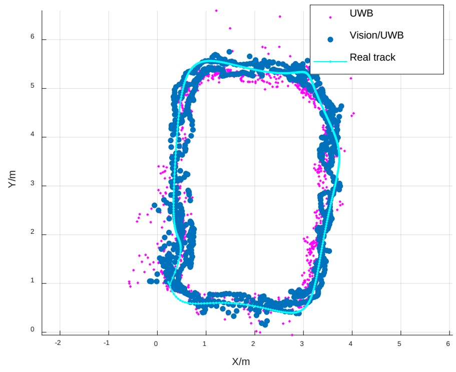

(a) UWB/visual fusion

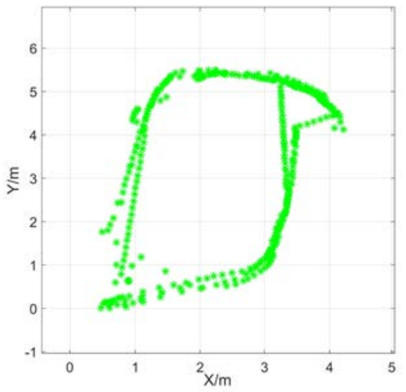

(b) Visual positioning

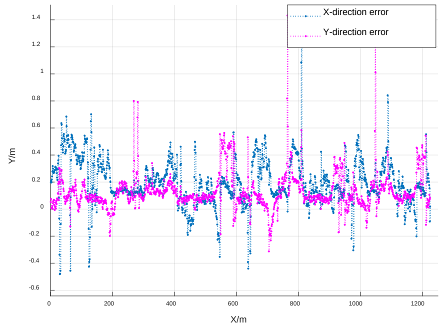

(c) Fusion positioning errors

Fig.12 Location results of UWB / vision fusion in light changing environment

5.3.2 Experiments in sparse texture environment

Figure 13 shows the positioning results in the sparsely textured corridors and classrooms with white walls. In Figure 13(a), the red and blue curves present the UWB and the UWB/vision integrated positioning results, respectively, while the green curve presents the real trajectory. The integrated positioning results were in good agreement with the actual trajectory and had the root mean square error of ±0.17m. In the integration, UWB provides the absolute positioning information and also functions as the initial vision positioning parameters. In case the vision positioning fails, the positioning can be resumed on the spot, thereby the continuous positioning is ensured. Figure 13(c) plots the positioning errors, in which the blue line is for UWB, and the red line for the UWB/vision fusion. From our analysis, about 53% of the points from the integrated solution were at an accuracy level of ±0.1 meters, about 22% at an accuracy of ±0.1-

±0.2 meters, 25% at an accuracy of ±0.2-±0.3 meters, and 10% at an accuracy of ±0.3-±0.4 meters.

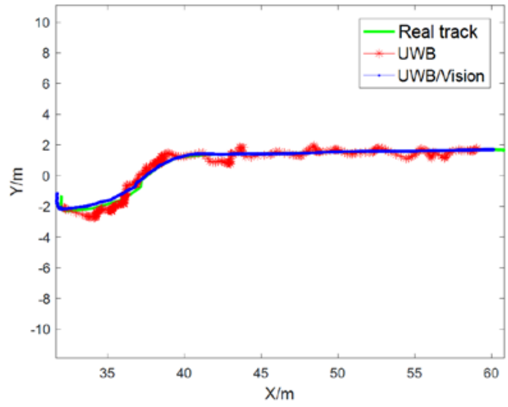

(a) UWB/visual fusion positioning results

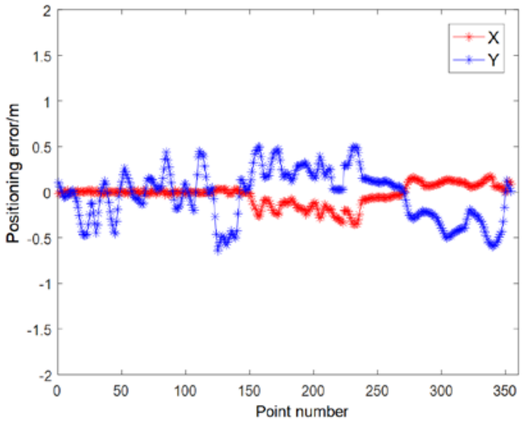

(b) UWB positioning residual

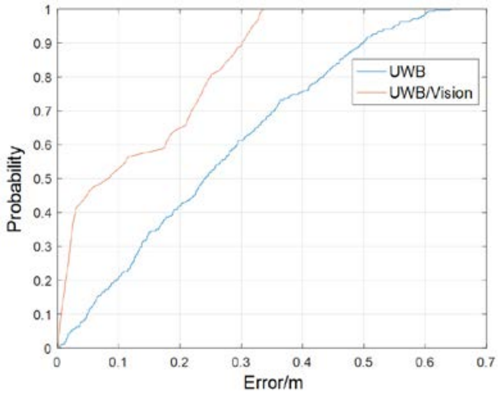

(c) Residual distribution curve

Fig. 13 Results from the UWB/vision fusion in sparse texture environment

6 Conclusions

To have aimed at the problems in the UWB indoor positioning, whose performance has been restricted by the location and number of available base stations, indoor non-line-of-sight and the inability to perceive the indoor environment in real time, this paper proposed a positioning approach based on heterogeneous information constraints such as UWB, PDR and vision. The UWB positioning model based on robust EKF can adjust the gain matrix according to the predicted residuals to reduce or eliminate the influence of gross errors on the state vector. The error in 2D planar positioning was about ±0.13m. Compared with the least squares and EKF algorithms, the positioning accuracy was increased by 88.98% and 53.57%, respectively. Apparently, UWB provides the absolute spatial reference for the PDR positioning and suppresses the divergence of the PDR positioning. At the same time, the use of the PDR technique in our experiments increased the positioning availability of the UWB technique, complementarily solved the positioning problem caused by poor UWB signal coverage or fully obstructed areas, and helped with indoor maps to suppress the PDR heading divergence and positioning divergence. The fusion positioning model based on UWB/vision nicely solved the problems of the scale errors in monocular vision SLAM, frequently required re-initialization due to environmental factors (resulting in discontinuous positioning), and the challenges due to sparse textures or frequent lighting changes in indoor environments, and achieved a positioning accuracy of ±0.2m.

Although the integrated positioning strategy based on multi-source heterogeneous information has made great progress, it is still facing certain difficulty to satisfy the requirements of indoor and outdoor high-precision seamless positioning in emergency rescues such as urban fires and earthquakes. Therefore, the multi-sensor fusion that integrates positioning and scene perception, and wearable or simply assembled devices, when one conducts the positioning in complex environments, is still our next focus.

References

[1] LIU, Jingnan; GUO, Wenfei; GUO, Chi; et al (2020): Rethinking ubiquitous mapping in the intelligentage[J] . Acta Geodaeticaet Cartographica Sinica, 2020, 49(4):403-414.

[2] DENG, Zhongliang (2016): Status and

development of navigation and location services[J]. Satellite Applocation, 2016, 50(2):43-47.

[3] YANG, Yuanxi; XU, Yangyin; LI, Jinlong; et al (2018): Progress and performance evaluation of BeiDou global navigation satellite system: Data analysis based on BDS-3 demonstration system[J]. Science China Earth Sciences, 2018, 61(5):614-624.

[4] JIANG, Weiping (2017): Challenges and opportunities of GNSS reference station network[J]. Acta Geodaetica et Cartographica Sinica, 2017, 46(10): 1379-1388.

[5] CHEN, Zhenghua; ZOU, Han; JIANG, Hao; et al (2015): Fusion of WiFi, smartphone sensors and landmarks using the Kalman filter for indoor localization [J]. Sensors, 2015, 15(1):715-732.

[6] XU, Liyuan (2019): Research on UWB-based relative localization algorithms in blind envrionment. Beijing:University of Science and Technology Beijing, 2019.

[7] STELLA, M.; RUSSO, M.; BEGUSIC, D.; et al (2012): RF localization in indoor environment[J]. Radioengineering, 2012, 21(2):557-567.

[8] CHEN, Ruizhi (2017): Mobile thinking engine leads intelligent location service[J]. Journal of Navigation and Positioning, 2017, 5(1):1-3.

[9] KRIZ, P; MALY, F and KOZEL, T (2016): Improving indoor localization using bluetooth low energy beacons[J]. Mobile Information Systems,2016,(2016-4-19), 2016, 2016(pt.2):1-11.

[10] SHI, Guowei and MING, Ying (2016): Survey of indoor positioning systems based on ultra-wideband (UWB) technology[C]. Wireless Communications, Networking and Applications. Springer. 2016: 1269-78.

[11] WANG, Chuanyang (2020): Study on UWB Positioning Method and Configuration Optimization [D]. China University of Mining and Technology.

[12] ZHANG, Hao; LIU Xing; Gulliver T A; et al (2013): AOA Estimation for UWB Positioning Using a Mono-station Antenna Array [J]. Journal of Electronics & Information Technology, 2013, 35(08):2024-2028.

[13] WANG, Changqiang; XU, Aigong; SUI, xin (2017):An indoor dynamic positioning method of UWB TW-TOA[J]. Science of Surveying and Mapping, 2017, v.42; No.234(12):151-156.

[14] KREISER D; MARTYNENKO D; KLYMENKO O; et al (2015): Simple and efficient localization method for IR-UWB systems based on two-way ranging[C]. 2015 IEEE MTT-S International Conference on Microwaves for Intelligent Mobility (ICMIM), 2015, pp. 1-4.

[15] WYMEERSCH H (2012): A Machine Learning Approach to Ranging Error Mitigation for UWB Localization[J]. IEEE Transactions on Communications, 2012, 60(6):1719-1728.

[16] LI Qiyue; WU Zhong; LI Jie; et al (2015): NLOS error elimination algorithm based on Improved Kalman filter [J]. Journal of Electronic Measurement and Instrumentation, 2015, 29(10):1513-1519.

[17] MENG Jing; ZHANG Qinyu; ZHANG Naitong; et al (2011): Modeling the distance error and performance analysis in IR-UWB positioning system[J]. Journal on Communications, 2011, 32(06):10-16.

[18] ZHENG L; ZHOU W; TANG W; et al(2016): A 3D indoor positioning system based on low-cost MEMS sensors [J]. Simulation Modelling Practice and Theory, 2016:45-56.

[19] LIANG, J Z, CORSO, N, TURNER, E; et al (2013): Image based localization in indoor environments[C]// Computing for Geospatial Research and Application (COM.Geo), 2013 Fourth International Conference on. IEEE, 2013.

[20] FRAUNDORFER, F and SCARAMUZZA, D (2012): Visual Odometry : Part II: Matching, Robustness, Optimization, and Applications[J]. IEEE Robotics & Automation Magazine, 2012, 19(2):78-90.

[21] RENAUDIN, V; MERMINOD, B; KASSER, M (2008): Optimal data fusion for pedestrian navigation based on UWB and MEMS[C]. 2008 IEEE/ION Position, Location and Navigation

Symposium, 2008,1(3):753-761.

[22] ZHANG, M; VYDHYANATHAN, A; YOUNG, A; et al(2012): Robust height tracking by proper accounting of nonlinearities in an integrated UWB/MEMS-based-IMU/baro system[C]. Position Location and Navigation Symposium(PLANS), 2012 IEEE/ION,2012:414-421.

[23] NYQVIST, H E; SKOGLUND, M A; HENDEBY, G; et al (2015): Pose Estimation Using Monocular Vision and Inertial Sensors Aided with Ultra Wide Band[C]// 2015 International Conference on Indoor Positioning and Indoor Navigation (IPIN). IEEE, 2015.

[24] QIAO, Z; XU, A; SUI, X; et al (2018): An integrated indoor positioning method using ORB-SLAM/UWB[J]. Navig. Positioning 2018, 6, 29-34.

[25] WANG, Jianguo (2008): Test Statistics in Kalman Filtering[J]. Journal of Global Positioning Systems, 2008, 7(1):81-90.

[26] HAN, Houzeng (2017): Research on the Key Models of INS aided BDS/GPS High Precision Kinematic Positioning [D]. China University of Mining and Technology.

[27] HAN, Houzeng; WANG, Jian; LIU Fei, et al (2019): An emergency seamless positioning technique based on ad hoc UWB Networking Using Robust EKF[J]. Sensors, 2019, 19(14).

[28] YU, Xuexiang and LU, Weicai (2000): Robust Kalman filtering model for dynamic data processing of GPS monitoring networks[J]. Journal of China University of Mining & Technology, 2000, 29(6): 553-557.

[29] WANG, Jianguo. (2009): Reliability Analysis in Kalman Filteirng[J]. Journal of Global Positioning Systems, 2009, 8(1):101-111.

[30] LIU, Fei; WANG, Jian; ZHANG, Jixian; et al (2019): An indoor localization method for pedestrians base on combined UWB/PDR/Floor Map[J]. Sensors, 2019, 19(11): 2578.

[31] LIU, Chunyan (2015): Study on the pedestrian indoor positioning algorithms based on WIFI and inertial technology[D]. Jiangsu:China University of Mining and Technology, 2015.

[32] MUR-ARTAL, R; TARDOS, J D (2017): ORB-SLAM2: An open-source SLAM system for monocular, Stereo, and RGB-D Cameras[J]. IEEE Transactions on Robotics, 2017, 1-8.

[33] LIU, Fei; ZHANG, Jixian; WANG, Jian; et al (2020): An UWB/Vision fusion scheme for determining pedestrians' indoor location[J]. Sensors, 2020, 20(4):1139.

Authors

Nan Guo [Photo] is

Wei JIANG,

Jing LI,

Fei LIU,

Jie DONG,

Journal of Global Positioning Systems (*2021*)
Vol. 17, No. 2: 179-188
DOI: 10.5081/jgps.17.2.179

Journal of Global Positioning Systems
2021

A Comparative Analysis on Inter-frequency Data Quality of Quad-constellation GNSS on a Smartphone

Yanjie Li Changsheng Cai*
School of Geosciences and Info-Physics, Central South University, Changsha 410083, People's Republic of China
* Corresponding author, cscai@hotmail.com

Abstract: This paper comprehensively analyzes the inter-frequency data quality of the quad-constellation Global Navigation Satellite System (GNSS) of GPS, GLONASS, BDS and Galileo on a smartphone. A series of indices, i.e. the number of visible satellites, data integrity rate, multipath, carrier-to-noise ratio (C/No), cycle-slip ratio and observation residuals, are employed to evaluate the data quality with a comparison between different constellations and frequencies. Experiments were conducted using the firstly released dual-frequency smartphone of Xiaomi Mi8. The results show that the GPS and BDS exhibit the best tracking performance in an open-sky environment with an average of 7 observed satellites at each epoch, which is 3 or 4 satellites more than the Galileo and GLONASS. In addition, the GPS data integrity rate is higher than the other constellations by about 20%-25%. The GPS suffers a multipath effect two times larger than the Galileo on the L1/E1 frequencies, but they are almost equal on the L5/E5a frequencies. For all four constellations, the C/No is mostly concentrated at 20-35 dB-Hz. Further, the C/No on the L1/E1 frequencies increases by 3-4 dB-Hz over the L5/E5a frequencies. The GLONASS observations exhibit the most serious cycle slip occurrence rate at a ratio of 100, which is significantly larger than the other constellations. Regarding the residuals, the phase RMS residuals for all four constellations are at a few millimeters, whereas the pseudorange residuals of GLONASS are the most prominent with an RMS of over 6 m, which is 3-4 times larger than the other constellations. The precise point positioning (PPP) results show that the convergence time and positioning accuracy can be effectively improved by adding GPS and Galileo data at L5/E5a.

Key words: smartphone; GNSS; quad-constellation; inter-frequency; data quality

1. Introduction

Smartphones play an important role to promote the social and technical development in the age of mobile Internet. However, most smartphone applications depend on location information. In recent years, the demand for smartphone-based high-precision positioning services is increasing. In May 2016, Google announced to open the GNSS raw data interface for Android smartphones, which creates a condition for smartphone's high-precision positioning applications. However, most smartphones typically use linear polarized antennas due to limited space [1], resulting in degraded GNSS data quality when compared with the geodetic GNSS receivers, which largely restricts smartphones' positioning performance. Evaluating smartphones' GNSS data quality can aid to adopt appropriate strategies or develop suitable algorithms to reduce its negative effect.

Since the GNSS observation quality has a big impact on the positioning performance, the

Editor in charge: Dr. Junping Chen

smartphone GNSS data quality analysis has become a hot research subject. [2] firstly evaluated the raw GNSS observation quality on Android smart terminals and demonstrated that the pseudorange observations can only provide meter-level positioning accuracy, while the carrier-phase observations have the potential for centimeter-level positioning. [3] further compared the Nexus 9 tablet, Samsung Galaxy S8 smartphone and Huawei Honor v8 smartphone with the geodetic receiver in terms of the GNSS observation noise and concluded that the pseudorange observation noise of Nexus 9 is 10 times greater than the survey-grade receiver, while the carrier-phase observation noise is 3-5 times greater. By contrast, the observation noise of the latter two smartphones is much worse because of a duty-cycle issue. Meanwhile, smartphone observations are easily subject to gross errors [4]. Another major difference between the smartphone and geodetic receiver is the carrier-to-noise density ratio (C/No). The C/No of a smartphone is typically 10 dB-Hz lower than that of a geodetic receiver [2,5]. Meanwhile, the smartphone C/No varies rapidly even for the case at high satellite elevations [3]. Further, the smartphone C/No is more relevant to the pseudorange noise than the satellite elevation angles [6,7]. The duty cycle is a unique power-saving mechanism equipped in most smartphones. [7] and [4] show that the phase and pseudorange measurement inconsistency will increase and the accuracy of the doppler measurement will be reduced from cm/s to dm/s when the duty cycle mechanism is turned on. Fortunately, this mechanism can be turned off since the 9th version of the Android operating system was released in 2017 to acquire consecutive carrier-phase observations, which provides a possibility for carrier-phase-based high-precision positioning. Additionally, smartphone tests demonstrate that the linearly polarized antenna embedded inside smartphones is very sensitive to the multipath effect, which makes the multipath effect become a main error source in the smartphone-based GNSS positioning [8].

The integrated multi-frequency and multi-constellation GNSS positioning has become an inevitable trend. Data quality is vital to determine the positioning performance. This study presents a comprehensive comparative analysis on inter-frequency and inter-constellation smartphone GNSS data quality. The Xiaomi Mi8 smartphone is used to collect the GNSS observations for a case study since it is the first one to support the dual-frequency and quad-constellation GNSS signals. The data quality characteristics are comprehensively analyzed by means of indices such as the number of visible satellites, data integrity rate, multipath effect, carrier-to-noise ratio, cycle-slip ratio and observation residuals.

2. Methodology

The data integrity rate is capable of reflecting the lack rate of GNSS data, and thus it is usually used to assess smartphones' GNSS signal reception capability. The data integrity rate can be expressed as a ratio of the actual received data (A_j^s) against the theoretical received data (T_j^s):

$$Ratio_j^s = A_j^s / T_j^s \tag{1}$$

where s and j denote the satellite and frequency, respectively. The theoretical reception data is calculated based on the satellite elevation mask angle and broadcast ephemeris [9].

The multipath effect is a major error source in the smartphone-based positioning. The multipath effect at an epoch (M_i) can be estimated using the multipath combination [10,11]:

$$M_i = P_i - \frac{f_i^2 + f_j^2}{f_i^2 - f_j^2}\varphi_i\lambda_i + \frac{2 f_j^2}{f_i^2 - f_j^2}\varphi_j\lambda_j \tag{2}$$

where i and j ($i \neq j$) denotes two different frequencies. P is the pseudorange observation. φ is the carrier-phase observation. λ is the wavelength at the corresponding frequency f. M_i contains multipath effect, ambiguity term and hardware delay biases. The latter two items are stable and thus can be obtained by calculating the mean value of M_i at 15 consecutive epochs free of cycle slips [9], which is denoted as $\bar{M}_i$. Therefore, the multipath effect (MP_i) can be derived as:

$$MP_i = M_i - \bar{M}_i \tag{3}$$

The cycle slip ratio (CSR) reflects the stability of the carrier phase observations. The more cycle slips occur, the more challengeable to achieve high-precision positioning solutions. The CSR is defined as the number of cycle slips every 1,000 epochs to reflect the occurrence frequency of cycle slips, as seen in Eq. (4):

$$CSR = \frac{1000}{o/n} \tag{4}$$

where n is the number of epochs when cycle slips occur and o is the number of all observed epochs. The geometry-free (GF) combination method [12] and the Melbourne–Wübbena (MW) method [13,14] are jointly used to detect dual-frequency cycle slips, whereas the code minus phase method and the loss of lock indicator (LLI) are jointly used to detect the single-frequency cycle slips [15].

To extract the observation noise, a zero-baseline method is commonly used [10,16]. But for smartphones, the zero-baseline method is difficult to be applied due to the inseparable receiver and antenna. In this study, we employ the four-order differential method to analyze the noise of observations [17]. First, an inter-satellite differencing operation is made to eliminate the receiver clock offset by choosing the highest-elevation satellite as a reference satellite. The inter-satellite single differences of pseudorange and carrier phase observations are derived as:

$$\nabla P^{m,n} = \nabla \rho^{m,n} + \nabla dt_{orb}^{m,n} + c \cdot \nabla dt_r^{m,n} + \nabla dI^{m,n} + \nabla dT^{m,n} + \nabla \varepsilon_P^{m,n} \tag{5}$$

$$\lambda \nabla \varphi^{m,n} = \nabla \rho^{m,n} + \nabla dt_{orb}^{m,n} + c \cdot \nabla dt_r^{m,n} + \lambda \cdot \nabla N^{m,n} - \nabla dI^{m,n} + \nabla dT^{m,n} + \nabla \varepsilon_\varphi^{m,n} \tag{6}$$

where ∇ is the single difference operator and m , n denote the reference and non-reference satellites, respectively. P and φ represent the pseudorange and carrier-phase observation, respectively. ρ is the geometric range between the receiver and satellite. c is the light speed. d_{orb} and dt_r are the satellite orbital error and clock bias . dI 、dT denote the ionospheric and tropospheric delay errors, respectively. λ is the carrier phase wavelength, N is the ambiguity term, and ε is the observation noise term.

Secondly, the three-order differences of $\nabla P^{m,n}(t)$ between epochs are further made to eliminate systemic biases [3]. To simplify the expression, we set $\nabla P^{m,n}(t)$=$SD(t)$. According to the error propagation law, the pseudorange observation noise is obtained below:

$$\varepsilon_P(t) = \frac{SD_P(t+3) - 3SD_P(t+2) + 3SD_P(t+1) - SD_P(t)}{2\sqrt{10}} \tag{7}$$

Similarly, the carrier phase observation noise can be obtained as:

$$\varepsilon_\varphi(t) = \frac{SD_\varphi(t+3) - 3SD_\varphi(t+2) + 3SD_\varphi(t+1) - SD_\varphi(t)}{2\sqrt{10}} \tag{8}$$

3. Data quality analysis of smartphone GNSS observations

3.1 Data description

A Xiaomi Mi8 smartphone equipped with a Broadcom BCM47755 chip and a linear polarization antenna is used for data collection with an open-sky view in static mode. The station is located on the top of mining building at Central South University, China, as displayed in Figure 1. The observation was made on November 23, 2019 from GPS time 2:00 to 12:00 with a data sampling interval of 1 s. The software of Geo++ Rinex Logger (V2.1.3) is used to transform the raw data information into the standard RINEX 3.02 format data. The Xiaomi Mi8 smartphone can receive quad-constellation signals at the same time, including GPS, GLONASS, BDS, and Galileo, but dual-frequency data can only be acquired from GPS and Galileo L1/L5 and E1/E5a signals, and the rest observations are all single-frequency data. The received GNSS signals come from GPS satellites of BLOCK IIA, BLOCK IIR, BLOCK IIR-M and BLOCK IIF, GLONASS satellites of GLONASS-M and GLONASS-K1, BDS satellite of GEO (Geosynchronous Earth Orbit), IGSO (Inclined

Geosynchronous Satellite Orbit) and MEO (Medium Earth Orbit), and Galileo satellites of Galileo-1 and Galileo-2.

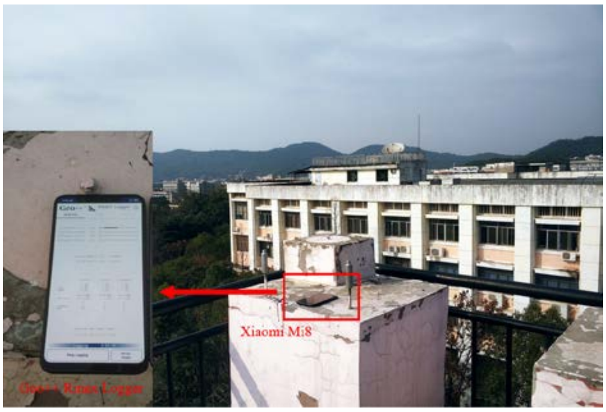

Figure 1 Smartphone data collection on the top of mining building at Central South University

3.2 GNSS signal reception capability analysis

Figure 2 shows the number of satellite observations for each satellite type and signal frequency. As can be seen from Figure 2(a), the Xiaomi Mi8 smartphone has the best ability to capture GPS signals. In the entire observation period, over 20 GPS satellites can be tracked. The GLONASS and BDS are followed with more than 10 satellites. It is noted that the carrier phase signal reception ability is slightly weaker than its pseudorange signal. In Figure 2(b), it is seen that only one BDS GEO satellite was observed, which suggests that the linearly polarized antenna is probably insensitive to the high-orbit GEO signals. Due to the limited number of GPS BLOCK IIF satellites, the observation number on the L5 frequency is almost half of those on the L1 frequency for GPS satellites. Unlike GPS, the numbers of the Galileo observations on the E1 and E5a frequencies are equal.

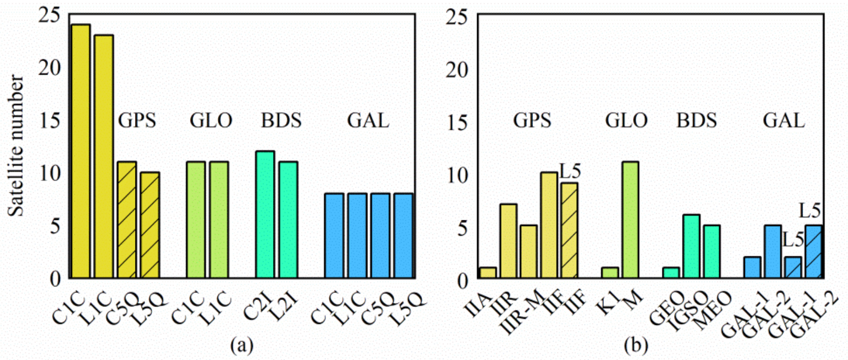

Figure 2 Number of observed satellites for different frequencies (a) and satellite types (b)

Figure 3 depicts the number of visible satellites for different constellations and frequencies during the entire observation period. On average, 7.8, 3.4, 7.5, and 3.5 satellites are tracked for GPS, GLONASS, BDS, and Galileo on the L1/G1/B1/E1 frequencies, and 2.5, 2.7 satellites are tracked for GPS and Galileo on the L5/E5a frequencies, respectively. It is obvious that an average of over 6 GPS and BDS satellites on the L1/B1 frequencies can be observed, while the observed Galileo and GLONASS satellite number on the E1/G1 frequencies is significantly less with an average of about 4. This demonstrates that the GPS and BDS satellites can be tracked more easily when compared with the Galileo and GLONASS satellites. That is probably dependent on the GNSS chip and antenna embedded inside the smartphone. In addition, the average tracked numbers of GPS BLOCK IIF and Galileo satellites are 3.0 and 3.5 at each epoch on the L1/E1 frequencies, which are more than those on the L5/E5a frequencies by about 17% and 30%. This indicates that the Xiaomi Mi8 smartphone has a greater tracking ability for the L1/E1 signals than the L5/E5a signals.

The pseudorange and carrier phase data integrity rates for different constellations and frequencies during the entire observation period are listed in Table 1. The average data integrity rates for GPS/GLONASS/BDS/Galileo constellations are

60.3%, 37.6%, 38.2% and 35.5%, respectively. The results reveal that the GPS data integrity rate is 20%-25% higher than the other constellations. Meanwhile, the data integrity rate for the L5/E5a signals is obviously lower than the L1/E1 signals on the whole. Further, the carrier phase observations are more prone to missing data than the pseudorange observations, especially for L5/E5a signals. The maximum difference for different constellations exceeds 20%.

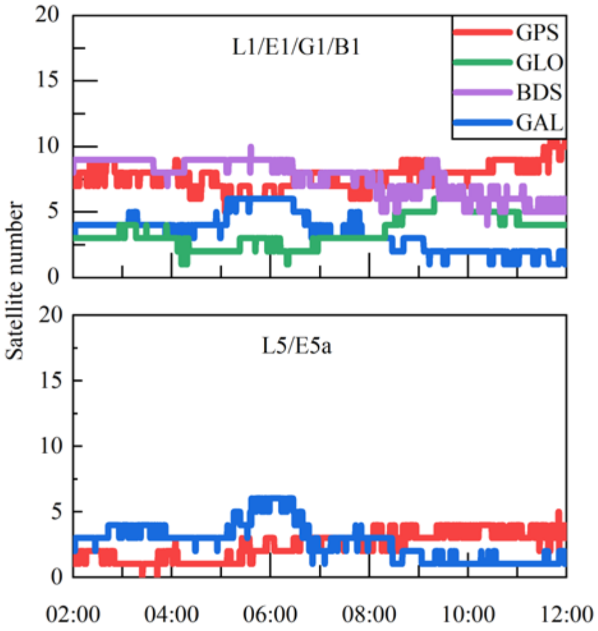

Figure 3 Number of visible satellites for different constellations and frequencies

Table 1 Data integrity rate of different observations for each frequency and constellation

Satellite type	Pseudorange		Carrier phase	
	L1/E1/G1/B1	L5/E5a	L1/E1/G1/B1	L5/E5a
GPS	75.1	61.2	60.1	44.6
GLONASS	40.2	-	35.0	-
BDS	42.9	-	33.5	-
Galileo	38.4	41.3	34.9	27.2

3.3 Analysis of C/No, multipath and cycle slip

Figure 4 depicts the frequency distribution histogram of the C/No at two different frequencies and four different constellations. The corresponding RMS statistical values are also displayed in Figure 4. For a geodetic receiver, the C/No generally varies from 35 dB-Hz to 55 dB-Hz [4,7], while the C/No of the Xiaomi Mi8 smartphone is primarily concentrated at 20-35 dB-Hz for all constellations and frequencies, which is typically 15-20 dB-Hz lower than that of geodetic receivers. The C/No of the BDS B1, Galileo E5a, and GPS L5 signals are more concentrated below 30 dB-Hz while the C/No of the GLONASS G1, GPS L1 and Galileo E1 signals are mostly distributed in the range of over 30 dB-Hz. The C/No RMSs of four constellations on the L1/E1/G1/B1 differ less than 2 dB-Hz. Further, the C/No one the L1/E1 frequencies is stronger than that on the L5/E5a frequencies by over 3-4 dB-Hz, indicating that there exists a noticeable difference for the power of the signal at the two different frequencies.

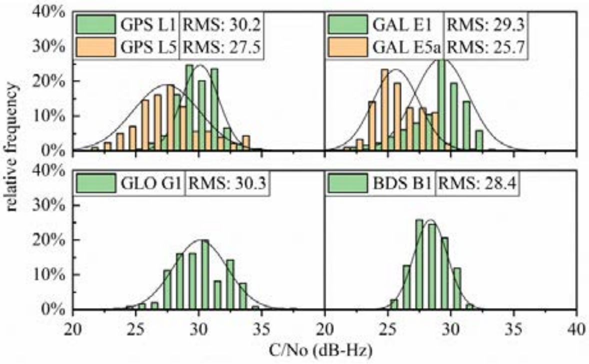

Figure 4 Frequency distribution histogram of carrier-to-noise ratio

Figure 5 shows the pseudorange multipath effects and the carrier phase cycle slip ratios. Based on Eq.(2) and Eq.(3), the pseudorange multipath effect of GPS and Galileo are acquired using dual-frequency observations and displayed in Figure 5 (a) along with its RMS statistical values. It is obvious that the GPS and Galileo pseudorange multipath RMSs are about 2.1 m and 1.3 m on the L1/E1 frequencies, and 0.6 m and 0.7 m on the L5/E5a frequencies, which are nearly 10 times larger than that of the geodetic receivers in an open area [18]. Further, the GPS pseudorange multipath effect is almost two times larger than the Galileo on the L1/E1 frequencies. For both constellations of GPS and Galileo, the pseudorange multipath effect is larger on the L1/E1 frequencies than the E1/E5a frequencies by about 71%

and 46%, respectively.

Figure 5 (b) shows the cycle-slip ratio for four constellations. Although the cycle slip detection is insensitive to single-frequency small cycle slips, the GLONASS observations still are found to contain cycle slips at over 100 epochs every 1,000 epochs. By contrast, the cycle slip ratio for geodetic receivers is usually less than 10 [19], indicating that the smartphone GLONASS observations are susceptible to lock-lose. On the contrary, the BDS has the lowest cycle-slip ratio at about 14 as compared to the other constellations.

3.4 Analysis of observation residuals

The pseudorange and carrier-phase observation residuals can well reflect the observation quality. Figures 6 and 7 show the sequences of pseudorange and carrier phase observation residuals for different constellations. Their corresponding RMS residuals statistical values with respect to different satellite types are listed in Table 2. Part epochs' residuals are not displayed as inter-satellite single-difference operation cannot be made due to the number of satellites is less than two.

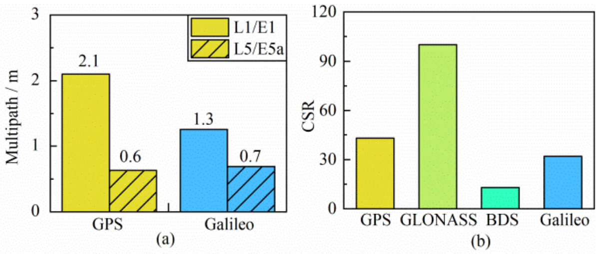

Figure 5 Pesudorange multipath effects (a) and carrier phase cycle slip ratio (b)

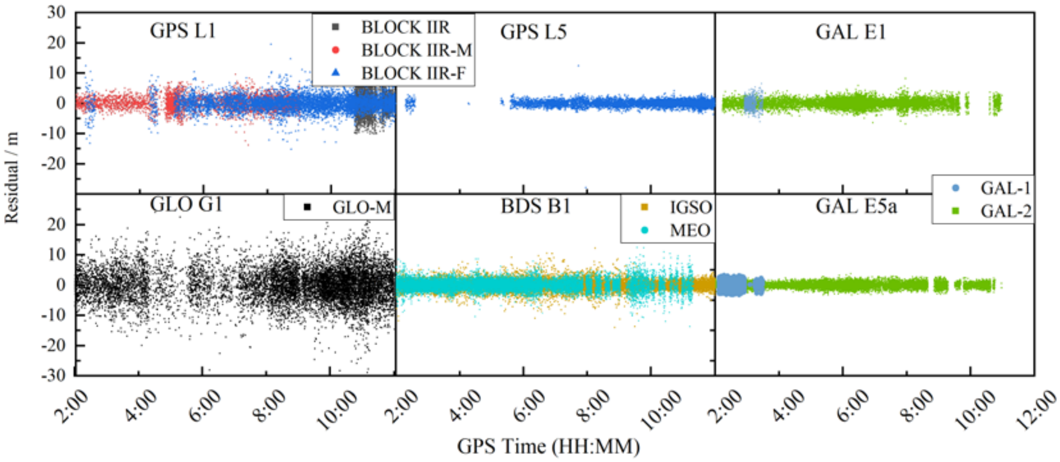

Figure 6 Pseudorange observation residuals for different GNSS constellations

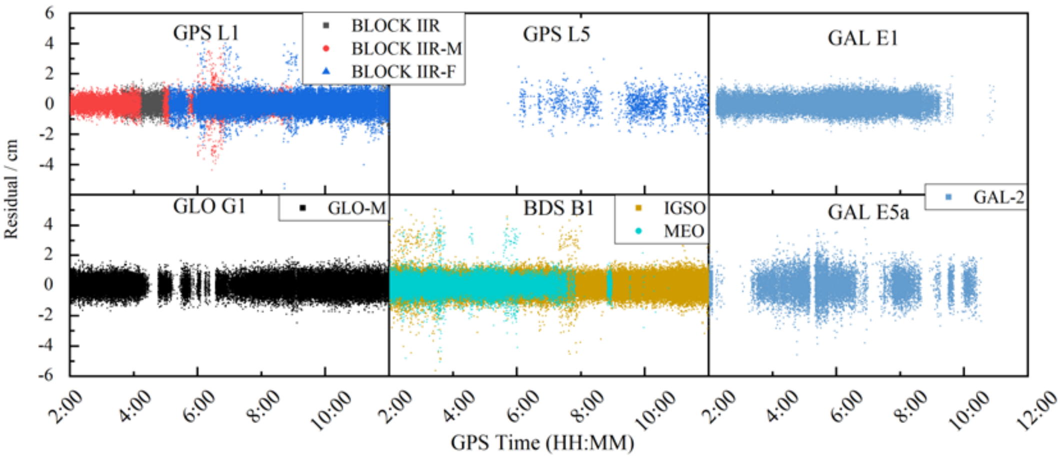

Figure 7 Carrier phase observation residuals for different GNSS constellations

Table 2 RMS statistics of pseudorange residuals and carrier phase residuals

	Satellite type	Pseudorange / m		Carrier phase / cm	
		L1/E1/G1/B1	L5/E5a	L1/E1/G1/B1	L5/E5a
GPS	BLOCK IIA	-	-	-	-
	BLOCK IIR	2.45	-	0.49	-
	BLOCK IIR-M	2.23	-	0.46	-
	BLOCK IIF	2.54	0.90	0.49	0.76
Galileo	GAL-1	2.32	1.08	-	-
	GAL-2	1.21	0.88	0.43	0.78
GLONASS	GLO_K1	-	-	-	-
	GLO_M	6.18	-	0.49	-
BDS	GEO	-	-	-	-
	IGSO	1.63	-	0.52	-
	MEO	1.70	-	0.47	-

According to Figure 6 and Table 2, it is apparently that the GPS and Galileo pseudorange observation accuracies on the L5/E5a frequencies are better than those on the L1/E1 frequencies. The GPS pseudorange RMS residuals on the L1 frequency are approximately twice larger than those on the L5 frequency. Galileo exhibits the highest pseudorange observation precision among all four constellations. Its RMS residuals are less than 1.5 m on the E1 frequency and 1 m on the E5a frequency. However, its signal reception capability is relatively poor, resulting in inadequate pseudorange observation data. As compared to the other constellations, the GLONASS pseudorange observations have the lowest precision with a RMS residuals of over 6 m, which is 3-4 times larger than the other constellations, probably attributing to its frequency division multiple access mode [10]. The Galileo pseudorange precision varies significantly from different satellite types, while it is not the case for the other constellations.

In contrast to the pseudorange observation residuals, the carrier phase observation precision on the L5/E5a frequencies is approximately 3-4 mm lower than that of the L1/E1 frequencies. Meanwhile, the carrier observation precision varies little between different constellations as well as various satellite types with a RMS residuals value of about 5 mm.

4. Results of smartphone-based precise point positioning (PPP)

PPP is a high-precision positioning technique without a need of any reference station, which is very suitable for smartphone-based GNSS positioning. Because most smartphones can only generate single-frequency GNSS data, the single-frequency (SF) method is widely applied. This section compares the dual-frequency-PPP (DF-PPP) and the SF-PPP performance. Undifferenced and uncombined PPP model is adopted due to a large number of single-frequency data [20]. In the DF-PPP scenario, all dual-frequency data and single-frequency data are used. The SF-PPP scenario uses only the first-frequency data. Global Ionospheric Map (GIM) products are treated as pseudo-observables to reduce the effect of ionospheric errors on the single-frequency observations [8]. Satellite phase center offsets (PCO) and phase center variations (PCV) from International GNSS Service (IGS) are corrected and smartphone PCO is corrected using the recommended value from the reference [21]. The cut-off elevation is set to 10°. A C/No-dependent observation weighting method [22] is applied instead of the elevation-angle-dependent weighting method.

The experiment data is the same as in section 3.1. A known point is located near the smartphone at a distance of only a few centimeters. Thus, the coordinates of the known point can be used as references. The observation period is forced to reset the filter into 4 sessions with a session length of 2.5 hours for the sake of statistical computation of the convergence time and positioning accuracy. The position filter is considered to be converged when the positioning errors reach ±1m and keep within ±1 m, and the positioning error is calculated using root mean square (RMS) after convergence. Figure 8 shows the PPP errors in the east, north and up directions using the DF-PPP and SF-PPP models in four sessions. The DF-PPP model can converge to 1 m within 20 minutes in most sessions in the east and north directions, while the convergence time of the SF-PPP is about 2-3 times longer when compared to the DF-PPP. The convergence time of DF-PPP is improved about 68%, 69% and 53% when compared to the SF-PPP in east, north and up directions, respectively. Regarding the positioning accuracy, the DF-PPP RMS errors in all sessions reach 0.35 m, 0.30 and 0.52 m in the east, north and up directions, which improves the positioning accuracy by 24%, 27% and 20% over the SF-PPP model, respectively. In conclusion, the convergence time and positioning accuracy can be effectively improved by adding the observations on the L5/E5a frequency.

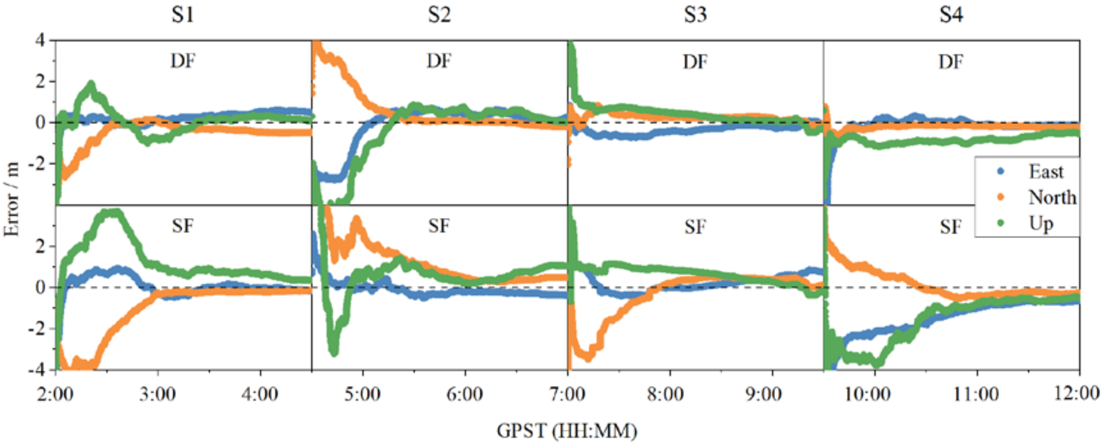

Figure 8 Positioning errors using DF-PPP and SF-PPP models in the east, north and up directions (‘S’ denotes ‘Session’)

5. Conclusions

The GNSS observation data quality is a key factor to determine the smartphone positioning performance. This manuscript comprehensively analyzes the smartphone GNSS data quality characteristics on two frequencies and four constellations based on the first released dual-frequency Xiaomi Mi8 smartphone. The data quality is evaluated through a series of indices such as signal reception capability, multipath, carrier-to-noise ratio, cycle-slip ratio, and observation residuals. Finally, the smartphone-based PPP positioning results are also presented.

The analysis results indicate that the GPS and BDS satellites have the best tracking performance with an average of up to 7 satellites per epoch, which is 3-4 more than the other constellations. The GNSS observation on the L1/E1 frequencies has a stronger signal reception ability than that on the L5/E5a frequencies. The GPS data integrity rate is 20%-25% higher than the other constellations, and the data integrity rate for the L5/E5a signal is obviously lower than the L1/E1 signal. In addtion, the C/No on the L1/E1 frequencies is stronger than that on the L5/E5a frequencies by over 3-4 dB-Hz. The C/No RMSs of four constellations on the L1/E1/G1/B1 frequencies differ slightly less than 2 dB-Hz. The GPS multipath effect is nearly two times larger than that of the Galileo on the L1/E1 frequencies, but they are almost equal on the L5/E5a frequencies.

The results also indicate that the GLONASS has the highest cycle slip ratio among all four constellations, while the BDS has the lowest cycle slip ratio. Similarly, the GLONASS has the largest pseudorange observation RMS residuals at over 6 m, which is 3-4 times higher than those of the other constellations. For all constellations and frequencies, the carrier phase residual precision is at a few millimeters and varies slightly from constellations and frequencies. It should be noted that all conclusions are achieved based on the used Xiaomi Mi8 smartphone. More types of smartphone data quality evaluation will be made in the future.

The positioning results demonstrate that the PPP convergence time can be improved by about 68%, 69%

and 53% in the east, north and up directions, and the positioning accuracy can be improved by about 24%, 27% and 20% after adding the observations on the L5/E5a frequencies to the first-frequency GNSS observations, respectively.

Acknowledgment:

The financial support from the National Key Research and Development Program of China (No. 2020YFA0713501), the National Natural Science Foundation of China (No. 42174040), the Hunan Natural Science Foundation (No.2020JJ4111), and the Hunan Provincial Innovation Foundation for Postgraduate (No. CX20200241) are appreciated.

References:

[1] Pesyna K M, Heath R W, Humphreys T E. Centimeter positioning with a smartphone-quality GNSS antenna. Proceedings of ION GNSS+ 2014, Tampa, Florida, 8-12 September 2014, pp. 1568-1577.

[2] Banville S, Van Diggelen F. Precise positioning using raw GPS measurements from Android smartphones. GPS World, 2016, 27(11): 43-48.

[3] Li G , Geng J . Characteristics of raw multi-GNSS measurement error from Google Android smart devices. GPS Solutions, 2019, 23(3).

[4] Liu W, Shi X, Zhu F, et al. Quality analysis of multi-GNSS raw observations and a velocity-aided positioning approach based on smartphones. Advances in Space Research, 2019, 63(8): 2358-2377.

[5] Riley S, Lentz W, Clare A. On the path to precision-observations with android GNSS observables. Proceedings of the 30th International Technical Meeting of The Satellite Division of The Institute of Navigation (ION GNSS+ 2017). 2017: 116-129.

[6] Zhang X , Tao X , Zhu F , et al. Quality Assessment of GNSS observations from an Android N smartphone and positioning performance analysis using time-differenced filtering approach. GPS Solutions, 2018, 22(3):70.

[7] Paziewski J, Sieradzki R, Baryla R. Signal characterization and assessment of code GNSS positioning with low-power consumption smartphones. GPS Solutions, 2019, 23(4): 98.

[8] Wang G, Bo Y, Yu Q, et al. Ionosphere-constrained single-frequency PPP with an Android smartphone and assessment of GNSS observations. Sensors, 2020, 20(20): 5917.

[9] Vaclavovic P, Dousa J. G-Nut/Anubis: Open-source Tool for multi-GNSS data monitoring with a multipath detection for new signals, frequencies and constellations. IAG 150 Years. Springer, Cham, 2015: 775-782.

[10] Cai C, He C, Santerre R, et al. A comparative analysis of measurement noise and multipath for four constellations: GPS, BeiDou, GLONASS and Galileo. Survey review, 2016, 48(349): 287-295.

[11] Li B, Zang N, Ge H, et al. Single-frequency PPP models: analytical and numerical comparison. Journal of Geodesy, 2019, 93(12): 2499-2514.

[12] Blewitt G. An automatic editing algorithm for GPS data. Geophysical research letters, 1990, 17(3): 199-202.

[13] Melbourne W. The case for ranging in GPS-based geodetic systems. Proc. 1st int. symp. on precise positioning with GPS. 1985: 373-386.

[14] Wubbena G. Software developments for geodetic positioning with GPS using TI 4100 code and carrier measurements. Proceedings 1st international symposium on precise positioning with the global positioning system. US Department of Commerce, 1985: 403-412.

[15] Zhao J, Hernández-Pajares M, Li Z, et al. High-rate Doppler-aided cycle slip detection and repair method for low-cost single-frequency receivers. GPS Solutions, 2020, 24(3): 1-13.

[16] Amiri-Simkooei A R , Tiberius C C J M . Assessing receiver noise using GPS shortbaseline time series. GPS Solutions, 2007, 11(1): 21-35.

[17] Pirazzi G, Mazzoni A, Biagi L, et al. Preliminary

performance analysis with a GPS+Galileo enabled chipset embedded in a smartphone. Proceedings of ION GNSS+ 2017, Portland, Oregon, 25-29 September 2017, pp. 101-115.

[18] Cai C, Gao Y, Pan L, et al. An analysis on combined GPS/COMPASS data quality and its effect on single point positioning accuracy under different observing conditions. Advances in Space Research, 2014, 54(5): 818-829.

[19] Li J., Wang J., Xiong X., et al. Quality checking and analysis on GPS data in northeast asia. Geomatics and Information Science of Wuhan University, 2006(03): 209-212.

[20] Zhou F, Dong D, Li W, et al. GAMP: An open-source software of multi-GNSS precise point positioning using undifferenced and uncombined observations. GPS Solutions, 2018, 22(2): 1-10.

[21] Wanninger L., Heßelbarth A. GNSS code and carrier phase observations of a Huawei P30 smartphone: Quality assessment and centimeter-accurate positioning. GPS Solutions, 2020, 24(2), 1-9.

[22] Wang L, Li Z, Wang N, et al. Real-time GNSS precise point positioning for low-cost smart devices. GPS Solutions, 2021, 25(2): 1-13.

Authors

[photo] Yanjie Li …

[photo] Changsheng Cai ..

***Journal of Global Positioning Systems* (*2021*)**
Vol. 17, No. 2: 189-207
DOI: 10.5081/jgps.17.2.189

Analysis of real-time multi-GNSS satellite products of Wuhan University for rapid response of precise positioning

Qi Zhang[1], Ran Zeng[1], Shaoming Xin[1], Xing Zhou[2]

1 GNSS Research Center, Wuhan University
2 Academy of Surveying and Mapping Engineering of Gansu Province

Abstract：When users need to quickly process GNSS data, they often need the satellite orbit and clock products with the minimum latency and the highest precision, and it is a good solution to receive the real-time satellite RTCM SSR correction stream to recover the precise satellite orbit and clock products in real time and then store them in an offline repository for rapid response of precise positioning. In this paper, the real-time multi-GNSS orbit and clock RTCM SSR correction stream broadcast by SSRC00WHU0 mountpoint of Wuhan University is used to recover precise satellite orbit and clock products in real time. First, the seven-day orbit files and clock files were obtained and stored locally, and compared with the final MGEX precise satellite orbit and clock products. The results show that the real-time orbit and clock products of GPS and Galileo satellites have the best accuracy, followed by GLONASS satellites and BDS satellites. The real-time orbit products can reach the accuracy level of 5 cm for GPS satellites, 8 cm for Galileo satellites, 15 cm for GLONASS satellites and 16 cm for BDS-3 satellites, and the real-time clock products can reach the accuracy level of 0.43 ns for GPS satellites, 0.44 ns for Galileo satellites, 0.91 ns for GLONASS satellites and 3.14 ns for BDS satellites. Then, the observation data of 20 IGS stations randomly distributed around the world from DOY 150 to 156 in 2021 were processed by static precise point positioning (PPP) mode using the recovered real-time products. The results show that the average positioning accuracy can reach 1.57 cm, 0.76 cm and 1.67 cm in east, north and up direction for static PPP, respectively. Finally, using the recovered real-time products and the final products, the GPS observation data collected in aviation were processed in pseudo real-time in a kinematic mode. The results show that the RMSs of positioning errors are 8.5 cm, 2.4 cm and 16.5 cm in the east, north and up direction, respectively. In addition, one-day multi-GNSS observation data at 20 IGS stations were processed in a kinematic PPP mode, and the results show that the average positioning accuracy is 3.11 cm, 2.04 cm and 4.94 cm in east, north and up directions.

Key words：IGS RTS；precise point positioning；real-time positioning；precise orbit and clock corrections；multi-GNSS

1 Introduction

Precise point positioning (PPP) uses precise satellite orbit and clock products as well the correction model or parameter estimation to eliminate the effects of various related errors, providing global users at an accuracy level of centimeter to millimeter [1][2]. As the precise satellite orbit and clock products provided by International GNSS Services (IGS) usually have some time delays, the production time of the final products can reach up to 13 days, so they are mainly used in the post-processing mode [3][4]. For real-time PPP (RT PPP) users or users who need to process GNSS data quickly, orbit and clock products

Editor-in-charge: Dr. Changsheng Cai

with lower latency are urgently needed. IGS rapid clocks have a latency of 16 hours and have a sampling rate of only 5 min, which can hardly satisfy the requirement of positioning precision. IGS ultra-rapid products can be obtained in real time, but the prediction accuracy of satellite clock is low at about 3 ns, and the prediction error increases with time, which cannot satisfy the precision requirements either[5]. Therefore, in this case, we urgently need the other orbit and clock products with the minimum latency and the highest precision. It is a good solution to save IGS real-time products in real time and store them in an offline repository.

In order to meet the needs of real-time precise applications, IGS officially launched real-time service (RTS) in 2013[6][7]. The RTS products include Global Navigation Satellite System (GNSS) satellite orbit and satellite clock corrections, which correspond to broadcast ephemeris, broadcast in the form of RTCM (Radio Technical Commission for Maritime Services) state space representation (SSR) correction stream[8]. The RTS products broadcast over the Internet using Networked Transport of RTCM via Internet Protocol (NTRIP) and are available through several analysis centers around the world[5][6]. By receiving the GNSS satellite orbit and clock correction stream and recovering precise orbits and clock in real time with use of broadcast ephemeris, then saving them in an offline repository, users can obtain the highest precision satellite orbit and clock products with minimum latency, and then quickly or even real-time process GNSS data. Hadas et al. [3] examined the availability and latency of real-time correction. The results show that the availability of corrections was beyond 95% for GPS and beyond 90% for GLONASS. XU and YUAN 16] shows that the real-time orbit accuracy of most satellites can reach centimeter level and the real-time clock accuracy can reach sub-nanosecond level except BDS geostationary satellites. Chen et al.[17] shows that hourly static PPP using real-time products provides coordinates with precision of 2~3 cm in the north and 3~4 cm in the east and up components, for any location around the globe, and the precisions of 2.2 cm, 4.2 cm and 6.1 cm are obtained in the north, east, and up directions for the kinematic PPP, respectively. Kazmierski et al.[9] made a comprehensive evaluation of real-time orbit and clock corrections. Elsobeiey and Al-Harbi[6] shows that using IGS RTS products in real-time PPP can improve the position solution root mean square (RMS) by about 50% compared with the solution obtained from the predicted part of the IGS ultra-rapid products.

In this paper, the satellite orbit and clock SSR correction stream broadcast by IGS Analysis Center of Wuhan University is received in real time, and the precise satellite orbit and clock products are recovered in real time, and their integrity and accuracy are analyzed with reference to the final MGEX precise satellite orbit and clock products released by Wuhan University Analysis Center[10]. Using the open source software PRIDE PPP-AR Ⅱ developed by PRIDE Lab research group of Wuhan University[11][12], the observation data from globally distributed IGS stations are processed in static and kinematic PPP models and the aviation data are processed in pseudo real-time kinematic PPP model by using the recovered real-time satellite precise orbit and clock products and final products, respectively. The in real-time PPP accuracy is analyzed to evaluate the performance of the real-time recovered satellite orbit and clock products.

2 Real-time precise satellite orbit and clock products based on SSR correction

2.1 Recovery of precise orbits

The satellite orbit and clock corrections in RTCM-SSR format can be expressed as follows[8]:

$$\Delta_{SSR}(t_0) = (IODE, \delta P_r, \delta P_a, \delta P_c, \delta \dot{P}_r, \delta \dot{P}_a, \delta \dot{P}_c, C_0, C_1, C_2) \quad (1)$$

where t_0 is the Issue of Data (IOD); $IODE$ represents the corresponding broadcast ephemeris used for the calculation of the current orbit and clock corrections; $(\delta P_r, \delta P_a, \delta P_c)$ are the orbital correction components in radial, along-track, and cross-track directions; $(\delta \dot{P}_r, \delta \dot{P}_a, \delta \dot{P}_c)$ are the correction rates in radial, along-track, and cross-track directions;

(C_0, C_1, C_2) are the polynomial coefficient terms of the real-time satellite clock corrections.

The above satellite orbit corrections are defined in the RAC (radial, along-track, and cross-track) orbital coordinate system. However, the broadcast ephemeris uses the Earth-Centered-Earth Fixed (ECEF) coordinate system. Therefore, the real-time orbit corrections must be converted from the RAC coordinate system to the ECEF coordinate system before it can be applied to the broadcast ephemeris, and then precise satellite coordinates can be obtained[3][6].

For any epoch t, the orbit correction δP in RAC orbital coordinate system at epoch t can be derived by[5]:

$$\delta P = \begin{bmatrix} \delta_r \\ \delta_a \\ \delta_c \end{bmatrix} = \begin{bmatrix} \delta P_r \\ \delta P_a \\ \delta P_c \end{bmatrix} + \begin{bmatrix} \delta \dot{P}_r \\ \delta \dot{P}_a \\ \delta \dot{P}_c \end{bmatrix} (t - t_0) \qquad (2)$$

where δ_r, δ_a, and δ_c are the orbital correction components in radial, along-track, and cross-track directions.

Then, compute the transformation matrix R from RAC to ECEF, and the corresponding ECEF orbit corrections is derived by[5]:

$$R = [e_r, e_a, e_c] = \left[\frac{v}{|v|} \times \frac{r \times v}{|r \times v|}, \frac{v}{|v|}, \frac{r \times v}{|r \times v|}\right] \qquad (3)$$

$$\begin{bmatrix} \delta_x \\ \delta_y \\ \delta_z \end{bmatrix} = R \begin{bmatrix} \delta_r \\ \delta_a \\ \delta_c \end{bmatrix} \qquad (4)$$

where r, v are the satellite position vector and velocity vector computed from the broadcast ephemeris; δ_x, δ_y, and δ_z are the correction components in X, Y, and Z directions in ECEF coordinate system.

Finally, by applying real-time ECEF orbit corrections to broadcast satellite coordinates, the precise satellite orbit coordinates are calculated[5]:

$$\begin{bmatrix} X \\ Y \\ Z \end{bmatrix}_{prec} = \begin{bmatrix} X \\ Y \\ Z \end{bmatrix}_{brdc} - \begin{bmatrix} \delta_x \\ \delta_y \\ \delta_z \end{bmatrix} \qquad (5)$$

where $(X, Y, Z)_{prec}$ are the precise satellite coordinates in the ECEF coordinate system and $(X, Y, Z)_{brdc}$ are the broadcast satellite coordinates.

It should be noted that there are generally two reference points for satellite position corrections provided in satellite orbit SSR correction stream, the satellite antenna phase center (APC), and the satellite Center of Mass (CoM). If the reference point is the antenna phase center, the satellite antenna phase deviation correction is needed to obtain the satellite centroid coordinates in the ECEF coordinate system. Typically, the reference of the SSR correction stream is indicated in the corresponding information description of the mountpoint that receives the SSR correction stream.

2.2 Recovery of precise clock

At epoch t, precise satellite clock can be calculated by applying satellite clock corrections to broadcast satellite clock[8]:

$$\left.\begin{aligned} \delta C &= C_0 + C_1(t - t_0) + C_2(t - t_0)^2 \\ dt_{prec} &= dt_{brdc} - \frac{\delta C}{c} \end{aligned}\right\} \qquad (6)$$

where $C_0, C_1,$ and C_2 are the polynomial coefficient terms of the real-time satellite clock corrections; c is the speed of light in meters per second in the vacuum; dt_{brdc} is the satellite clock computed according to the broadcast ephemeris; dt_{prec} is the precise satellite clock.

3 Quality analysis of real time products

In this study, the SSRC00WHU0 mountpoint of Wuhan University is selected, and the BNC software[13] is used to receive the satellite orbit and clock SSR correction stream in real time. The correction stream provides correction information for GPS, GLONASS, Galileo, BDS and takes CoM as the reference point. The SSR correction stream of 7 days from May 30 to June 5, 2021 is collected in real time. Combined with the broadcast ephemeris, the corresponding precise satellite orbits and clock are recovered and recorded in real time in files in SP3 and CLK format (the interval of both products is 5 s), and these files are stored locally, so as to facilitate the follow-up analysis of the integrity of the real-time correction stream and the accuracy of the recovered precise satellite orbit and clock products.

In this section, the final MGEX products released by Wuhan University Analysis Center is taken as a reference, and the quality of the recovered real-time products is analyzed in terms of integrity, orbit accuracy and clock accuracy.

3.1 Integrity

In practical work, the real-time correction stream will be affected by the stability of the data source itself, the transmission network and the receiving software. Therefore, data of some epochs in the recovered real-time products will be missed. Taking each satellite as a unit, we statistically analyze the integrity of the recovered real-time products for 7 consecutive days from May 30 to June 5, 2021. The integrity rate of a satellite is defined as:

$$\alpha = \frac{m_{available}}{m_{theoretical}} \tag{7}$$

where $m_{available}$ is the total number of epochs of the satellite's data actually contained in the product; $m_{theoretical}$ is the total number of epochs of the satellite's data theoretically contained in the product. For example, if the interval of the correction stream is 5 s, then the $m_{theoretical}$ for one day should be $86400/5 = 17280$ epochs.

Table 1 shows the data integrity rate of real-time products. As can be seen from Table 1, the satellite data during the experimental period are relatively complete, and the real-time products record the orbit and clock information of 113 GPS/GLONASS/Galileo/BDS satellites. It should be noted that the recovered real-time precise satellite products do not include all satellites of all systems, because there is no corresponding information of those satellites in Table 1 in the real-time SSR correction stream during the test.

Among the satellites in Table 1, the integrity rate of 111 satellites (98% of the total) is more than 70%; the integrity rate of the remaining two satellites (R09 and R15) is very low, which is 13.10% and 19.40%, respectively, mainly because the analysis center broadcasts only a small amount of real-time SSR correction information for these two satellites during the experimental period. The integrity rate of 100 satellites (88% of the total) is more than 80%. The integrity rate of 69 satellites (61% of the total) is more than 90%, with a maximum of 96.77%. From the point of view of different systems, the average integrity rate of GPS satellites is 94.27%. By contrast, the average integrity rate of GLONASS satellites is only 81.64%, which is mainly caused by the particular impact of R15 and R09 satellites during the period. The average integrity rate of Galileo satellites is 92.97%. The average integrity rate of BDS satellite is 85.38%. For BDS satellites, it is worth noting that there are obvious differences between BDS-2 and BDS-3 satellites. The average integrity rate of the BDS-2 satellites is 91.44%. By contrast, the average integrity rate of the BDS-3 satellites is only 82.01%. The average integrity rate of the BDS-3 satellites is about 10% lower than that of the BDS-2. Generally speaking, the integrity of the GPS and Galileo satellites is the best, followed by the BDS satellites, and the integrity of the GLONASS satellites is the worst.

3.2 Accuracy of real-time precise orbits

Taking the final MGEX precise orbit products released by Wuhan University Analysis Center as a reference, the accuracy of the real-time orbit products in SP3 format on 7 consecutive days is analyzed and evaluated. Since the data interval of the final orbit products is 15 minutes whereas the data interval of the real-time orbit products is 5s, in order to avoid additional errors caused by data interpolation, only the data at the same epoch for the final products and the real-time products are compared, and the RMS (root mean square) values of the orbit differences in along-track, cross-track and radial directions for each satellite during the experimental period are calculated according to formula (8), so as to represent the accuracy of real-time satellite orbit products[5]:

Table 1 Satellite data integrity rate of real-time products

PRN	Integrity	PRN	Integrity	PRN	Integrity	PRN	Integrity	PRN	Integrity

	rate %		rate %		rate %		rate %		rate %
G01	93.89	G27	94.06	E01	93.38	C05	93.31	C34	83.26
G02	94.68	G28	94.77	E02	93.01	C06	92.39	C35	78.78
G03	95.53	G29	96.77	E03	93.65	C07	92.47	C36	84.06
G04	96.10	G30	94.60	E04	93.12	C08	95.70	C37	82.71
G05	95.81	G31	95.74	E05	94.77	C09	95.92	C38	76.38
G06	92.89	G32	93.85	E07	93.85	C10	90.92	C39	80.71
G07	92.86	R01	89.95	E08	94.64	C11	90.23	C40	78.72
G08	94.20	R02	89.90	E09	92.03	C12	85.32	C41	74.61
G09	95.23	R03	89.26	E11	90.09	C13	93.39	C42	71.87
G10	95.35	R04	90.43	E12	91.25	C14	91.92	C43	73.54
G12	89.49	R05	90.61	E13	95.05	C16	93.51	C44	71.71
G13	94.58	R07	89.53	E15	92.63	C19	84.50	C45	70.08
G14	94.39	R08	89.17	E19	91.90	C20	85.36	C46	73.79
G15	95.86	R09	13.10	E21	94.56	C21	87.18		
G16	95.86	R12	88.50	E24	91.32	C22	85.13		
G17	95.31	R13	87.50	E25	92.84	C23	88.27		
G18	95.44	R14	90.07	E26	93.85	C24	88.35		
G19	96.11	R15	19.40	E27	93.84	C25	87.91		
G20	95.63	R16	90.54	E30	93.21	C26	87.73		
G21	93.31	R17	89.61	E31	91.62	C27	89.13		
G22	79.34	R18	89.62	E33	91.79	C28	90.95		
G23	95.01	R19	90.25	C01	96.65	C29	87.07		
G24	94.24	R20	84.42	C02	89.66	C30	85.59		
G25	95.59	R21	88.86	C03	74.62	C32	81.94		
G26	95.79	R24	90.50	C04	95.59	C33	84.83		

$$RMS = \sqrt{\left(\sum_{i=1}^{n} \Delta_i{}^2\right)/n} \tag{8}$$

where Δ_i is the orbit difference of the epoch i; n is the number of all epochs.

Figures 1 ~ 3 show the RMS differences of along-track, cross-track and radial directions for the GPS, GLOANSS and Galileo satellite orbits between the real-time products and the final products within 7 days. As can be seen from figure 1, the accuracy of the GPS real-time orbit is mostly lower than 5 cm in three directions, however, the accuracy of G14 satellite is slightly larger with an along-track error of 8.20 cm. At the same time, it can also be found that the along-track accuracy of the GPS real-time orbit is slightly worse than the cross-track and radial accuracies. As can be seen from figure 2, except for R09 and R20 satellites, the orbit accuracy of most GLONASS satellites in real-time products is lower than 15 cm in three directions, and the cross-track orbital accuracy of most GLONASS satellites is the highest in the three directions. It can be seen from figure 3 that, similar to GPS, the real-time orbit of Galileo has the characteristics that the accuracy is the best in the radial direction, and the worst in the along-track direction. The real-time orbit accuracy of most Galileo satellites is within 8 cm in the along-track direction, within 6 cm in the cross-track direction, and within 4 cm in the radial direction.

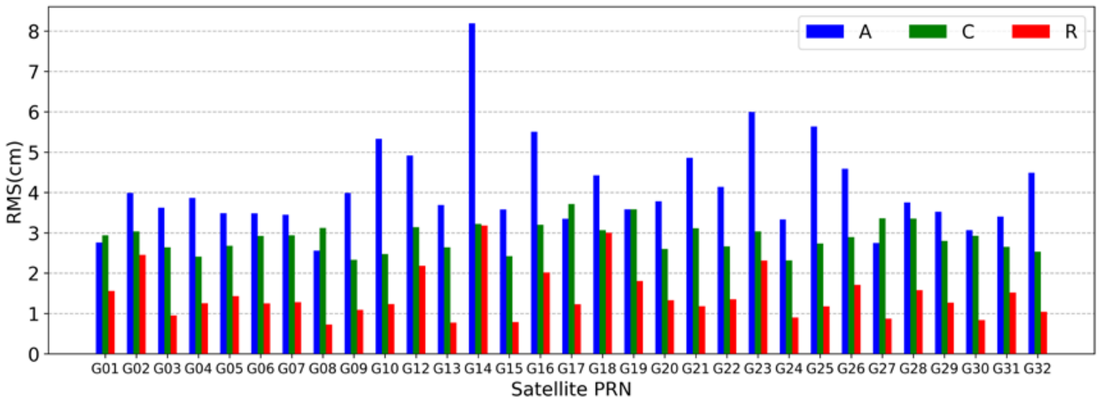

Fig.1 Along-track (A), Cross-track (C) and Radial (R) accuracy of GPS satellite orbit of real-time products

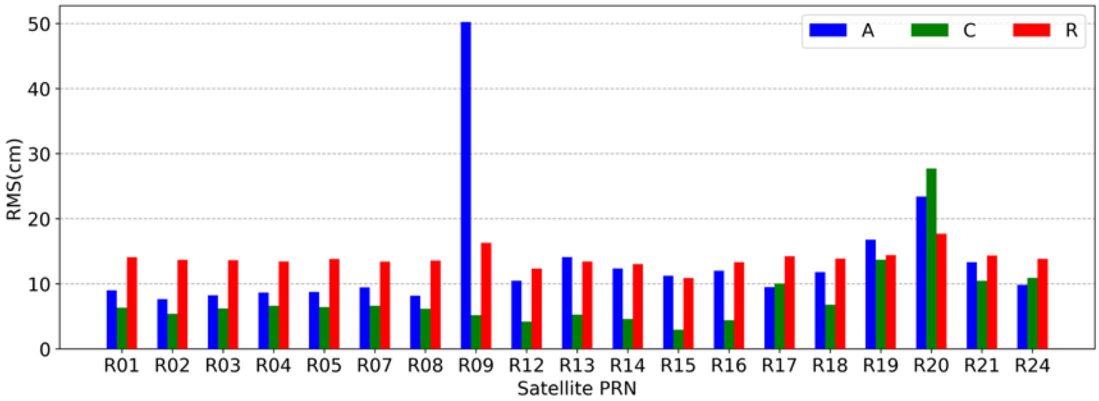

Fig.2 Along-track (A), Cross-track (C) and Radial (R) accuracy of GLONASS satellite orbit of real-time products

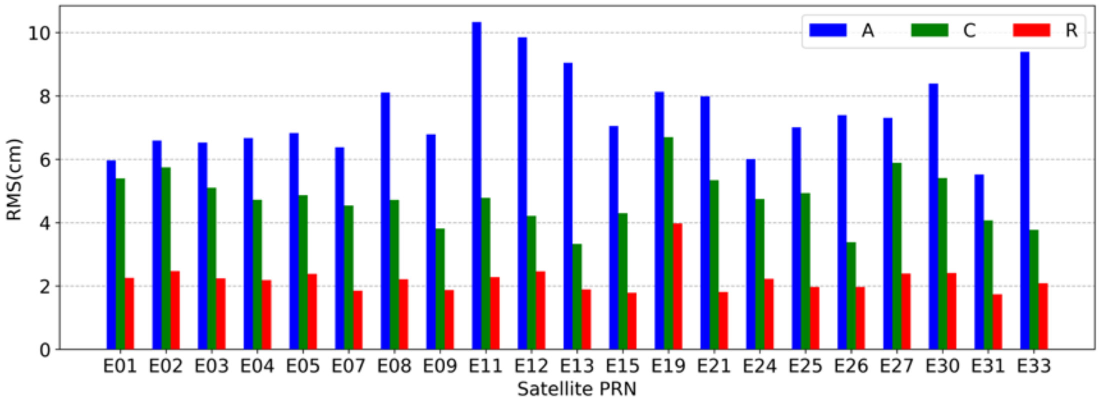

Fig.3 Along-track (A), Cross-track (C) and Radial (R) accuracy of Galileo satellite orbit of real-time products

Figures 4 and 5 show the RMS differences of along-track, cross-track and radial directions for the BDS Geostationary Earth Orbit (GEO) and BDS inclined geosynchronous orbits (IGSO) / medium Earth orbit (MEO) satellite orbits between the real-time products and the final products within 7 days, respectively. It should be noted that in figure 5, the IGSO/MEO satellites are divided into two parts for display according to the attributes of BDS-2 and BDS-3. At the same time, the GEO satellites in figure 4 are all BDS-2 satellites, so it is convenient to find the difference between BDS-2 and BDS-3 satellites. As can be seen from figures 4 and 5, during the experimental period, the real-time orbit accuracy of the BDS GEO satellite is generally low, which is the worst among all systems. Generally, it has meter-level accuracy in the cross-track and radial directions, and even up to more than ten meters in the along-track direction. The real-time orbit accuracy of the BDS IGSO/MEO satellites is significantly improved compared with the GEO satellites, most IGSO/MEO satellites can reach an accuracy level within 20 cm, which is similar to that of GLONASS satellites, but the along-track accuracy of some satellites is poor, exceeding 30 cm.

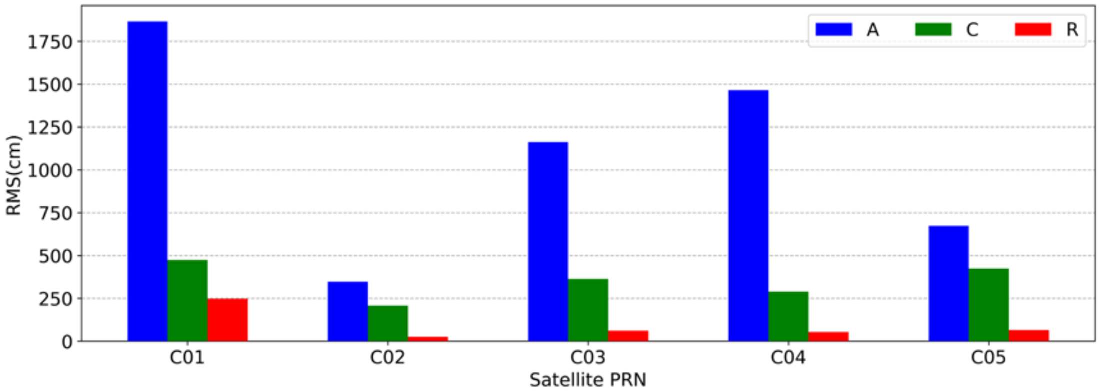

Fig.4 Along-track (A), Cross-track (C) and Radial (R) accuracy of BDS GEO satellite orbit of real-time products

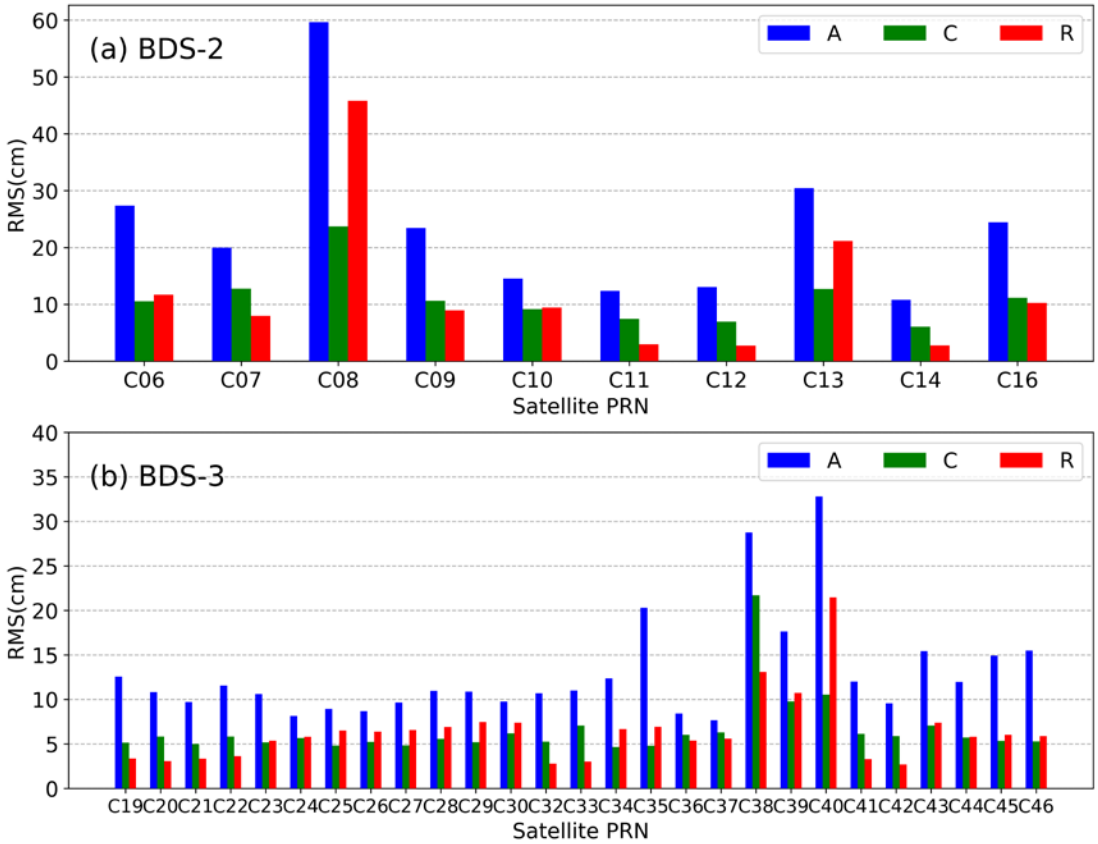

Fig.5 Along-track (A), Cross-track (C) and Radial (R) orbital accuracy of BDS IGSO/MEO satellites for real-time products. (It is divided into two parts: **a** BDS-2, **b** BDS-3)

The real-time orbit accuracy of BDS-3 satellites is much higher than that of BDS-2 satellites. The average orbital accuracy of all BDS-2 satellites in the along-track, cross-track and radial directions is 383.22 cm, 124.63 cm and 38.46 cm, which is mainly caused by the poor accuracy of GEO satellites. The average accuracy of all BDS-3 satellites in the along-track, cross-track and radial directions is 13.01 cm, 6.52 cm and 6.39 cm, which is 97%, 95% and 83% higher than those of BDS-2 satellites in the along-track, cross-track and radial directions, respectively. Even if the BDS-2 GEO satellites are not considered in the accuracy statistics, the average RMS values of the remaining BDS-2 satellites in the along-track, cross-track and radial directions are 23.61 cm, 11.12 cm and 12.38 cm, which are 1.8, 1.7, 1.9 times larger than those of the BDS-3 satellites, respectively. In fact, the real-time orbit accuracy of the BDS-2 satellite is still worse than that of the BDS-3 satellites. Overall, the real-time BDS orbit accuracy still has a great room for improvement.

Table 2 shows the average RMS differences between the real-time orbits and the final orbits of satellites of different systems during the experimental period. It can be seen from Table 2 that the real-time orbit accuracy of GPS satellites is the highest among all systems, and its average accuracy in the along-track, cross-track and radial directions is 4.10 cm, 2.89 cm and 1.46 cm, respectively. The average accuracy of Galileo satellites in the along-track, cross-track and radial directions is 7.49 cm, 4.75 cm and 2.21 cm, respectively, which is only slightly worse than that of GPS satellites. It has the second-best orbit accuracy among all systems. Both GPS and Galileo satellites have the best real-time orbit accuracy in the radial direction, and the worst in the along-track direction. Next are the BDS IGSO/MEO and GLONASS satellites, whose real-time orbit accuracy is equivalent in the along-track and cross-track directions. In the radial direction, the BDS IGSO/MEO satellites perform better than the GLONASS satellites. Finally, the average accuracy of the BDS GEO satellites in the along-track, cross-track and radial directions is 1102.42 cm, 351.65 cm and 90.62 cm, respectively, which is the worst.

3.3 Accuracy of real-time precise clocks

Similarly, the real-time clock products in CLK format for 7 consecutive days is compared with the final MGEX precise clock products released by Wuhan University Analysis Center to analyze its accuracy. Because the clock products generated by different analysis centers use different reference clocks, there is a systematic deviation between the clock products. In this paper, the quadratic difference method is used to calculate the accuracy of the real-time precise clock. Firstly, one of the satellites of each system is selected as a reference satellite (in this paper, G01, R01, E01 and C01 are selected, respectively). Then, the other satellites make a difference with the reference satellite clock at the same epoch of the real-time clock product and the final clock product, thus eliminating the impact of different reference clocks. Then make a second-order difference between the first-order difference results of the real-time product and the final product. Finally, the formula (9) is used to calculate the RMS value of the quadratic difference to represent the accuracy of the real-time clock products[5]:

Table 2 Average orbit accuracy of satellites for different systems in real-time products

Satellite system	Average accuracy in different directions (cm)		
	Along-track	Cross-track	Radial
GPS	4.10	2.89	1.46
Galileo	7.49	4.75	2.21
BDS IGSO/MEO	15.88	7.76	8.00
GLONASS	13.43	7.90	13.86
BDS GEO	1102.42	351.65	90.62

$$RMS = \sqrt{\sum_{i=1}^{n} (\Delta_i - \bar{\Delta})^2 / n} \tag{9}$$

where Δ_i is the quadratic difference of the epoch i of each satellite; $\bar{\Delta}$ is the mean value of the quadratic difference sequence of each satellite clock; n is the number of epochs.

Figure 6 shows the RMS values calculated according to formula (9) for GPS, GLOANSS, Galileo and BDS real-time precise satellite clock over a 7-day period. It can be seen from figure 6 (a) that there are obvious differences in real-time clock accuracy among different GPS satellites. Most GPS satellites can achieve an accuracy level better than 0.6 ns, and the best accuracy is 0.15 ns (G19), but the accuracy of G08/G09/G10/G25/G27/G28 satellites is obviously poor, and the worst accuracy is only 0.90 ns (G08). Overall, the average real-time clock accuracy of all GPS satellites is 0.43 ns, which is the highest among all satellites of all constellations. As can be seen from figure 6 (b), the real-time clock accuracy of each satellite of GLONASS system is very close. The real-time clock accuracy of GLONASS satellites basically fluctuates between 0.8~1.0 ns. The best accuracy is 0.59 ns (R15), and the worst is only 1.14 ns (R20). The average real-time clock accuracy of all GLONASS satellites is 0.91 ns. As can be seen from figure 6 (c), the real-time clock accuracy of Galileo satellites is relatively higher. Except for the poor accuracy of E04 and E11 satellites, which are 0.89 and 0.83 ns, respectively, the other satellites can achieve an accuracy level of better than 0.6 ns. The average accuracy of all Galileo satellites is 0.44 ns, which is similar to GPS satellites. It can be seen from Figure 6 (d) that the real-time clock accuracy of the BDS satellites is relatively poor compared with the other systems. For about 54% of the BDS satellites, their clock accuracy is more than 3 ns. The worst accuracy is 6.76 ns (C30), and the best accuracy is only 1.25 ns (C09), which is relatively poor compared with the other systems. The average real-time clock accuracy of BDS is only 3.45 ns, which is much worse than that of the other constellation satellites. Unlike the orbit, there is no significant difference in the clock accuracy between the BDS GEO and IGSO/MEO satellites, and between the BDS-2 and BDS-3 satellites, which may be due to the quadratic difference method that eliminates the systematic deviation.

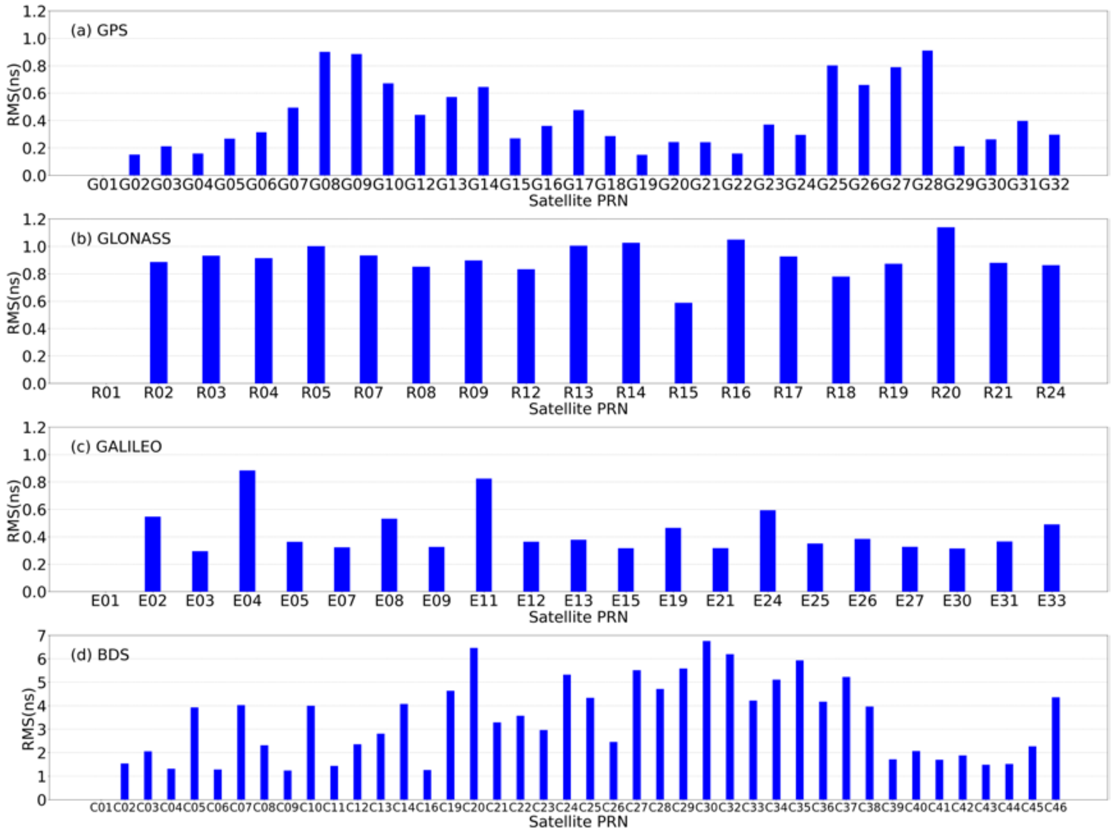

Fig.6 Accuracy of satellite clocks of real-time products for (**a**) GPS, (**b**) GLONASS, (**c**) Galileo, (**d**) BDS. (Due to the poor accuracy of BDS satellites, the scale of y-axis in **d** subplot is different from that in **a**, **b** and **c** subplots)

On the whole, during the experimental period, the real-time clock accuracy of GPS and Galileo satellites is relatively higher, followed by GLONASS satellites. Taking the final products as a reference, their accuracy can reach the sub-nanometer level, which is much higher than that of the IGS ultra-rapid products. It should be noted that the BDS satellites only have the accuracy of a few nanoseconds, and its real-time clock accuracy is the worst.

4 The application of real-time products in RTPPP

The real time precise satellite orbit and clock products are mainly used in real-time PPP (RTPPP), to achieve rapid response to GNSS data processing. Therefore, this section indirectly verifies the quality and application effect of the real-time products through static and pseudo-real-time kinematic PPP. The open source PPP GNSS data processing software PRIDE PPP-AR Ⅱ developed by Prof. Jianghui Geng (Songfeng Yang, etc.) of GNSS Research Center of Wuhan University is used in the test[18]. The software can support GPS, GLONASS, Galileo, BDS-2/3 and QZSS processing, handle high-frequency data up to 50Hz in a variety of processing modes. The software can be applied to large dynamic mobile platforms, and has good positioning and application performance.

Table 3 Test setup and data processing strategies

Items	Models/Strategies
Processing mode	Static;
	Kinematic;
Constellations	GPS/GLONASS/Galileo/BDS;
Observations	Ionospheric-free linear combination code and carrier-phase measurements;
Priori noise	Pseudorange: 0.3 m;
	Carrier-phase: 0.01 cycles;
Elevation cutoff angle	7°
Data interval	Static: 30 s;
	Kinematic: 0.5 s, 30 s;
Precise satellite orbits and clocks	Real-time products derived from real-time stream: SSRC00WHU0 (CoM) + broadcast ephemeris;
	Final MGEX products released by Wuhan University Analysis Center;
Code biases	Using CODE’s DCB products to correct the satellite-end P1C1 and P2C2 differential code biases (DCB)
Receiver antenna phase center	PCO and PCV values from igs14.atx file
Tidal displacements	Corrected by IERS Convention 2010
Relativistic effect	Corrected
Phase windup	Corrected
Station coordinates	Static: Estimated as a constant value for one day;
	Kinematic: Estimated as white noise;
Receiver clocks	Estimated as white noise, one value for each GNSS system
Zenith tropospheric delay	Mapping function: Global Mapping Function (GMF)[14]
	Saastamonien model[15] + Estimated as piece-wise constant
Horizontal troposphere gradients	Estimated as piece-wise constant
Ionosphere delays	First-order ionosphere delay is eliminated using the ionosphere-free combination; Higher-order ionosphere delay is corrected using the CODE global ionosphere maps
Phase ambiguities	Float constants for each continuous arc

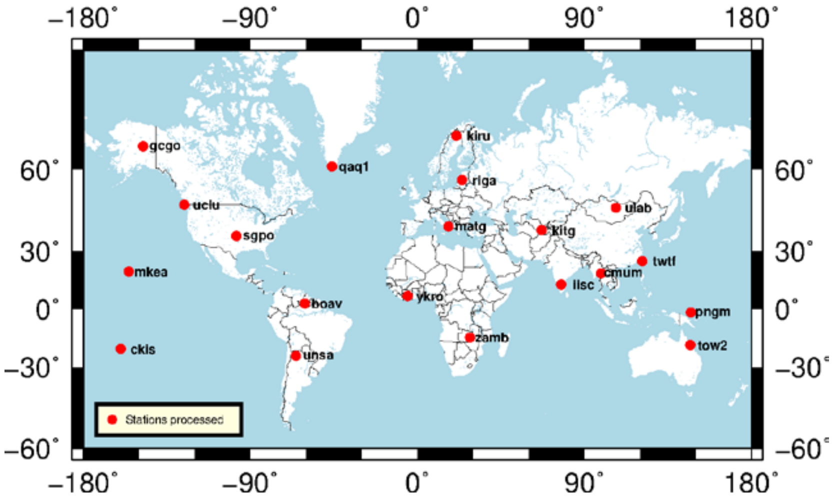

Fig.7 IGS stations used for static test

4.1 Static test

As shown in figure 7, 20 globally distributed IGS stations are randomly selected to conduct static PPP processing using the daily observation data from May 30th to June 5th (DOY 150~156) in 2021. The specific processing strategies in the test are shown in the static mode section in Table 3. At the same time, as a reference, keeping all other processing strategies unchanged, this section also uses the final MGEX orbit and clock products released by Wuhan University Analysis Center to process the same observation data in the static PPP mode.

In this study, the weekly combination coordinates provided by IGS are used as reference coordinates, the difference between the daily solution of static PPP at each station and the corresponding reference coordinate is calculated, and is converted to the ENU (east, north, and up) coordinate directions to get the positioning error which is used to evaluate the positioning accuracy. Figures 8 and 9 show the RMS of the positioning errors using the final products and the real-time products during the 7 days of the test, respectively. It can be seen from Figure 8 that for the static PPP using the final products, the daily float solution of most stations can achieve the accuracy of better than 6.0 mm in the east and north directions and better than 1.0 cm in the up direction. The positioning accuracy at CMUM station in the up direction is slightly worse than that of other stations, which is 1.02 cm. In general, the positioning accuracies in the east and north directions are comparable, and better than that in the up direction. As can be seen from Figure 9, for the static PPP using real-time products, the positioning accuracy of the corresponding daily float solution is slightly worse than that of the final products, but most stations can achieve the accuracy of better than 2.0 cm in the east and north direction and better than 3.0 cm in the up direction. The positioning accuracy in the east direction of YKRO and ZAMB station is slightly worse than other stations.

Table 4 shows the specific RMS of the positioning errors in the direction of east, north and up at each station. It can be seen from Table 4 that using the final products for static PPP processing, the results are in good agreement with the IGS weekly combination solution. The optimal positioning accuracy can reach 1.0 mm in east direction, 0.7 mm in north direction and 2.2 mm in up direction. The average positioning accuracy in east, north and up directions is 0.26 cm, 0.29 cm, 0.53 cm, respectively. In contrast, the positioning accuracy of the results using real-time products is slightly lower. The optimal positioning accuracy in east, north and up directions is 6.6 mm, 3.0 mm and 6.2 mm, respectively, and the average positioning accuracy in east, north and up directions is 1.57 cm, 0.76 cm, 1.67 cm, respectively. Overall, the positioning accuracy at each station is comparable, the positioning accuracy in north direction is the best, and the worst in up direction.

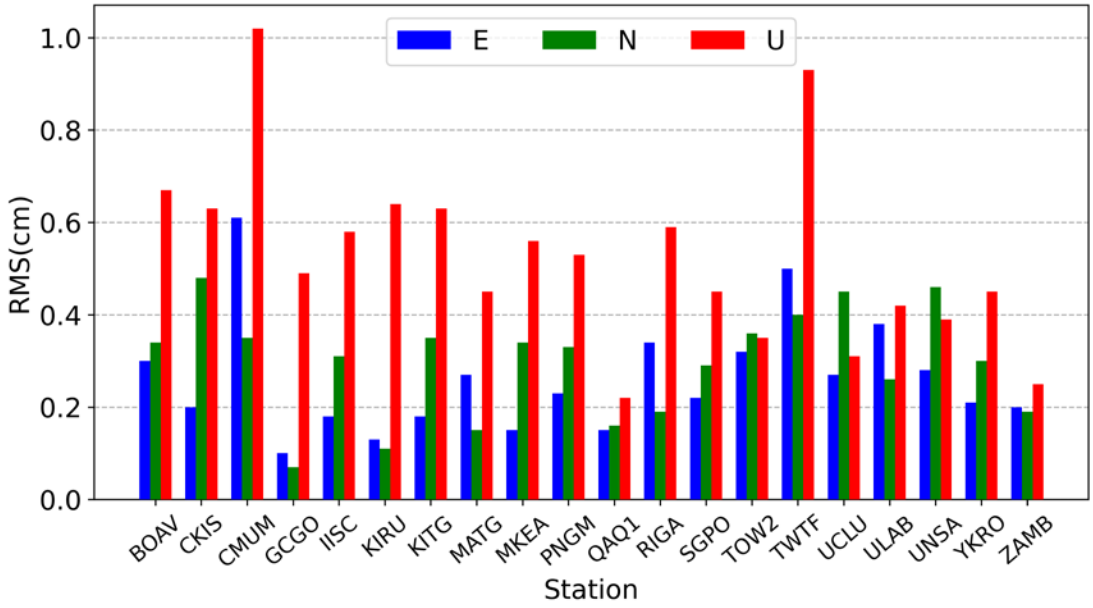

Fig.8 The RMS of the positioning errors using the final products in static PPP test

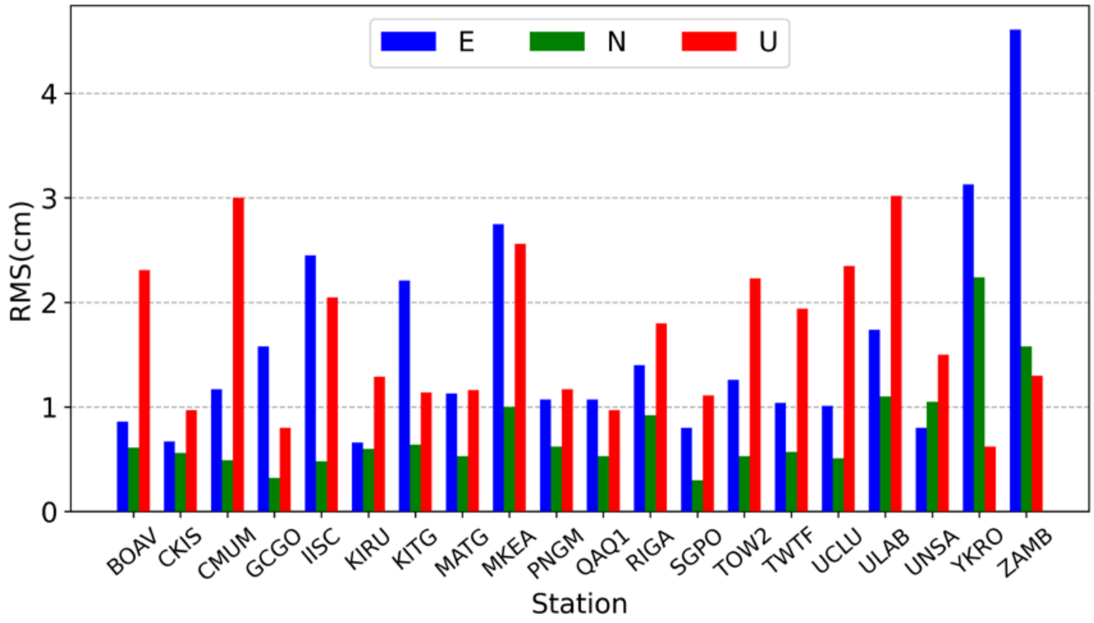

Fig.9 The RMS of the positioning errors using the real-time products in static PPP test

4.2 Kinematic test

In the kinematic test, firstly, this study indirectly verifies the application effect of real-time products by pseudo real-time kinematic PPP processing using GPS observation data collected in aviation. In this test, the aircraft mainly flew in the northeast of Hainan Province in China. The flight trajectory is shown by the red solid line in Fig. 10, in which the red triangle represents the reference station. The test was carried out on May 29, 2021. The observation time is about 3.5 hours and the data sampling rate is 0.5 seconds. The specific processing strategy in the test is shown in the kinematic mode section in Table 3. The processing mode of PRIDE PPP-AR Ⅱ software is set to kinematic mode, and the final products released by Wuhan University Analysis Center and real-time products are used to process the GPS observation data respectively while the other settings are kept the same, and the corresponding kinematic positioning results are obtained.

Table 4 Comparison of positioning accuracy between using final products and real-time products

Station	Final MGEX products RMS (cm)			Real-time products RMS (cm)		
	East	North	Up	East	North	Up
BOAV	0.30	0.34	0.67	0.86	0.61	2.31
CKIS	0.20	0.48	0.63	0.67	0.56	0.97
CMUM	0.61	0.35	1.02	1.17	0.49	3.00
GCGO	0.10	0.07	0.49	1.58	0.32	0.80
IISC	0.18	0.31	0.58	2.45	0.48	2.05
KIRU	0.13	0.11	0.64	0.66	0.60	1.29
KITG	0.18	0.35	0.63	2.21	0.64	1.14
MATG	0.27	0.15	0.45	1.13	0.53	1.16
MKEA	0.15	0.34	0.56	2.75	1.00	2.56
PNGM	0.23	0.33	0.53	1.07	0.62	1.17
QAQ1	0.15	0.16	0.22	1.07	0.53	0.97
RIGA	0.34	0.19	0.59	1.40	0.92	1.80
SGPO	0.22	0.29	0.45	0.80	0.30	1.11
TOW2	0.32	0.36	0.35	1.26	0.53	2.23
TWTF	0.50	0.40	0.93	1.04	0.57	1.94
UCLU	0.27	0.45	0.31	1.01	0.51	2.35
ULAB	0.38	0.26	0.42	1.74	1.10	3.02
UNSA	0.28	0.46	0.39	0.80	1.05	1.50
YKRO	0.21	0.30	0.45	3.13	2.24	0.62
ZAMB	0.20	0.19	0.25	4.61	1.58	1.30
Average	0.26	0.29	0.53	1.57	0.76	1.67

Fig.10 The flight trajectory of the aircraft in the kinematic test

In order to evaluate the positioning accuracy of the kinematic positioning results, this study uses the RTKLIB software to process the experimental data using kinematic relative positioning mode, and the integer ambiguity resolution is set to "fix and hold" to obtain the fixed solution (the reference station is located near Qionghai City, Hainan, and the maximum baseline length is up to 100 km). Taking the relative positioning results output by RTKLIB as the reference results (with the increase of baseline length, the positioning accuracy of reference results may decrease), the positioning error is obtained by calculating the difference between the kinematic PPP float positioning results of the final/real-time products and the reference results in ENU coordinate system.

Fig. 11 shows the time series of the position difference between the kinematic PPP float positioning result and the reference result in the directions of east, north and up. The blue curve represents the position errors using the final products, and the orange curve represents the position errors using the real-time products. It can be seen from Figure 11 that the two time series are very consistent with each other. The RMS of the position errors between the kinematic PPP positioning results based on the final products and the reference results are 8.08 cm, 2.09 cm and 17.86 cm, respectively, in the east, north and up directions. The RMS of the position errors between the kinematic PPP positioning results based on the real-time products and the reference results are 8.53 cm, 2.41 cm and 16.47 cm, respectively, in the east, north and up directions. Only the GPS observation data were processed in this aviation test. Through the research and analysis of the quality of the real-time products in the previous sections, compared with the final products, the average accuracy of the real-time GPS orbits is better than 5 cm, and the average accuracy of the real-time GPS clock is 0.43 ns. It can be considered that the real-time GPS products is actually very close to the final products, so the “Rt” positioning result is also very close to “Fin”. This indirectly proves that the real-time GPS precise satellite orbit and clock products recovered by SSR correction stream have relatively high accuracy, and it can also achieve the similar positioning accuracy as the final products when it is used by users. The above results also fully demonstrate the advantages and potential of the solution of real-time recovery of precise satellite orbit and clock products and storing them in an offline repository, that is, users can use these products to process GNSS data with minimum latency or even real-time without waiting for the release of the IGS final products. At the same time, they can also obtain the positioning results with an optimal accuracy of the centimeter level.

In addition, because only GPS data are collected in the above aviation test, in order to fully verify the quality of GPS, GLONASS, Galileo and BDS satellites in real-time products, this study uses 20 IGS stations as shown in the Section 4.1 and uses PRIDE PPP-AR II software to process the GPS, GLONASS, Galileo and BDS observation data of all stations on DOY 154, 2021 using kinematic PPP mode. Similarly, as a comparison, the final MGEX products of Wuhan University and real-time products were used in the test. Figure 12 selects the TWTF station and shows the difference of the time series in the east, north and up directions between the results obtained by using the final products and real-time products and the reference coordinates. As can be seen from Figure 12, the positioning accuracy of using the real-time products is slightly worse than that of using the final products, and the RMS values of the kinematic solution differences in the east, north and up directions are 1.67 cm, 1.66 cm and 3.94 cm, respectively, which are slightly higher than the corresponding RMS values of the final products. Table 5 shows the RMS values of the sequence of differences between the kinematic solutions and the reference coordinates obtained by using the final products and real-time products of all stations in the east, north and up directions. It can be seen from Table 5 that the kinematic solutions obtained by using the final products have very high positioning accuracy, and the corresponding RMS values of the kinematic solution in east, north and up directions of each station are smaller than those of the kinematic solutions obtained by using the real-time products. The average positioning accuracy of the kinematic solutions of all stations obtained by using final products in east, north and up directions is 0.88 cm,0.89 cm and 2.23 cm, respectively. The kinematic solutions obtained by using the real-time products generally have the accuracy levels of centimeters in horizontal directions and centimeters to decimeters in vertical direction. The average positioning accuracy of kinematic solutions obtained by using real-time products in east, north and up directions is 3.11 cm, 2.04 cm and 4.94 cm, respectively. Although this level of positioning accuracy is slightly lower than that of the final products, it can still meet the requirements of positioning accuracy in near real-time applications that require rapid PPP processing (usually within a few hours).

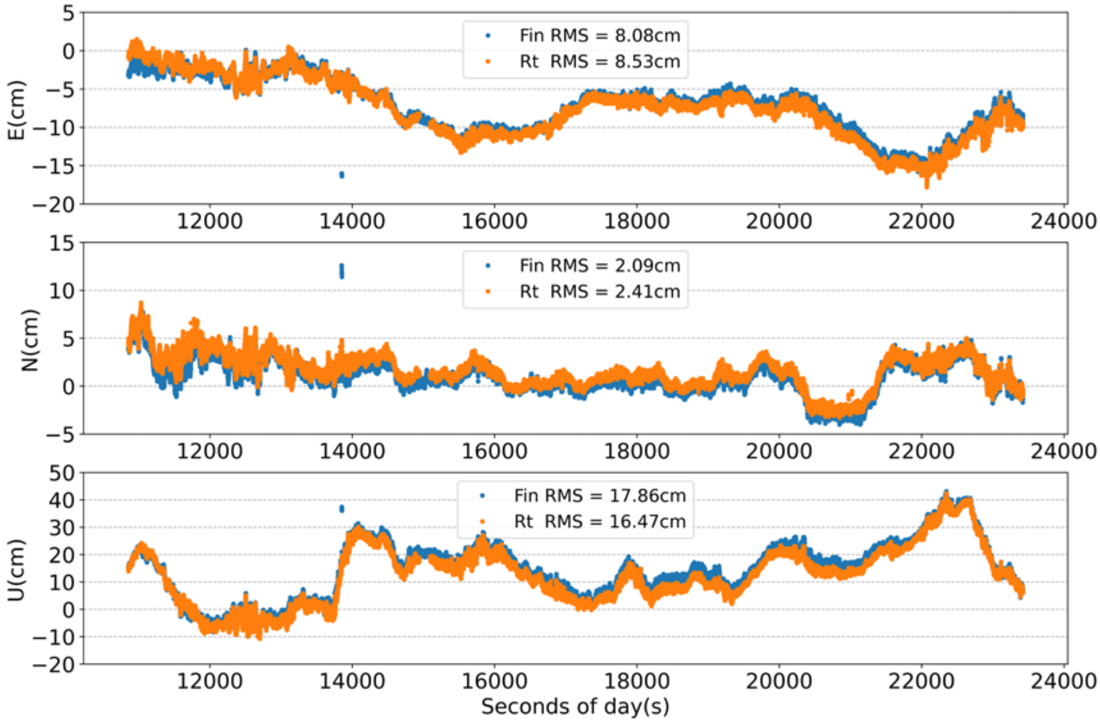

Fig.11 Position difference between the kinematic PPP float positioning results and the reference result

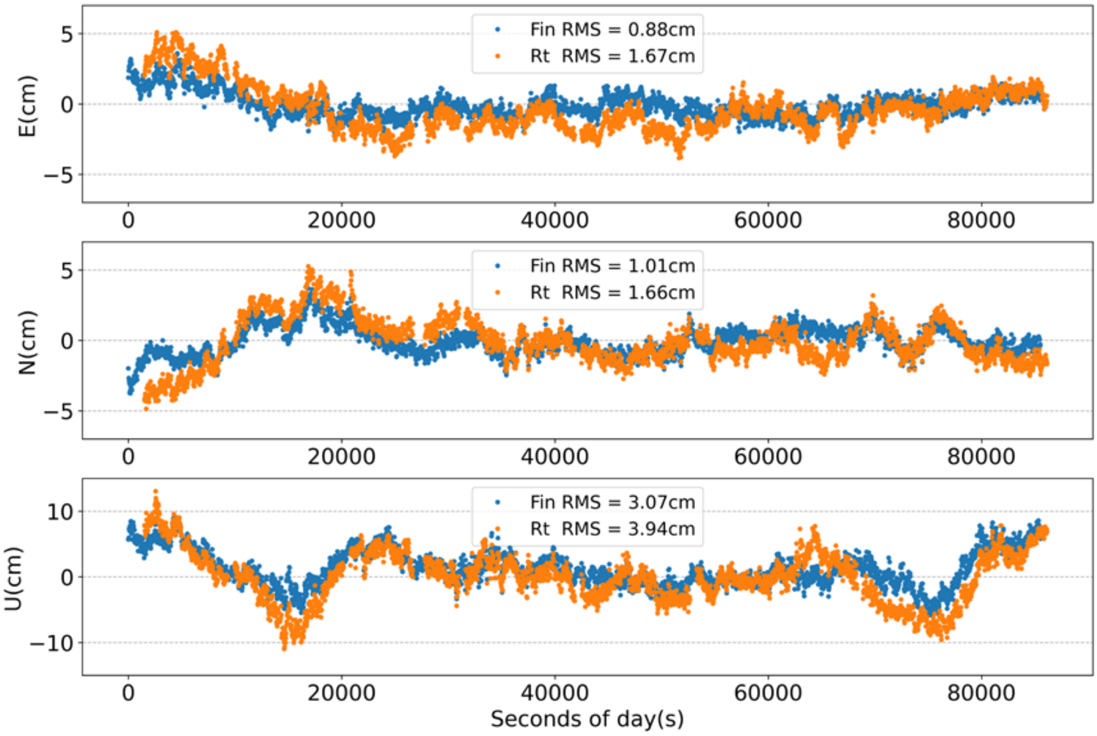

Fig.12 Kinematic PPP results of TWTF station processed by using final products and real-time products on DOY154, 2021

Table 5 Comparison of positioning accuracy of kinematic PPP between using final products and real-time products

Station	RMS of Fin (cm)			RMS of Rt (cm)		
	East	North	Up	East	North	Up
BOAV	1.32	1.32	2.70	2.42	1.77	4.36
CKIS	0.82	0.74	1.57	1.77	1.44	4.79
CMUM	2.71	2.35	7.63	5.97	4.14	10.35
GCGO	0.82	0.70	1.99	2.90	2.06	4.42
IISC	1.43	0.96	3.61	4.52	1.78	5.22
KIRU	0.48	0.46	1.48	2.75	2.56	3.87
KITG	0.67	0.82	1.55	4.45	1.64	5.12
MATG	0.67	0.57	1.39	2.28	1.94	4.75
MKEA	0.86	0.67	1.91	4.05	1.52	3.39
PNGM	0.59	0.74	1.29	7.16	2.83	7.81
QAQ1	0.52	0.43	0.89	2.60	2.38	3.80
RIGA	0.53	0.59	1.23	2.64	3.06	5.50
SGPO	1.10	1.01	2.01	2.57	1.45	3.84
TOW2	0.40	0.63	1.34	2.50	1.21	5.32
TWTF	0.88	1.01	3.07	1.67	1.66	3.94
UCLU	0.89	1.59	4.68	2.28	2.47	5.25
ULAB	0.73	0.68	1.18	2.42	1.81	4.73
UNSA	0.86	0.62	1.94	2.08	1.80	5.06
YKRO	0.82	1.01	2.14	2.35	2.09	4.03
ZAMB	0.51	0.64	1.02	2.82	1.13	3.21
Average	0.88	0.89	2.23	3.11	2.04	4.94

5 Conclusions

IGS RTS provides real-time multi-GNSS satellite orbit and clock correction streams with reference to broadcast ephemeris, which allows us to obtain precise satellite orbit and clock products with the minimum latency and the highest precision. These products can be used in scenarios such as RTPPP where GNSS data needs to be processed quickly.

In this paper, the method of using SSR correction information and broadcast ephemeris to recover precise satellite orbits and clocks is introduced in detail. Then, the SSRC00WHU0 mountpoint of Wuhan University which provides GPS, GLONASS, Galileo, BDS correction information is selected, and the precise satellite orbit and clock products of 7 days are recovered. Taking the final MGEX products released by Wuhan University Analysis Center as a reference, the quality of the real-time precise satellite orbit and clock products is evaluated. Finally, using the real-time products and the final products, the multi-GNSS observation data (GPS, GLONASS, Galileo and BDS) of 20 randomly distributed IGS stations around the world are processed in static and kinematic PPP modes, and the GPS observation data collected by aviation are processed in pseudo real-time kinematic PPP mode, in order to evaluate the application performance of real-time products and the positioning accuracy in RTPPP.

The results of quality analysis show that (1) For the real-time orbit products, the GPS satellites can achieve the accuracy of about 5 cm. Galileo is a little worse, and its accuracy is about 8 cm. The accuracy of GLONASS is similar to that of BDS IGSO/MEO, and it can reach about 15 cm. The accuracy of BDS GEO satellites is low to the level of more than ten meters, which is the worst of all satellites; (2) For the real-time clock products, similarly, GPS satellites have the highest clock accuracy, which can reach

0.43 ns. Galileo satellites are basically at the same accuracy level as GPS satellites, with an average accuracy of 0.44 ns. GLONASS satellites are slightly worse, but they can still achieve sub-nanosecond accuracy of 0.91 ns. The real-time clock accuracy of BDS satellites is the worst at only 3.14 ns. Generally speaking, the real-time orbit and clock products of GPS and Galileo satellites have relatively higher accuracy, followed by GLONASS satellites. The accuracy of BDS satellite is relatively poor, so we should pay attention to it when using it.

For the PPP performance, the experimental results show that (1) Although the positioning accuracy of static PPP, is slightly worse than that using the final products, the average positioning accuracy of 1.57 cm, 0.76 cm and 1.67 cm in east, north and up directions can be achieved by using real-time products. In general, the positioning accuracy in the north direction is the best, followed by the east direction and up directions; (2) For pseudo real-time kinematic GPS PPP, the positioning results obtained by using the final products and the real-time products are very consistent, and the RMS of the position difference in the directions of east, north and up are 8.1 cm, 2.1 cm, 17.9 cm and 8.5 cm, 2.4 cm, 16.5 cm, respectively, compared with the reference results; (3) For GPS, GLONASS, Galileo and BDS kinematic PPP, the average positioning accuracy in east, north and up directions is 3.11 cm, 2.04 cm and 4.94 cm, respectively.

The study basically shows the advantages of the solution of using SSR correction stream to recover the precise satellite orbit and clock products in real time, that is, low latency and high precision, which can play an important role in the application of real-time precise positioning.

References

[1] Zumberge, J. F ., Heflin, M. B., Jefferson, D. C., Watkins, M. M., & Webb, F . H. (1997). Precise point positioning for the efficient and robust analysis of GPS data from large networks. Journal of Geophysical Research: Solid Earth, 102(B3), 5005–5017

[2] Kouba, Jan and Héroux, Pierre. (2001) Precise Point Positioning Using IGS Orbit and Clock Products. GPS SOLUTIONS 5(2), 12-28

[3] Hadas, Tomasz and Bosy, Jaroslaw. (2015) IGS RTS precise orbits and clocks verification and quality degradation over time. GPS SOLUTIONS 19(1), 93-105

[4] Kazmierski, Kamil, Zajdel, Radoslaw and Sośnica, Krzysztof. (2020) Evolution of orbit and clock quality for real-time multi-GNSS solutions. GPS SOLUTIONS 24(4)

[5] Wang, Liang, Li, Zishen, Ge, Maorong, Neitzel, Frank, Wang, Zhiyu and Yuan, Hong. (2018) Validation and Assessment of Multi-GNSS Real-Time Precise Point Positioning in Simulated Kinematic Mode Using IGS Real-Time Service. Remote Sensing 10(2), 337

[6] Elsobeiey, Mohamed and Al-Harbi, Salim. (2016) Performance of real-time Precise Point Positioning using IGS real-time service. GPS SOLUTIONS 20(3), 565-571

[7] Caissy, Mark, Agrotis, Loukis, Weber, Georg, Hernandez-Pajares, Manuel and Hugentobler, Urs. (2012) "Coming soon: The international GNSS real-time service", north Coast Media, LLC. 52

[8] RTCM Standard 10403.3, Differential GNSS (Global Navigation Satellite Systems) Services – Version 3, October 7, 2016

[9] Kazmierski, Kamil, Sośnica, Krzysztof and Hadas, Tomasz. (2018) Quality assessment of multi-GNSS orbits and clocks for real-time precise point positioning. GPS SOLUTIONS 22(1)

[10] Montenbruck, Oliver, Steigenberger, Peter, Prange, Lars, Deng, Zhiguo, Zhao, Qile, Perosanz, Felix, Romero, Ignacio, Noll, Carey, Stürze, Andrea, Weber, Georg, Schmid, Ralf, MacLeod, Ken and Schaer, Stefan. (2017) The Multi-GNSS Experiment (MGEX) of the International GNSS Service (IGS) – Achievements, prospects and challenges. ADVANCES IN SPACE RESEARCH 59(7), 1671-1697

[11] Geng, Jianghui, Chen, Xingyu, Pan, Yuanxin, Mao, Shuyin, Li, Chenghong, Zhou, Jinning and

Zhang, Kunlun. (2019) PRIDE PPP-AR: an open-source software for GPS PPP ambiguity resolution. GPS SOLUTIONS 23(4), 1-10

[12] Geng, Jianghui, Yang, Songfeng and Guo, Jiang. (2021) Assessing IGS GPS/Galileo/BDS-2/BDS-3 phase bias products with PRIDE PPP-AR. Satellite Navigation 2(1)

[13] Weber, G. , Mervart, L. , A Stürze, A Rülke, & Stcker, D. . (2016). BKG Ntrip Client (BNC) Version 2.12

[14] Boehm, J., Niell, A., Tregoning, P. and Schuh, H. (2006) Global Mapping Function (GMF): A new empirical mapping function based on numerical weather model data. GEOPHYSICAL RESEARCH LETTERS 33(7)

[15] Saastamoinen, J. (1972) Contributions to the theory of atmospheric refraction. Bulletin géodésique 105(1), 279-298

[16] XU Li, YUAN Yunbin. Analysis on multi-GNSS SSR products from different analysis centers[J]. Journal of Navigation and Positioning, 2020, 8(6): 71-81

[17] Junping Chen , Haojun Li , Bin Wu , Yize Zhang , Jiexian Wang & Congwei Hu (2013) Performance of Real-Time Precise Point Positioning, Marine Geodesy, 36:1, 98-108, DOI: 10.1080/01490419.2012.699503

[18] Geng J, Mao S (2021) Massive GNSS network analysis without baselines: Undifferenced ambiguity resolution. J. Geophys. Res. 126(10), e2020JB021558. doi:10.1029/2020JB021558

Authors

[photo] Qi Zhang

[photo] Ran Zeng

[photo] Shaoming Xin

[photo] Xing Zhou

***Journal of Global Positioning Systems* (*2021*)**
Vol. 17, No. 2: 208-238
DOI: 10.5081/jgps.17.2.208

A Survey of Simultaneous Localization and Mapping with an Envision in 6G Wireless Networks

Baichuan Huang[1,2*], Jun Zhao[2], Sheng Luo[1,3], Jingbin Liu [1]
1. State Key Laboratory of Information Engineering in Surveying, Mapping and Remote Sensing, Wuhan University, Wuhan 430079, China
2. School of Computer Science and Engineering, Nanyang Technological University, Singapore
3. Hi-Target Surveying Instrument Co. Ltd, Guangzhou, China
* Corresponding Author, huangbaichuan@whu.edu.cn

Abstract: Simultaneous Localization and Mapping (SLAM) achieves the purpose of simultaneous positioning and map construction based on self-perception. The paper makes an overview in SLAM including Lidar SLAM, visual SLAM, and their fusion. For Lidar or visual SLAM, the survey illustrates the basic type and product of sensors, open source system in sort and history, deep learning embedded, the challenge and future. Additionally, visual inertial odometry is supplemented. For Lidar and visual fused SLAM, the paper highlights the multi-sensors calibration, the fusion in hardware, data, task layer. The open question and an envision in 6G wieless networks with SLAM end the paper. The contributions of this paper can be summarized as follows: the paper provides a high quality and full-scale overview in SLAM. It's very friendly for new researchers to hold the development of SLAM and learn it very obviously. Also, the paper can be considered as dictionary for experienced researchers to search and find new interested orientation.

Keywords: Survey, SLAM (Simultaneous Localization and Mapping), Lidar SLAM, Visual SLAM, Lidar and Vision Fused, User guidance.

1. Introduction

SLAM is the abbreviation of Simultaneous Localization and Mapping, which contains two main tasks, localization and mapping. It is a significant open problem in mobile robotics: to move precisely, a mobile robot must have an accurate environment map; however, to build an accurate map, the mobile robot's sensing locations must be known precisely [1]. In this way, simultaneous map building and localization can be seen to present a question of "which came first, the chicken or the egg?" (The map or the motion?)

In 1990, [2] firstly proposed the use of the EKF (Extended Kalman Filter) for incrementally estimating the posterior distribution over robot pose along with the positions of the landmarks. In fact, starting from the unknown location of the unknown environment, the robot locates its own position and attitude through repeated observation of environmental features in the movement process, and then builds an incremental map of the surrounding environment according to its own position, so as to achieve the purpose of simultaneous positioning and map construction. Localization is a very complex and hot point in recent years. The technologies of localization depend on environment and demand for cost, accuracy, frequency and robustness, which can be achieved by GPS (Global Positioning System), IMU (Inertial Measurement Unit), and wireless signal, etc.[3,4]. But GPS can only work well outdoors and IMU system has cumulative error [5]. The technology of wireless, as an active system, can't make a balance between cost and accuracy. With the fast

Editor in charge: Dr.-Ing. Qian Sun

development, SLAM equipped with Lidar, camera, IMU and other sensors springs up in last years.

Begin with filter-based SLAM, methods called incremental smoothing and mapping (iSAM, etc.) gradually become the fouc. But Graph-based SLAM play a dominant role now (such as g2o, etc.). The algorithm derives from KF (Kalman Filter), EKF and PF (Particle Filter) to graph-based optimization. And single thread has been replaced by multi-thread. The technology of SLAM also changed from the earliest prototype of military use to later robot applications with the fusion of multi sensors.

The organization of this paper can be summarized as follows: in Section II, Lidar SLAM including Lidar sensors, open source Lidar SLAM system, deep learning in Lidar and challenge as well as future will be illustrated. Section III highlights the visual SLAM including camera sensors, different density of open source visual SLAM system, visual inertial odometry SLAM, deep learning in visual SLAM and future. In Section IV, the fusion of Lidar and vision will be demonstrated. Finally, the paper identifies several directions for future research of SLAM and provides high quality and full-scale user guide for new researchers in SLAM.

Table 1 Comparison of the different methods

Methods	Feature
Lidar SLAM	more stable and robust
Visual SLAM	cheaper
Lidar and Visual SLAM	more powerful

2. Lidar SLAM

In 1991, [1] used multiple servo-mounted sonar sensors and EKF filter to equip robots with SLAM system. Begin with sonar sensors, the birth of Lidar makes SLAM system more reliable and robustness.

2.1 Lidar Sensors

Lidar sensors can be divided into 2D Lidar and 3D Lidar, which are defined by the number of Lidar beams. In terms of production process, Lidar can also be divided into mechanical Lidar, hybrid solid-state Lidar like MEMS (micro-electro-mechanical) and solid-state Lidar. Solid-state Lidar can be produced by the technology of phased array and flash.

Velodyne: In mechanical Lidar, it has VLP-16, HDL-32E and HDL-64E. In hybrid solid-state Lidar, it has Ultra puck auto with 32E.

SLAMTEC: it has low cost Lidar and robot platform such RPLIDAR A1, A2 and R3.

Ouster: it has mechanical Lidar from 16 to 128 channels.

Quanergy: S3 is the first issued solid-state Lidar in the world and M8 is the mechanical Lidar. The S3-QI is the micro solid-state Lidar.

Ibeo: It has Lux 4L and Lux 8L in mechanical Lidar. Cooperated with Valeo, it issued a hybrid solid-state Lidar named Scala.

In the trend, miniaturization and lightweight solid state Lidar will occupied the market and be satisfied with most application. Other Lidar companies include but not limited to **sick, Hokuyo, HESAI, RoboSense, LeddarTech, ISureStar, benewake, Livox, Innovusion, Innoviz, Trimble, Leishen Intelligent System.**

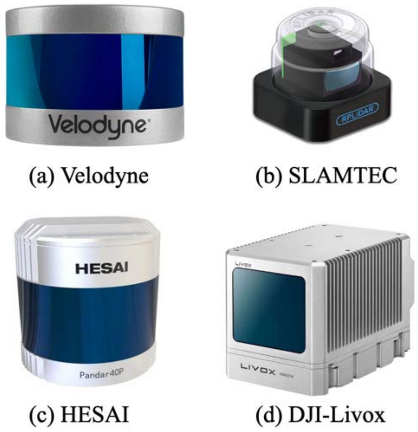

(a) Velodyne (b) SLAMTEC (c) HESAI (d) DJI-Livox

Figure 1. Lidar Sensors

2.2 Lidar SLAM System

Lidar SLAM system is reliable in theory and technology. [6] illustrated the theory in math about how to simultaneous localization and mapping with 2D Lidar based on probabilistic. Furthre, [7] make surveys about 2D Lidar SLAM system.

Table 2 Comparison of the different Lidar SLAM

Methods	Feature
2D Lidar SLAM	easier to positioning
3D Lidar SLAM	powerful to perceive

2.2.1 2D SLAM

Gmapping: it is the most used SLAM package in robots based on RBPF (Rao-Blackwellisation Partical Filter) method. It adds scan-match method to estimate the position [6,8]. It is the improved version with Grid map based on FastSLAM [9,10].

HectorSlam: it combines a 2D SLAM system and 3D navigation with scan-match technology and an inertial sensing system [11].

KartoSLAM: it is a graph-based SLAM system [12].

LagoSLAM: its basic is the graph-based SLAM, which is the minimization of a nonlinear non-convex cost function [13].

CoreSLAm: it is an algorithm to be understood with minimum loss of performance [14].

Cartographer: it is a SLAM system from Google [15]. It adopted sub-map and loop closure to achieve a better performance in product grade. The algorithm can provide SLAM in 2D and 3D across multiple platforms and sensor configurations.

2.2.2 3D SLAM

Loam: it is a real-time method for state estimation and mapping using a 3D Lidar [16]. It also has back and forth spin version and continuous scanning 2D Lidar version.

Lego-Loam: it takes in point cloud from a Velodyne VLP-16 Lidar (placed horizontal) and optional IMU data as inputs. The system outputs 6D pose estimation in real-time and has global optimization and loop closure [17].

Cartographer: it supports 2D and 3D SLAM [15].

IMLS-SLAM: it presents a new low-drift SLAM algorithm based only on 3D LiDAR data based on a scan-to-model matching framework [18].

2.2.3 Deep Learning with Lidar SLAM

Feature & Detection: PointNetVLAD [19] allows end-to-end training and inference to extract the global descriptor from a given 3D point cloud to solve point cloud based retrieval for place recognition. **VoxelNet** [20] is a generic 3D detection network that unifies feature extraction and bounding box prediction into a single stage, end-to-end trainable deep network. Other work can be seen in **BirdNet** [21]. **LMNet** [22] describes an efficient single-stage deep convolutional neural network to detect objects and outputs an objectness map and the bounding box offset values for each point. **PIXOR** [23] is a proposal-free, single-stage detector that outputs oriented 3D object estimates decoded from pixel-wise neural network predictions. **Yolo3D** [24] builds on the success of the one-shot regression meta-architecture in the 2D perspective image space and extend it to generate oriented 3D object bounding boxes from LiDAR point cloud. **PointCNN** [25] proposes to learn a X-transformation from the input points. The X-transformation is applied by element-wise product and sum operations of typical convolution operator. **MV3D** [26] is a sensory-fusion framework that takes both Lidar point cloud and RGB images as input and predicts oriented 3D bounding boxes. **PU-GAN** [27] presents a new point cloud upsampling network based on a generative adversarial network (GAN). Other similar work can be seen in this best paper in CVPR2018 but not limited to [28].

Recognition & Segmentation: In fact, the method of segmentation to 3D point cloud can be divided into Edge-based, region growing, model fitting, hybrid method, machine learning application and deep learning [29]. Here the paper focuses on the methods of deep learning. **PointNet** [30] designs a novel type of neural network that directly consumes point clouds, which has the function of classification, segmentation and semantic analysis. **PointNet++** [31] learns hierarchical features with increasing scales of contexts. **VoteNet** [32] constructs a 3D detection pipeline for point cloud as a end-to-end 3D object detection network, which is based on PointNet++. **SegMap** [33] is a map representation solution to the localization and mapping problem based on the extraction of segments in 3D point clouds. SqueezeSeg [34-36] are convolutional neural nets with recurrent CRF (Conditional random fields) for real-time road-object segmentation from 3d Lidar point cloud. **PointSIFT** [37] is a semantic segmentation framework for 3D point clouds. It is based on a simple module which extracts features from neighbor points in eight directions. **PointWise** [38] presents a convolutional neural network for semantic segmentation and object recognition with 3D point clouds. **3P-RNN** [39] is a novel end-to-end approach for unstructured point cloud semantic segmentation along two horizontal directions to exploit the inherent contextual features. Other similar work can be seen but not limited to **SPG** [40] and the review [29]. **SegMatch** [41] is a loop closure method based on the detection and matching of 3D segments. **Kd-Network** [42] is designed for 3D model recognition tasks and works with unstructured point clouds. **DeepTemporalSeg** [43] propose a deep convolutional neural network (DCNN) for the semantic segmentation of a LiDAR scan with temporally consistency. **LU-Net** [44] achieve the function of semantic segmentation instead of applying some global 3D segmentation method. Other similar work can be seen but not limited to **PointRCNN** [45].

Localization: **L3-Net** [46] is a novel learning-based LiDAR localization system that achieves centimeter-level localization accuracy. **SuMa++** [47] computes semantic segmentation results in point-wise labels for the whole scan, allowing us to build a semantically-enriched map with labeled surfels and improve the projective scan matching via semantic constraints.

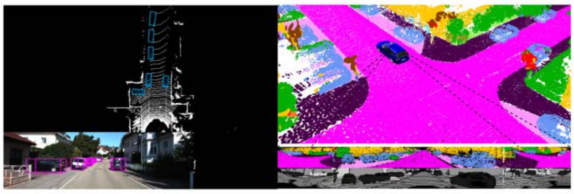

(a) MV3D (b) Suma++

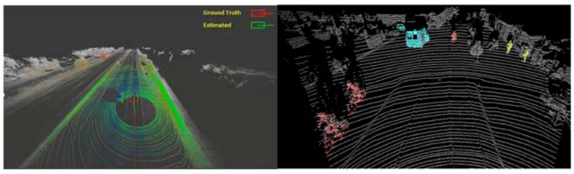

(c) L3-Net (d) LU-Net

Figure 2. Deep Learning in Lidar SLAM

2.3 Challenge and Future

2.3.1 Cost and Adaptability

The advantage of Lidar is that it can provide 3D information, and it is not affected by night and light change. In addition, the angle of view is relatively large and can reach 360 degrees. But the technological threshold of Lidar is very high, which lead to long development cycle and unaffordable cost on a large scale. In the future, miniaturization, reasonable cost, solid state, and achieving high reliability and adaptability is the trend.

2.3.2 Low-Texture and Dynamic Environment

Most SLAM system can just work in a fixed environment but things change constantly. Besides, low-Texture environment like long corridor and big pipeline will make trouble for Lidar SLAM. [48] uses IMU to assist 2D SLAM to solve above obstacles. Further, [49] incorporates the time dimension into the mapping process to enable a robot to maintain an accurate map while operating in dynamical environments. How to make Lidar SLAM more robust to low-texture and dynamic environment, and how to keep map updated should be taken into consideration more deeply.

2.3.3 Adversarial Sensor Attack

Deep Neural Network is easily attacked by adversarial samples, which is also proved in camera-based perception. But in Lidar-based perception, it is highly important but unexplored. By relaying attack, [50] firstly spoofs the Lidar with interference in output data and distance estimation. The novel saturation attack completely incapacitate a Lidar from sensing a certain direction based on Velodyne’s VLP-16. [51] explores the possibility of strategically controlling the spoofed attack to fool the machine learning model. The paper regards task as an optimization problem and design modeling methods for the input perturbation function and the objective function., which improves the attack success rates to around 75%. The adversarial sensor attack will spoof the SLAM system based on Lidar point cloud, which is invisible as hardly found and defended. In the case, research on how to prevent the Lidar SLAM system from adversarial sensor attack should be a new topic.

3. Visual SLAM

As the development of CPU and GPU, the capability of graphics processing becomes more and more powerful. Camera sensors getting cheaper, more lightweight and more versatile at the same time. The past decade has seen the rapid development of visual SLAM. Visual SLAM using camera also make the system cheaper and smaller compare with Lidar system. Now, visual SLAM system can run in micro PC and embedded device, even in mobile devices like smart phones [52-56].

Visual SLAM includes collection of sensors' data such as camera or inertial measurement unit , Visual Odometry or Visual Inertial Odometry in front end, Optimization in back end, Loop closure in back end and Mapping [57]. Relocalization is the additional modules for stable and accurate visual SLAM [58].

In process of Visual Odometry, in addition to the method based on features or template matching, or correlation methods to determine the motion of the camera, there is another method relying on the Fourier-Mellin Transform [59]. [60] and [61] give the example in the environment with no distinct visual features when use the ground-facing camera.

3.1 Visual Sensors

The most used sensors that visual SLAM based are cameras. In detail, camera can be divided into monocular camera, stereo camera, RGB-D camera, event camera, etc.

Monocular camera: visual slam based on monocular camera have a scale with real size of track and map. That's say that the real depth can't be got by monocular camera, which called Scale Ambiguity [62]. The SLAM based on Monocular camera has to initialization, and face the problem of drift.

Stereo camera: stereo camera is a combination of two monocular camera but the distance called baseline between the two monocular camera is known. Although the depth can be got based on calibration, correction, matching and calculation, the process will be a waste of lost of resources.

RGB-D camera: RGB-D camera also called depth camera because the camera can output depth in pixel directly. The depth camera can be realized by technology of stereo, structure-light and TOF. The theory of Structure-light is that infrared laser emits some pattern with structure feature to the surface of object. Then the IR camera will collect the change of patter due to the different depth in the surface. TOF will measure the time of laser's flight to calculate the distance.

Event camera: [63] illustrates that instead of capturing images at a fixed rate, event camera measures per-pixel brightness changes asynchronously. Event camera has very high dynamic range (140 dB vs. 60 dB), high temporal resolution (in the order of us), low power consumption, and do not suffer from motion blur. Hence, event cameras can performance better than traditional camera in high speed and high dynamic range. The example of the event camera are Dynamic Vision Sensor [64-67], Dynamic Line Sensor [68], Dynamic and Active-Pixel Vision Sensor [69], and Asynchronous Time-based Image Sensor [70].

Next the product and company of visual sensors will be introduced:

Microsoft: Kinectc v1(structured-light), Kinect v2(TOF), Azure Kinect(with microphone and IMU).

Intel: 200 Series, 300 Series, Module D400 Series, D415(Active IR Stereo, Rolling shutter), D435(Active IR Stereo, Global Shutter), D435i(D435 with IMU).

Stereolabs ZED: ZED Stereo camera(depth up to 20m).

MYNTAI: D1000 Series(depth camera), D1200(for smart phone), S1030 Series(standard stereo camera).

Occipital Structure: Structure Sensor(Suitable for ipad).

Samsung: Gen2 and Gen3 dynamic vision sensors and event-based vision solution [65].

Other depth camera can be listed as follows but not limited to **Leap Motion, Orbbec Astra, Pico Zense, DUO, Xtion, Camboard, IMI, Humanplus, PERCIPIO.XYZ, PrimeSense**. Other event camera can be listed as follows but not limited to **iniVation, AIT(AIT Austrian Institute of Technology), SiliconEye, Prophesee, CelePixel, Dilusense**.

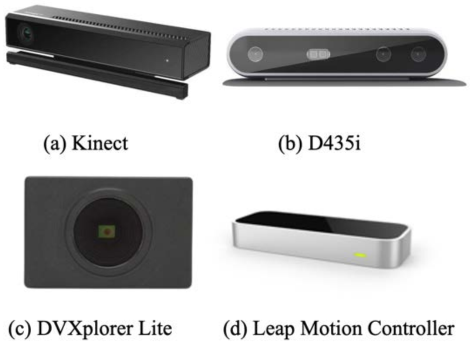

Figure 3. Visual Sensors

3.2 Visual SLAM System

The method of utilizing information from image can be classified into direct method and feature based method. Direct method leads to semiDense and dense construction while feature based method cause sparse construction. Next, some visual slam will be introduced (ATAM7 is a visual SLAM toolkit for beginners [58]):

Table 3 Comparison of the different Visual SLAM

Methods	Feature
Sparse Vslam	positioning, faster
Semi-Dense Vslam	Balance
Dense Vslam	Reconstruction, slow

3.2.1 Sparse Visual SLAM

MonoSLAM: it (monocular) is the first real-time mono SLAM system, which is based on EKF [71].

PTAM: it (monocular) is the first SLAM system that parallel tracking and mapping. It firstly adopts Bundle Adjustment to optimize and concept of key frame [54,72]. The later version supports a trivially simple yet effective relocalization method [73].

ORB-SLAM: it (monocular) uses three threads: Tracking, Local Mapping and Loop Closing [52,74]. **ORB-SLAM v2** [75] supports monocular, stereo, and RGB-D cameras. **CubemapSLAM** [76] is a SLAM system for monocular fisheye cameras based on ORB-SLAM. **Visual Inertial ORB-SLAM** [77,78] explains the initialization process of IMU and the joint optimization with visual information.

proSLAM: it (stereo) is a lightweight visual SLAM system with easily understanding [79].

ENFT-sfm: it (monocular) is a feature tracking method which can efficiently match feature point correspondences among one or multiple video sequences [80]. The updated version **ENFT-SLAM** can run in large scale.

OpenVSLAm: it (all types of cameras) [81] is based on an indirect SLAM algorithm with sparse features. The excellent point of OpenVSLAM is that the system supports perspective, fisheye, and equirectangular, even the camera models you design.

TagSLAM: it realizes SLAM with AprilTag fiducial markers [82]. Also, it provides a front end to the GTSAM factor graph optimizer, which can design lots of experiments.

Other similar work can be listed as follows but not limited to **UcoSLAM** [83].

3.2.2 SemiDense Visual SLAM

LSD-SLAM: it (monocular) proposes a novel direct tracking method which operates on Lie Algebra and direct method [84]. [85] make it supporting stereo cameras and [86] make it supporting omnidirectional cameras. Other similar work with omnidirectional cameras can be seen in [87].

SVO: it (monocular) is Semi-direct Visual Odoemtry [88]. It uses sparse model-based image alignment to get a fast speed. The update version is extended to multiple cameras, fisheye and catadioptric ones [78]. [78] gives detailed math proof about VIO. **CNN-SVO** [89] is the version of SVO with the depth prediction from a single-image depth prediction network.

DSO: it (monocular) [90,91] is a new work from the author of LSD-SLAM [84]. The work creates a visual odoemtry based on direct method and sparse method without detection and description of feature point.

EVO: it (Event camera) [92] is an event-based visual odometry algorithm. Our algorithm is unaffected by motion blur and operates very well in challenging, high dynamic range conditions with strong illumination changes. Other semiDense SLAM based on event camera can be seen in [93]. Other VO (visual odometry) system based on event camera can be seen in [94,95].

3.2.3 Dense Visual SLAM

DTAM: it (monocular) can reconstruct 3D model in real time based on minimizing a global spatially regularized energy functional in a novel non-convex optimization framework, which is called direct method [96,97].

MLM SLAM: it (monocular) can reconstruct dense 3D model online without graphics processing unit (GPU) [98]. The key contribution is a multi-resolution depth estimation and spatial smoothing process.

Kinect Fusion: it (RGB-D) is almost the first 3D reconstruction system with depth camera [99,100].

DVO: it (RGB-D) proposes a dense visual SLAM method, an entropy-based similarity measure for keyframe selection and loop closure detection based g2o framework [101-103].

RGBD-SLAM-V2: it (RGB-D) can reconstruct accurate 3D dense model without the help of other sensors [104].

Kintinuous: it (RGB-D) is a visual SLAM system with globally consistent point and mesh reconstructions in real-time [105-107].

RTAB-MAP: it (RGB-D) supports simultaneous localization and mapping but it's hard to be basis to develop upper algorithm [108-110]. The latter version support both visual and Lidar SLAM [111].

Dynamic Fusion: it (RGB-D) presents the first dense SLAM system capable of reconstructing non-rigidly deforming scenes in real-time based Kinect Fusion [112]. **VolumeDeform** [113] also realizes real-time non-rigid reconstruction but not open source. The similar work can be seen in **Fusion4D** [114].

Elastic Fusion: it (RGB-D) is a real-time dense visual SLAM system capable of capturing comprehensive dense globally consistent surfel-based maps of room scale environments explored using an RGB-D camera [115,116].

InfiniTAM: it (RGB-D) is a real time 3D reconstruction system with CPU in Linux, IOS, Android platform [55,117,118].

Bundle Fusion: it (RGB-D) supports robust tracking with recovery from gross tracking failures and re-estimates the 3D model in real-time to ensure global consistency [119].

KO-Fusion: it (RGB-D) [120] proposes a dense RGB-D SLAM system with kinematic and odometry measurements from a wheeled robot.

SOFT-SLAM: it (stereo) [121] can create dense map with the advantages of large loop closing, which is based on SOFT [122] for pose estimation.

Other works can be listed as follows but not limited to **SLAMRecon**, RKD-SLAM [123] and **RGB-D SLAM** [124]. **Maplab** [125], **PointNVSNet** [126], **MID-Fusion** [127] and **MaskFusion** [128] will introduced in next chapter.

3.2.4 Visual Inertial Odometry SLAM

The determination of visual slam is technically challenging. Monocular visual SLAM has problems such as necessary initialization, scale ambiguity and scale drift [129]. Although stereo camera and RGB-D camera can solve the problems of initialization and scale, some obstacles can't be ignored such as fast movement (solved with Global Shuttle or fisheye even panoramic camera), small field of view, large calculation, occlusion, feature loss, dynamic scenes and changing light. Recently, VIO (visual inertial odometry SLAM) becomes the popular research.

First of all, [130-132] start some try in VIO. [77,78] give the samples and math proof in visual-inertial odeometry. [133] use several rounds of visual-inertial bundle adjustment to make a robust initialization for VIO. Specially, tango [134], Dyson 360 Eye and hololens [135] are the real products of VIO and receive good feedback. In addition to this, ARkit (filter-based) from Apple, ARcore (filter-based) from Google, Inside-out from uSens are the technology of VIO. PennCOSYVIO [136] synchronizes data from a VI-sensor (stereo camera and IMU), two Project Tango hand-held devices, and three GoPro Hero 4 cameras and calibrates intrinsically and extrinsically. Next some open source VIO system will be introduced [137]:

SSF: it (loosely-coupled, filter-based) is a time delay compensated single and multi sensor fusion framework based on an EKF [138].

MSCKF: it (tightly-coupled, filter-based) is adopted by Google Tango based on extended Kalman filter [139]. But the similar work called **MSCKF-VIO** [140] open the source.

ROVIO: it (tightly-coupled, filter-based) is an extended Kalman Filter with tracking of both 3D landmarks and image patch features [141]. It supports monocular camera.

OKVIS: it (tightly-coupled, optimization-based) is an open and classic Keyframe-based Visual-Inertial SLAM [130]. It supports monocular and stereo camera based sliding window estimator.

VINS: **VINS-Mono** (tightly-coupled, optimization-based) [53,142,143] is a real-time SLAM framework for Monocular Visual-Inertial Systems. The open source code runs on Linux, and is fully integrated with ROS. **VINS-Mobile** [144,145] is a real-time monocular visual-inertial odometry running on compatible iOS devices. Furthermore, **VINS-Fusion** supports multiple visual-inertial sensor types (GPS, mono camera + IMU, stereo cameras + IMU, even stereo cameras only). It has online spatial calibration, online temporal calibration and visual loop closure.

ICE-BA: it (tightly-coupled, optimization-based) presents an incremental, consistent and efficient bundle adjustment for visual-inertial SLAM, which performs in parallel both local BA over the sliding window and global BA over all keyframes, and outputs camera pose and updated map points for each frame in real-time [146].

Maplab: it (tightly-coupled, optimization-based) is an open, research-oriented visual-inertial mapping framework, written in C++, for creating, processing and manipulating multi-session maps. On the one hand, maplab can be considered as a ready-to-use visual-inertial mapping and localization system. On the other hand, maplab provides the research community with a collection of multi-session mapping tools that include map merging, visual-inertial batch optimization, loop closure, 3D dense reconstruction [125].

Other solutions can be listed as follows but not limited to **VI-ORB** (tightly-coupled, optimization-based) [77] (the works by the author of ORB-SLAM, but not open source), StructVIO [147]. RKSLAM [148] can reliably handle fast motion and strong rotation for AR applications. Other VIO system based on event camera can be listed as follows but not limited to [149-151]. **mi-VINS** [152] uses multiple IMU, which can work if IMU sensor failures.

In VIO, visual images can enhance the inertial navigation algorithm. To deal with the correlation between the generated visual odometry and also about the multiframe visual odometry, [153] integrates the features tracked from all overlapping image frames by a sequential de-correlation the Kalman filter measurement update with fever computation resources consumption. The proposed method is referred as multi-frame visual odometry (MFVO) [154]. In the image-aided inertial integrated navigation, the relative positions of visual odometry are pairwise correlated in terms of time. The shaping filter proposed [155] uses Cholesky factors based on that the measurement noise is only correlated with the ones from the previous epoch.

VIO SLAM based on deep learning can be seen in [156]. It shows a network that performs visual-inertial odometry (VIO) without inertial measurement unit (IMU) intrinsic parameters or the extrinsic calibration between an IMU and camera. [157] provides a network to avoid the calibration between camera and IMU.

3.2.5 Deep Learning with Visual SLAM

Nowadays, deep learning plays a critical role in the maintenance of computer vision. As the development of visual SLAM, more and more focus are paid into deep learning with SLAM. The term "semantic SLAM" refers to an approach that includes the semantic information into the SLAM process to enhance the performance and representation by providing high-level understanding, robust performance, resource awareness, and task driven perception. Next, we will introduce the implement of SLAM with semantic information in these aspects:

Feature & Detection: Pop-up SLAM (Monocular) [158] proposes real-time monocular plane SLAM to demonstrate that scene understanding could improve both state estimation and dense mapping especially in low-texture environments. The plane measurements come from a pop-up 3D plane model applied to each single image. [159] gets semantic key points predicted by a convolutional network (convnet). **LIFT** [160] can get more dense feature points than SIFT. **DeepSLAM** [161] has a significant performance gap in the presence of image noise when catch the feature points. **SuperPoint** [162] presents a self-supervised framework for training interest point detectors and descriptors suitable for a large number of multiple-view geometry problems in computer vision. [163] proposes to use the easy-to-labeled 2D detection and discrete viewpoint classification together with a light-weight semantic inference method to obtain rough 3D object measurements. **GCN-SLAM** [164] presents a deep learning-based network, GCNv2, for generation of key points and descriptors. [165] fuses information about 3D shape, location, and, if available, semantic class. **SalientDSO** [166] can realize visual saliency and environment perception with the aid of deep learning. [167] integrates the detected objects as the quadrics models into the SLAM system. **CubeSLAM** (Monocular) is a 3D Object Detection and SLAM system [168] based on cube model. It achieve object-level mapping, positioning, and dynamic object tracking. [169] combines the cubeSLAM (high-level object) and Pop-up SLAM (plane landmarks) to make map more denser, more compact and semantic meaningful compared to feature point based SLAM. **MonoGRNet** [170] is a geometric reasoning network for monocular 3D object detection and localization. Feature based on event camera can be seen but not limited to [171,172]. About the survey in deep learning for detection, [173] could be a good choice.

Recognition & Segmentation: **SLAM++** (CAD model) [174] presents the major advantages of a new ‘object oriented’ 3D SLAM paradigm, which takes full advantage in the loop of prior knowledge that many scenes consist of repeated, domain-specific objects and structures. [175] combines the state-of-art deep learning method and LSD-SLAM based on video stream from a monocular camera. 2D semantic information are transferred to 3D mapping via correspondence between connective keyframes with spatial consistency. **Semanticfusion** (RGBD) [176] combines CNN (Convolutional Neural Network) and a state-of-the-art dense Simultaneous Localization and Mapping (SLAM) system, ElasticFusion [116] to build a semantic 3D map. [177] leverages sparse, feature-based RGB-D SLAM, image-based deep-learning object detection and 3D unsupervised segmentation. **MarrNet** [178] proposes an end-to-end trainable framework, sequentially estimating 2.5D sketches and 3D object shapes. **3DMV** (RGB-D) [179] jointly combines RGB color and geometric information to perform 3D semantic segmentation of RGB-D scans. **Pix3D** [180] study 3D shape modeling from a single image. **ScanComplete** [181] is a data-driven approach which takes an incomplete 3D scan of a scene as input and predicts a complete 3D model, along with per-voxel semantic labels. **Fusion++** [182] is an online object-level SLAM system which builds a persistent and accurate 3D graph map of arbitrary reconstructed objects. As an RGB-D camera browses a cluttered indoor scene, **Mask-RCNN** instance segmentations are used to initialise compact per-object Truncated Signed Distance Function (TSDF) reconstructions with object size dependent resolutions and a novel 3D foreground mask. **SegMap** [183] is a map representation based on 3D segments allowing for robot localization, environment reconstruction, and semantics extraction. **3D-SIS** [184] is a novel neural network architecture for 3D semantic instance segmentation in commodity RGB-D scans. **DA-RNN** [185] uses a new recurrent neural network architecture for semantic labeling on RGB-D videos. **DenseFusion** [186] is a generic framework for estimating 6D pose of a set of known objects from RGB-D images. Other work can be seen in CCNet [187]. To recognize based on event camera, [188-191] are the best paper to be investigated.

Recovery Scale: **CNN-SLAM** (Monocular) [192] estimates the depth with deep learning. Another work can be seen in **DeepVO** [193], **GS3D** [194] . **UnDeepVO** [195] can get the 6-DoF pose and the depth using a monocular camera with deep learning. Google proposes the work [196] that present a method for predicting dense depth in scenarios where both a monocular camera and people in the scene are freely moving based on unsupervised learning. Other methods to get real scale in Monocular can be seen in [197,198]. **GeoNet** [199] is a jointly unsupervised learning framework for monocular depth, optical flow and ego-motion estimation from videos. **CodeSLAM** [200] proposes a depth map from single image, which can be optimised efficiently jointly with pose variables. **Mono-stixels** [201] uses the depth, motion and semantic information in dynamic scene to estimate depth. **GANVO** [202] uses an unsupervised learning framework for 6-DoF pose and monocular depth map from unlabelled image, using deep convolutional Generative Adversarial Networks. **GEN-SLAM** [203] outputs the dense map with the aid of conventional geometric SLAM and the topological constraint in monocular. [204] proposes a training objective that is invariant to changes in depth range and scale. Other similar work can be seen in **DeepMVS** [205] and **DeepV2D** [206]. Based on event camera, depth estimation can be applied in monocular camera [207,208] and stereo camera [209].

Pose Output & Optimization: [210] is a stereo-VO under the synchronicity. [211] utilizes a CNN to estimate motion from optical flow. **PoseNet** [212] can get the 6-DOF pose from a single RGB image without the help of optimization. **VInet** (Monocular) [213] firstly estimates the motion in VIO, reducing the dependence of manual synchronization and calibration. **DeepVO** (Monocular) [214] presents a novel end-to-end framework for monocular VO by using deep Recurrent Convolutional Neural Networks (RCNNs). The similar work can be seen in **SFMlearner** [215] and **SFM-Net** [216]. **VSO** [217] proposes a novel visual semantic odometry (VSO) framework to enable medium-term continuous tracking of points using semantics. **MID-Fusion** (RGBD, dense point cloud) [127] estimates the pose of each existing moving object using an object-oriented tracking method and associate segmented masks with existing models and incrementally fuse corresponding color, depth, semantic, and foreground object probabilities into each object model. Other similar works can be seen in **VidLoc** [218]. Besides, [219,220] are using event camera to output the ego-motion.

Long-term Localization: [221] formulates an optimization problem over sensor states and semantic landmark positions that integrates metric information, semantic information, and data associations. [222] proposes a novel unsupervised deep neural network architecture of a feature embedding for visual loop closure. [223] shows the semantic information is more effective than the traditional feature descriptors. **X-View** [224] leverages semantic graph descriptor matching for global localization, enabling localization under drastically different view-points. [225] proposes a solution that represents hypotheses as multiple modes of an equivalent non-Gaussian sensor model to determine object class labels and measurement-landmark correspondences. About the application based on event camera, [226] are worthy to be read.

Dynamic SLAM: RDSLAM [227] is a novel real-time monocular SLAM system which can robustly work in dynamic environments based on a novel online keyframe representation and updating method. **DS-SLAM** [228] is a SLAM system with semantic information based on optimized ORB-SLAM. The semantic information can make SLAM system more robust in dynamic environment. **MaskFusion** (RGB-D, dense point cloud) is a real-time, object-aware, semantic and dynamic RGB-D SLAM system [128] based on Mask R-CNN [229]. The system can label the objects with semantic information even in continuously and independent motion. The related work can be seen in **Co-Fusion** [230]. **Detect-SLAM** [231] integrates SLAM with a deep neural network based object detector to make the two functions mutually beneficial in an unknown and dynamic environment. **DynaSLAM** [232] is a SLAM system for monocular, stereo and RGB-D camera in dynamic environments with aid of static map. **StaticFusion** [233] proposes a method for robust dense RGB-D SLAM in dynamic environments which detects moving objects and simultaneously reconstructs the background structure. The related work based on dynamic environment can be also seen in **RGB-D SLAM** [124] and [234-236].

Recently, some works utilizes deep-learning to dominate the whole process of SLAM. **SimVODIS** [237] can output the depth and the relative pose between frames, while detecting objects and segmenting the object boundaries.

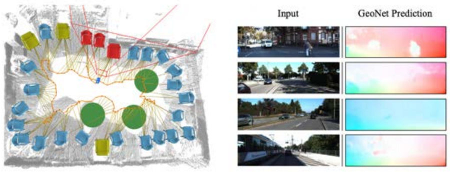

(a) SLAM++ (b) GeoNet

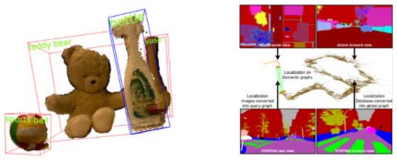

(c) MaskFusion (d) X-View

Figure 4. Deep Learning in Visual SLAM

3.3 Challenge and Future

3.3.1 Robustness and Portability

Visual SLAM still face some important obstacles like the illumination condition, high dynamic environment, fast motion, vigorous rotation and low texture environment. Firstly, global shutter instead of rolling shutter is fundamental to achieve accurate camera pose estimation. Event camera such as dynamic vision sensors is capable of producing up to one million events per second which is enough for very fast motions in high speed and high dynamic range. Secondly, using semantic features like edge, plane, surface features, even reducing feature dependencies, such as tracking with join edges, direct tracking, or a combination of machine learning may become the better choice. Thirdly, based mathematical machinery for SfM/SLAM, the precise mathematical formulations to outperform implicitly learned navigation functions over data is preferred.

The future of SLAM has can be expected that one is SLAM based on smart phones or embedded platforms such as UAV (unmanned aerial vehicle) and another is detailed 3D reconstruction, scene understanding with deep learning. How to balance real-time and accuracy is the vital open question. The solutions pertaining to dynamic, unstructured, complex, uncertain and large-scale environments are yet to be explored [238].

3.3.2 Multiple Sensors Fusion

The actual robots and hardware devices usually do not carry only one kind of sensor, and often a fusion of multiple sensors. For example, the current research on VIO on mobile phones combines visual information and IMU information to realize the complementary advantages of the two sensors, which provides a very effective solution for the miniaturization and low cost of SLAM. **DeLS-3D** [239] design is a sensor fusion scheme which integrates camera videos, motion sensors (GPS/IMU), and a 3D semantic map in order to achieve robustness and efficiency of the system. There are sensors listed as follows but not limited to Lidar, Sonar, IMU, IR, camera, GPS, radar, etc. The choice of sensors is dependent on the environment and required type of map.

3.3.3 Semantics SLAM

In fact, humans recognize the movement of objects based on perception not the features in image. Deep learning in SLAM can realize object recognition and segmentation, which help the SLAM system perceive the surrounding better. Semantics SLAM can also do a favor in global optimization, loop closure and relocalization. [240]: Traditional approaches for simultaneous localization and mapping (SLAM) depend on geometric features such as points, lines (**PL-SLAM** [241], **StructSLAM** [242]), and planes to infer the environment structure. The aim of high-precision real-time positioning in large-scale scenarios could be achieved by semantics SLAM, which teaches robots perceive as humans.

3.3.4 Software & hardware

SLAM is not an algorithm but an integrated, complex technology [243]. It not only depend on software, but also hardware. The future SLAM system will focus in the deep combination of algorithm and sensors. Based on illustration above, the domain specific processors rather than general processor, integrated sensors module rather than separate sensor like just camera will show great potential. The above work make the developer focus on the algorithm and accelerate the release of real products.

4. Lidar and Visual SLAM System

4.1 Multiple Sensors Calibration

Camera & IMU: **Kalibr** [244] is a toolbox that solves the following calibration problems: Multiple camera calibration, Visual-inertial calibration (camera-IMU) and Rolling Shutter Camera calibration. **Vins-Fusion** [143] has online spatial calibration and online temporal calibration. **MSCKF-VIO** [140] also has the calibration for camera and IMU. **mc-VINS** [245] can calibrate the extrinsic parameters and time offset between all multiple cameras and IMU. Besides, **IMU-TK** [246][247] can calibrate internal parameter of IMU. Other work can be seen in [248]. [249] proposes a end to end network for monocular VIO, which fuses data from camera and IMU.

Camera & Depth: **BAD SLAM** [250] proposes a calibrated benchmark for this task that uses synchronized global shutter RGB and depth cameras.

Camera & Camera: **mcptam** [251] is a SLAM system using multi-camera. It can also calibrate the intrinsic and extrinsic parameters. **MultiCol-SLAM** [252] is a multi-fisheye camera SLAM. Besides, the updated version of SVO can also support multiple cameras. Other similar work can be seen in **ROVIO** [253].

Lidar & IMU: **LIO-mapping** [254] introduces a tightly coupled lidar-IMU fusion method. **Lidar-Align** is a simple method for finding the extrinsic calibration between a 3D Lidar and a 6-Dof pose sensor. Extrinsic calibration of Lidar can be seen in [255][256]. The doctoral thesis [257] illustrate the work of Lidar calibration.

Camera & Lidar: [258] introduces a probabilistic monitoring algorithm and a continuous calibration optimizer that enable camera-laser calibration online, automatically. **Lidar-Camera** [259] proposes a novel pipeline and experimental setup to find accurate rigid-body transformation for extrinsically calibrating a LiDAR and a camera using 3D-3D point correspondences. **RegNet** [260] is the first deep convolutional neural network (CNN) to infer a 6 degrees of freedom (DOF) extrinsic calibration between multi-modal sensors, exemplified using a scanning LiDAR and a monocular camera. **LIMO** [261] proposes a depth extraction algorithm from LIDAR measurements for camera feature tracks and estimating motion. **CalibNet** [262] is a self-supervised deep network capable of automatically estimating the 6-DoF rigid body transformation between a 3D LiDAR and a 2D camera in real-time. The calibration tool from **Autoware** can calibrate the signal beam Lidar and camera. . Other work can be seen as follows but not limited to [263-265].

Other work like **SVIn2** [266] demonstrates an underwater SLAM system fusing Sonar, Visual, Inertial, and Depth Sensor, which is based on OKVIS. [267] proposes a new underwater camera-IMU calibration model and [268] detects underwater obstacle using semantic image Segmentation. **WiFi-SLAM** [269] demonstrates a novel SLAM technology with wireless signal named WiFi. [270] uses the mmWave to locate even the NLOS robots and [271,272] introduce more technique about localization with the aid of wirless signals. **KO-Fusion** [120] fuses visual and wheeled odometer. [273] uses a thermal camera with IMU in visually degraded environments e.g. darkness.

4.2 Lidar and Visual Fusion

Hardware layer: **Pandora** from HESAI is a software and hardware solution integrating 40 beams Lidar, five color cameras and recognition algorithm. The integrated solution can comfort developer from temporal and spatial synchronization. Understanding the exist of **CONTOUR** and **STENCIL** from **KAARTA** will give you a brainstorming.

Data layer: Lidar has sparse, high precision depth data and camera has dense but low precision depth data, which will lead to image-based depth upsampling and image-based depth inpainting/completion. [274] presents a novel method for the challenging problem of depth image upsampling. [275] relies only on basic image processing operations to perform depth completion of sparse Lidar depth data. With deep learning, [276] proposes the use of a single deep regression network to learn directly from the RGB-D raw data, and explore the impact of number of depth samples. [277] considers CNN operating on sparse inputs with an application to depth completion from sparse laser scan data. **DFuseNet** [278] proposes a CNN that is designed to upsample a series of sparse range measurements based on the contextual cues gleaned from a high resolution intensity image. Other similar work can be seen as follows but not limited to [279][280]. **LIC-Fusion** [281] fuses IMU measurements, sparse visual features, and extracted LiDAR points.

Task layer: [282] fuses stereo camera and Lidar to perceive. [283] fuses radar, Lidar, and camera to detect and classify moving objects. Other traditional work can be seen but not limited to [284-286]. [287] can augment VO by depth information such as provided by RGB-D cameras, or from Lidars associated with cameras even if sparsely available. **V-Loam** [288] presents a general framework for combining visual odometry and Lidar odometry. The online method starts with visual odometry and scan matching based Lidar odometry refines the motion estimation and point cloud registration simultaneously. **VL-SLAM** [289] is concerned with the development of a system that combines an accurate laser odometry estimator, with algorithms for place recognition using vision for achieving loop detection. [290] aims at the tracking part of SLAM using an RGB-D camera and 2d low-cost LIDAR to finish a robust indoor SLAM by a mode switch and data fusion. **VIL-SLAM** [291] incorporates tightly-coupled stereo VIO with Lidar mapping and Lidar enhanced visual loop closure. [292] combines monocular camera images with laser distance measurements to allow visual SLAM without errors from increasing scale uncertainty. In deep learning, many methods to detect and recognize fusing data from camera and Lidar such as **PointFusion** [293], **RoarNet** [294], **AVOD** [295], **MV3D** [26], **FuseNet** [296]. Other similar work can be seen in [297]. Besides, [298] exploits both Lidar as well as cameras to perform very accurate localization with a an end-to-end learnable architecture. [299] fuses 3D Lidar and monocular camera.

4.3 Challenge and Future[300]

Data Association: the future of SLAM must integrate multi-sensors. But different sensors have different data types, time stamps, and coordinate system expressions, needed to be processed uniformly. Besides, physical model establishment, state estimation and optimization between multi-sensors should be taken into consideration.

Integrated Hardware: at present, there is no suitable chip and integrated hardware to make technology of SLAM more easily to be a product. On the other hand, if the accuracy of a sensor degrades due to malfunctioning, off-nominal conditions, or aging, the quality of the sensor measurements (e.g., noise, bias) does not match the noise model. The robustness and integration of hardware should be followed. Sensors in front-end should have the capability to process data and the evolution from hardware layer to algorithm layer, then to function layer to SDK should be innovated to application.

Crowdsourcing: decentralized visual SLAM is a powerful tool for multi-robot applications in environments where absolute positioning systems are not available [301]. Co-optimization visual multi-robot SLAM need decentralized data and optimization, which is called crowdsourcing. The privacy in the process of decentralized data should come into attention. The technology of differential privacy [302][303] maybe do a favor.

High Definition Map: High Definition Map is vital for robots. But which type of map is the best for robots? Could dense map or sparse map navigate, positioning and path plan? A related open question for long-term mapping is how often to update the information contained in the map and how to decide when this information becomes outdated and can be discarded.

Adaptability, Robustness, Scalability: as we know, no SLAM system now can cover all scenarios. Most of it requires extensive parameter tuning in order to work correctly for a given scenario. To make robots perceive as humans, appearance-based instead of feature-based method is preferred, which will help close loops integrated with semantic information between day and night sequences or between different seasons.

Ability against risk and constraints: Perfect SLAM system should be failure-safe and failure-aware. It's not the question about relocalization or loop closure here. SLAM system must have ability to response to risk or failure. In the same time, an ideal SLAM solution should be able run on different platforms no matter the computational constraints of platforms. How to balance the accuracy, robustness and the limited resource is a challenging problem [137].

Application: the technology of SLAM has a wide application such as: large-scale positioning, navigation and 3D or semantic map construction, environment recognition and understanding, ground robotics, UAV, VR/AR/MR, AGV(Automatic Guided Vehicle), automatic drive, virtual interior decorator, virtual fitting room, immersive online game, earthquake relief, video segmentation and editing.

Open question: Will end-to-end learning dominate SLAM?

5. An Envision in 6G Wireless

Nowadays, 5G has been developed widely to communicate more quickly and massively [272]. But for robots and autonomous driving cars, the technology of SLAM need greater data rates and less latency that 5G can't afford. Unlike 100 Gbps of data rates for 5G, 6G can provide greater data rates due to the frequency in 100 GHz to 3 THz (terahertz).

THz is the last unexplored band in the radio frequency spectrum. Less than the THz, the radio bands are called microwave. The radio frequency of optical bands , which are regarded as visible light communications (VLC), are more than THz [304]. The 6G technology will need no supports such as multiple-input multiple-output (MIMO) in 5G represented as mmWave communications. As for the difference with VLC, 6G with the THz communications will not affected by the light changes and NLOS.

5.1 Lidar and Visual Fusion

For the advance of wireless communication system, industry and academic are urged to pay attention to the research of 6G. Next, we will introduce some advantages of 6G [305].

Low Latency: Less than 1 msec end-to-end latency;

Data rate: High data rates up to 1 Tbps;

Ultra-high bandwidth: Very broad frequency bands;

Energy save: Very high energy efficiency;

Ubiquitous connection: Enable to connect global network including the massive intelligent things and the emergence of smart surface and environment such as walls, roads even the whole buildings.

Intelligent network: AI and RISs make it smarter and beyond classical big data analytics and edge computation.

Ubiquitous connection: Enable to connect everything.

6G is supposed as the platforms to serve for communication, computation, and storage resources with the aid of AI [306].

5.2 6G in Simultaneous Localization and Mapping

SLAM can be divided into radio-based (such as satellite positioning, cellular and WiFi) and sensor-based (such as Lidar, IMU and camera) [307]. With the wireless technology, the technology of SLAM can be achieved by constructing the map of environment and projecting the angle and the time of arrival to estimate the locations from the users. The conventional mmWave method utilizing AoA-based positioning or a combination of path loss and AoA, and RSSI [271]. With the aid of Reconfigurable intelligent surfaces (RISs), localization and mapping can improve accuracy and extended physical coverage.

It's apparent that 6G with THz will create centimeter level accuracy even in NLOS environment and 6G will provide a network to sense and localization rather than a independent source [308] for SLAM. Cause the greater data rates, the massive computations can be conducted in remote device or machine, which relief the pressure of computer power in robots and autonomous driving cars.

In the future, THz will enable the robots and autonomous driving cars with new capability of sensing the gas, air quality, health detection, body scanning and so on. Plus, with the aid of THz, computer vision will be augmented to see the NLOS views, which will play a vital role in rescue and sensing. In the basic, the accuracy of positioning will be improved to sub-centimeter level and the map of surrounding environment will be constructed as 3D maps without any calibration and prior knowledge, which is hard to realized before. Moreover, 6G and AI will achieve excellent successes again in future digital society with the full connectivity demands.

References

[1] John J Leonard and Hugh F Durrant-Whyte. Simultaneous map build- ing and localization for an autonomous mobile robot. In Proceedings IROS'91: IEEE/RSJ International Workshop on Intelligent Robots and Systems' 91, pages 1442–1447. Ieee, 1991.

[2] Randall Smith, Matthew Self, and Peter Cheeseman. Estimating un- certain spatial relationships in robotics. In Autonomous robot vehicles, pages 167–193. Springer, 1990.

[3] Baichuan Huang, Jingbin Liu, Wei Sun, and Fan Yang. A robust indoor positioning method based on bluetooth low energy with separate channel information. Sensors, 19(16):3487, 2019.

[4] Jingbin Liu, Ruizhi Chen, Yuwei Chen, Ling Pei, and Liang Chen. iparking: An intelligent indoor location-based smartphone parking service. Sensors, 12(11):14612–14629, 2012.

[5] Jingbin Liu, Ruizhi Chen, Ling Pei, Robert Guinness, and Heidi Kuusniemi. A hybrid smartphone indoor positioning solution for mobile lbs. Sensors, 12(12):17208–17233, 2012.

[6] Sebastian Thrun, Wolfram Burgard, and Dieter Fox. Probabilistic robotics. MIT press, 2005.

[7] Joao Machado Santos, David Portugal, and Rui P Rocha. An evalu- ation of 2d slam techniques available in robot operating system. In 2013 IEEE International Symposium on Safety, Security, and Rescue Robotics (SSRR), pages 1–6. IEEE, 2013.

[8] Giorgio Grisetti, Cyrill Stachniss, Wolfram Burgard, et al. Improved techniques for grid mapping with rao-blackwellized particle filters. IEEE transactions on Robotics, 23(1):34, 2007.

[9] Michael Montemerlo, Sebastian Thrun, Daphne Koller, Ben Wegbreit, et al. Fastslam: A factored solution to the simultaneous localization and mapping problem. *Aaai/iaai*, 593598, 2002.

[10] Michael Montemerlo, Sebastian Thrun, Daphne Koller, Ben Wegbreit, et al. Fastslam 2.0: An improved particle filtering algorithm for simultaneous localization and mapping that provably converges. In *IJCAI*, pages 1151–1156, 2003.

[11] Stefan Kohlbrecher, Oskar Von Stryk, Johannes Meyer, and Uwe Klingauf. A flexible and scalable slam system with full 3d motion estimation. In *2011 IEEE International Symposium on Safety, Security, and Rescue Robotics*, pages 155–160. IEEE, 2011.

[12] Kurt Konolige, Giorgio Grisetti, Rainer Kümmerle, Wolfram Burgard, Benson Limketkai, and Regis Vincent. Efficient sparse pose adjustment for 2d mapping. In *2010 IEEE/RSJ International Conference on Intelligent Robots and Systems*, pages 22–29. IEEE, 2010.

[13] Luca Carlone, Rosario Aragues, José A Castellanos, and Basilio Bona. A linear approximation for graph-based simultaneous localization and mapping. *Robotics: Science and Systems VII*, pages 41–48, 2012.

[14]BSteuxandOTinySLAMElHamzaoui.Aslamalgorith minlessthan 200 lines c-language program. *Proceedings of the Control Automation Robotics & Vision (ICARCV), Singapore*, pages 7–10, 2010.

[15] Wolfgang Hess, Damon Kohler, Holger Rapp, and Daniel Andor. Real- time loop closure in 2d lidar slam. In *2016 IEEE International Conference on Robotics and Automation (ICRA)*, pages 1271–1278. IEEE, 2016.

[16] Ji Zhang and Sanjiv Singh. Loam: Lidar odometry and mapping in real-time. In *Robotics: Science and Systems*, volume 2, page 9, 2014.

[17] Tixiao Shan and Brendan Englot. Lego-loam: Lightweight and ground- optimized lidar odometry and mapping on variable terrain. In *2018 IEEE/RSJ International Conference on Intelligent Robots and Systems (IROS)*, pages 4758–4765. IEEE, 2018.

[18] Jean-Emmanuel Deschaud. Imls-slam: scan-to-model matching based on 3d data. In *2018 IEEE International Conference on Robotics and Automation (ICRA)*, pages 2480–2485. IEEE, 2018.

[19] Mikaela Angelina Uy and Gim Hee Lee. Pointnetvlad: Deep point cloud based retrieval for large-scale place recognition. In *Proceedings of the IEEE Conference on Computer Vision and Pattern Recognition*, pages 4470–4479, 2018.

[20] Yin Zhou and Oncel Tuzel. Voxelnet: End-to-end learning for point cloud based 3d object detection. In *Proceedings of the IEEE Confer- ence on Computer Vision and Pattern Recognition*, pages 4490–4499, 2018.

[21] Jorge Beltrán, Carlos Guindel, Francisco Miguel Moreno, Daniel Cruzado, Fernando Garcia, and Arturo De La Escalera. Birdnet: a 3d object detection framework from lidar information. In *2018 21st International Conference on Intelligent Transportation Systems (ITSC)*, pages 3517–3523. IEEE, 2018.

[22]KazukiMinemura,HengfuiLiau,AbrahamMonrroy,andShinpeiKato. Lmnet: Real-time multiclass object detection on cpu using 3d lidar. In *2018 3rd Asia-Pacific Conference on Intelligent Robot Systems (ACIRS)*, pages 28–34. IEEE, 2018.

[23] Bin Yang, Wenjie Luo, and Raquel Urtasun. Pixor: Real-time 3d object detection from point clouds. In *Proceedings of the IEEE conference on Computer Vision and Pattern Recognition*, pages 7652–7660, 2018.

[24] Waleed Ali, Sherif Abdelkarim, Mahmoud Zidan, Mohamed Zahran, and Ahmad El Sallab. Yolo3d: End-to-end real-time 3d oriented object bounding box detection from lidar point cloud. In *Proceedings of the European Conference on Computer Vision (ECCV)*, pages 0–0, 2018.

[25]YangyanLi,RuiBu,MingchaoSun,WeiWu,XinhanDi,andBaoquan Chen. Pointcnn: Convolution on x-transformed points. In *Advances in Neural Information Processing Systems*, pages 820–830, 2018.

[26] Xiaozhi Chen, Huimin Ma, Ji Wan, Bo Li, and Tian Xia. Multi-view 3d object detection network for autonomous driving. In *Proceedings of the IEEE Conference on Computer Vision and Pattern Recognition*, pages 1907–1915, 2017.

[27] Ruihui Li, Xianzhi Li, Chi-Wing Fu, Daniel Cohen-Or, and Pheng- Ann Heng. Pu-gan: A point cloud upsampling adversarial network. In *Proceedings of the IEEE International Conference on Computer Vision*, pages 7203–7212, 2019.

[28] Hang Su, Varun Jampani, Deqing Sun, Subhransu Maji, Evangelos Kalogerakis, Ming-Hsuan Yang, and Jan Kautz. Splatnet: Sparse lattice networks for point cloud processing. In *Proceedings of the IEEE Conference on Computer Vision and Pattern Recognition*, pages 2530– 2539, 2018.

[29] E Grilli, F Menna, and F Remondino. A review of point clouds segmentation and classification algorithms. The International Archives of Photogrammetry, Remote Sensing and Spatial Information Sciences, 42:339, 2017.

[30] Charles R Qi, Hao Su, Kaichun Mo, and Leonidas J Guibas. Pointnet: Deep learning on point sets for 3d classification and segmentation. *arXiv preprint arXiv:1612.00593*, 2016.

[31] Charles R Qi, Li Yi, Hao Su, and Leonidas J Guibas. Pointnet++: Deep hierarchical feature learning on point sets in a metric space. *arXiv preprint arXiv:1706.02413*, 2017.

[32] Charles R Qi, Or Litany, Kaiming He, and Leonidas J Guibas. Deep hough voting for 3d object detection in point clouds. *arXiv preprint arXiv:1904.09664*, 2019.

[33] Renaud Dube, Andrei Cramariuc, Daniel Dugas, Juan Nieto, Roland Siegwart, and Cesar Cadena. SegMap: 3d segment mapping using data-driven descriptors. In *Robotics: Science and Systems (RSS)*, 2018.

[34] Bichen Wu, Alvin Wan, Xiangyu Yue, and Kurt Keutzer. Squeezeseg: Convolutional neural nets with recurrent crf for real-time road-object segmentation from 3d lidar point cloud. *ICRA*, 2018.

[35] Bichen Wu, Xuanyu Zhou, Sicheng Zhao, Xiangyu Yue, and Kurt Keutzer. Squeezesegv2: Improved model structure and unsupervised domain adaptation for road-object segmentation from a lidar point cloud. In *ICRA*, 2019.

[36] XiangyuYue,BichenWu,SanjitASeshia,KurtKeutzer,andAlbertoL Sangiovanni-Vincentelli. A lidar point

cloud generator: from a virtual world to autonomous driving. In *ICMR*, pages 458–464. ACM, 2018.

[37] Mingyang Jiang, Yiran Wu, Tianqi Zhao, Zelin Zhao, and Cewu Lu. Pointsift: A sift-like network module for 3d point cloud semantic segmentation. *arXiv preprint arXiv:1807.00652*, 2018.

[38] Binh-Son Hua, Minh-Khoi Tran, and Sai-Kit Yeung. Pointwise convo- lutional neural networks. In *Computer Vision and Pattern Recognition (CVPR)*, 2018.

[39] Xiaoqing Ye, Jiamao Li, Hexiao Huang, Liang Du, and Xiaolin Zhang. 3d recurrent neural networks with context fusion for point cloud semantic segmentation. In *Proceedings of the European Conference on Computer Vision (ECCV)*, pages 403–417, 2018.

[40] Loic Landrieu and Martin Simonovsky. Large-scale point cloud semantic segmentation with superpoint graphs. In *Proceedings of the IEEE Conference on Computer Vision and Pattern Recognition*, pages 4558–4567, 2018.

[41] Renaud Dube ́, Daniel Dugas, Elena Stumm, Juan Nieto, Roland Sieg- wart, and Cesar Cadena. Segmatch: Segment based place recognition in 3d point clouds. In *2017 IEEE International Conference on Robotics and Automation (ICRA)*, pages 5266–5272. IEEE, 2017.

[42] Roman Klokov and Victor Lempitsky. Escape from cells: Deep kd- networks for the recognition of 3d point cloud models. In *Proceedings of the IEEE International Conference on Computer Vision*, pages 863– 872, 2017.

[43] Ayush Dewan and Wolfram Burgard. Deeptemporalseg: Temporally consistent semantic segmentation of 3d lidar scans. *arXiv preprint arXiv:1906.06962*, 2019.

[44] Pierre Biasutti, Vincent Lepetit, Jean-Franois Aujol, Mathieu Brdif, and Aurlie Bugeau. Lu-net: An efficient network for 3d lidar point cloud semantic segmentation based on end-to-end-learned 3d features and u-net. 08 2019.

[45] Shaoshuai Shi, Xiaogang Wang, and Hongsheng Li. Pointrcnn: 3d ob- ject proposal generation and detection from point cloud. In *Proceedings of the IEEE Conference on Computer Vision and Pattern Recognition*, pages 770–779, 2019.

[46] Lu Weixin, Zhou Yao, Wan Guowei, Hou Shenhua, and Song Shiyu. L3-net: Towards learning based lidar localization for autonomous driv- ing. In *IEEE Conference on Computer Vision and Pattern Recognition (CVPR)*, 2019.

[47] Chen Xieyuanli, Milioto Andres, and Emanuelea Palazzolo. Suma++: Efficient lidar-based semantic slam. In *2019 IEEE/RSJ International Conference on Intelligent Robots and Systems (IROS)*. IEEE, 2019.

[48] Zhongli Wang, Yan Chen, Yue Mei, Kuo Yang, and Baigen Cai. Imu- assisted 2d slam method for low-texture and dynamic environments. *Applied Sciences*, 8(12):2534, 2018.

[49] Aisha Walcott-Bryant, Michael Kaess, Hordur Johannsson, and John J Leonard. Dynamic pose graph slam: Long-term mapping in low dynamic environments. In *2012 IEEE/RSJ International Conference on Intelligent Robots and Systems*, pages 1871–1878. IEEE, 2012.

[50] Hocheol Shin, Dohyun Kim, Yujin Kwon, and Yongdae Kim. Illusion and dazzle: Adversarial optical channel exploits against lidars for automotive applications. In *International Conference on Cryptographic Hardware and Embedded Systems*, pages 445–467. Springer, 2017.

[51] Yulong Cao, Chaowei Xiao, Benjamin Cyr, Yimeng Zhou, Won Park, Sara Rampazzi, Qi Alfred Chen, Kevin Fu, and Z Morley Mao. Adversarial sensor attack on lidar-based perception in autonomous driving. *arXiv preprint arXiv:1907.06826*, 2019.

[52] Raul Mur-Artal, Jose Maria Martinez Montiel, and Juan D Tardos. Orb-slam: a versatile and accurate monocular slam system. *IEEE transactions on robotics*, 31(5):1147–1163, 2015.

[53] Tong Qin, Peiliang Li, and Shaojie Shen. Vins-mono: A robust and versatile monocular visual-inertial state estimator. *IEEE Transactions on Robotics*, 34(4):1004–1020, 2018.

[54] Georg Klein and David Murray. Parallel tracking and mapping on a camera phone. In *2009 8th IEEE International Symposium on Mixed and Augmented Reality*, pages 83–86. IEEE, 2009.

[55] O. Ka ̈hler, V. A. Prisacariu, C. Y. Ren, X. Sun, P. H. S Torr, and D. W. Murray. Very High Frame Rate Volumetric Integration of Depth Images on Mobile

Device. *IEEE Transactions on Visualization and Computer Graphics (Proceedings International Symposium on Mixed and Augmented Reality 2015*, 22(11), 2015.

[56] Simon Lynen, Torsten Sattler, Michael Bosse, Joel A Hesch, Marc Pollefeys, and Roland Siegwart. Get out of my lab: Large-scale, real- time visual-inertial localization. In *Robotics: Science and Systems*, volume 1, 2015.

[57] Xiang Gao, Tao Zhang, Yi Liu, and Qinrui Yan. *14 Lectures on Visual SLAM: From Theory to Practice*. Publishing House of Electronics Industry, 2017.

[58] Takafumi Taketomi, Hideaki Uchiyama, and Sei Ikeda. Visual slam algorithms: A survey from 2010 to 2016. *IPSJ Transactions on Computer Vision and Applications*, 9(1):16, 2017.

[59] B Srinivasa Reddy and Biswanath N Chatterji. An fft-based technique for translation, rotation, and scale-invariant image registration. *IEEE transactions on image processing*, 5(8):1266–1271, 1996.

[60] Tim Kazik and Ali Haydar Göktoğan. Visual odometry based on the fourier-mellin transform for a rover using a monocular ground-facing camera. In *2011 IEEE International Conference on Mechatronics*, pages 469–474. IEEE, 2011.

[61] Merwan Birem, Richard Kleihorst, and Norddin El-Ghouti. Visual odometry based on the fourier transform using a monocular ground- facing camera. *Journal of Real-Time Image Processing*, 14(3):637–646, 2018.

[62] Liu Haomin, Zhang Guofeng, and Bao hujun. A survy of monocular simultaneous localization and mapping. *Journal of Computer-Aided Design & Computer Graphics*, 28(6):855–868, 2016.

[63]GuillermoGallego,TobiDelbruck,GarrickOrchard,ChiaraBartolozzi, and Davide Scaramuzza. Event-based vision: A survey. 2019.

[64] Patrick Lichtsteiner, Christoph Posch, and Tobi Delbruck. A 128x128 120db 15us latency asynchronous temporal contrast vision sensor. *IEEE journal of solid-state circuits*, 43(2):566–576, 2008.

[65] Bongki Son, Yunjae Suh, Sungho Kim, Heejae Jung, Jun-Seok Kim, Changwoo Shin, Keunju Park, Kyoobin Lee, Jinman Park, Jooyeon Woo, et al. 4.1 a 640× 480 dynamic vision sensor with a 9µm pixel and 300meps address-event representation. In *2017 IEEE International Solid-State Circuits Conference (ISSCC)*, pages 66–67. IEEE, 2017.

[66] Christoph Posch, Daniel Matolin, Rainer Wohlgenannt, Thomas Maier, and Martin Litzenberger. A microbolometer asynchronous dynamic vision sensor for lwir. *IEEE Sensors Journal*, 9(6):654–664, 2009.

[67] Michael Hofstatter, Peter Schön, and Christoph Posch. A sparc- compatible general purpose address-event processor with 20-bit l0ns- resolution asynchronous sensor data interface in 0.18 µm cmos. In *Proceedings of 2010 IEEE International Symposium on Circuits and Systems*, pages 4229–4232. IEEE, 2010.

[68] Christoph Posch, Michael Hofstatter, Daniel Matolin, Guy Vanstraelen, Peter Schon, Nikolaus Donath, and Martin Litzenberger. A dual-line optical transient sensor with on-chip precision time-stamp generation. In *2007 IEEE International Solid-State Circuits Conference. Digest of Technical Papers*, pages 500–618. IEEE, 2007.

[69] Christian Brandli, Raphael Berner, Minhao Yang, Shih-Chii Liu, and Tobi Delbruck. A 240× 180 130 db 3 µs latency global shutter spatiotemporal vision sensor. *IEEE Journal of Solid-State Circuits*, 49(10):2333–2341, 2014.

[70] Christoph Posch, Daniel Matolin, and Rainer Wohlgenannt. A qvga 143 db dynamic range frame-free pwm image sensor with lossless pixel-level video compression and time-domain cds. *IEEE Journal of Solid-State Circuits*, 46(1):259–275, 2010.

[71] Andrew J Davison, Ian D Reid, Nicholas D Molton, and Olivier Stasse. Monoslam: Real-time single camera slam. *IEEE Transactions on Pattern Analysis & Machine Intelligence*, (6):1052–1067, 2007.

[72] Georg Klein and David Murray. Parallel tracking and mapping for small ar workspaces. In *Proceedings of the 2007 6th IEEE and ACM International Symposium on Mixed and Augmented Reality*, pages 1– 10. IEEE Computer Society, 2007.

[73] Georg Klein and David Murray. Improving the agility of keyframe- based slam. In *European Conference on Computer Vision*, pages 802– 815. Springer, 2008.

[74] Ethan Rublee, Vincent Rabaud, Kurt Konolige, and Gary R Bradski. Orb: An efficient alternative to sift or surf. In *ICCV*, volume 11, page 2. Citeseer, 2011.

[75] Raul Mur-Artal and Juan D Tardo´s. Orb-slam2: An open-source slam system for monocular, stereo, and rgb-d cameras. *IEEE Transactions on Robotics*, 33(5):1255–1262, 2017.

[76] Yahui Wang, Shaojun Cai, Shi-Jie Li, Yun Liu, Yangyan Guo, Tao Li, and Ming-Ming Cheng. Cubemapslam: A piecewise-pinhole monocular fisheye slam system. In *Asian Conference on Computer Vision*, pages 34–49. Springer, 2018.

[77] Rau´ l Mur-Artal and Juan D Tardo´ s. Visual-inertial monocular slam with map reuse. *IEEE Robotics and Automation Letters*, 2(2):796– 803, 2017.

[78] Christian Forster, Luca Carlone, Frank Dellaert, and Davide Scara- muzza. On-manifold preintegration for real-time visual–inertial odom- etry. *IEEE Transactions on Robotics*, 33(1):1–21, 2016.

[79] D.Schlegel,M.Colosi,andG.Grisetti.ProSLAM:GraphSLAMfrom a Programmer's Perspective. In *2018 IEEE International Conference on Robotics and Automation (ICRA)*, pages 1–9, 2018.

[80] Guofeng Zhang, Haomin Liu, Zilong Dong, Jiaya Jia, Tien-Tsin Wong, and Hujun Bao. Efficient non-consecutive feature tracking for robust structure-from-motion. *IEEE Transactions on Image Processing*, 25(12):5957–5970, 2016.

[81] Shinya Sumikura, Mikiya Shibuya, and Ken Sakurada. Openvslam: a versatile visual slam framework, 2019.

[82] Bernd Pfrommer and Kostas Daniilidis. Tagslam: Robust slam with fiducial markers. *arXiv preprint arXiv:1910.00679*, 2019.

[83] Rafael Munoz-Salinas and Rafael Medina-Carnicer. Ucoslam: Simul- taneous localization and mapping by fusion of keypoints and squared planar markers. *arXiv preprint arXiv:1902.03729*, 2019.

[84] Jakob Engel, Thomas Scho¨ps, and Daniel Cremers. Lsd-slam: Large- scale direct monocular slam. In *European conference on computer vision*, pages 834–849. Springer, 2014.

[85] Jakob Engel, Jo¨ rg Stu¨ ckler, and Daniel Cremers. Large-scale direct slam with stereo cameras. In *2015 IEEE/RSJ International Conference on Intelligent Robots and Systems (IROS)*, pages 1935–1942. IEEE, 2015.

[86] David Caruso, Jakob Engel, and Daniel Cremers. Large-scale direct slam for omnidirectional cameras. In *2015 IEEE/RSJ International Conference on Intelligent Robots and Systems (IROS)*, pages 141–148. IEEE, 2015.

[87] Jianfeng Li, Xiaowei Wang, and Shigang Li. Spherical-model-based slam on full-view images for indoor environments. *Applied Sciences*, 8(11):2268, 2018.

[88] Christian Forster, Zichao Zhang, Michael Gassner, Manuel Werl- berger, and Davide Scaramuzza. Svo: Semidirect visual odometry for monocular and multicamera systems. *IEEE Transactions on Robotics*, 33(2):249–265, 2016.

[89] ShingYanLoo,AliJahaniAmiri,SyamsiahMashohor,SaiHongTang, and Hong Zhang. Cnn-svo: Improving the mapping in semi-direct visual odometry using single-image depth prediction. *arXiv preprint arXiv:1810.01011*, 2018.

[90] Jakob Engel, Vladlen Koltun, and Daniel Cremers. Direct sparse odometry. *CoRR*, abs/1607.02565, 2016.

[91] Jakob Engel, Vladlen Koltun, and Daniel Cremers. Direct sparse odom- etry. *IEEE transactions on pattern analysis and machine intelligence*, 40(3):611–625, 2017.

[92] Henri Rebecq, Timo Horstscha¨fer, Guillermo Gallego, and Davide Scaramuzza. Evo: A geometric approach to event-based 6-dof parallel tracking and mapping in real time. *IEEE Robotics and Automation Letters*, 2(2):593–600, 2016.

[93] Yi Zhou, Guillermo Gallego, Henri Rebecq, Laurent Kneip, Hongdong Li, and Davide Scaramuzza. Semi-dense 3d reconstruction with a stereo event camera. In *Proceedings of the European Conference on Computer Vision (ECCV)*, pages 235–251, 2018.

[94] David Weikersdorfer, Raoul Hoffmann, and Jo¨rg Conradt. Simulta- neous localization and mapping for event-based vision systems. In *International Conference on Computer Vision Systems*, pages 133–142. Springer, 2013.

[95] David Weikersdorfer, David B Adrian, Daniel Cremers, and Jo¨rg Conradt. Event-based 3d slam with a depth-augmented dynamic vision sensor. In *2014 IEEE*

International Conference on Robotics and Automation (ICRA), pages 359–364. IEEE, 2014.

[96] Javier Civera, Andrew J Davison, and JM Martinez Montiel. Inverse depth parametrization for monocular slam. *IEEE transactions on robotics*, 24(5):932–945, 2008.

[97] Richard A Newcombe, Steven J Lovegrove, and Andrew J Davison. Dtam: Dense tracking and mapping in real-time. In *2011 international conference on computer vision*, pages 2320–2327. IEEE, 2011.

[98] W Nicholas Greene, Kyel Ok, Peter Lommel, and Nicholas Roy. Multi-level mapping: Real-time dense monocular slam. In *2016 IEEE International Conference on Robotics and Automation (ICRA)*, pages 833–840. IEEE, 2016.

[99] Richard A Newcombe, Shahram Izadi, Otmar Hilliges, David Molyneaux, David Kim, Andrew J Davison, Pushmeet Kohli, Jamie Shotton, Steve Hodges, and Andrew W Fitzgibbon. Kinectfusion: Real- time dense surface mapping and tracking. In *ISMAR*, volume 11, pages 127–136, 2011.

[100]ShahramIzadi,DavidKim,OtmarHilliges,DavidMolyneaux,Richard Newcombe, Pushmeet Kohli, Jamie Shotton, Steve Hodges, Dustin Freeman, Andrew Davison, et al. Kinectfusion: real-time 3d reconstruction and interaction using a moving depth camera. In *Proceedings of the 24th annual ACM symposium on User interface software and technology*, pages 559–568. ACM, 2011.

[101] Frank Steinbrücker, Jürgen Sturm, and Daniel Cremers. Real-time visual odometry from dense rgb-d images. In *2011 IEEE International Conference on Computer Vision Workshops (ICCV Workshops)*, pages 719–722. IEEE, 2011.

[102] Christian Kerl, Jürgen Sturm, and Daniel Cremers. Robust odometry estimation for rgb-d cameras. In *2013 IEEE International Conference on Robotics and Automation*, pages 3748–3754. IEEE, 2013.

[103] Christian Kerl, Jürgen Sturm, and Daniel Cremers. Dense visual slam for rgb-d cameras. In *2013 IEEE/RSJ International Conference on Intelligent Robots and Systems*, pages 2100–2106. IEEE, 2013.

[104] Felix Endres, Jürgen Hess, Jürgen Sturm, Daniel Cremers, and Wolfram Burgard. 3-d mapping with an rgb-d camera. *IEEE transactions on robotics*, 30(1):177–187, 2013.

[105] Thomas Whelan, Michael Kaess, Maurice Fallon, Hordur Johannsson, John J Leonard, and John McDonald. Kintinuous: Spatially extended kinectfusion. 2012.

[106] Thomas Whelan, Michael Kaess, Hordur Johannsson, Maurice Fallon, John J Leonard, and John McDonald. Real-time large-scale dense rgb- d slam with volumetric fusion. *The International Journal of Robotics Research*, 34(4-5):598–626, 2015.

[107] Thomas Whelan, Hordur Johannsson, Michael Kaess, John J. Leonard, and John Mcdonald. Robust real-time visual odometry for dense rgb-d mapping. In *IEEE International Conference on Robotics and Automation*, 2011.

[108] Mathieu Labbe and François Michaud. Online global loop closure detection for large-scale multi-session graph-based slam. In *2014 IEEE/RSJ International Conference on Intelligent Robots and Systems*, pages 2661–2666. IEEE, 2014.

[109] MM Labbé and F Michaud. Appearance-based loop closure detection in real-time for large-scale and long-term operation. *IEEE Transactions on Robotics*, pages 734–745.

[110] Mathieu Labbé and François Michaud. Memory management for real- time appearance-based loop closure detection. In *2011 IEEE/RSJ International Conference on Intelligent Robots and Systems*, pages 1271–1276. IEEE, 2011.

[111] Mathieu Labbé and François Michaud. Rtab-map as an open-source lidar and visual simultaneous localization and mapping library for large-scale and long-term online operation. *Journal of Field Robotics*, 36(2):416–446, 2019.

[112] Richard A Newcombe, Dieter Fox, and Steven M Seitz. Dynamicfu- sion: Reconstruction and tracking of non-rigid scenes in real-time. In *Proceedings of the IEEE conference on computer vision and pattern recognition*, pages 343–352, 2015.

[113] Matthias Innmann, Michael Zollhöfer, Matthias Nießner, Christian Theobalt, and Marc Stamminger. Volumedeform: Real-time volumetric non-rigid reconstruction. In *European Conference on Computer Vision*, pages 362–379. Springer, 2016.

[114] Mingsong Dou, Sameh Khamis, Yury Degtyarev, Philip Davidson, Sean Ryan Fanello, Adarsh Kowdle, Sergio Orts Escolano, Christoph Rhemann, David Kim, Jonathan Taylor, et al. Fusion4d: Real-time performance capture of challenging scenes. *ACM Transactions on Graphics (TOG)*, 35(4):114, 2016.

[115] Thomas Whelan, Stefan Leutenegger, R Salas-Moreno, Ben Glocker, and Andrew Davison. Elasticfusion: Dense slam without a pose graph. Robotics: Science and Systems, 2015.

[116] Thomas Whelan, Renato F Salas-Moreno, Ben Glocker, Andrew J Davison, and Stefan Leutenegger. Elasticfusion: Real-time dense slam and light source estimation. *The International Journal of Robotics Research*, 35(14):1697–1716, 2016.

[117] V A Prisacariu, O Kähler, S Golodetz, M Sapienza, T Cavallari, P H S Torr, and D W Murray. InfiniTAM v3: A Framework for Large-Scale 3D Reconstruction with Loop Closure. *arXiv pre-print arXiv:1708.00783v1*, 2017.

[118]OlafKähler,VictorAdrianPrisacariu,andDavidW. Murray.Real-time large-scale dense 3d reconstruction with loop closure. In *Computer Vision - ECCV 2016 - 14th European Conference, Amsterdam, The Netherlands, October 11-14, 2016, Proceedings, Part VIII*, pages 500– 516, 2016.

[119] Angela Dai, Matthias Nießner, Michael Zollöfer, Shahram Izadi, and Christian Theobalt. Bundlefusion: Real-time globally consistent 3d re- construction using on-the-fly surface re-integration. *ACM Transactions on Graphics 2017 (TOG)*, 2017.

[120]Charlie Houseago, Michael Bloesch, and Stefan Leutenegger. Ko- fusion: Dense visual slam with tightly-coupled kinematic and odo- metric tracking. In *2019 International Conference on Robotics and Automation (ICRA)*, pages 4054–4060. IEEE, 2019.

[121]Igor Cvišic, Josip Cesic, Ivan Markovic, and Ivan Petrovic. Soft- slam: Computationally efficient stereo visual slam for autonomous uavs. *Journal of field robotics*, 2017.

[122]IgorCvišićandIvanPetrović.Stereoodometrybase doncarefulfeature selection and tracking. In *2015 European Conference on Mobile Robots (ECMR)*, pages 1–6. IEEE, 2015.

[123] Haomin Liu, Chen Li, Guojun Chen, Guofeng Zhang, Michael Kaess, and Hujun Bao. Robust keyframe-based dense slam with an rgb-d camera. *arXiv preprint arXiv:1711.05166*, 2017.

[124] Weichen Dai, Yu Zhang, Ping Li, and Zheng Fang. Rgb-d slam in dynamic environments using points correlations. *arXiv preprint arXiv:1811.03217*, 2018.

[125] T. Schneider, M. T. Dymczyk, M. Fehr, K. Egger, S. Lynen, I. Gilitschenski, and R. Siegwart. maplab: An open framework for research in visual-inertial mapping and localization. *IEEE Robotics and Automation Letters*, 2018.

[126] Jing Xu Hao Su Rui Chen, Songfang Han. Point-based multi-view stereo network. *arXiv preprint arXiv:1908.04422*, 2019.

[127] Binbin Xu, Wenbin Li, Dimos Tzoumanikas, Michael Bloesch, Andrew Davison, and Stefan Leutenegger. Mid-fusion: Octree-based object- level multi-instance dynamic slam. *arXiv preprint arXiv:1812.07976*, 2018.

[128] M. Runz, M. Buffier, and L. Agapito. Maskfusion: Real-time recog- nition, tracking and reconstruction of multiple moving objects. In *2018 IEEE International Symposium on Mixed and Augmented Reality (ISMAR)*, pages 10–20, Oct 2018.

[129] Hauke Strasdat, J Montiel, and Andrew J Davison. Scale drift-aware large scale monocular slam. *Robotics: Science and Systems VI*, 2(3):7, 2010.

[130] Stefan Leutenegger, Simon Lynen, Michael Bosse, Roland Siegwart, and Paul Furgale. Keyframe-based visual–inertial odometry using non- linear optimization. *The International Journal of Robotics Research*, 34(3):314–334, 2015.

[131] Guoquan Huang, Michael Kaess, and John J Leonard. Towards consis- tent visual-inertial navigation. In *2014 IEEE International Conference on Robotics and Automation (ICRA)*, pages 4926–4933. IEEE, 2014.

[132] Mingyang Li and Anastasios I Mourikis. High-precision, consistent ekf-based visual-inertial odometry. *The International Journal of Robotics Research*, 32(6):690–711, 2013.

[133] Carlos Campos, J. M. M. Montiel, and Juan D. Tardós. Fast and robust initialization for visual-inertial slam. *2019 International Conference on Robotics and Automation (ICRA)*, pages 1288–1294, 2019.

[134] Mark Froehlich, Salman Azhar, and Matthew Vanture. An investigation of google tango® tablet for low cost 3d scanning. In *ISARC. Pro- ceedings of the International Symposium on Automation and Robotics in Construction*, volume 34. Vilnius Gediminas Technical University, Department of Construction Economics , 2017.

[135] Mathieu Garon, Pierre-Olivier Boulet, Jean-Philippe Doironz, Luc Beaulieu, and Jean-Franc ̧ois Lalonde. Real-time high resolution 3d data on the hololens. In *2016 IEEE International Symposium on Mixed and Augmented Reality (ISMAR-Adjunct)*, pages 189–191. IEEE, 2016.

[136] Bernd Pfrommer, Nitin Sanket, Kostas Daniilidis, and Jonas Cleveland. Penncosyvio: A challenging visual inertial odometry benchmark. In 2017 IEEE International Conference on Robotics and Automation (ICRA), pages 3847–3854. IEEE, 2017.

[137] Jeffrey Delmerico and Davide Scaramuzza. A benchmark comparison of monocular visual-inertial odometry algorithms for flying robots. In *2018 IEEE International Conference on Robotics and Automation (ICRA)*, pages 2502–2509. IEEE, 2018.

[138] Stephan M Weiss. *Vision based navigation for micro helicopters*. PhD thesis, ETH Zurich, 2012.

[139] Anastasios I Mourikis and Stergios I Roumeliotis. A multi-state con- straint kalman filter for vision-aided inertial navigation. In *Proceedings 2007 IEEE International Conference on Robotics and Automation*, pages 3565–3572. IEEE, 2007.

[140] Ke Sun, Kartik Mohta, Bernd Pfrommer, Michael Watterson, Sikang Liu, Yash Mulgaonkar, Camillo J Taylor, and Vijay Kumar. Robust stereo visual inertial odometry for fast autonomous flight. *IEEE Robotics and Automation Letters*, 3(2):965–972, 2018.

[141] Michael Bloesch, Sammy Omari, Marco Hutter, and Roland Siegwart. Robust visual inertial odometry using a direct ekf-based approach. In *2015 IEEE/RSJ international conference on intelligent robots and systems (IROS)*, pages 298–304. IEEE, 2015.

[142] Peiliang Li, Tong Qin, Botao Hu, Fengyuan Zhu, and Shaojie Shen. Monocular visual-inertial state estimation for mobile augmented reality. In *2017 IEEE International Symposium on Mixed and Augmented Reality (ISMAR)*, pages 11–21. IEEE, 2017.

[143] Tong Qin and Shaojie Shen. Online temporal calibration for monocular visual-inertial systems. In *2018 IEEE/RSJ International Conference on Intelligent Robots and Systems (IROS)*, pages 3662–3669. IEEE, 2018.

[144] Tong Qin and Shaojie Shen. Robust initialization of monocular visual- inertial estimation on aerial robots. In *2017 IEEE/RSJ International Conference on Intelligent Robots and Systems (IROS)*, pages 4225–4232. IEEE, 2017.

[145] Zhenfei Yang and Shaojie Shen. Monocular visual–inertial state esti- mation with online initialization and camera–imu extrinsic calibration. *IEEE Transactions on Automation Science and Engineering*, 14(1):39– 51, 2016.

[146] Haomin Liu, Mingyu Chen, Guofeng Zhang, Hujun Bao, and Yingze Bao. Ice-ba: Incremental, consistent and efficient bundle adjustment for visual-inertial slam. In *Proceedings of the IEEE Conference on Computer Vision and Pattern Recognition*, pages 1974–1982, 2018.

[147] Danping Zou, Yuanxin Wu, Ling Pei, Haibin Ling, and Wenxian Yu. Structvio: Visual-inertial odometry with structural regularity of man- made environments. *IEEE Transactions on Robotics*, 2019.

[148] Haomin Liu, Guofeng Zhang, and Hujun Bao. Robust keyframe-based monocular slam for augmented reality. In *2016 IEEE International Symposium on Mixed and Augmented Reality (ISMAR)*, pages 1–10. IEEE, 2016.

[149] Elias Mueggler, Guillermo Gallego, Henri Rebecq, and Davide Scara- muzza. Continuous-time visual-inertial odometry for event cameras. *IEEE Transactions on Robotics*, 34(6):1425–1440, 2018.

[150] Alex Zihao Zhu, Nikolay Atanasov, and Kostas Daniilidis. Event-based visual inertial odometry. In *2017 IEEE Conference on Computer Vision and Pattern Recognition (CVPR)*, pages 5816–5824. IEEE, 2017.

[151] Kaleb J Nelson. Event-based visual-inertial odometry on a fixed-wing unmanned aerial vehicle. Technical report, AIR FORCE INSTITUTE OF TECHNOLOGY WRIGHT-PATTERSON AFB OH WRIGHT- PATTERSON, 2019.

[152] Kevin Eckenhoff, Patrick Geneva, and Guoquan Huang. Sensor- failure-resilient multi-imu

visual-inertial navigation. *2019 International Conference on Robotics and Automation (ICRA)*, pages 3542–3548, 2019.

[153] E Jared Shamwell, Kyle Lindgren, Sarah Leung, and William D Nothwang. Unsupervised deep visual-inertial odometry with online error correction for rgb-d imagery. *IEEE transactions on pattern analysis and machine intelligence*, 2019.

[154] Hongyun Lee, Matthew McCrink, and James W Gregory. Visual- inertial odometry for unmanned aerial vehicle using deep learning. In *AIAA Scitech 2019 Forum*, page 1410, 2019.

[155] Shichao Yang, Yu Song, Michael Kaess, and Sebastian Scherer. Pop- up slam: Semantic monocular plane slam for low-texture environments. In *2016 IEEE/RSJ International Conference on Intelligent Robots and Systems (IROS)*, pages 1222–1229. IEEE, 2016.

[156] Georgios Pavlakos, Xiaowei Zhou, Aaron Chan, Konstantinos G Derpa- nis, and Kostas Daniilidis. 6-dof object pose from semantic keypoints. In *2017 IEEE International Conference on Robotics and Automation (ICRA)*, pages 2011–2018. IEEE, 2017.

[157] Kwang Moo Yi, Eduard Trulls, Vincent Lepetit, and Pascal Fua. Lift: Learned invariant feature transform. In *European Conference on Computer Vision*, pages 467–483. Springer, 2016.

[158]Daniel DeTone, Tomasz Malisiewicz, and Andrew Rabinovich. Toward geometric deep slam. *arXiv preprint arXiv:1707.07410*, 2017.

[159] Daniel DeTone, Tomasz Malisiewicz, and Andrew Rabinovich. Su- perpoint: Self-supervised interest point detection and description. In *Proceedings of the IEEE Conference on Computer Vision and Pattern Recognition Workshops*, pages 224–236, 2018.

[160] Peiliang Li, Qin Tong, and Shaojie Shen. Stereo vision-based semantic 3d object and ego-motion tracking for autonomous driving. In *Euro- pean Conference on Computer Vision*, 2018.

[161] Jiexiong Tang, Ludvig Ericson, John Folkesson, and Patric Jensfelt. Gcnv2: Efficient correspondence prediction for real-time slam. *arXiv preprint arXiv:1902.11046*, 2019.

[162] Margarita Grinvald, Fadri Furrer, Tonci Novkovic, Jen Jen Chung, Cesar Cadena, Roland Siegwart, and Juan Nieto. Volumetric instance- aware semantic mapping and 3d object discovery. *arXiv preprint arXiv:1903.00268*, 2019.

[163] Huai-Jen Liang, Nitin J Sanket, Cornelia Fermu ̈ller, and Yiannis Aloimonos. Salientdso: Bringing attention to direct sparse odometry. *IEEE Transactions on Automation Science and Engineering*, 2019.

[164] Mehdi Hosseinzadeh, Yasir Latif, Trung Pham, Niko Suenderhauf, and Ian Reid. Structure aware slam using quadrics and planes. In *Asian Conference on Computer Vision*, pages 410–426. Springer, 2018.

[165] Shichao Yang and Sebastian Scherer. Cubeslam: Monocular 3-d object slam. *IEEE Transactions on Robotics*, 2019.

[166] Shichao Yang and Sebastian Scherer. Monocular object and plane slam in structured environments. *IEEE Robotics and Automation Letters*, 4(4):3145–3152, 2019.

[167] Zengyi Qin, Jinglu Wang, and Yan Lu. Monogrnet: A geometric reasoning network for 3d object localization. *The Thirty-Third AAAI Conference on Artificial Intelligence (AAAI-19)*, 2019.

[168] Xavier Lagorce, Sio Hoi Ieng, and Ryad Benosman. Event-based features for robotic vision. In *IEEE/RSJ International Conference on Intelligent Robots & Systems*, 2013.

[169] Elias Mueggler, Chiara Bartolozzi, and Davide Scaramuzza. Fast event- based corner detection. In *BMVC*, 2017.

[170] Xiongwei Wu, Doyen Sahoo, and Steven CH Hoi. Recent advances in deep learning for object detection. *arXiv preprint arXiv:1908.03673*, 2019.

[171 Renato F. Salas-Moreno, Richard A. Newcombe, Hauke Strasdat, Paul H. J. Kelly, and Andrew J. Davison. Slam++: Simultaneous localisation and mapping at the level of objects. In *Computer Vision & Pattern Recognition*, 2013.

[172] Xuanpeng Li and Rachid Belaroussi. Semi-dense 3d semantic mapping from monocular slam. 2016.

[173] John McCormac, Ankur Handa, Andrew Davison, and Stefan Leuteneg- ger. Semanticfusion: Dense 3d semantic mapping with convolutional neural networks. In *2017 IEEE International Conference on Robotics and automation (ICRA)*, pages 4628–4635. IEEE, 2017.

[174] Niko Sunderhauf, Trung T. Pham, Yasir Latif, Michael Milford, and Ian Reid. Meaningful maps with object-oriented semantic mapping. In *IEEE/RSJ International Conference on Intelligent Robots & Systems*, 2017.

[175]Jiajun Wu, Yifan Wang, Tianfan Xue, Xingyuan Sun, Bill Freeman, and Josh Tenenbaum. Marrnet: 3d shape reconstruction via 2.5 d sketches. In *Advances in neural information processing systems*, pages 540–550, 2017.

[176] Angela Dai and Matthias Nießner. 3dmv: Joint 3d-multi-view pre- diction for 3d semantic scene segmentation. In *Proceedings of the European Conference on Computer Vision (ECCV)*, pages 452–468, 2018.

[177] Xingyuan Sun, Jiajun Wu, Xiuming Zhang, Zhoutong Zhang, Chengkai Zhang, Tianfan Xue, Joshua B Tenenbaum, and William T Freeman. Pix3d: Dataset and methods for single-image 3d shape modeling. In *IEEE Conference on Computer Vision and Pattern Recognition (CVPR)*, 2018.

[178] Angela Dai, Daniel Ritchie, Martin Bokeloh, Scott Reed, Ju ̈rgen Sturm, and Matthias Nießner. Scancomplete: Large-scale scene completion and semantic segmentation for 3d scans. In *Proceedings of the IEEE Conference on Computer Vision and Pattern Recognition*, pages 4578– 4587, 2018.

[179] John McCormac, Ronald Clark, Michael Bloesch, Andrew J. Davison, and Stefan Leutenegger. Fusion++: Volumetric object-level slam. *2018 International Conference on 3D Vision (3DV)*, pages 32–41, 2018.

[180] Renaud Dube ́, Andrei Cramariuc, Daniel Dugas, Juan Nieto, Roland Siegwart, and Cesar Cadena. Segmap: 3d segment mapping using data- driven descriptors. *arXiv preprint arXiv:1804.09557*, 2018.

[181] Ji Hou, Angela Dai, and Matthias Nießner. 3d-sis: 3d semantic instance segmentation of rgb-d scans. In *Proceedings of the IEEE Conference on Computer Vision and Pattern Recognition*, pages 4421–4430, 2019.

[182] Yu Xiang and Dieter Fox. Da-rnn: Semantic mapping with data associated recurrent neural networks. *arXiv preprint arXiv:1703.03098*, 2017.

[183] Chen Wang, Danfei Xu, Yuke Zhu, Roberto Mart ́ın-Mart ́ın, Cewu Lu, Li Fei-Fei, and Silvio Savarese. Densefusion: 6d object pose estimation by iterative dense fusion. In *Proceedings of the IEEE Conference on Computer Vision and Pattern Recognition*, pages 3343–3352, 2019.

[184] Zilong Huang, Xinggang Wang, Lichao Huang, Chang Huang, Yunchao Wei, and Wenyu Liu. Ccnet: Criss-cross attention for semantic segmentation. *arXiv preprint arXiv:1811.11721*, 2018.

[185]EvangelosStromatias,MiguelSoto,Mar ́ıaTeresaSerranoGotarredona, and Bernabe ́ Linares Barranco. An event-based classifier for dynamic vision sensor and synthetic data. *Frontiers in Neuroscience, 11 (art ́ıculo 360)*, 2017.

[186] Jean-Matthieu Maro and Ryad Benosman. Event-based gesture recog- nition with dynamic background suppression using smartphone com- putational capabilities. *arXiv preprint arXiv:1811.07802*, 2018.

[187] Saeed Afshar, Tara Julia Hamilton, Jonathan C Tapson, Andre ́ van Schaik, and Gregory Kevin Cohen. Investigation of event-based mem- ory surfaces for high-speed detection, unsupervised feature extraction, and object recognition. *Frontiers in neuroscience*, 12:1047, 2018.

[188] Alejandro Linares-Barranco, Antonio Rios-Navarro, Ricardo Tapiador- Morales, and Tobi Delbruck. Dynamic vision sensor integration on fpga-based cnn accelerators for high-speed visual classification. *arXiv preprint arXiv:1905.07419*, 2019.

[189] Keisuke Tateno, Federico Tombari, Iro Laina, and Nassir Navab. Cnn- slam: Real-time dense monocular slam with learned depth prediction. In *Proceedings of the IEEE Conference on Computer Vision and Pattern Recognition*, pages 6243–6252, 2017.

[190] Vikram Mohanty, Shubh Agrawal, Shaswat Datta, Arna Ghosh, Vishnu Dutt Sharma, and Debashish Chakravarty. Deepvo: A deep learning approach for monocular visual odometry. *arXiv preprint arXiv:1611.06069*, 2016.

[191] Buyu Li, Wanli Ouyang, Lu Sheng, Xingyu Zeng, and Xiaogang Wang. Gs3d: An efficient 3d object detection framework for autonomous driving. In *Proceedings of the IEEE Conference on Computer Vision and Pattern Recognition*, pages 1019–1028, 2019.

[192] Ruihao Li, Sen Wang, Zhiqiang Long, and Dongbing Gu. Undeepvo: Monocular visual odometry through unsupervised deep learning. In *2018 IEEE International Conference on Robotics and Automation (ICRA)*, pages 7286–7291. IEEE, 2018.

[193] Zhengqi Li, Tali Dekel, Forrester Cole, Richard Tucker, Noah Snavely, Ce Liu, and William T Freeman. Learning the depths of moving people by watching frozen people. In *Proceedings of the IEEE Conference on Computer Vision and Pattern Recognition*, pages 4521–4530, 2019.

[194] D. Frost, V. Prisacariu, and D. Murray. Recovering stable scale in monocular slam using object-supplemented bundle adjustment. *IEEE Transactions on Robotics*, 34(3):736–747, June 2018.

[195] Edgar Sucar and Jean Bernard Hayet. Bayesian scale estimation for monocular slam based on generic object detection for correcting scale drift. 2017.

[196] Zhichao Yin and Jianping Shi. Geonet: Unsupervised learning of dense depth, optical flow and camera pose. In *CVPR*, 2018.

[197] Michael Bloesch, Jan Czarnowski, Ronald Clark, Stefan Leutenegger, and Andrew J Davison. Codeslamlearning a compact, optimisable representation for dense visual slam. In *Proceedings of the IEEE Conference on Computer Vision and Pattern Recognition*, pages 2560– 2568, 2018.

[198] Fabian Brickwedde, Steffen Abraham, and Rudolf Mester. Mono- stixels: monocular depth reconstruction of dynamic street scenes. In *2018 IEEE International Conference on Robotics and Automation (ICRA)*, pages 1–7. IEEE, 2018.

[199] Yasin Almalioglu, Muhamad Risqi U. Saputra, Pedro Porto Buarque de Gusma˜o, Andrew Markham, and Agathoniki Trigoni. Ganvo: Unsupervised deep monocular visual odometry and depth estimation with generative adversarial networks. *2019 International Conference on Robotics and Automation (ICRA)*, pages 5474–5480, 2018.

[200]Punarjay Chakravarty, Praveen Narayanan, and Tom Roussel. Gen- slam: Generative modeling for monocular simultaneous localization and mapping. *arXiv preprint arXiv:1902.02086*, 2019.

[201]KatrinLasinger,Rene´Ranftl,KonradSchindler,and VladlenKoltun. Towards robust monocular depth estimation: Mixing datasets for zero- shot cross-dataset transfer. *arXiv:1907.01341*, 2019.

[202] Po-Han Huang, Kevin Matzen, Johannes Kopf, Narendra Ahuja, and Jia-Bin Huang. Deepmvs: Learning multi-view stereopsis. In *Pro- ceedings of the IEEE Conference on Computer Vision and Pattern Recognition*, pages 2821–2830, 2018.

[203] Jia Deng Zachary Teed. Deepv2d: Video to depth with differentiable structure from motion. *arXiv:1812.04605*, 2018.

[204] Germain Haessig, Xavier Berthelon, Sio-Hoi Ieng, and Ryad Benos- man. A spiking neural network model of depth from defocus for event- based neuromorphic vision. *Scientific reports*, 9(1):3744, 2019.

[205] Guillermo Gallego, Henri Rebecq, and Davide Scaramuzza. A unifying contrast maximization framework for event cameras, with applications to motion, depth, and optical flow estimation. In *Proceedings of the IEEE Conference on Computer Vision and Pattern Recognition*, pages 3867–3876, 2018.

[206] Zhen Xie, Shengyong Chen, and Garrick Orchard. Event-based stereo depth estimation using belief propagation. *Frontiers in neuroscience*, 11:535, 2017.

[207] Kishore Reddy Konda and Roland Memisevic. Learning visual odom- etry with a convolutional network. In *VISAPP (1)*, pages 486–490, 2015.

[208] Gabriele Costante, Michele Mancini, Paolo Valigi, and Thomas A Ciarfuglia. Exploring representation learning with cnns for frame-to- frame ego-motion estimation. *IEEE robotics and automation letters*, 1(1):18–25, 2015.

[209] Alex Kendall, Matthew Grimes, and Roberto Cipolla. Posenet: A convolutional network for real-time 6-dof camera relocalization. In *Proceedings of the IEEE international conference on computer vision*, pages 2938–2946, 2015.

[210] Ronald Clark, Sen Wang, Hongkai Wen, Andrew Markham, and Niki Trigoni. Vinet: Visual-inertial odometry as a sequence-to-sequence learning problem. In *Thirty-First AAAI Conference on Artificial Intelligence*, 2017.

[211] Sen Wang, Ronald Clark, Hongkai Wen, and Niki Trigoni. Deepvo: Towards end-to-end visual odometry with deep recurrent convolutional neural networks. In

2017 IEEE International Conference on Robotics and Automation (ICRA), pages 2043–2050. IEEE, 2017.

[212] Tinghui Zhou, Matthew Brown, Noah Snavely, and David G Lowe. Unsupervised learning of depth and ego-motion from video. In *Proceedings of the IEEE Conference on Computer Vision and Pattern Recognition*, pages 1851–1858, 2017.

[213] Sudheendra Vijayanarasimhan, Susanna Ricco, Cordelia Schmid, Rahul Sukthankar, and Katerina Fragkiadaki. Sfm-net: Learning of structure and motion from video. *arXiv preprint arXiv:1704.07804*, 2017.

[214]Konstantinos Nektarios Lianos, Johannes L. Schnberger, Marc Polle- feys, and Torsten Sattler. Vso: Visual semantic odometry. In *European Conference on Computer Vision (ECCV)*, 2018.

[215] Ronald Clark, Sen Wang, Andrew Markham, Niki Trigoni, and Hongkai Wen. Vidloc: A deep spatio-temporal model for 6-dof video-clip relocalization. In *Proceedings of the IEEE Conference on Computer Vision and Pattern Recognition*, pages 6856–6864, 2017.

[216] Guillermo Gallego, Christian Forster, Elias Mueggler, and Davide Scaramuzza. Event-based camera pose tracking using a generative event model. *arXiv preprint arXiv:1510.01972*, 2015.

[217] David Reverter Valeiras, Garrick Orchard, Sio-Hoi Ieng, and Ryad B Benosman. Neuromorphic event-based 3d pose estimation. *Frontiers in neuroscience*, 9:522, 2016.

[218] Sean L. Bowman, Nikolay Atanasov, Kostas Daniilidis, and George J. Pappas. Probabilistic data association for semantic slam. In *IEEE International Conference on Robotics & Automation*, 2017.

[219] Nate Merrill and Guoquan Huang. Lightweight unsupervised deep loop closure. *arXiv preprint arXiv:1805.07703*, 2018.

[220] Erik Stenborg, Carl Toft, and Lars Hammarstrand. Long-term visual localization using semantically segmented images. pages 6484–6490, 2018.

[221] Abel Gawel, Carlo Del Don, Roland Siegwart, Juan Nieto, and Cesar Cadena. X-view: Graph-based semantic multi-view localization. *IEEE Robotics and Automation Letters*, 3(3):1687–1694, 2018.

[222] Kevin Doherty, Dehann Fourie, and John Leonard. Multimodal seman- tic slam with probabilistic data association. In *2019 IEEE International Conference on Robotics and Automation (ICRA). IEEE*, 2019.

[223] Andrea Censi, Jonas Strubel, Christian Brandli, Tobi Delbruck, and Davide Scaramuzza. Low-latency localization by active led markers tracking using a dynamic vision sensor. In *2013 IEEE/RSJ Interna-tional Conference on Intelligent Robots and Systems*, pages 891–898. IEEE, 2013.

[224] Wei Tan, Haomin Liu, Zilong Dong, Guofeng Zhang, and Hujun Bao. Robust monocular slam in dynamic environments. In *2013 IEEE International Symposium on Mixed and Augmented Reality (ISMAR)*, pages 209–218. IEEE, 2013.

[225] Chao Yu, Zuxin Liu, Xin-Jun Liu, Fugui Xie, Yi Yang, Qi Wei, and Qiao Fei. Ds-slam: A semantic visual slam towards dynamic envi- ronments. In *2018 IEEE/RSJ International Conference on Intelligent Robots and Systems (IROS)*, pages 1168–1174. IEEE, 2018.

[226] Waleed Abdulla. Mask r-cnn for object detection and instance segmen- tation on keras and tensorflow, 2017.

[227] Martin Ru ̈nz and Lourdes Agapito. Co-fusion: Real-time segmentation, tracking and fusion of multiple objects. In *2017 IEEE International Conference on Robotics and Automation (ICRA)*, pages 4471–4478. IEEE, 2017.

[228] Fangwei Zhong, Wang Sheng, Ziqi Zhang, China Chen, and Yizhou Wang. Detect-slam: Making object detection and slam mutually beneficial. In *IEEE Winter Conference on Applications of Computer Vision*, 2018.

[229] Berta Bescos, Jose ́ M Fa ́cil, Javier Civera, and Jose ́ Neira. Dynaslam: Tracking, mapping, and inpainting in dynamic scenes. *IEEE Robotics and Automation Letters*, 3(4):4076–4083, 2018.

[230] Raluca Scona, Mariano Jaimez, Yvan R Petillot, Maurice Fallon, and Daniel Cremers. Staticfusion: Background reconstruction for dense rgb-d slam in dynamic environments. In *2018 IEEE International Conference on Robotics and Automation (ICRA)*, pages 1–9. IEEE, 2018.

[231] Zemin Wang, Qian Zhang, Jiansheng Li, Shuming Zhang, and Jingbin Liu. A computationally efficient semantic slam solution for dynamic scenes. *Remote Sensing*, 11(11):1363, 2019.

[232] Linhui Xiao, Jinge Wang, Xiaosong Qiu, Zheng Rong, and Xudong Zou. Dynamic-slam: Semantic monocular visual localization and mapping based on deep learning in dynamic environment. *Robotics and Autonomous Systems*, 117:1–16, 2019.

[233] Ioan Andrei Baˆrsan, Peidong Liu, Marc Pollefeys, and Andreas Geiger. Robust dense mapping for large-scale dynamic environments. In *2018 IEEE International Conference on Robotics and Automation (ICRA)*, pages 7510–7517. IEEE, 2018.

[234] Se-Ho Kim Ue-Hwan Kim and Jong-Hwan Kim. Simvodis: Simultane- ous visual odometry, object detection, and instance segmentation. *IEEE Transactions on Pattern Analysis and Machine Intelligence, Under Review*, 2019.

[235] Muhammad Sualeh and Gon-Woo Kim. Simultaneous localization and mapping in the epoch of semantics: A survey. *International Journal of Control, Automation and Systems*, 17(3):729–742, 2019.

[236] Peng Wang, Ruigang Yang, Binbin Cao, Wei Xu, and Yuanqing Lin. Dels-3d: Deep localization and segmentation with a 3d semantic map. In *Proceedings of the IEEE Conference on Computer Vision and Pattern Recognition*, pages 5860–5869, 2018.

[237] Nikolay Atanasov, Sean L Bowman, Kostas Daniilidis, and George J Pappas. A unifying view of geometry, semantics, and data association in slam. In *IJCAI*, pages 5204–5208, 2018.

[238]RubenGomez-Ojeda,Francisco-AngelMoreno,DavidZun˜iga-Noe¨l, Davide Scaramuzza, and Javier Gonzalez-Jimenez. Pl-slam: a stereo slam system through the combination of points and line segments. *IEEE Transactions on Robotics*, 2019.

[239] Huizhong Zhou, Danping Zou, Ling Pei, Rendong Ying, Peilin Liu, and Wenxian Yu. Structslam: Visual slam with building structure lines. *IEEE Transactions on Vehicular Technology*, 64(4):1364–1375, 2015.

[240] Sren Riisgaard and Morten Rufus Blas. Slam for dummies: A tutorial approach to simultaneous localization and mapping. Technical report, 2005.

[241] Joern Rehder, Janosch Nikolic, Thomas Schneider, Timo Hinzmann, and Roland Siegwart. Extending kalibr: Calibrating the extrinsics of multiple imus and of individual axes. In *2016 IEEE International Conference on Robotics and Automation (ICRA)*, pages 4304–4311. IEEE, 2016.

[242] Kevin Eckenhoff, Patrick Geneva, Jesse Bloecker, and Guoquan Huang. Multi-camera visual-inertial navigation with online intrinsic and ex- trinsic calibration. *2019 International Conference on Robotics and Automation (ICRA)*, pages 3158–3164, 2019.

[243] A. Tedaldi, A. Pretto, and E. Menegatti. A robust and easy to implement method for imu calibration without external equipments. In *Proc. of: IEEE International Conference on Robotics and Automation (ICRA)*, pages 3042–3049, 2014.

[244] A. Pretto and G. Grisetti. Calibration and performance evaluation of low-cost imus. In *Proc. of: 20th IMEKO TC4 International Symposium*, pages 429–434, 2014.

[245] Mingyang Li, Hongsheng Yu, Xing Zheng, and Anastasios I Mourikis. High-fidelity sensor modeling and self-calibration in vision-aided in- ertial navigation. In *2014 IEEE International Conference on Robotics and Automation (ICRA)*, pages 409–416. IEEE, 2014.

[246] Changhao Chen, Stefano Rosa, Yishu Miao, Chris Xiaoxuan Lu, Wei Wu, Andrew Markham, and Niki Trigoni. Selective sensor fusion for neural visual-inertial odometry. In *Proceedings of the IEEE Conference on Computer Vision and Pattern Recognition*, pages 10542–10551, 2019.

[247] Thomas Schops, Torsten Sattler, and Marc Pollefeys. Bad slam: Bundle adjusted direct rgb-d slam. In *The IEEE Conference on Computer Vision and Pattern Recognition (CVPR)*, June 2019.

[248] Adam Harmat, Michael Trentini, and Inna Sharf. Multi-camera tracking and mapping for unmanned aerial vehicles in unstructured environments. *Journal of Intelligent & Robotic Systems*, 78(2):291– 317, 2015.

[249] Steffen Urban and Stefan Hinz. MultiCol-SLAM - a modular real-time multi-camera slam system. *arXiv preprint arXiv:1610.07336*, 2016.

[250] Michael Bloesch, Michael Burri, Sammy Omari, Marco Hutter, and Roland Siegwart. Iterated extended kalman filter based visual-inertial odometry using direct photometric feedback. *The International Journal of Robotics Research*, 36(10):1053–1072, 2017.

[251] Haoyang Ye, Yuying Chen, and Ming Liu. Tightly coupled 3d lidar inertial odometry and mapping. *arXiv preprint arXiv:1904.06993*, 2019.

[252] Deyu Yin, Jingbin Liu, Teng Wu, Keke Liu, Juha Hyyppa¨, and Ruizhi Chen. Extrinsic calibration of 2d laser rangefinders using an existing cuboid-shaped corridor as the reference. *Sensors*, 18(12):4371, 2018.

[253] Shoubin Chen, Jingbin Liu, Teng Wu, Wenchao Huang, Keke Liu, Deyu Yin, Xinlian Liang, Juha Hyyppa¨, and Ruizhi Chen. Extrinsic calibration of 2d laser rangefinders based on a mobile sphere. *Remote Sensing*, 10(8):1176, 2018.

[254] Jesse Sol Levinson. *Automatic laser calibration, mapping, and local- ization for autonomous vehicles*. Stanford University, 2011.

[255] Jesse Levinson and Sebastian Thrun. Automatic online calibration of cameras and lasers. In *Robotics: Science and Systems*, volume 2, 2013.

[256] A. Dhall, K. Chelani, V. Radhakrishnan, and K. M. Krishna. LiDAR- Camera Calibration using 3D-3D Point correspondences. *ArXiv e- prints*, May 2017.

[257] Nick Schneider, Florian Piewak, Christoph Stiller, and Uwe Franke. Regnet: Multimodal sensor registration using deep neural networks. In *2017 IEEE intelligent vehicles symposium (IV)*, pages 1803–1810. IEEE, 2017.

[258] Johannes Graeter, Alexander Wilczynski, and Martin Lauer. Limo: Lidar-monocular visual odometry. 2018.

[259] Ganesh Iyer, J Krishna Murthy, K Madhava Krishna, et al. Calib- net: self-supervised extrinsic calibration using 3d spatial transformer networks. *arXiv preprint arXiv:1803.08181*, 2018.

[260] Faraz M Mirzaei, Dimitrios G Kottas, and Stergios I Roumeliotis. 3d lidar–camera intrinsic and extrinsic calibration: Identifiability and analytical least-squares-based initialization. *The International Journal of Robotics Research*, 31(4):452–467, 2012.

[261] Ryoichi Ishikawa, Takeshi Oishi, and Katsushi Ikeuchi. Lidar and camera calibration using motions estimated by sensor fusion odometry. In *2018 IEEE/RSJ International Conference on Intelligent Robots and Systems (IROS)*, pages 7342–7349. IEEE, 2018.

[262] Jesse Levinson and Sebastian Thrun. Automatic online calibration of cameras and lasers. In *Robotics: Science and Systems*, 2013.

[263] Sharmin Rahman, Alberto Quattrini Li, and Ioannis Rekleitis. Svin2: An underwater slam system using sonar, visual, inertial, and depth sensor.

[264] Changjun Gu, Yang Cong, and Gan Sun. Environment driven under- water camera-imu calibration for monocular visual-inertial slam. *2019 International Conference on Robotics and Automation (ICRA)*, pages 2405–2411, 2019.

[265] Bilal Arain, Chris McCool, Paul Rigby, Daniel Cagara, and Matthew Dunbabin. Improving underwater obstacle detection using semantic image segmentation. *2019 International Conference on Robotics and Automation (ICRA)*, pages 9271–9277, 2019.

[266] Brian Ferris, Dieter Fox, and Neil D Lawrence. Wifi-slam using gaussian process latent variable models. In *IJCAI*, volume 7, pages 2480–2485, 2007.

[267] Mohammed Aladsani, Ahmed Alkhateeb, and Georgios C Trichopou- los. Leveraging mmwave imaging and communications for simul- taneous localization and mapping. In *ICASSP 2019-2019 IEEE International Conference on Acoustics, Speech and Signal Processing (ICASSP)*, pages 4539–4543. IEEE, 2019.

[268] Ojas Kanhere and Theodore S Rappaport. Position locationing for millimeter wave systems. In *2018 IEEE Global Communications Conference (GLOBECOM)*, pages 206–212. IEEE, 2018.

[269] Theodore S Rappaport, Yunchou Xing, Ojas Kanhere, Shihao Ju, Arjuna Madanayake, Soumyajit Mandal, Ahmed Alkhateeb, and Geor- gios C Trichopoulos. Wireless communications and applications above 100 ghz: Opportunities and challenges for 6g and beyond. *IEEE Access*, 7:78729–78757, 2019.

[270] Shehryar Khattak, Christos Papachristos, and Kostas Alexis. Keyframe- based direct thermalinertial odometry. *2019 International Conference on Robotics and Automation (ICRA)*, pages 3563–3569, 2019.

[271] David Ferstl, Christian Reinbacher, Rene Ranftl, Matthias Ru¨ther, and Horst Bischof. Image guided depth upsampling using anisotropic total generalized variation. In *Proceedings of the IEEE International*

Conference on Computer Vision, pages 993–1000, 2013.

[272] Jason Ku, Ali Harakeh, and Steven L Waslander. In defense of classical image processing: Fast depth completion on the cpu. In *2018 15th Conference on Computer and Robot Vision (CRV)*, pages 16–22. IEEE, 2018.

[273] Fangchang Mal and Sertac Karaman. Sparse-to-dense: Depth prediction from sparse depth samples and a single image. In *2018 IEEE International Conference on Robotics and Automation (ICRA)*, pages 1–8. IEEE, 2018.

[274] Jonas Uhrig, Nick Schneider, Lukas Schneider, Uwe Franke, Thomas Brox, and Andreas Geiger. Sparsity invariant cnns. In *2017 Interna- tional Conference on 3D Vision (3DV)*, pages 11–20. IEEE, 2017.

[275] Shreyas S Shivakumar, Ty Nguyen, Steven W Chen, and Camillo J Tay- lor. Dfusenet: Deep fusion of rgb and sparse depth information for im- age guided dense depth completion. *arXiv preprint arXiv:1902.00761*, 2019.

[276] Zhao Chen, Vijay Badrinarayanan, Gilad Drozdov, and Andrew Rabi- novich. Estimating depth from rgb and sparse sensing. In *Proceedings of the European Conference on Computer Vision (ECCV)*, pages 167–182, 2018.

[277] Abdelrahman Eldesokey, Michael Felsberg, and Fahad Shahbaz Khan. Propagating confidences through cnns for sparse data regression. *arXiv preprint arXiv:1805.11913*, 2018.

[278] Xingxing Zuo, Patrick Geneva, Woosik Lee, Yong Liu, and Guoquan Huang. Lic-fusion: Lidar-inertial-camera odometry. *arXiv preprint arXiv:1909.04102*, 2019.

[279] Olivier Aycard, Qadeer Baig, Siviu Bota, Fawzi Nashashibi, Sergiu Nedevschi, Cosmin Pantilie, Michel Parent, Paulo Resende, and Trung- Dung Vu. Intersection safety using lidar and stereo vision sensors. In *2011 IEEE Intelligent Vehicles Symposium (IV)*, pages 863–869. IEEE, 2011.

[280] Ricardo Omar Chavez-Garcia and Olivier Aycard. Multiple sensor fusion and classification for moving object detection and tracking. *IEEE Transactions on Intelligent Transportation Systems*, 17(2):525– 534, 2015.

[281] Hyunggi Cho, Young-Woo Seo, BVK Vijaya Kumar, and Ragu- nathan Raj Rajkumar. A multi-sensor fusion system for moving object detection and tracking in urban driving environments. In *2014 IEEE International Conference on Robotics and Automation (ICRA)*, pages 1836–1843. IEEE, 2014.

[282] Tao Wang, Nanning Zheng, Jingmin Xin, and Zheng Ma. Integrating millimeter wave radar with a monocular vision sensor for on-road obstacle detection applications. *Sensors*, 11(9):8992–9008, 2011.

[283] Guowei Wan, Xiaolong Yang, Renlan Cai, Hao Li, Yao Zhou, Hao Wang, and Shiyu Song. Robust and precise vehicle localization based on multi-sensor fusion in diverse city scenes. In *2018 IEEE International Conference on Robotics and Automation (ICRA)*, pages 4670–4677. IEEE, 2018.

[284] Ji Zhang, Michael Kaess, and Sanjiv Singh. Real-time depth enhanced monocular odometry. In *2014 IEEE/RSJ International Conference on Intelligent Robots and Systems*, pages 4973–4980. IEEE, 2014.

[285] Ji Zhang and Sanjiv Singh. Visual-lidar odometry and mapping: Low- drift, robust, and fast. In *2015 IEEE International Conference on Robotics and Automation (ICRA)*, pages 2174–2181. IEEE, 2015.

[286] Yoshua Nava. *Visual-LiDAR SLAM with loop closure*. PhD thesis, Masters thesis, KTH Royal Institute of Technology, 2018.

[287] Yinglei Xu, Yongsheng Ou, and Tiantian Xu. Slam of robot based on the fusion of vision and lidar. In *2018 IEEE International Conference on Cyborg and Bionic Systems (CBS)*, pages 121–126. IEEE, 2018.

[288] Weizhao Shao, Srinivasan Vijayarangan, Cong Li, and George Kantor. Stereo visual inertial lidar simultaneous localization and mapping. *arXiv preprint arXiv:1902.10741*, 2019.

[289] Franz Andert, Nikolaus Ammann, and Bolko Maass. Lidar-aided cam- era feature tracking and visual slam for spacecraft low-orbit navigation and planetary landing. In *Advances in Aerospace Guidance, Navigation and Control*, pages 605–623. Springer, 2015.

[290] Danfei Xu, Dragomir Anguelov, and Ashesh Jain. Pointfusion: Deep sensor fusion for 3d bounding box

estimation. In *Proceedings of the IEEE Conference on Computer Vision and Pattern Recognition*, pages 244–253, 2018.

[291] Kiwoo Shin, Youngwook Paul Kwon, and Masayoshi Tomizuka. Roar- net: A robust 3d object detection based on region approximation refinement. *arXiv preprint arXiv:1811.03818*, 2018.

[292] Jason Ku, Melissa Mozifian, Jungwook Lee, Ali Harakeh, and Steven Waslander. Joint 3d proposal generation and object detection from view aggregation. *IROS*, 2018.

[293] Caner Hazirbas, Lingni Ma, Csaba Domokos, and Daniel Cremers. Fusenet: Incorporating depth into semantic segmentation via fusion- based cnn architecture. In *Asian conference on computer vision*, pages 213–228. Springer, 2016.

[294] Zining Wang, Wei Zhan, and Masayoshi Tomizuka. Fusing birds eye view lidar point cloud and front view camera image for 3d object detection. In *2018 IEEE Intelligent Vehicles Symposium (IV)*, pages 1–6. IEEE, 2018.

[295] Ming Liang, Bin Yang, Shenlong Wang, and Raquel Urtasun. Deep continuous fusion for multi-sensor 3d object detection. In *Proceedings of the European Conference on Computer Vision (ECCV)*, pages 641– 656, 2018.

[296] Shuo Gu, Tao Lu, Yigong Zhang, Jose M Alvarez, Jian Yang, and Hui Kong. 3-d lidar+ monocular camera: An inverse-depth-induced fusion framework for urban road detection. *IEEE Transactions on Intelligent Vehicles*, 3(3):351–360, 2018.

[297] Cesar Cadena, Luca Carlone, Henry Carrillo, Yasir Latif, Davide Scaramuzza, Jose´ Neira, Ian Reid, and John J Leonard. Past, present, and future of simultaneous localization and mapping: Toward the robust-perception age. *IEEE Transactions on robotics*, 32(6):1309– 1332, 2016.

[298] Titus Cieslewski, Siddharth Choudhary, and Davide Scaramuzza. Data- efficient decentralized visual slam. In *2018 IEEE International Con- ference on Robotics and Automation (ICRA)*, pages 2466–2473. IEEE, 2018.

[299] Cynthia Dwork. Differential privacy. *Encyclopedia of Cryptography and Security*, pages 338–340, 2011.

[300] Frank McSherry and Kunal Talwar. Mechanism design via differential privacy. In *FOCS*, volume 7, pages 94–103, 2007.

[301] Hadi Sarieddeen, Nasir Saeed, Tareq Y Al-Naffouri, and Mohamed- Slim Alouini. Next generation terahertz communications: A rendezvous of sensing, imaging and localization. *arXiv preprint arXiv:1909.10462*, 2019.

[302] Khaled B Letaief, Wei Chen, Yuanming Shi, Jun Zhang, and Ying- Jun Angela Zhang. The roadmap to 6g: Ai empowered wireless networks. *IEEE Communications Magazine*, 57(8):84–90, 2019.

[303] Walid Saad, Mehdi Bennis, and Mingzhe Chen. A vision of 6g wireless systems: Applications, trends, technologies, and open research problems. *IEEE network*, 2019.

[304] Henk Wymeersch, Jiguang He, Benoˆıt Denis, Antonio Clemente, and Markku Juntti. Radio localization and mapping with reconfigurable intelligent surfaces. *arXiv preprint arXiv:1912.09401*, 2019.

[305] Marco Giordani, Michele Polese, Marco Mezzavilla, Sundeep Rangan, and Michele Zorzi. Towards 6g networks: Use cases and technologies. *arXiv preprint arXiv:1903.12216*, 2019.

[306] Walid Saad, Mehdi Bennis, and Mingzhe Chen. A vision of 6g wireless systems: Applications, trends, technologies, and open research problems. *IEEE network*, 2019.

[307] Henk Wymeersch, Jiguang He, Benoˆıt Denis, Antonio Clemente, and Markku Juntti. Radio localization and mapping with reconfigurable intelligent surfaces. *arXiv preprint arXiv:1912.09401*, 2019.

[308] Marco Giordani, Michele Polese, Marco Mezzavilla, Sundeep Rangan, and Michele Zorzi. Towards 6g networks: Use cases and technologies. *arXiv preprint arXiv:1903.12216*, 2019.

Authors

Baichuan Huang has graduated with a master's degree in Computer Application Technology in the State Key Laboratory of Information Engineering in Surveying, Mapping and Remote Sensing, Wuhan University. He gained bachelor's degree in school of electronic information, Wuhan University in 2018. During the period of postgraduate, he was award for winning the National scholarship by Ministry of Education of the People's Republic of China. His research focuses on indoor location with communication, Simultaneous localization and mapping (SLAM), Multi-view stereo reconstruction in 3D computer vision.

Jun Zhao (S'10-M'15) is currently an Assistant Professor in the School of Computer Science and Engineering at Nanyang Technological University (NTU) in Singapore. He received a PhD degree in Electrical and Computer Engineering from Carnegie Mellon University (CMU) in the USA (advisors: Virgil Gligor, Osman Yagan; collaborator: Adrian Perrig), affiliating with CMU's renowned CyLab Security \& Privacy Institute, and a bachelor's degree from Shanghai Jiao Tong University in China. Before joining NTU first as a postdoc with Xiaokui Xiao and then as a faculty member, he was a postdoc at Arizona State University as an Arizona Computing PostDoc Best Practices Fellow (advisors: Junshan Zhang, Vincent Poor). His research interests are Communications \& Networks, Security and AI. One of his first-authored papers was shortlisted for the best student paper award in IEEE International Symposium on Information Theory (ISIT) 2014, a prestigious conference in information theory.

Sheng Luo graduated from Information Engineering University and got his Ph.D. degree in 2014. Now he is a postdoctoral researcher in both Hi-Target Surveying Instrument Co. Ltd and State Key Laboratory of Information Engineering in Surveying, Mapping and Remote Sensing, Wuhan University. His research focuses on UAV-borne Lidar applications on emergency surveying and mapping and 3D Laser SLAM technology.

Jingbin Liu is a Professor in Positioning and Navigation with State Key Laboratory of Information Engineering in Surveying, Mapping and Remote Sensing (LIESMARS) in Wuhan University, China. He received his Ph.D Degree in 2008 from Wuhan University. Dr.Liu worked as Specialist Research Scientist with Finnish Geospatial Research Institute (FGI, formerly known as Finnish Geodetic Institute) from 2008 to 2016. His interest areas include indoor and outdoor positioning, smartphone navigation, indoor mobile mapping, and GNSS/INS/SLAM integration technology.

Journal of Global Positioning Systems (*2021*)

Vol. 17, No. 2: 239-241

An Investigation on Short-Term Prediction of Severe Weather Events Based on GNSS-derived Atmospheric Information

Author: **Haobo Li** (lihaobocumt@163.com)
Supervisors: **Dr. Kefei Zhang and Dr. Xiaoming Wang**
University: **China University of Mining and Technology**

Abstract

In recent years, the increasing frequency of natural disasters caused by various types of severe weather events (SWEs) has resulted in more and more damage and losses to properties and livelihoods. These phenomena highlight a pressing need to understand the intrinsic nature of these events and develop reliable and robust methods for the nowcasting and very short-range forecasting (VSRF) of SWEs, thus to prevent and mitigate the influences brought by all kinds of natural disasters. Facing with the high demand of the VSRF of SWEs, it is necessary to obtain and use various kinds meteorological data with high accuracy and high spatiotemporal resolution in an effective way. Atmospheric water vapor (WV), which is recognized as an essential climate variable, greatly affects the atmosphere stability, the hydrological and energy cycles, and the formation of cloud and rainfall. As one of the most active components in the atmosphere, the evolution of WV has significant implications for determining the intensity, time and extent of potential SWEs. Therefore, to refine the service for the monitoring and detection of SWEs, it is of great importance to obtain the amount of WV contained in the atmosphere and capture its movements. However, the rapid change and dynamic characteristics of WV make it an extremely difficult task to obtain its accurate and timely spatiotemporal distributions in the troposphere using traditional observing techniques such as radiosonde, water vapor radiometers, and etc. With the rapid deployment and development for nearly four decades, the Global Navigation Satellite Systems (GNSS) has been widely used in the remote sensing of atmospheric variables, e.g., zenith total delay (ZTD) and precipitable water vapor (PWV). This is mainly due to the high accuracy, high spatiotemporal resolution and all-weather capability of GNSS observations. Hence, the availability of atmospheric information retrieved from GNSS has opened new avenues and new possibilities for GNSS meteorological applications of the detection of SWEs.

This dissertation focuses on the retrieval of GNSS-derived atmospheric products with high accuracy and high spatiotempeoral resolution, and then apply them to the nowcasting and VSRF of SWEs. The research include: the retrieval of atmospheric products from ground-based GNSS radio signals and their accuracy evaluation, the feature analysis of atmospheric variables and their responses to SWEs, short-term prediction of SWEs using threshold-based models, anomaly-based models and back propagation neural network (BPNN) algorithm. The detailed research contents and major contributions are outlined as follows:

(1) The dissertation firstly illustrates the principles of atmospheric information estimation from ground-based GNSS, then clearly describes the theoretical algorithms, empirical models and various kinds of strategies about the whole processing procedure from GNSS signals to atmospheric delay, ZTD and finally to PWV. The Hong Kong region was selected as the experimental area, the ZTD series over the 10-year study period 2010-2019 at the 15 GNSS stations in the region were estimated using the Precise Point Positioning (PPP) technique based on the RTKLIB software with the near real-time (NRT) strategy. Then, with the incorporation of meteorological data and empirical models, PWV estimates over the same period can be obtained. Finally, the ZTDs provided by the International GNSS service (IGS) and the PWVs estimated from the sounding profiles were adopted to assess the accuracy of those products derived from GNSS observations.

(2) To more comprehensively take the atmospheric environment conditions into account, this study not only obtained the time series of ZTD and PWV over the study period, but also collected the temperature, pressure, relative humidity and the actual records of SWEs within the experimental area. In addition, the two variables of day of year (DOY) and hour of day (HOD), which represent the seasonal and diurnal variations of time-varying variables were also considered. Then, to investigate the correlation between each two of these variables, the Pearson correlation coefficient was adopted to conduct the cross-correlation analysis. Furthermore, this study also used the principal component analysis (PCA) method to figure out each variable’s responses to the occurrence of SWEs and test their contributions and effectiveness in the detection of SWEs, which can be recognized as reference for selecting appropriate predictors in model development.

(3) In this study, severe rainfall event was chosen as an example of SWEs, thus the synoptic process for the formation of severe rainfall event was described in detail. Due to the threshold-based model is easy to operate and has simple principles, hence this study adopted this type of model to develop the 5-factor PWV-based model and the 7-factor ZTD-based model. The two types of new models used five and seven kinds of derivatives from PWV and ZTD series, respectively. It is noted that this study is the first to consider the predictors obtained from the descending trends in the PWV and ZTD series to detect the onset of severe rainfall events. The experimental results of the two types of models suggest that it is promising to use these model to obtain better prediction results and they can be used as effective complements to the operational models.

(4) Analyzing the anomaly series of a variable in response to a weather event is a common practice in the meteorological community, however, for variables derived from GNSS observations, this type of analysis has not been reported in the existing literature, let alone for the application of heavy rainfall detection. Hence, this study is the first to analyze the anomaly and cumulative anomaly time series of GNSS-derived atmospheric products to detect SWEs, and two kinds of new models using anomaly and cumulative anomaly series of GNSS-derived products were proposed. Compared with the threshold-based models, there is no need for those anomaly-based models to select a specific threshold value, thus the efficiency for model development can be greatly improved. However, due to the rapid temporal variation in the GNSS-derived tropospheric variables, their anomaly time series may contain a larger number of high-frequency noisy signals; hence, using the anomaly series of rapidly changing variables for severe rainfall detection is likely to result in poor performance. By using the cumulative anomaly series of these variables to detect severe precipitation events can effectively overcome this problem because those large noises can be effectively filtered out and the integrity of the information contained in the raw time series can be also ensured. In addition, the advantage of using cumulative anomaly series also lies in that the formation of severe rainfall events is a timely response to the accumulated effects of weather parameters over a long period rather than instantaneous features, hence the prediction performance resulted from using cumulative anomaly time series can be further improved in

comparison to that from using the anomaly series.

(5) Based on all the previous studies and discussions, this study also proposed a new method, which is a hybrid of threshold-based model and anomaly-based model, for the VSRF of severe rainfall events. The calculation of the anomaly series of a predictor is to minimize the data range for optimizing the threshold selection process; then, with the obtained anomaly series of a predictor, the improved percentile method was adopted to calculate its specific threshold. In addition, those state-of-the-art techniques proposed for each step contained in the development of a robust detecting model was also utilized in the new method. Consequently, it can be concluded from the experimental results that the anomaly-based percentile thresholds of predictors derived from the PWV/ZTD time series have the potential to be applied to the severe rainfall detection with a reasonably good accuracy.

(6) It can be clearly seen that the above models did not take the meteorological variables, e.g., temperature, pressure, and their impacts on the formation of the onset of SWEs into consideration. Therefore, this study also proposed a new model based on the improved BPNN algorithm, which has the ability of self-learning, nonlinear mapping and fast convergence. The predictors contained in the new model were PWV, ZTD, temperature, pressure, relative humidity, DOY and HOD. Prior to the model training phase, several factors that affecting the model's performance including the selection of hyperparameters, the length of training samples, and its time period were investigated, thus a principle for model development was formulated. While after the training and validation phases of the modelling were completed, the weight maps of the well-trained model were further investigated for the knowledge of the interior structure of the technique and for the determination of the most active variables.

Keywords: Global Navigation Satellite System (GNSS); GNSS meteorology (GNSS/MET); zenith total delay (ZTD); precipitable water vapor (PWV); very short-range forecasting (VSRF); severe weather events

***Journal of Global Positioning Systems* (*2021*)**
Vol. 17, No. 2: 242-243

Journal of Global Positioning Systems
2021

Integer Ambiguity Resolution for Smartphone based multi-GNSS data

Guangcai Li, guangcai.li@whu.edu.cn

Supervisor: **Dr. Jianghui Geng**

School/University: **School of Geodesy and Surveying Engineering, Wuhan University**

Defense Date: **May 22, 2021**

Abstract

Smartphones are integrated with consumer-grade GNSS chips and inertial sensors, providing an effective research platform for tapping the potential of miniaturized, low-cost sensors for high-precision positioning. However, for the GNSS observations of smartphones, phase biases generated by the low-cost GNSS chips and severe multipath errors introduced by the embedded antenna, resulting in unresolved carrier phase ambiguity.

To solve these problems, this dissertation conducts an in-depth study on the key technologies of GNSS ambiguity resolution and other high-precision positioning for smartphones. The error characteristics of smartphone GNSS observations were analyzed, the carrier phase bias estimation method and multipath mitigation method were proposed, and the smartphone GNSS centimeter-level ambiguity-fixed solutions were obtained. Based on this, we further explored methods such as synchronous integration of smartphone GNSS with the accelerometer, and obtained higher precision and higher resolution positioning results. As a result, the feasibility of centimeter-level high-precision positioning using consumer-grade GNSS chips, antennas and inertial sensors embedded in smartphones was demonstrated. Meanwhile, these works can provide theoretical methods and technical support for high-precision positioning using miniaturized, low-cost GNSS and inertial sensors.

Chapter 1 provides an introduction to this thesis.

Chapter 2 presents the basic GNSS positioning theory such as functional model, stochastic model, estimator and ambiguity resolution methods.

In Chapter 3, the quality and error characteristics of recent smartphone multi-GNSS observations are systematically analyzed. Some error characteristics that distinguish survey receivers, such as low signal strength, uneven gain, a weak correlation between signal strength and elevation, frequent cycle slips, and high observation noise, have been found. In addition, duty-cycle, anomalous “jagged” distribution phase error, clock misalignment, and inconsistent pseudorange and phase clock issues in smartphone GNSS observations have also been identified. In addition, the theoretical parameters of the noise versus C/N_0 model are provided for different smartphones GNSS chipsets.

The next two chapters, Chapters 4 and 5, form two important parts of this thesis. The first one deals with the phase bias problem generated by the smartphone GNSS chip in Chapter 4. The second one deals with the severe multipath error issue introduced by the embedded antenna of the smartphone.

In Chapter 4, a double-difference carrier phase bias

and inter-frequency phase bias (IFB) rate extraction method based on the zero/short baseline is proposed. By using this method, the phase biases and the phase IFB rate inconsistent issues of smartphone GNSS observations are found. To solve this problem, a gain filtering-based online phase biases correction method is proposed, and the dual-frequency and full-constellation GNSS ambiguity resolution for the smartphone is implemented.

Two multipath mitigation methods are proposed in Chapter 5. One method is based on the stochastic model compensation of double-difference code-minus-carrier combined observations, and the other method combines stochastic model compensation and functional model correction. Based on these methods, dual-frequency and multi-system GNSS ambiguity resolution is implemented on the smartphone using its embedded GNSS antenna.

Chapter 6 conducts an application study of high-precision broadband positioning based on consumer-grade GNSS chips and accelerometers using smartphones as the research platform. A method to synchronize and integrate Android GNSS with accelerometer data and a single-receiver GNSS/acceleration tight integrated positioning method based on inter-satellite difference are successively proposed. Experimental results show that smartphones using these methods can capture broadband vibrations at centimeter resolution.

Chapter 7 summarizes the thesis and provides an outlook for future research.

Journal of Global Positioning Systems (*2021*)
Vol. 17, No. 2: 244-246

An Investigation on Short-Term Prediction of Severe Weather Events Based on GNSS-derived Atmospheric Information

Haobo Li, lihaobocumt@163.com

Supervisors: **Dr. Kefei Zhang and Dr. Xiaoming Wang**

University: **China University of Mining and Technology**

Defense Date: **Nov 19, 2021**

Abstract

In recent years, the increasing frequency of natural disasters caused by various types of severe weather events (SWEs) has resulted in more and more damage and losses to properties and livelihoods. These phenomena highlight a pressing need to understand the intrinsic nature of these events and develop reliable and robust methods for the nowcasting and very short-range forecasting (VSRF) of SWEs, thus to prevent and mitigate the influences brought by all kinds of natural disasters. Facing with the high demand of the VSRF of SWEs, it is necessary to obtain and use various kinds of meteorological data with high accuracy and high spatiotemporal resolution in an effective way. Atmospheric water vapor (WV), which is recognized as an essential climate variable, greatly affects the atmosphere stability, the hydrological and energy cycles, and the formation of cloud and rainfall. As one of the most active components in the atmosphere, the evolution of WV has significant implications for determining the intensity, time and extent of potential SWEs. Therefore, to refine the service for the monitoring and detection of SWEs, it is of great importance to obtain the amount of WV contained in the atmosphere and capture its movements. However, the rapid change and dynamic characteristics of WV make it an extremely difficult task to obtain its accurate and timely spatiotemporal distributions in the troposphere using traditional observing techniques such as radiosonde, water vapor radiometers, and etc. With the rapid deployment and development for nearly four decades, the Global Navigation Satellite Systems (GNSS) has been widely used in the remote sensing of atmospheric variables, e.g., zenith total delay (ZTD) and precipitable water vapor (PWV). This is mainly due to the high accuracy, high spatiotemporal resolution and all-weather capability of GNSS observations. Hence, the availability of atmospheric information retrieved from GNSS has opened new avenues and new possibilities for GNSS meteorological applications of the detection of SWEs

This dissertation focuses on the retrieval of GNSS-derived atmospheric products with high accuracy and high spatiotemporal resolution, and then apply them to the nowcasting and VSRF of SWEs. The research include: the retrieval of atmospheric products from ground-based GNSS radio signals and their accuracy evaluation, the feature analysis of atmospheric variables and their responses

to SWEs, short-term prediction of SWEs using threshold-based models, anomaly-based models and back propagation neural network (BPNN) algorithm. The detailed research contents and major contributions are outlined as follows:

(1) The dissertation firstly illustrates the principles of atmospheric information estimation from ground-based GNSS, then clearly describes the theoretical algorithms, empirical models and various kinds of strategies about the whole processing procedure from GNSS signals to atmospheric delay, ZTD and finally to PWV. The Hong Kong region was selected as the experimental area, the ZTD series over the 10-year study period 2010-2019 at the 15 GNSS stations in the region were estimated using the Precise Point Positioning (PPP) technique based on the RTKLIB software with the near real-time (NRT) strategy. Then, with the incorporation of meteorological data and empirical models, PWV estimates over the same period can be obtained. Finally, the ZTDs provided by the International GNSS service (IGS) and the PWVs estimated from the sounding profiles were adopted to assess the accuracy of those products derived from GNSS observations.

(2) To more comprehensively take the atmospheric environment conditions into account, this study not only obtained the time series of ZTD and PWV over the study period, but also collected the temperature, pressure, relative humidity and the actual records of SWEs within the experimental area. In addition, the two variables of day of year (DOY) and hour of day (HOD), which represent the seasonal and diurnal variations of time-varying variables were also considered. Then, to investigate the correlation between each two of these variables, the Pearson correlation coefficient was adopted to conduct the cross-correlation analysis. Furthermore, this study also used the principal component analysis (PCA) method to figure out each variable’s responses to the occurrence of SWEs and test their contributions and effectiveness in the detection of SWEs, which can be recognized as reference for selecting appropriate predictors in model development.

(3) In this study, severe rainfall event was chosen as an example of SWEs, thus the synoptic process for the formation of severe rainfall event was described in detail. Due to the threshold-based model is easy to operate and has simple principles, hence this study adopted this type of model to develop the 5-factor PWV-based model and the 7-factor ZTD-based model. The two types of new models used five and seven kinds of derivatives from PWV and ZTD series, respectively. It is noted that this study is the first to consider the predictors obtained from the descending trends in the PWV and ZTD series to detect the onset of severe rainfall events. The experimental results of the two types of models suggest that it is promising to use these model to obtain better prediction results and they can be used as effective complements to the operational models.

(4) Analyzing the anomaly series of a variable in response to a weather event is a common practice in the meteorological community, however, for variables derived from GNSS observations, this type of analysis has not been reported in the existing literature, let alone for the application of heavy rainfall detection. Hence, this study is the first to analyze the anomaly and cumulative anomaly time series of GNSS-derived atmospheric products to detect SWEs, and two kinds of new models using anomaly and cumulative anomaly series of GNSS-derived products were proposed. Compared with the threshold-based models, there is no need for those anomaly-based models to select a specific threshold value, thus the efficiency for model development can be greatly improved. However, due to the rapid temporal variation in the GNSS-derived tropospheric variables, their anomaly time series may contain a larger number of high-frequency noisy signals; hence, using the anomaly series of rapidly changing variables for severe rainfall detection is likely to result in poor performance. By using the cumulative anomaly series of these variables to detect severe precipitation events can effectively overcome this problem because those large noises can be effectively filtered out and the integrity of the information contained in the raw time series can be also ensured. In addition, the advantage of using cumulative anomaly series also lies in that the

formation of severe rainfall events is a timely response to the accumulated effects of weather parameters over a long period rather than instantaneous features, hence the prediction performance resulted from using cumulative anomaly time series can be further improved in comparison to that from using the anomaly series.

(5) Based on all the previous studies and discussions, this study also proposed a new method, which is a hybrid of threshold-based model and anomaly-based model, for the VSRF of severe rainfall events. The calculation of the anomaly series of a predictor is to minimize the data range for optimizing the threshold selection process; then, with the obtained anomaly series of a predictor, the improved percentile method was adopted to calculate its specific threshold. In addition, those state-of-the-art techniques proposed for each step contained in the development of a robust detecting model was also utilized in the new method. Consequently, it can be concluded from the experimental results that the anomaly-based percentile thresholds of predictors derived from the PWV/ZTD time series have the potential to be applied to the severe rainfall detection with a reasonably good accuracy.

(6) It can be clearly seen that the above models did not take the meteorological variables, e.g., temperature, pressure, and their impacts on the formation of the onset of SWEs into consideration. Therefore, this study also proposed a new model based on the improved BPNN algorithm, which has the ability of self-learning, nonlinear mapping and fast convergence. The predictors contained in the new model were PWV, ZTD, temperature, pressure, relative humidity, DOY and HOD. Prior to the model training phase, several factors that affecting the model's performance including the selection of hyperparameters, the length of training samples, and its time period were investigated, thus a principle for model development was formulated. While after the training and validation phases of the modelling were completed, the weight maps of the well-trained model were further investigated for the knowledge of the interior structure of the technique and for the determination of the most active variables.

Keywords: Global Navigation Satellite System (GNSS); GNSS meteorology (GNSS/MET); zenith total delay (ZTD); precipitable water vapor (PWV); very short-range forecasting (VSRF); severe weather events

Volume 17, No. 2, 2021

Journal of Global Positioning Systems

Published by

International Association of Chinese Professionals in Global Positioning Systems (CPGPS)

www.cpgps.org

ISSN 1446-3156 (Print version)

ISSN 1446-3164 (CD-ROM Version)